UNIVERSIDAD
DE BURGOS

SOL GARCÍA RODRÍGUEZ

TESIS DOCTORAL

MODELIZACIÓN MATEMÁTICA DE LA RADIACIÓN SOLAR ULTRAVIOLETA

Dirigida por las Doctoras:

CRISTINA ALONSO TRISTÁN

ANA GARCÍA RODRÍGUEZ

Burgos, Noviembre 2023

Universidad De Burgos

Escuela De Doctorado

Cristina Alonso Tristán y Ana García Rodríguez hacen constar:

Que el presente trabajo, titulado “Modelización matemática de la radiación solar ultravioleta”, que presenta Sol García Rodríguez para la obtención del título de doctor ha sido realizado bajo su supervisión, en el Programa de Doctorado Interuniversitario en Eficiencia Energética y Sostenibilidad en Ingeniería y Arquitectura por la Universidad de Burgos, la Universidad de Vigo y la Universidad del País Vasco/Euskal Herriko Unibertsitatea (5600956; RD 99/2011).

Burgos, 10 de Noviembre de 2023

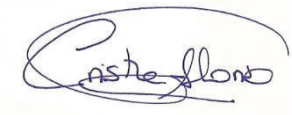

Fdo. Cristina Alonso Tristán

Fdo. Ana García Rodríguez

A Montse

Esta tesis doctoral se presenta en forma de compendio de publicaciones cumpliendo los requisitos establecidos en el Programa de Doctorado “Eficiencia Energética y Sostenibilidad en Ingeniería y Arquitectura”, Programa Interuniversitario de la Universidad de Burgos, de la Universidad del País Vasco/Euskal Herriko Unibertsitatea y de la Universidad de Vigo (RD 99/2011).

Las publicaciones recogen los resultados obtenidos en los diferentes trabajos de investigación desarrollados para alcanzar los objetivos planteados en la tesis doctoral. Las publicaciones referidas se enumeran, en orden de relación con los objetivos de la tesis, en el Epígrafe: Lista de Artículos y constituyen las Secciones I a IV de esta memoria de tesis. Los cuatro artículos que componen la tesis han sido publicados en revistas indexadas en el SCIE del Journal of Citation Reports (JCR).

Esta tesis ha sido financiada en convocatorias competitivas, gracias a los siguientes proyectos de investigación:

1.- Valoración técnica de los niveles de exposición a radiación solar en trabajos de exterior: identificación de grupos de riesgo y medidas de prevención. (INVESTUN/19/BU/004). Junta de Castilla y León. Dirección General de Trabajo y Prevención de riesgos laborales. IP: Montserrat Díez Mediavilla. 01/01/2019-31/12/2021.

2.- Análisis Espectral de la Radiación Solar: Aplicaciones Climáticas, Energéticas y Biológicas (RTI-2018-098900-B-I00). Ministerio de Universidades e Investigación Programa Estatal De I+D+i Orientada a los Retos de la Sociedad. IP: Cristina Alonso Tristán y Montserrat Díez Mediavilla. 1/01/2019-30/09/2022.

3.- Modelado espectral de la radiación solar en entornos urbanos: una oportunidad para la sostenibilidad de las ciudades. (TED2021-

131563B-I00). Agencia Estatal de Investigación. IP: Cristina Alonso Tristán. 1/12/2022-30/11/2024.

4.- Valoración técnica de los niveles óptimos de iluminación efectiva para la salud visual y psicológica en entornos laborales. (INVESTUN/22/BU/001). Junta de Castilla y León. Dirección General de Trabajo y Prevención de riesgos laborales. IP: Cristina Alonso Tristán. 1/01/2022-30/09/2024.

5.- Avances para un urbanismo de bajo consumo energético. (PID2022-139477OB-I00). Agencia Estatal de Investigación. IP: Cristina Alonso Tristán y David González Peña. 1/09/2023-31/08/2026.

Agradecimientos

En primer lugar, y como no podía ser de otra manera, gracias Montse, por haberme dado la oportunidad de hacer esta Tesis, por haber sido mi Directora hasta el último momento, por haber estado desde hace muchos años siempre ahí y habernos dado consejo cuando te lo hemos pedido, por habernos enseñado y demostrado que, aunque haya piedras en el camino, siempre hay que luchar y seguir hacia delante. Gracias por siempre.

Gracias, a mi Directora de Tesis Cristina, por apoyarme y ayudarme durante estos años a lograr este objetivo. Qué buen equipo hacíais Montse y tú.

A Ana, por haberse incorporado como Codirectora en estos últimos y difíciles meses, y haber estado al pie del cañón. Sin ti esto habría sido aún más complicado.

A SWIFT y, en especial, al “Grupo G” por haberme acogido como uno más desde el primer momento, aunque estos últimos meses haya estado un poco ausente, habéis sido un gran apoyo. Porque aún cuando los agobios nos persiguen, siempre sacamos tiempo para unas risas y un vermouth, y todo se hace más llevadero.

Por último, y no por ello menos importante, gracias a mi familia y, sobre todo, a mi madre, por haber hecho que mis tropiezos nunca se hayan convertido en caídas, por haberme aguantado en los malos momentos, por haberme apoyado y ayudado siempre... Gracias por estar siempre ahí.

Resumen

La radiación ultravioleta es la región del espectro solar cuya longitud de onda está comprendida entre 100 y $400\,\mathrm{nm}$. La importancia del conocimiento de esta radiación es debida a la gran influencia que tiene en distintos aspectos de la salud y la vida en la tierra. A pesar de la importancia de esta banda del espectro solar, muy pocas estaciones meteorológicas poseen sensores para su medición, por lo que es esencial poder determinar su valor a partir de otras variables que se miden de forma más habitual en estaciones terrestres.

En este trabajo se ha realizado un estudio matemático completo de esta banda del espectro solar en sus componentes global y eritemática ambas sobre el plano horizontal, utilizando diferentes estrategias que combinan modelos de regresiones multilineales tradicionales, y novedosas técnicas de aprendizaje automático basadas en redes neuronales artificiales. También se ha abordado una aplicación práctica de los modelos de ecuaciones estructurales, que ha permitido la obtención de información latente en datos cualitativos procedentes de encuestas en un grupo de control.

Los estudios realizados han permitido obtener modelos locales precisos de radiación UV y UV eritemática en función de las condiciones atmosféricas, determinadas según el tipo de cielo (todo tipo de cielo, cubierto, intermedio y claro) clasificados mediante la norma $\mathrm{ISO/CIE}$. Además, se ha realizado un estudio, mediante modelos de ecuaciones estructurales, de la influencia de la percepción subjetiva de las personas al riesgo que supone para la salud la radiación UV, y su repercusión en hábitos de comportamiento, como es el uso de ropa de protección en sus actividades al aire libre.

Abstract

Ultraviolet irradiation is the region of the solar spectrum with wavelengths ranging from 100 to 400nm. Understanding ultraviolet irradiation is crucial due to its significant impact on various aspects of health and life on Earth. Despite the importance of this band of the solar spectrum, very few meteorological stations are equipped with sensors to measure it. Therefore, it is essential to determine its value from other variables that are more commonly measured at ground stations.

In this study, a comprehensive mathematical analysis solar ultraviolet irradiation, including its global and erythemal components on the horizontal plane, was conducted using various strategies that combine traditional multiple linear regression models and innovative machine learning techniques based on artificial neural networks. Additionally, a practical application of structural equation models was employed to extract latent information from qualitative data obtained through surveys in a control group.

The conducted studies have allowed for the development of accurate local models for UV irradiation and erythemal UV irradiation based on atmospheric conditions, categorized according to the type of sky (all sky types, overcast, intermediate, and clear) as defined by the ISO/CIE standard. Furthermore, through structural equation models, an analysis was conducted on the influence of people's subjective perception of the health risks associated with UV irradiation and its impact on behavioural habits, such as the use of protective clothing during outdoor activities.

Listado de Artículos

Artículo I

Sol García-Rodríguez, Ignacio García, Ana García-Rodríguez, Montserrat Díez-Mediavilla and Cristina Alonso-Tristán (2022). *Solar Ultraviolet Irradiance Characterization under All Sky Conditions in Burgos, Spain.* Applied Siences 12 (20), 10407

DOI: https://doi.org/10.3390/app122010407

Journal Citation Reports:

Índice impacto (2022): 2.7 Cuartil: Q2 (42/92).

Categoría JCR: Engineering Multidisciplinary

Scimago Journal Rank:

Índice impacto (2022): 0.492 Cuartil: Q2 (141/427)

Categoría SJR: Engineering Miscellaneous

Número de citas: 1

Artículo II

M. Isabel Dieste-Velasco, **Sol García-Rodríguez**, Ana García-Rodríguez, Montserrat Díez-Mediavilla and Cristina Alonso-Tristán (2023). *Modeling Horizontal Ultraviolet Irradiance for All Sky Conditions by Using Artificial Neural Networks and Regression Models.* Applied Siences 13 (3), 1473

DOI: https://doi.org/10.3390/app13031473

Journal Citation Reports:

Índice impacto (2022): 2.7 Cuartil: Q2 (42/92).

Categoría JCR: Engineering Multidisciplinary

Scimago Journal Rank:

Índice impacto (2022): 0.492. Cuartil: Q2 (141/427)

Categoría SJR: Engineering Miscellaneous

Número de citas:1

Artículo III

Sol García-Rodríguez, Ana García-Rodríguez, Diego Granados-Lopez, Ignacio García and Cristina Alonso-Tristán (2023). *Ultraviolet Erythemal Irradiance (UVER) under Different Sky Conditions in Burgos, Spain: Multilinear Regression and Artificial Neural Network Models.* Applied Siences 13 (19), 10979

DOI: https://doi.org/10.3390/app131910979

Journal Citation Reports:

Índice impacto (2022): 2.7 Cuartil: Q2 (42/92).

Categoría JCR: Engineering Multidisciplinary

Scimago Journal Rank:

Índice impacto (2022): 0.492. Cuartil: Q2 (141/427)

Categoría SJR: Engineering Miscellaneous

Artículo IV

José Roberto Ribas, **Sol García Rodríguez**, Elena Arce Fariña, and Andrés Suárez-García (2022). *An Assessment on the Efficiency of Clothing with UV Protection among the Spanish Navy School Students.* Materials 15 (8), 6227

DOI: https://doi.org/10.3390/ma15186227

Journal Citation Reports:

Índice impacto (2022): 3.4 Cuartil: Q2 (57/160).

Categoría JCR: Physics, Applied

Scimago Journal Rank:

Índice impacto (2022): 0.563 Cuartil: Q2 (433/1218)

Categoría SJR: Materials Science

INDICE GENERAL DE LA TESIS

Listado de Figuras

Listado de Tablas

Nomenclatura

Símbolos

CC	cobertura nubosa $(\%)$
D	Fracción Difusa
DHI	Irradiancia Difusa Horizontal $(W \cdot m^{-2})$
DNI	Irradiancia Directa Normal $(W \cdot m^{-2})$
GHI	Irradiancia Global Horizontal $(W \cdot m^{-2})$
$GHUV$	Irradiancia Global Horizontal UV $(W \cdot m^{-2})$
$GHUVE$	Irradiancia Global Horizontal UV Eritemática $(W \cdot m^{-2})$
α	Altura solar
ε	Índice de claridad de Pérez
Δ	Índice de brillo de Pérez
ψ	Ángulo azimutal solar
θ_z	Ángulo zenital solar $(°)$
k_t	índice de claridad
m	masa óptica relativa del aire
r	coeficiente de correlación de Pearson
R^2	coeficiente de determinación
RH	humedad relativa $(\%)$
T	temperatura del aire $(ºC)$
TOC	contenido total de columna de ozono

Abreviaturas

ANN	red neuronal artificial
CIE	Comisión Internacional de la Iluminación
FOC	frecuencia de aparición (%)
LMBP	Levenberg-Marquardt Back-Propagation
MLR	regresión multilineal
ODS	Objetivos de Desarrollo Sostenible
nMBE	error de sesgo medio normalizado (%)
nRMSE	error cuadrático medio normalizado (%)
SEM	Modelos de ecuaciones estructurales

Capítulo 1. Introducción y Motivación del trabajo

1.1. La Radiación Ultravioleta

El sol es la principal fuente de energía que llega a la tierra, proporcionando la luz y el calor necesario para la vida. Ha sido considerado una figura divina en distintas culturas: Utu en la cultura sumeria, Ra en la egipcia, Helios en la griega, o Amaterasu en la sintoísta, son algunos de los ejemplos conocidos de la consideración del disco solar como deidad.

La energía solar es imprescindible en multitud de procesos, como la fotosíntesis de las plantas o el crecimiento de la biomasa. También influye en la vida animal y determina la dinámica de los procesos atmosféricos.

La energía solar es transmitida en forma de ondas electromagnéticas, con longitudes de onda que varían entre los 100 nm, límite inferior de la radiación ultravioleta y los 5000 nm, límite superior de la radiación infrarroja. Al conjunto de las longitudes de onda emitidas por el Sol se les denomina espectro solar.

Aunque la radiación ultravioleta (UV) solo supone entre el 5 y el 7% de la radiación total [1], su alta energía influye en gran medida en la vida en la Tierra [2]. Puede llegar a ser el principal factor de riesgo para la salud humana [3], y tiene elevada influencia en muchos procesos biológicos y fotoquímicos [4]. Por todo ello, su estudio es de gran interés. La radiación UV es la región del espectro solar cuya longitud de onda está comprendida entre 100 y 400 nm. La Comisión Internacional de Iluminación (CIE) divide la radiación UV en tres bandas espectrales: $\mathrm{UV-C}\,(100-280\ \mathrm{nm}), \mathrm{UV-B}\,(280-315\ \mathrm{nm})$ y $\mathrm{UV-A}\,(315-400\ \mathrm{nm})$. $\mathrm{UV-C}$ es absorbida completamente por la atmosfera

terrestre. El ozono atmosférico absorbe parcialmente las longitudes de onda del $\mathrm{UV-B}$ y débilmente las correspondientes al $\mathrm{UV-A}$ y, por tanto, estas longitudes de onda son transmitidas hasta la superficie terrestre [5].

La intensidad de la radiación UV que alcanza el nivel de la superficie terrestre, se ve fuertemente influenciada por la composición atmosférica, determinada por el contenido en ozono, aerosoles, vapor de agua y otros gases [6], la distribución y tipo de nubes [7,8] y distintas variables geométricas y geográficas (ángulo solar cenital, altura sobre el nivel del mar o albedo de la superficie) [9,10].

1.2. Riesgos y beneficios de la radiación ultravioleta

Los mayores riesgos para la salud humana, debido a la exposición a la radiación ultravioleta, se presentan en la piel. Se estima que anualmente se producen en el mundo 7.7 millones de casos de cáncer no melanoma y más de 300000 casos de melanoma maligno. Estas cifras pueden ser una subestimación del número real de casos, ya que no todas las lesiones cutáneas detectadas se analizan y, por tanto, no se comunican los posibles casos malignos [11]. El melanoma está provocado por la exposición habitual al sol y por las quemaduras solares repetitivas, mientras que el cáncer no melanoma se origina por la exposición habitual a la radiación ultravioleta [12].

Entre los cánceres de piel no melanoma, los más frecuentes en varios países, se encuentran el carcinoma de células basales y el de células escamosas. En un porcentaje muy alto, estos cánceres se pueden atribuir a la exposición a la radiación ultravioleta, diferenciando entre la exposición al sol en actividades de ocio, en las que se puede minimizar el riesgo adaptándolas a las condiciones ambientales, y la exposición al sol en entornos de trabajo, en la que la adaptación en muchos casos es difícil. Según la Organización Internacional del Trabajo (OIT) más de

500 millones de personas trabajan al aire libre durante largos periodos de tiempo y, por tanto, están expuestas a este tipo de cáncer [13].

Además de la incidencia de la radiación ultravioleta en el cáncer de piel, esta radiación puede provocar otro tipo de problemas en la piel o en otros órganos, e incluso puede concernir a la salud mental. Por ejemplo, los tejidos oculares más sensibles a la radiación ultravioleta son la retina, la córnea y el cristalino. El estrés oxidativo, potenciado por la exposición a la radiación UV, provoca afecciones oculares como la degeneración macular, el glaucoma, las cataratas, el síndrome de ojo seco y el pterigión [14].

La radiación UV también puede activar virus directamente relacionados con el cáncer de cuello de útero, como son los virus del herpes, el VIH y el virus del papiloma humano [15]. Además, puede afectar negativamente a los pacientes aquejados de fotodermatosis, entre los que se encuentran los que sufren lupus eritematoso, rosácea o dermatitis actínica crónica, y a ciertos enfermos de psoriasis, vitíligo o dermatitis atópica [16].

También se ha estudiado la influencia de la radiación UV en la salud mental de las personas, e incluso en cómo puede afectar el mes de su concepción en la predisposición a sufrir algunas enfermedades mentales. El rápido aumento de la radiación ultravioleta en primavera puede afectar al desarrollo de un embrión en los primeros meses de gestación, produciendo una estimulación excesiva del sistema nervioso central, que le pueda llegar a provocar esquizofrenia en etapas posteriores de su vida. En los pacientes con trastorno bipolar la disminución de la radiación ultravioleta desencadena habitualmente síntomas depresivos [17].

La radiación UV no solo tiene efectos negativos sobre la salud, sino que también produce beneficios en la misma. La radiación UVB, que es

absorbida por las células epidérmicas, produce cis-previtamina D, que es fundamental en la prevención de muchas enfermedades. Un mayor nivel de vitamina D_3 está asociado a un menor riesgo de sufrir diabetes I y esclerosis múltiple [16,18]. El aumento de la vitamina D_3, debido a la radiación UV, provoca un aumento de la cantidad de células T asesinas que destruyen las células cancerosas, por lo que la incidencia tanto del cáncer de vejiga en hombres y en mujeres, como del cáncer de ovario se ve reducida [15]. Además, las mujeres postmenopáusicas padecen a menudo déficit de vitamina D que les provoca sarcopenia, por lo que la exposición a la radiación ultravioleta mejora su calidad de vida al aumentar la cantidad de vitamina D, reduciendo su dolor y aumentando su fuerza muscular [19]. En latitudes altas, donde la radiación UVB es menor, las personas de piel oscura pueden sufrir déficit de vitamina D, debido a lo cual, los niños con estas características pueden sufrir raquitismo [20].

La radiación ultravioleta también aumenta la betaendorfina, que puede aliviar el dolor y favorecer la relajación, y la hormona adrenocorticotropina, que aumenta la producción de cortisol en las glándulas suprarrenales, beneficiando al sistema inmunológico. Además, el aumento de la luz solar en verano tiene efectos positivos en la salud cardiaca de las personas bajando su colesterol sérico y su presión arterial [18]. Así mismo, la radiación UV puede regular la psoriasis y la dermatitis atópica [16].

Se han realizado numerosos estudios acerca de la posible influencia de la radiación UV sobre la propagación del virus COVID-19, sin acuerdo unánime hasta el momento. Sagripanti [21] ha establecido que la mayor parte del virus se inactiva al exponerlo a mediodía, en verano, a la luz solar entre 11 y 34 minutos. Sin embargo, en invierno mantiene su actividad más de un día. Pérez-Gilabert et al. [22] ha indicado que, en España, la radiación UV aparece como el factor meteorológico

determinante en la incidencia de la enfermedad, de forma que niveles más altos de la radiación contribuirían a menores tasas de incidencia. Bernhard et al. [23] ha indicado que muchas de las afirmaciones realizadas sobre el espectro de acción de la radiación ultravioleta sobre SARS-Covid-19 o los tiempos de inactivación del virus no están suficientemente contrastados, si bien parece correcta la afirmación de que la radiación UV tiene efectos germicidas. De Carvalho et al. [24] ha señalado que el grado de infección por Sars-Covid-2 depende de la latitud y, a la vista de su estudio, sugiere que puede estar provocada como respuesta a la inmunosupresión inducida por la radiación UV.

1.3. Modelos de radiación ultravioleta y eritemática, y dosis medida

Pese a la importancia de la radiación UV, muchas de las estaciones meteorológicas terrestres no disponen de sensores para su medida, debido principalmente a los costes de mantenimiento de los equipos y a la complejidad de las rutinas de calibración [25–27]. Al no disponer de datos experimentales terrestres, se suele calcular la radiación UV a partir de su relación con otras variables que sí que están disponibles habitualmente. Se han publicado numerosos trabajos en los que se estudia la relación entre la irradiancia global horizontal ultravioleta $(\mathrm{GHUV}, \mathrm{W/m^2})$ y la irradiancia global horizontal $(\mathrm{GHI}, \mathrm{W/m^2})$, en diferentes partes del mundo y bajo distintas condiciones de cielo a partir del ratio $\mathrm{GHUV/GHI}$ [9,28–30]. La relación entre ambas variables está influenciada por el índice de claridad $(\mathrm{k_t})$, ya que cuando la nubosidad aumenta, la relación entre GHUV y GHI se incrementa [29], es decir, la presencia de nubes reduce GHI en mayor medida que GHUV [31–33], debido fundamentalmente a la mayor absorción de las bandas del infrarrojo por el vapor de agua. Otro factor importante es la localización del lugar de medición, ya que GHUV aumenta a nivel del suelo cuando el lugar está más cerca del Ecuador [34], por la incidencia más

perpendicular de la radiación, que disminuye el camino óptico de la radiación y por tanto, los fenómenos de absorción y dispersión en la atmósfera.

GHUV también aumenta cuando se incrementan el ángulo cenital solar o la elevación solar. Al aumentar el ángulo cenital, GHUV aumenta, debido a que los rayos UV solares, percibidos como ángulos sólidos, se distribuyen sobre mayores superficies del globo terrestre [10,30].

Para estimar la irradiancia UV frecuentemente se han utilizado modelos con relativamente pocas variables, que emplean principalmente datos experimentales de irradiancia global [9,28–30,35,36]. En diferentes estudios se han obtenido modelos de radiación UV a partir de distintos parámetros geométricos y atmosféricos, como coseno del ángulo cenital [37], albedo [38], aerosoles, etc. Por ejemplo, Wang et al. [39] utiliza relaciones exponenciales de la masa óptica relativa del aire, m, para modelar UV en condiciones de cielos claros, y extiende el modelo para todo tipo de cielos mediante factores relacionados con la nubosidad.

Otros autores, para estimar la radiación UV según las condiciones de cielo, la hacen depender del índice de brillo y del ángulo de elevación solar [40]. También se ha empleado el modelo de transferencia radiativa SMARTS para obtener modelos semi empíricos de la radiación UV, a partir de agua precipitable atmosférica, columna de ozono total (TOC), profundidad óptica del aerosol, temperatura diaria, humedad relativa, presión atmosférica y temperatura del punto de rocío [41].

La radiación ultravioleta eritemática, conocida como UVER, permite evaluar el impacto de la radiación ultravioleta en la piel. La UVER, según la norma ISO/CIE17166: 2019(E) [42] se determina aplicando una función de ponderación espectral del eritema en base a la respuesta de la piel humana a la radiación UV. El valor de la radiación UVER, se

obtiene ponderando la irradiancia espectral de la radiación UV en cada longitud de onda utilizando el factor de efectividad del eritema correspondiente y sumando estos valores ponderados para todas las longitudes de onda presentes en el espectro de la fuente.

Se ha analizado UVER para todo tipo de cielo, concluyendo que para cielos poco nubosos, un aumento de la nubosidad, produce una disminución de UVER [43]. Se ha determinado también la dependencia entre los niveles de ozono y UVER, comprobándose que la UVER disminuye cuando hay niveles más altos de ozono [44,45].

Al igual que para GHUV, la irradiancia global horizontal ultravioleta eritemática (GHUVE), también se ve muy influenciada por el ángulo cenital solar, ya que al aumentar θ_z disminuye GHUVE [43,46].

Para modelizar la radiación UVER, se han desarrollado diferentes modelos matemáticos utilizando distintas variables meteorológicas. El contenido de ozono en la atmósfera, representado por la TOC, la carga de aerosoles y el agua precipitable presentan una relación lineal con respecto a GHUVE/GHI, sin embargo, el índice de claridad k_t y θ_z presentan comportamientos polinómicos y exponenciales, respectivamente [47]. También se han empleado modelos de ANN para modelar UVER, utilizando como variable principal GHI [36,48,49] independientemente de las características del resto de variables utilizadas.

La Comisión Internacional de Protección contra Radiaciones No Ionizantes (ICNIRP por sus siglas en inglés) es una organización no gubernamental reconocida tanto por la Organización Mundial de la Salud, como por la OIT y por la Comisión de la Unión Europea, responsable del asesoramiento y orientación acerca de los riesgos que presentan las radiaciones no ionizantes para la salud. Sus principios de protección contra dichas radiaciones proporcionan la base científica

para programas de protección de la salud, tanto nacionales como internacionales.

La ICNIRP estableció en 2010 [50] el valor de la dosis estándar eritemática (Standard Erythemal Dose, SED) que permite valorar la capacidad de una fuente radiativa para producir eritema. Un SED equivale a $100\,\mathrm{J}\cdot\mathrm{m}^{-2}$ de exposición a la radiación eritemática UV efectiva. Las unidades de medida de la radiación eritemática son $\mathrm{W}\cdot\mathrm{m}^{-2}$ o $\mathrm{SED}\cdot\mathrm{h}^{-1}$. Este valor es independiente del individuo que recibe la radiación, a diferencia de la variable MED (dosis eritemática mínima) utilizada en ocasiones en fotobiología. En la variable MED influyen no solo la radiación recibida en un determinado momento, sino también otros factores como son la capacidad de bronceado del individuo, la gravedad de exposiciones anteriores, etc.

También se puede cuantificar la radiación eritemática UV a través del índice UV, conocido como UVI. Este índice se ve influenciado por las condiciones meteorológicas, y habitualmente es utilizado para determinar el riesgo de quemaduras solares. A partir de la SED se clasifican los distintos fototipos de piel (de I a VI) según su susceptibilidad a sufrir quemaduras solares (de muy sensible a insensible) [50].

Varios autores [13,51] han analizado la cantidad de radiación UV que recibe un individuo al efectuar su trabajo en su entorno laboral o vacacional. La dosis diaria de radiación UV, recomendada internacionalmente para trabajadores en el exterior, es 1.3 SED cada ocho horas de trabajo, pudiendo llegar a recibir una dosis diaria cinco veces superior a este valor. A principios del siglo XXI un trabajador de carreteras en España estaba expuesto a una dosis media de 6.11 SED por día, y en Croacia a 12 SED por día durante los meses de abril a octubre [51].

Los modelos sobre la dosis de radiación eritemática recibida en periodo de vacaciones, equiparan las dosis recibidas durante una semana en el antebrazo con la radiación media durante un año en Europa o América del Norte, concluyendo que la radiación recibida en un día completo de playa puede llegar a 50 SED [45].

1.4. Protocolo de Montreal y los Objetivos de Desarrollo Sostenible (ODSs)

El Protocolo de Montreal sobre sustancias que agotan la capa de ozono, firmado en 1987, ha sido ratificado por todos los países de Naciones Unidas. El Programa de las Naciones Unidas para el Desarrollo, ha ayudado a los países en desarrollo a poner en marcha las estrategias necesarias para preservar la capa de ozono [52].

La regeneración de la capa de ozono es fundamental en la mitigación de la radiación ultravioleta que llega a la tierra, como así lo indican varios autores [45,53,54]. Sin la aplicación del Protocolo de Montreal, la estimación del aumento del índice de radiación ultravioleta (UVI) en el periodo 1996-2020 sería de 10 a 20% en latitudes inferiores a 50º y hasta un 100% en el Polo Sur. Además, si todos los países pusieran en marcha las medidas del Protocolo, el UVI disminuiría sensiblemente [45]. Aunque no se ha conseguido que el número de casos de cáncer de piel disminuya, en algunos países se ha estabilizado en los jóvenes por las medidas establecidas a partir del Protocolo de Montreal [55]. La recuperación de la capa de ozono ha provocado una disminución de UV, fundamentalmente en los polos y en latitudes altas [45]. En la zona tropical y en latitudes medias del hemisferio norte, las emisiones de óxido nitroso han retrasado la recuperación de la capa de ozono e incluso han propiciado una disminución de la misma, lo que ha provocado un aumento de la radiación UV en los meses de mayo a septiembre [56]. En el Ártico, un episodio de agotamiento de ozono

estratosférico en la primavera de 2020, ha dado lugar a una radiación UV mucho más alta de lo habitual [53].

No solo la salud humana se ha beneficiado de la disminución de emisiones de sustancias que agotan la capa de ozono. También hay constancia de la incidencia de esta medida en el medio ambiente. La disminución de la radiación ultravioleta superficial total, se puede considerar beneficiosa para la vida marina, aunque estos beneficios se vean mitigados por otros factores como el aumento de la temperatura media terrestre o la acidificación de los océanos [57]. También se ha constatado una disminución en la fragmentación de los desechos plásticos, que tendrá su respuesta en la cantidad de microplásticos en los medios acuáticos [58].

En un estudio sobre radiación ultravioleta es pertinente una referencia a los Objetivos de Desarrollo Sostenible (ODS), dado el impacto de la radiación UV en la salud y el medio ambiente. Varios son los ODS relacionados con este hecho, entre ellos:

ODS 2: Hambre cero - La radiación UV moderada puede aumentar los flavonoides en ciertos cultivos y mejorar su capacidad nutritiva. Un aumento extremo de la radiación ultravioleta disminuiría la productividad de la agricultura, suponiendo este hecho un riesgo para el objetivo [59].

ODS 3: Buena salud y bienestar – La radiación ultravioleta tiene efectos directos en la salud de las personas [12,14,15], pero también puede tener otros indirectos, como la degradación de ciertos pesticidas [60].

ODS 10: Reducción de las desigualdades – La diferente accesibilidad a medios de protección contra la radiación ultravioleta, según las condiciones de vida de los países, supone un riesgo para alcanzar este objetivo [55].

ODS 14: Vida submarina - La radiación ultravioleta afecta a la vida submarina produciendo muerte de zooplancton y de corales [57].

1.5. Objetivos y organización del documento

El objetivo principal de este trabajo es la caracterización y modelización matemática de la radiación ultravioleta mediante algoritmos tradicionales y nuevas técnicas de inteligencia artificial. Como se ha visto en las secciones anteriores, la radiación UV tiene un impacto muy acusado en la salud y en la vida en la tierra, lo que justifica el estudio pormenorizado de esta componente de la radiación solar. Por otro lado, el modelado de series largas de datos meteorológicos, necesario para determinar tendencias sobre factores profundamente afectados por el cambio climático y de enorme importancia para la salud humana, hace imprescindible la utilización de la Ciencia de Datos para producir resultados comprensibles y extrapolables. En último lugar, las actuaciones de los individuos están determinadas por múltiples factores, muy complejos de determinar. El uso de modelos de ecuaciones estructurales permite validar hipótesis a priori “subjetivas” en relaciones causa-efecto multivariantes.

Para conseguir este objetivo principal se han planteado los siguientes objetivos parciales:

1º Caracterización de la radiación ultravioleta.

2º Modelado de la radiación ultravioleta.

3º Caracterización y modelado de la radiación ultravioleta eritemática.

4º Análisis de percepción del riesgo para la salud debido a la exposición a la radiación solar y su influencia en hábitos de comportamiento.

Estos objetivos parciales se han concretado en la publicación de cuatro artículos científicos en revistas bajo revisión por pares e indexadas en el Science Citation Index Expanded del Journal Citation Report en los primeros cuartiles de distintas categorías como queda reflejado en el Epígrafe Listado de Artículos de esta memoria.

Este documento se estructura mediante los siguientes capítulos:

Capítulo 1- Introducción y motivación. En este capítulo se define el objeto de este trabajo y se hace una revisión del estado del arte.

Capítulo 2- Datos experimentales. En este capítulo se describe la estación meteorológica del Grupo de Investigación SWIFT de la Universidad de Burgos, junto con los criterios de calidad aplicados a los datos utilizados en el trabajo. También se introduce la clasificación de cielos según el estándar ISO/CIE , utilizada para determinar las condiciones atmosféricas.

Capítulo 3- Análisis y caracterización estadística de la irradiancia UV global y la irradiancia UV eritemática. Se analiza estadísticamente, en diferentes intervalos temporales, los ratios irradiancia ultravioleta global horizontal e irradiancia ultravioleta eritemática y la radiación global horizontal (GHUV/GHI, GHUVE/GHI).

Capítulo 4- Modelado de la radiación ultravioleta. Se modelan las irradiancias GHUV y GHUVE mediante el empleo de regresiones multilineales (MLR) y redes neuronales (ANN).

Capítulo 5- Aspectos sociales y de la salud. Se analiza la relación entre la percepción ante el riesgo de la radiación ultravioleta y actitudes de uso de elementos de protección solar, de un determinado grupo de personas, mediante el empleo de Modelos de Ecuaciones Estructurales.

Capítulo 6- Conclusiones y líneas de futuro. Se resumen los logros obtenidos y se describen futuras líneas de investigación relacionadas con el presente trabajo.

Capítulo 2. Datos experimentales

2.1. Descripción de la Estación Meteorológica

Los datos experimentales que se han empleado para la elaboración de esta tesis doctoral se han obtenido de la estación meteorológica que posee el Grupo de Investigación SWIFT (Solar and Wind Feasibility Technologies) en la azotea de la Escuela Politécnica Superior-Rio Vena de la Universidad de Burgos $(42°21'04''\mathrm{N}, 3°41'20''\mathrm{O}, 856$ m de altura sobre el nivel del mar), mostrada en la Figura 1.

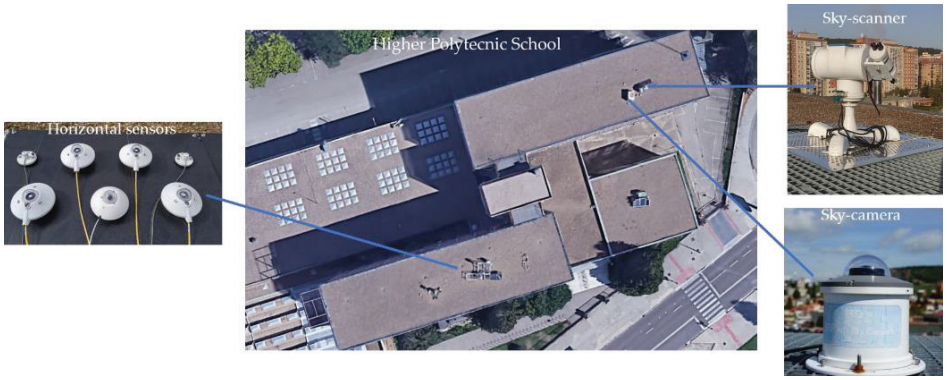

Figura 1. Ubicación del equipo experimental en la azotea de la Escuela Politécnica Superior, edificio A2, de la Universidad de Burgos, España (Fuente: Elaboración propia)

En dicha instalación se miden las variables meteorológicas temperatura ambiental, T, presión atmosférica, P, humedad relativa, HR, precipitación, w, velocidad y dirección del viento, velW, dirW.

La estación se encuentra provista de sensores de radiación solar, ubicados sobre el plano horizontal y sobre el plano vertical orientados según los cuatro puntos cardinales $(\mathrm{N}, \mathrm{S}, \mathrm{E}, \mathrm{O})$. Estos sensores son empleados para la caracterización de las diferentes componentes de la radiación solar (global, directa y difusa) y en distintas bandas del espectro solar. La irradiancia se determina mediante piranómetros, la iluminancia mediante luxómetros, la radiación fotosintéticamente activa (PAR) a través de sensores de fotones y la irradiancia ultravioleta en las

bandas A, B, y eritemática (E) mediante radiómetros de ultravioleta. En la Tabla 1 se recogen las características de los sensores ubicados en la instalación.

Tabla 1. Características de los sensores ubicados en la estación.

Tipo	Medida	Unidades	Marca	Modelo
Precipitación		mm	Campbell Scientific	52202 Electrically Heated Rainand Snow Gage
Viento		$m \cdot s^{-1}$	Campbell Scientific	03002 Wind Sentry Set
Presión		$mbar$	VAISALA	PTB110
Temperatura		$ºC$	Campbell Scientific	CS215
Irradiancia	N, S, E, O	$W \cdot m^{-2}$	K&Z	CM6b
Irradiancia	Glo, Dif, Dir	$W \cdot m^{-2}$	Hukseflux	SR12-T205
Iluminancia	N, S, E, O	lx	EKO	ML-020S
Iluminancia	Glo, Dif, Dir	lx	EKO	ML-020S
PAR	N, S, E, O	$\mu mol \cdot s^{-1} \cdot m^{-2}$	EKO	ML-020P
PAR	Glo, Dif, Dir	$\mu mol \cdot s^{-1} \cdot m^{-2}$	EKO	ML-020P
UV 5	N, S, E, O	$W \cdot m^{-2}$	K&Z	CUV 5
UV 5	Glo, Dif, Dir	$W \cdot m^{-2}$	K&Z	CUV 5
UV A	Glo, Dif, Dir, S	$W \cdot m^{-2}$	K&Z	SUV A
UV B	Glo, Dif, Dir, S	$W \cdot m^{-2}$	K&Z	SUV B
UV E	Glo, Dif, Dir, S	$W \cdot m^{-2}$	K&Z	SUV E
Difusa vertical	N, E, S, O	$W \cdot m^{-2}$	Hukseflux	SR11
Albedo		adim	Hukseflux	SRA01

(**N**: norte; **S**: sur; **E**: este; **O**: oeste; **Glo**: global; **Dir**: directa; **Dif**: Difusa)

Las medidas de cada variable meteorológica se han registrado cada 30 segundos, almacenándose los valores promedio diezminutales. Estos registros han sido posteriormente analizados y filtrados según los criterios de la red MESOR, descritos en el apartado 2.2 según los criterios de calidad más exigentes [62].

Además de los sensores de radiación para conocer la distribución de la irradiancia y de la iluminancia del cielo, la instalación posee un escáner de cielo comercial (sky scanner EKO modelo MS-321LR), que registra valores de ambas variables desde el amanecer hasta el atardecer. El sky scanner divide el cielo en 145 sectores, que se encuentran agrupados en ocho bandas, realizando un barrido completo de la cúpula celeste en 4 minutos, y repitiendo el proceso cada 10 minutos. Se ajusta mensualmente para medir exclusivamente durante las horas de luz diurna, desde la salida hasta la puesta de sol [63–65] y permite realizar la clasificación del cielo según los 15 tipos de la clasificación estándar $\mathrm{ISO/CIE}$ [66]. Para evitar mediciones erróneas se han descartado la primera y última medición del día, así como todas las mediciones de luminancia que se encuentran fuera del rango $0{,}1 - 50\,\mathrm{kcd}\cdot\mathrm{m}^{-2}$, siguiendo las especificaciones del equipo.

Se ha utilizado una cámara de cielo comercial (sky camera SONA 201D), con una resolución de imagen de 1158 × 1172 píxeles en el espacio de color RGB. Este equipo toma fotografías de la cúpula celeste (180º) en formato raw y emplea un algoritmo basado en inteligencia artificial para determinar la cobertura de nubes (CC), que es la proporción de la cúpula celeste cubierta por nubes. El programa de adquisición de datos está preparado para almacenar una imagen cada 15 segundos.

De los datos obtenidos en la estación, solo se han considerado válidos, aquellos registros diezminutales en los que todas las variables necesarias para los estudios han superado los criterios de calidad que

se detallan en la siguiente sección. Estos datos se han almacenado, procesado y publicado, en base horaria (y en base diezminutal previa solicitud), en formato abierto, a través de la página web del grupo, https://aers.ubu.es/, cumpliendo las recomendaciones de la EU Open Science Policy Platform (OSPP) [67] y la Ley de la Ciencia, la Tecnología y la Innovación 17/2022 [68].

Un resumen de las variables que se han utilizado en esta tesis se presenta en la Tabla 2. Las variables meteorológicas, $\mathrm{GHI, DHI, DNI, GHUVE, GHUVE, CC, HR, T}$ y WS se han obtenido directamente de las mediciones experimentales, y se han calculado los ángulos cenital, θ_z, y acimultal, ψ para cada momento. El resto de variables, incluyendo la fracción difusa, D [69], k_t [70], k'_d, el factor de brillo de Pérez, Δ [71], y el índice de claridad de Pérez, ε [71], se han calculado utilizando las ecuaciones descritas en la Tabla 2.

Tabla 2. Variables medidas y calculadas en la estación meteorológica.

Variables	Variables meteorológicas	Expresión	
DHI	Irradiancia Difusa Horizontal	medido	
DNI	Irradiancia Directa Normal	medido	
GHI	Irradiancia Global Horizontal	medido	
GHUV	Irradiancia Global Horizontal UV	medido	
GHUVE	Irradiancia Global Horizontal UV Eritemática	medido	
CC	Cobertura nubosa	medido	
RH	Humedad relativa	medido	
T	Temperatura del aire	medido	
WS	Velocidad viento	medido	
α	Ángulo altura solar	medido	
ψ	Ángulo acimutal solar	calculado	
θ_z	Ángulo cenital solar	calculado	
D	Fracción difusa	$\mathrm{D} = \frac{\mathrm{DHI}}{\mathrm{GHI}}$	(1)
k_t	Índice de claridad	$k_t = \frac{\mathrm{GHI}}{B_{sc} f_c \cos\theta_z}$	(2)
k'_d	Radiación difusa extraterrestre	$k_d = \frac{\mathrm{DHI}}{B_{sc}}$	(3)

Δ	Índice de brillo de Pérez	$\Delta = \frac{m \cdot DHI}{B_{sc} \cdot f_c \cdot \cos\theta_z}$	(4)
ε	Índice de claridad de Pérez	$\varepsilon = \frac{\frac{DHI + DNI}{DHI} + k(\theta_z)^3}{1 + k(\theta_z)^3}$	(5)

(*) B_{sc} es la constante solar ($1361.1\ W \cdot m^{-2}$ [72]). f_c es el valor medio de la excentricidad orbital de la Tierra. $k = 1.04$ (o $5.56 \cdot 10^{-6}$ si θ_z se expresa en grados centígrados).

2.2. Criterios de calidad de los datos experimentales

Los datos experimentales $GHI, GHUV, GHUVE, DHI, DNI$ han sido sometidos al control de calidad propuesto para el Proyecto MESoR [73]. Los datos correspondientes a ángulos de elevación solar inferiores a 5° se han descartado del análisis para mitigar los problemas de respuesta al coseno inherentes a los instrumentos de medida de la irradiancia.

El control de calidad del proceso MESoR está basado en el método de la Baseline Surface Radiation Network (BSRN) [74] al que añade criterios adicionales para el control de calidad de irradiancia sobre el plano inclinado y en otros rangos del espectro solar, como el visible. Sin embargo, entre estos rangos no se encuentran los correspondientes a la irradiancia UV o $UVER$. Por ello, ha sido necesario ajustar los criterios de control de calidad para incluir estas variables.

El procedimiento MESoR incluye tres niveles de control de calidad para la irradiancia, que se detallan a continuación:

1. Límites físicos: en este nivel se verifica que las medidas de irradiancia no excedan los valores correspondientes en la parte alta de la atmósfera. En la Tabla 3 se muestran los valores mínimos y máximos establecidos para cada variable analizada. Mientras Gueymard [72] obtuvo un valor de 1361.1 $W \cdot m^{-2}$ para la constante solar del espectro completo de la irradiancia solar (B_{sc}). Sin embargo, no existen valores estandarizados para la constante solar en los rangos del espectro de la

irradiancia UV (UV_{sc}) y UVER (UVE_{sc}). Por lo que, se calculó el valor de UV_{sc} integrando el espectro solar revisado por Gueymard [72] en el rango de longitudes de onda comprendido entre 280 nm y 400 nm, resultando un valor de 102.15 $W \cdot m^{-2}$. UVE_{sc} se estimó mediante la integración del producto del espectro solar mencionado y la función de ponderación espectral eritemática establecida por la norma ISO/CIE 17166:2019 (E) [42].

Tabla 3. Límites físicos para el control de calidad de la irradiancia, irradiancia UV e irradiancia UVER. (Fuente: Adaptada de [73])

Variable	Unidades	Valor mínimo	Valor máximo
GHI	$W \cdot m^{-2}$	- 4	$I_{SC} \cdot 1.5 \cdot (\cos \theta_z)^{1.2} + 100$
DHI	$W \cdot m^{-2}$	- 4	$I_{SC} \cdot 0.95 \cdot (\cos \theta_z)^{1.2} + 50$
DNI	$W \cdot m^{-2}$	- 4	I_{SC}
GHUV	$W \cdot m^{-2}$	0	$UV_{SC} \cdot 1.5 \cdot (\cos \theta_z)^{1.2} + 5$
DHUV	$W \cdot m^{-2}$	0	$UV_{SC} \cdot 0.95 \cdot (\cos \theta_z)^{1.2} + 2$
DNUV	$W \cdot m^{-2}$	0	UV_{SC}
GHUVE	$W \cdot m^{-2}$	0	$UVE_{SC} \cdot 1.5 \cdot (\cos \theta_z)^{1.2} + 1$

I_{SC} : irradiancia extraterrestre sobre el plano normal (considerando una constante solar de $1361.1\ W \cdot m^{-2}$ obtenida por Gueymard (2018)). UV_{SC} : irradiancia UV extraterrestre sobre el plano normal (considerando una constante solar UV de $102.15\ W \cdot m^{-2}$). UVE_{SC}: irradiancia UVER extraterrestre sobre el plano normal (considerando una constante solar UVER de $14.5\ W \cdot m^{-2}$).

2. Límites de cielo claro: Para la estimación de estos límites, el procedimiento MESoR propone utilizar el modelo de cielo claro desarrollado por Bird y Hulstrom [75], y así asegurar que las medidas de irradiancia no superen los valores correspondientes a un cielo claro (sin nubes) y limpio (sin aerosoles ni humedad). Debido a la ausencia de modelos para la estimación de la irradiancia UV en condiciones de cielo claro y limpio, se ajustaron una serie de modelos dependientes de la masa óptica relativa del aire (m), a partir de las simulaciones realizadas mediante el modelo de transferencia radiativa de la atmósfera SMARTS v 2.9.8 [41].

El modelo SMARTS permite la simulación de la transferencia de la radiación solar en la atmósfera en el rango espectral comprendido entre 280 y 4000 nm. Al tener la irradiancia UVER un espectro entre 250 y 400 nm, está fuera de los límites de simulación de SMARTS. Por ello, no ha sido posible ajustar un modelo de cielo claro para esta componente de la radiación solar. La Tabla 4 recoge los límites de cielo claro para las distintas variables consideradas.

Tabla 4. Límites de cielo claro para el control de calidad de la irradiancia, irradiancia UV e irradiancia UVER. (Fuente: Adaptada de [73])

Variable	Unidades	Condición	Valor máximo
GHI	$\mathrm{W \cdot m^{-2}}$	$\theta_z < 85º$	$\mathrm{GHI_{clear}}$
DHI	$\mathrm{W \cdot m^{-2}}$	$\theta_z < 85º$	$\mathrm{GHI_{clear}}$
DNI	$\mathrm{W \cdot m^{-2}}$	$\theta_z < 85º$	$\mathrm{DNI_{clear}}$
GHUV	$\mathrm{W \cdot m^{-2}}$	$\theta_z < 85º$	$\frac{1.78513\ \mathrm{m^2} + 177.076\ \mathrm{m} + 2594.06}{13.8072\ \mathrm{m^2} + 25.6894\ \mathrm{m} + 1}$
DHUV	$\mathrm{W \cdot m^{-2}}$	$\theta_z < 85º$	$\frac{0.0284353\mathrm{m^2} - 0.773392\mathrm{m} + 34.2974}{0.0393782\mathrm{m^2} + 0.593745\mathrm{m} + 1}$
DNUV	$\mathrm{W \cdot m^{-2}}$	$\theta_z < 85º$	$\frac{0.613588\mathrm{m^2} - 14.0356\mathrm{m} + 88.664}{0.0966512\mathrm{m^2} + 0.474748\mathrm{m} + 1}$

$\mathrm{GHI_{clear}}$: irradiancia global sobre el plano horizontal correspondiente a una atmósfera clara y limpia calculada de acuerdo con el modelo de Bird y Hulstrom [75]. $\mathrm{DNI_{clear}}$: irradiancia directa sobre el plano normal correspondiente a una atmósfera clara y limpia calculada de acuerdo con el modelo de Bird y Hulstrom [75]. m: masa óptica relativa de aire.

3. Coherencia o redundancia: este nivel de control de calidad se divide en dos partes. Por un lado, se verifica la coherencia entre la medida de irradiancia global y la suma de las componentes difusa horizontal y directa normal corregida al plano horizontal. Por otro lado, se analiza la coherencia entre las medidas de irradiancia difusa y global, para niveles bajos de irradiancia directa, las medidas de difusa no deben ser significativamente mayores a las medidas de irradiancia global.

La Tabla 5 muestra los distintos criterios cuyo valor mínimo y máximo depende de la posición del sol y del valor de irradiancia global.

Tabla 5. Criterios de coherencia para el control de calidad de la irradiancia, irradiancia UV e irradiancia UVER. (Fuente: Adaptada de [73])

Variable	Condición	Valor mínimo	Valor máximo
$\frac{\mathrm{GHI}}{(\mathrm{DHI}+\mathrm{DNI}\cdot\cos\theta_z)}$	$\mathrm{GHI} > 50\ \mathrm{W}\cdot\mathrm{m}^{-2}$ $\theta_z < 75º$	0.92	1.08
$\frac{\mathrm{GHI}}{(\mathrm{DHI}+\mathrm{DNI}\cdot\cos\theta_z)}$	$\mathrm{GHI} > 50\ \mathrm{W}\cdot\mathrm{m}^{-2}$ $85º > \theta_z > 75º$	0.85	1.15
$\mathrm{DHI/GHI}$	$\mathrm{GHI} > 50\ \mathrm{W}\cdot\mathrm{m}^{-2}$ $\theta_z < 75º$	–	1.05
$\mathrm{DHI/GHI}$	$\mathrm{GHI} > 50\ \mathrm{W}\cdot\mathrm{m}^{-2}$ $85º > \theta_z > 75º$	–	1.10
$\frac{\mathrm{GHUV}}{(\mathrm{DHUV}+\mathrm{DNUV}\cdot\cos\theta_z)}$	$\mathrm{GHUV} > 2\ \mathrm{W}\cdot\mathrm{m}^{-2}$ $\theta_z < 75º$	0.92	1.08
$\frac{\mathrm{GHUV}}{(\mathrm{DHUV}+\mathrm{DNUV}\cdot\cos\theta_z)}$	$\mathrm{GHUV} > 2\ \mathrm{W}\cdot\mathrm{m}^{-2}$ $85º > \theta_z > 75º$	0.85	1.15
$\mathrm{DHUV/GHUV}$	$\mathrm{GHUV} > 2\ \mathrm{W}\cdot\mathrm{m}^{-2}$ $\theta_z < 75º$	-	1.05
$\mathrm{DHUV/GHUV}$	$\mathrm{GHUV} > 2\ \mathrm{W}\cdot\mathrm{m}^{-2}$ $85º > \theta_z > 75º$	-	1.10

2.3. Análisis de los cielos

Como se ha comentado en la introducción de esta tesis doctoral, las condiciones de cielo afectan en gran medida a la cantidad de radiación UV que llega a la tierra. A falta de instrumentos de medida para determinar experimentalmente la cantidad de ozono, o la presencia de aerosoles en la atmósfera, se ha optado por realizar una caracterización de la atmósfera a través de los tipos de cielo.

Los cielos de la ciudad de Burgos se han clasificado según la norma ISO/CIE [66], que considera la distribución angular de la radiancia y luminancia del cielo. La Comisión Internacional de Iluminación (Commision Internationale de L´Éclairage o CIE) clasifica los cielos en 15 tipos, agrupándolos en 3 categorías. Considera cielos cubiertos a los tipos de cielo del 1 al 5, cielos parcialmente cubiertos o intermedios a

los tipos del 6 al 10 y cielos claros a los tipos del 11 al 15, como se muestra en la Figura 2. La clasificación de cielos según la norma ISO/CIE precisa de la utilización de un sky scanner, dispositivo poco habitual en las instalaciones meteorológicas terrestres [76], pero disponible en la instalación experimental del Grupo de Investigación.

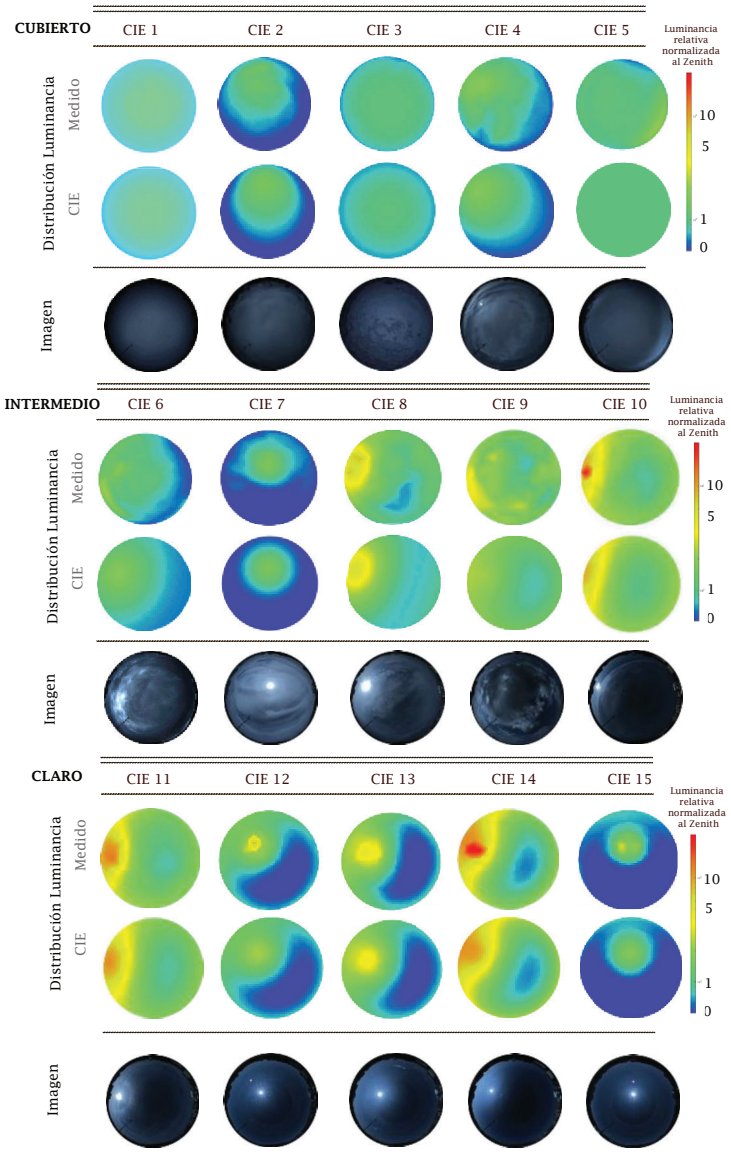

Figura 2. Condiciones de los 15 tipos de cielo estándar CIE, distribución de luminancia CIE y luminancia experimental. Imágenes registradas con Sky Camera (SONA201D) y medidas experimentales obtenidas mediante el Sky Scanner (MS-321LR) en Burgos (Fuente: Elaboración propia)

A lo largo de los últimos años, se han llevado a cabo diferentes campañas experimentales que han permitido la caracterización del cielo en la ciudad de Burgos, según el estándar ISO/CIE. En la Tabla 6 se recoge la frecuencia de ocurrencia (FOC, %) de los tipos de cielo durante dichas campañas experimentales según sean cubiertos, intermedios o claros. De forma general, los cielos en Burgos son claros, con predominancia de cielos correspondientes a los tipos 13 y 12 con una frecuencia de aparición de 19% y 18.3%, respectivamente.

Tabla 6. Frecuencia de ocurrencia (FOC) según los tipos de cielo CIE en Burgos.

Ref	Campaña experimental	FOC (%)	CIE predominante
[65]	06-16/ 05-17	Cubiertos: 23.7 Intermedios: 20 Claros: 56.3	CIE 12 (18.3%)
[77]	09-16/ 01-19	-	CIE 7 (13%)
[63]	09-16/ 01-20	Cubiertos: 15 Intermedios: 33 Claros: 52	-
[78]	04-19/ 02-21	Cubiertos: 21.9 Intermedios: 24.5 Claros: 53.6	CIE 13 (17.4%)
[61]	09-20/ 06-22	Cubiertos: 32.4 Intermedios: 23 Claros: 44.6	CIE 13 (19%)

La Figura 3 recoge los valores de la frecuencia de aparición del tipo de cielo en la campaña realizada entre septiembre de 2020 y junio de 2022. Se observa que en esta campaña los cielos predominantes corresponden al tipo de cielo 13, clasificado como cielo claro, con una frecuencia de aparición superior al 18%. Los tipos de cielo 1 (correspondiente a cielos cubiertos) y los cielos 11 y 12 (clasificados como cielos claros) han presentado un FOC que varía entre el 10 y el 13%. Los cielos con menor frecuencia de aparición (inferior al 2%) han sido los tipos de cielos 5, 9 y 15.

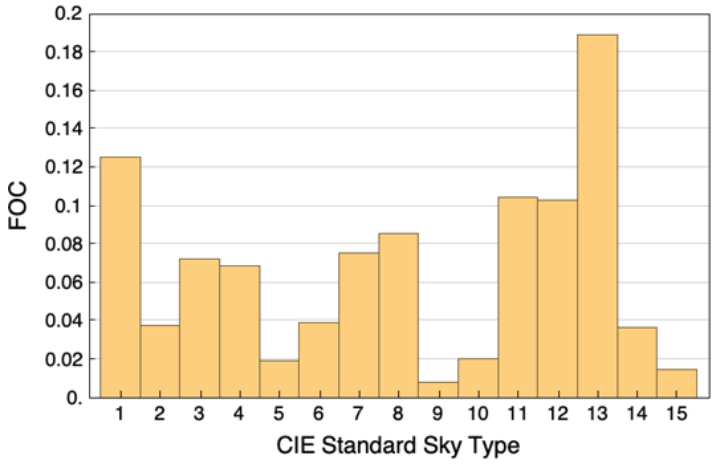

Figura 3. Frecuencia de Ocurrencia (FOC) de cada tipo de cielo estándar $\mathrm{ISO/CIE}$ en Burgos (España) desde el 14 de septiembre de 2020 hasta el 6 de junio de 2022 (Fuente: [61])

Dado que, son escasos los lugares en el mundo donde existen datos de clasificación del cielo estándar $\mathrm{ISO/CIE}$, también se ha realizado una clasificación basada en el índice de claridad, $\mathrm{k_t}$, [70], parámetro que relaciona la radiación global horizontal con la radiación solar extraterrestre según la ecuación (2) de la Tabla 2. Según este parámetro, los cielos se clasifican en cubiertos, $0 \leq \mathrm{k_t} \leq 0{,}35$, parcialmente cubiertos, $0{,}35 < \mathrm{k_t} \leq 0{,}65$, y cielos despejados, $0{,}65 < \mathrm{k_t} \leq 1$ [65]. En la Figura 4 se observa que, en la campaña anteriormente comentada, los cielos predominantes en Burgos han sido cielos claros, con un FOC superior al 35%. La predominancia de cielos claros ha sido mayor cuando se realiza la clasificación según la norma $\mathrm{ISO/CIE}$ que cuando se realiza según el valor de $\mathrm{k_t}$. Los cielos intermedios han sido los menos frecuentes, obteniéndose un FOC menor según la clasificación CIE frente a la de $\mathrm{k_t}$.

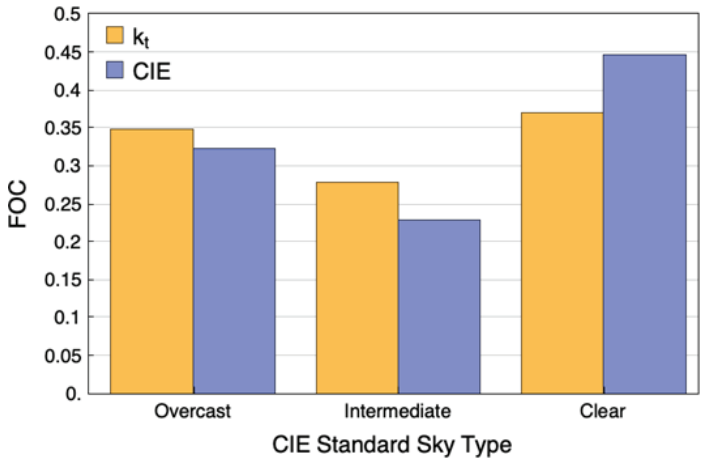

Figura 4. Frecuencia de aparición (FOC) de las clasificaciones de cielo CIE y $\mathrm{k_t}$ del cielo en Burgos (España) del 14 de septiembre de 2020 al 6 de junio de 2022 (Fuente: [61])

Capítulo 3. Análisis y caracterización estadística de la Irradiancia UV global y la Irradiancia UV eritemática

Previamente al modelado de las componentes de la radiación ultravioleta se ha estimado conveniente realizar la caracterización estadística de los datos experimentales, y su dependencia con la granularidad de los registros (diezminutal, horaria, diaria, mensual y estacional). Esta caracterización se realiza de forma tradicional al analizar la radiación solar y sus componentes, tanto global como difusa o directa. Por ejemplo, Jacovides et al. [79] a partir de datos horarios analiza la media mensual de la radiación global, UVB y UVA. Mientras que, para modelizar la radiación UVER, Junk et al. [80] emplea datos diarios. Sudhakar et al. [81] modeliza la radiación fotosintéticamente activa (PAR) a partir de datos horarios y mensuales, sin embargo, Garcia-Rodríguez et al. [82] emplea datos diezminutales. Foyo-Moreno et al. [83] para estimar la fracción difusa de la PAR utiliza datos horarios. Duan et al. [84] calcula el ratio entre el infrarrojo cercano y la radiación global horizontal a partir de datos horarios.

Las características de cualquier componente de la radiación solar dependen, en gran medida, de las condiciones atmosféricas, representadas mediante las condiciones de cielo. La caracterización de cielo, como se ha expuesto en capítulos anteriores, se ha realizado bien a través de la caracterización estándar $\mathrm{ISO/CIE}$ o bien mediante el parámetro $\mathrm{k_t}$.

3.1. Caracterización de la Irradiancia Solar Ultravioleta para todo tipo de cielo en Burgos, España

En el primero de los artículos que conforman esta tesis [85], se ha analizado la relación $\mathrm{GHUV/GHI}$ en Burgos, en diferentes intervalos

temporales (diezminutales, horarios, diarios, mensuales y estacionales) en función de las condiciones de cielo, durante la campaña experimental realizada entre septiembre de 2020 y junio de 2022 (22 meses completos).

Los cielos se han clasificado según el estándar $\mathrm{ISO/CIE}$, siguiendo el procedimiento descrito en el punto 2.3 (Clasificación de los cielos) de esta tesis. Conocidas las características de los cielos en Burgos, mayoritariamente cielos claros, se ha evaluado la relación $\mathrm{GHUV/GHI}$ para los diferentes intervalos temporales.

Analizados los valores promedio diezminutales, obtenidos a partir de los datos registrados cada 30 segundos en la estación experimental, se observa que el ratio $\mathrm{GHUV/GHI}$ ha tomado valores entre el 1% y el 10%, concentrándose los valores más altos en las primeras horas del día, y disminuyendo significativamente durante las horas centrales.

Al analizar $\mathrm{GHUV/GHI}$ según valores horarios (Figura 5), calculados como el promedio de los valores diezminutales, registrados desde el amanecer al anochecer, durante toda la campaña experimental, se observa que este ratio se ha mantenido casi constante a lo largo de todo el día, aumentando ligeramente en las primeras horas, estabilizándose en las horas centrales y volviendo a aumentar al atardecer. Al amanecer y al atardecer se ha producido la mayor dispersión de los datos (1.9% a las $5{:}00\mathrm{h}$ y a las $19{:}00\mathrm{h}$) siendo la media horaria de $3.98\% \pm 0.82\%$.

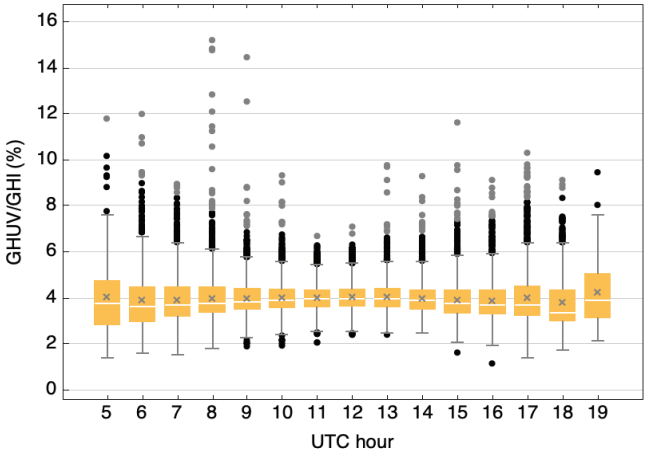

Figura 5. Gráfico de cajas y bigotes de los promedios horarios de $\mathrm{GHUV/GHI}$ utilizando los datos de 10 minutos (Fuente: [61])

Los valores mensuales, calculados también a partir del promedio de los datos diezminutales, se observan en la Figura 6. Los valores se han mantenido casi constantes durante todo el año, con un pequeño descenso del valor durante los meses de julio y agosto. Los meses de diciembre y enero han sido los que han presentado una mayor dispersión de los datos, siendo sus rangos intercuartílicos del 1.56% y 1.51% y la desviación estándar del 1.27% y 1.29% respectivamente. El máximo y el mínimo se han alcanzado en los meses de diciembre $(4.35\% \pm 1.29\%)$ y julio $(3.82\% \pm 0.69\%)$, respectivamente.

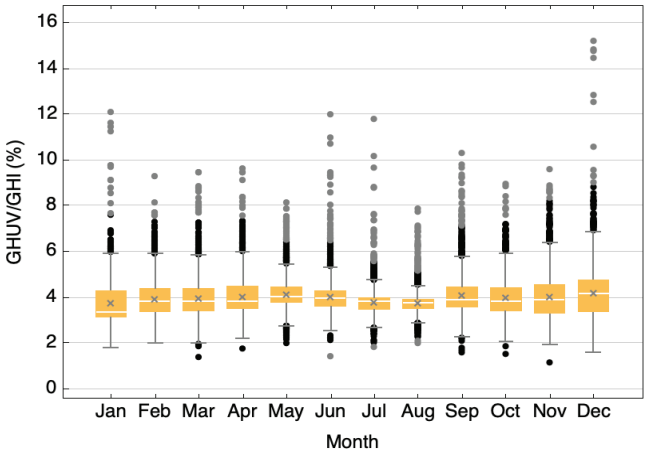

Figura 6. Gráfico de cajas y bigotes de los promedios mensuales de $\mathrm{GHUV/GHI}$ utilizando los datos de 10 minutos (Fuente:[61])

En la Figura 7 se observa que en otoño e invierno los datos han presentado una mayor dispersión, mientras que en verano se ha producido la menor dispersión.

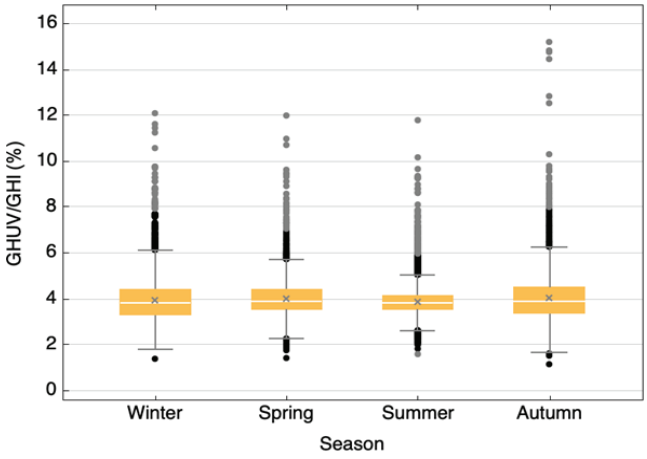

Figura 7. Gráfico de cajas y bigotes de los promedios estacionales de $\mathrm{GHUV/GHI}$ basados en los conjuntos de 10 min (Fuente: [61])

Al analizar el ratio para cada tipo de cielo estándar $\mathrm{ISO/CIE}$ (Figura 8), los valores más altos se han presentado para los tipos de cielo 5 y 1 ($5.48 \pm 0.92\%$ y $4.73 \pm 0.76\%$, respectivamente), que pertenecen a cielos cubiertos.

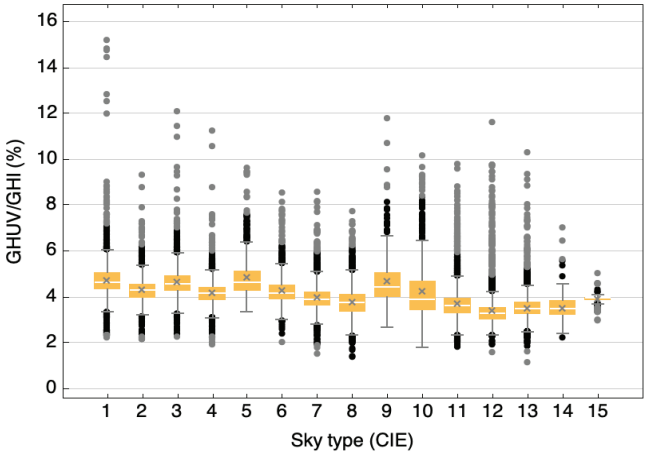

Figura 8. Gráfico de cajas y bigotes de la media del ratio $\mathrm{GHUV/GHI}$ para cada tipo de cielo CIE utilizando los datos de 10 min (Fuente: [61])

La comparativa del análisis estadístico según los tipos de cielo $\mathrm{ISO/CIE}$ y según la clasificación de los datos a partir de la variable $\mathrm{k_t}$ se observa en la Figura 9. En los dos casos, la relación $\mathrm{GHUV/GHI}$ ha sido menor en los cielos claros y mayor en los cielos cubiertos, siendo los valores medios y los valores de dispersión similares en ambos casos.

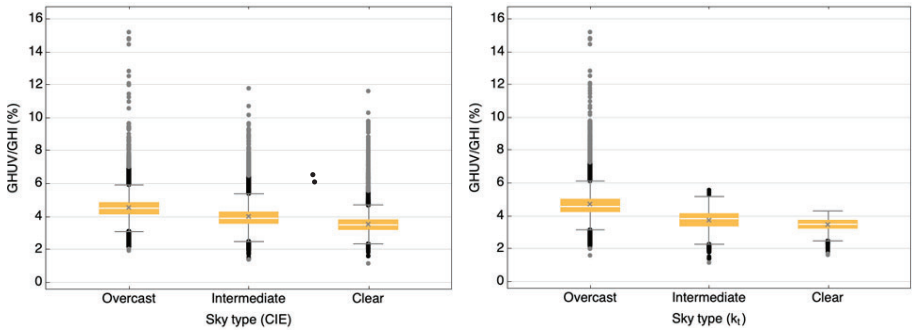

(a) (b)

Figura 9. Gráfico de cajas y bigotes de los valores medios de $\mathrm{GHUV/GHI}$ para (a) cada grupo de tipo de cielo CIE y (b) para cada clasificación según $\mathrm{k_t}$, basada en los conjuntos de datos de 10 min (Fuente:[61])

La dependencia mutua entre las dos variables, GHUV y GHI, se ha establecido para los datos promedio diezminutales, horarios y diarios mediante modelos de regresión lineal con intercepto $(\mathrm{GHUV} = \mathrm{a} \cdot \mathrm{GHI} + \mathrm{b})$, y modelos proporcionales $(\mathrm{GHUV} = \mathrm{a} \cdot \mathrm{GHI})$, debido a que la formulación de la ecuación afecta a la calidad de los resultados [86]. Como se observa en la Figura 10, aunque en ambos casos se han obtenido resultados adecuados, $(\mathrm{R}^2 > 0.97)$, los modelos de regresión lineal sin intercepto, han superado ligeramente las prestaciones del modelo proporcional. A medida que aumenta la granularidad de la muestra, R^2 se ha incrementado, no presentando diferencias significativas los valores de la pendiente ni de la desviación típica de los datos ajustados según diferentes intervalos de tiempo.

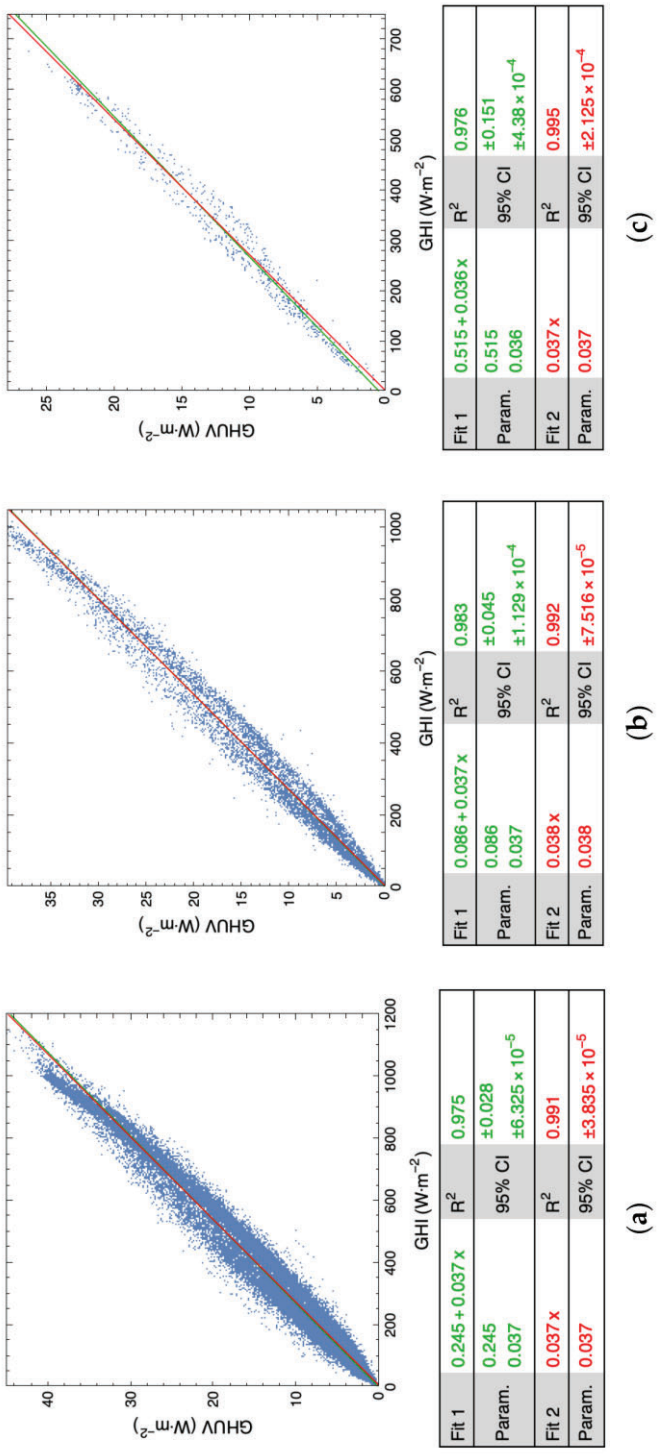

Figura 10. GHUV y GHI desde septiembre de 2020 a junio de 2022 (Fuente:[61])

3.2. Caracterización de la Irradiancia Ultravioleta Eritemática en Burgos

Siguiendo el mismo procedimiento que el empleado en la caracterización de la irradiancia UV global, en el tercer artículo de la tesis [87] se ha analizado, la relación $\mathrm{GHUVE/GHI}$ en Burgos, durante la campaña experimental realizada entre septiembre de 2020 y junio de 2022, en diferentes intervalos temporales (horarios, diarios, mensuales y estacionales) obtenidos como promedios de los datos diezminutales, así como la dependencia de esta relación con las características de la atmósfera definidas a partir de los distintos tipos de cielo.

Analizados los valores horarios de la relación $\mathrm{GHUVE/GHI}$, según la Figura 11, se ha observado que estos han aumentado paulatinamente desde el amanecer hasta el mediodía, para después disminuir hasta el atardecer. En las horas centrales, entre las $10{:}00\mathrm{h}$ y las $14{:}00\mathrm{h}$, los valores han presentado una mayor dispersión, alcanzándose el valor máximo de $\mathrm{GHUVE/GHI}$ a las $12{:}00\ \mathrm{h}$ $(4.2 \cdot 10^{-2}\%)$.

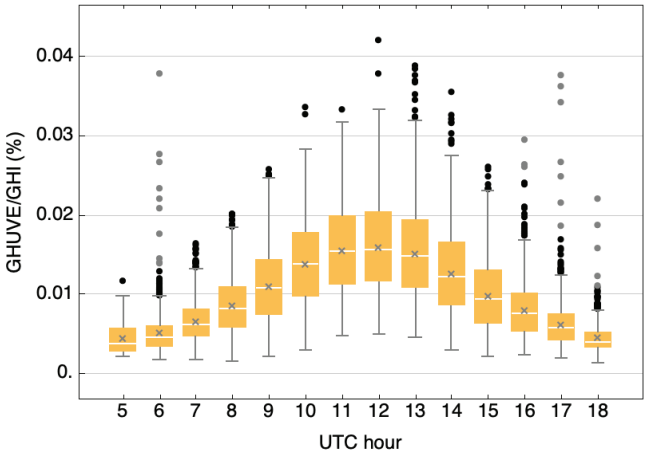

Figura 11. Gráfico de cajas y bigotes del ratio $\mathrm{GHUVE/GHI}$ basado en datos de 10 minutos agrupados por horas UTC (Fuente: [87])

Estudiado el valor del ratio $\mathrm{GHUVE/GHI}$ mensual (Figura 12), se comprueba que éste ha aumentado gradualmente de enero a mayo, permaneciendo casi constante hasta el mes de agosto, y disminuyendo el resto del año. El valor mínimo se ha producido en el mes de abril $(1 \cdot 10^{-3}\%)$, y el valor máximo se ha registrado en el mes de julio $(4.2 \cdot 10^{-2}\%)$.

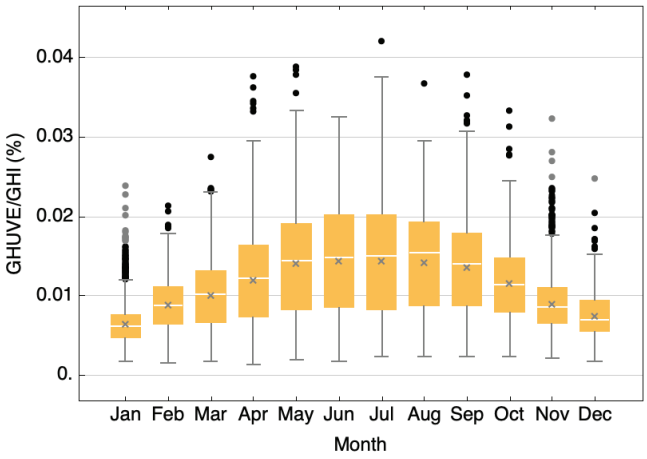

Figura 12. Gráfico de cajas y bigotes del ratio $\mathrm{GHUVE/GHI}$ basado en datos de 10 minutos agrupados por meses (Fuente:[87])

Como se contempla en la Figura 13, el mayor valor de la relación y la mayor dispersión de los datos se ha producido en los meses de verano, mientras que en los meses de invierno el ratio ha tomado el menor valor, siendo la dispersión de los datos, en esta estación, menor que en el resto (rango intercuartílico $5 \cdot 10^{-3}\%$ y desviación estándar $4 \cdot 10^{-3}\%$).

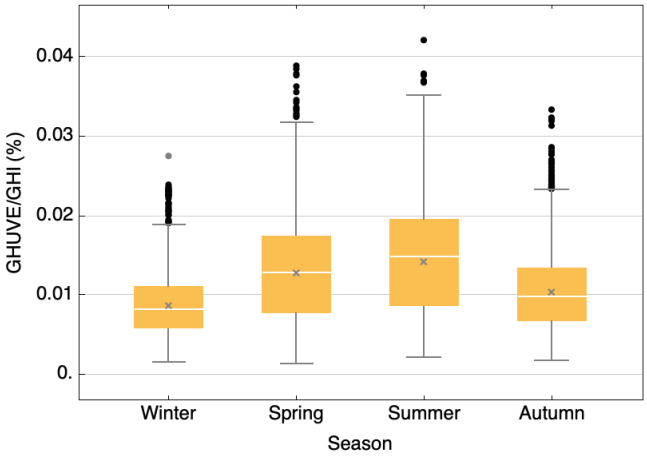

Figura 13. Gráfico de cajas y bigotes del ratio $\mathrm{GHUVE/GHI}$ basado en datos de 10 minutos agrupados por estaciones (Fuente:[87])

Evaluado el ratio $\mathrm{GHUVE/GHI}$ según los 15 tipos de cielos $\mathrm{ISO/CIE}$ (Figura 14 (a)), se ha observado que en los cielos claros la relación ha tomado el valor máximo para el cielo tipo 15 y el mínimo para el cielo tipo 12. Además, para el tipo de cielo 15 los valores han presentado una menor dispersión. En la Figura 14 (b) se observa que para los 3 tipos de cielo $\mathrm{ISO/CIE}$ (cubiertos, intermedios y claros), los valores obtenidos han sido muy similares. El valor medio de la relación ha variado entre $1.1 \cdot 10^{-2}\%$ y $1.2 \cdot 10^{-2}\%$ y el rango intercuartílico entre $8 \cdot 10^{-3}$ y $9 \cdot 10^{-3}\%$.

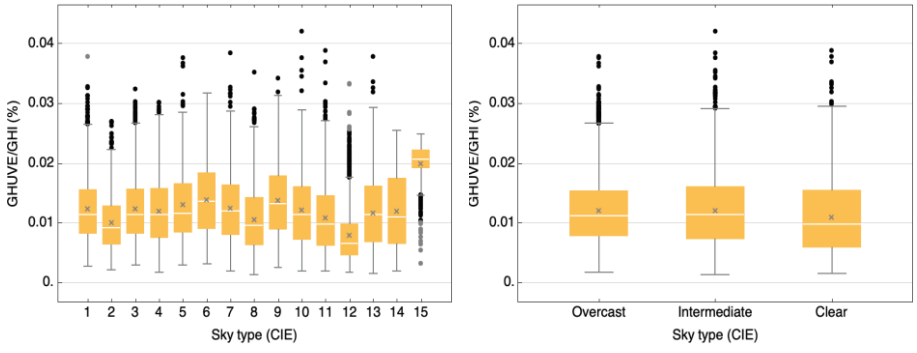

(a) (b)

Figura 14. Gráfico de cajas y bigotes del ratio $\mathrm{GHUVE/GHI}$ basada en datos de 10 minutos agrupados (a) por tipo de cielo estándar $\mathrm{ISO/CIE}$ (1 a 15) (b) por grupo de tipo de cielo (cubierto, intermedio, claro) (Fuente:[87])

Una vez realizada la caracterización estadística de las irradiancias UV global, y UV eritemática se ha comparado el comportamiento de ambas. Se comprueba que mientras los valores medios horarios de GHUV/GHI han variado muy poco a lo largo del día y la mayor dispersión de los datos se ha producido al amanecer y al atardecer, los valores medios horarios de GHUVE/GHI han aumentado hasta el mediodía, para luego disminuir hasta el atardecer, produciéndose la mayor dispersión de los datos en las horas centrales del día.

Los valores medios mensuales de GHUV/GHI se han mantenido casi constantes a lo largo del año, con una pequeña disminución en los meses de julio y agosto. La mayor dispersión se ha presentado en los meses de diciembre y enero. Los valores medios mensuales de GHUVE/GHI han aumentado de enero a mayo, manteniéndose casi constantes hasta el mes de agosto, mes a partir del cual disminuye hasta finalizar el año. La mayor dispersión se ha producido en el mes de julio.

Una vez analizados los valores medios estacionales de GHUV/GHI, se observa que estos se han mantenido prácticamente constantes en las 4 estaciones, produciéndose la mayor dispersión de los datos en otoño e invierno. Los valores medios estacionales de GHUVE/GHI son mayores en primavera y verano, presentándose en invierno el menor valor medio. La mayor dispersión se ha producido en verano.

Estudiado el comportamiento de los ratios clasificados según el tipo de cielo (cubierto, intermedio y claro), se observa que el valor medio de GHUV/GHI ha sido mayor en los cielos cubiertos y menor en los cielos claros, mientras que el valor medio de GHUVE/GHI se ha mantenido prácticamente constante en los 3 tipos.

Capítulo 4. Modelado de la Radiación Ultravioleta

A lo largo de esta tesis doctoral, se ha realizado el modelado de la radiación UV global y la radiación UV eritemática mediante dos estrategias distintas: empleo de regresiones multilineales y de redes neuronales. Aunque la bibliografía, descrita en el capítulo Introducción, recoge otras técnicas y modelos para estas mismas variables, los modelos de regresiones multilineales (MLR) presentan una serie de ventajas: establecen relaciones sencillas entre las variables independientes y la variable dependiente, permitiendo comprobar la variación que sufre la variable dependiente al modificar cada una de las variables independientes [88–90]. A partir de las MLR se pueden analizar, mediante modelos lineales múltiples, modelos más complejos [89]. También se pueden utilizar como aproximación, en el caso de no conocer las relaciones entre las variables [89], o como punto de partida de otros modelos más avanzados [88]. Sin embargo, estos modelos presentan ciertas desventajas, ya que es crucial que la selección de variables independientes se realice correctamente, y no siempre es fácil determinar cuáles son las más idóneas [90]. Además, conocer las relaciones causales entre las variables puede tener dificultad, y en determinados casos interpretar el resultado puede convertirse en un reto [88]. Si hay variables correlacionadas entre sí, la significación estadística de una determinada variable independiente depende del conjunto de variables independientes seleccionadas [90].

De igual modo, las redes neuronales presentan una serie de ventajas: al procesar la información que se les proporciona en paralelo [91,92], la red neuronal es capaz de continuar con el proceso aunque se produzca un fallo en una neurona [92,93]. Son expertas en organizar su propio aprendizaje [91,92], e identificar patrones complejos [92–94]; una vez

realizado el proceso de aprendizaje, son capaces de generalizarlo a situaciones no incluidas en el mismo [91,92,95]. Sin embargo, también presentan ciertas desventajas. Al actuar como “cajas negras” recibiendo datos, procesándolos y generando respuestas, no es fácil conocer el proceso seguido para obtener los resultados, por lo que detectar fallos o analizar si el resultado obtenido es óptimo, no resulta sencillo [91,93]. Como las redes neuronales no son capaces de interpretar los resultados obtenidos, sino que simplemente los muestran, es imprescindible realizar un análisis crítico de la respuesta que interprete el sentido físico de la misma [92]. Por último, para que un patrón pueda ser identificado correctamente, es preciso utilizar una gran cantidad de datos para su entrenamiento y test [92] .

Antes de realizar el modelado de las variables estudiadas, se han seleccionado las variables meteorológicas que tienen más influencia en la variable modelada. Esta selección ha permitido identificar las variables que se encuentran relacionadas entre sí dentro de un conjunto de parámetros, y eliminar aquellos que se han considerado irrelevantes o que su contribución ha sido escasa o nula en la definición de la variable modelada. Esta técnica, “feature selection” en inglés, ha sido fundamental para obtener modelos con adecuado rendimiento, reduciendo su complejidad y mejorando su precisión. Existen numerosas técnicas de selección de variables: coeficiente de correlación de Pearson, importancia de la permutación [96,97], eliminación recursiva de variables [98,99], Boruta [100], muchas de ellas ajustadas al tipo de modelado que se realizará posteriormente. Una de las técnicas más utilizadas, por su sencillez y aplicabilidad, es el coeficiente de correlación de Pearson (r). Dicho coeficiente se ha utilizado para determinar el grado de correlación entre la variable modelada y las variables meteorológicas disponibles. Si la correlación es directa o inversa, r toma los valores 1 y -1, respectivamente.

Cuando toma valores próximos o iguales a 0, se considera que la correlación es débil o nula. La regla de Thumb [101] establece cinco intervalos de r para analizar la correlación entre las variables. Si $|r| < 0{,}3$ la correlación es insignificante, si $0.3 \leq |r| < 0.5$ débil, $0.5 \leq |r| < 0.7$ la correlación es moderada, si $0.7 \leq |r| < 0.9$ fuerte y $0.9 \leq |r| < 1$ es muy fuerte. El modelado de la variable estudiada se ha realizado a partir de las variables cuya correlación es fuerte o muy fuerte. Solo en el caso de que no se hayan obtenido resultados favorables en el modelado a partir de estas variables, se ha considerado la introducción de variables con correlación moderada, siempre que la interacción entre las variables seleccionadas como entradas al modelo haya sido débil o insignificante.

Evaluada la influencia que han presentado las variables meteorológicas, para cada tipo de cielo, con la variable estudiada se ha realizado el modelado mediante regresiones multilineales (MLR) y redes neuronales artificiales (ANN).

La efectividad de los modelos se ha analizado a partir de los indicadores estadísticos tradicionales: coeficiente de correlación (R^2), error cuadrático medio normalizado (nRMSE) y el error de sesgo medio normalizado (nMBE), calculados según las ecuaciones (8), (9) y (10).

$$R^2 = \frac{\sum_{i=1}^{n}\left(\mathrm{Variable}_{mod} - \overline{\mathrm{Variable}}_{mod}\right)\left(\mathrm{Variable}_{exp} - \overline{\mathrm{Variable}}_{exp}\right)}{\sqrt{\sum_{i=1}^{n}\left(\left(\mathrm{Variable}_{mod} - \overline{\mathrm{Variable}}_{mod}\right)^2\left(\mathrm{Variable}_{exp} - \overline{\mathrm{Variable}}_{exp}\right)^2\right)}} \quad (8),$$

$$\mathrm{nRMSE} = \frac{1}{\overline{\mathrm{Variable}}_{exp}}\sqrt{\frac{\sum_{i=1}^{n}\left(\mathrm{Variable}_{mod} - \mathrm{Variable}_{exp}\right)^2}{n}}\,100(\%) \quad (9),$$

$$\mathrm{nMBE} = \frac{1}{\overline{\mathrm{Variable}}_{exp}}\frac{\sum_{i=1}^{n}\left(\mathrm{Variable}_{mod} - \mathrm{Variable}_{exp}\right)}{n}\,100(\%) \quad (10),$$

en las que n representa, en cada caso, el número de datos experimentales que se han utilizado para el ajuste del modelo o para la correspondiente prueba; $\mathrm{Variable}_{\mathrm{exp}}$ es el valor experimental de la variable a modelar, y $\mathrm{Variable}_{\mathrm{mod}}$ el valor modelado de la variable de estudio.

Las redes neuronales programadas para la modelización de la variable estudiada se han entrenado mediante el algoritmo de Levenberg-Marquardt Back-Propagation (LMBP). Estas redes están compuestas por tres capas: capa de entrada, capa oculta y capa de salida. El conjunto de valores empleado se ha dividido en tres grupos: el 70% de los valores se han empleado para entrenar la red, el 15% para su validación, y el 15% restante se han empleado para testar los modelos. Los datos de entrenamiento, mediante un proceso iterativo, se han empleado para determinar la matriz ponderada y el sesgo. Se ha considerado que el entrenamiento ha concluido cuando el rendimiento del modelo resultante, calculado a partir de los datos de validación, ha alcanzado la calidad deseada. El conjunto de datos de prueba se ha empleado para calcular la bondad del modelo calibrado. Una vez que se han obtenido y validado los distintos modelos para cada tipo de cielo, se ha testado el modelo en el conjunto de datos de prueba.

A partir del análisis de R^2, nRMSE y nMBE de las distintas combinaciones de variables de entrada se ha obtenido la red neuronal óptima. El modelo seleccionado es aquel con mejores indicadores de bondad (un alto valor de R^2 y un bajo valor de nRMSE y nMBE) logrado a partir del número más reducido de variables, intentando además, que las variables utilizadas en el modelo sean habitualmente medidas en las estaciones meteorológicas terrestres.

Además de modelar la radiación ultravioleta (GHUV y GHUVE) mediante el empleo de redes neuronales también se han desarrollado modelos mediante regresiones multilineales (MLR). Estos modelos de regresión

se han desarrollado con el 85% de los datos, y se han testado con el 15% restante. Los datos empleados para construir los modelos de regresión han sido los mismos que los utilizados en los modelos de redes neuronales y el test de ambos procedimientos se ha realizado sobre el mismo conjunto de datos.

En este punto cabe señalar, que el alcance y la aplicabilidad de los modelos desarrollados viene determinado por el conjunto de datos utilizados en el modelado o en el entrenamiento de la red. Cuando los datos proceden de una única localización, el modelo tendrá, por naturaleza, carácter local. En caso de que el conjunto de datos utilizado para generar el modelo, provenga de diferentes localizaciones, generalizará más o menos el mismo, en función de la diferente climatología y/o características geográficas de las localizaciones implicadas. En todo caso, la validez del modelo requerirá datos suficientes para realizar el test completo en la localización de interés. Esta es la principal limitación de los modelos desarrollados en esta tesis.

4.1. Modelización de la irradiancia ultravioleta horizontal para todas las condiciones del cielo mediante redes neuronales artificiales y modelos de regresión.

El procedimiento anteriormente descrito se ha utilizado en el segundo de los artículos que conforman esta tesis [102], para modelar la irradiancia ultravioleta global sobre el plano horizontal (GHUV) en Burgos, a partir de los datos diezminutales experimentalmente obtenidos entre marzo de 2020 y mayo de 2022 en la instalación meteorológica.

A partir del coeficiente de correlación de Pearson (r), descrito en el Capítulo 3, se han seleccionado las variables a utilizar para realizar los modelos de redes neuronales y de regresión multilineal para modelar

GHUV. Las variables disponibles en este caso fueron la irradiancia global horizontal, GHI, la irradiancia directa normal, DNI, la irradiancia difusa horizontal, DHI, cobertura de nubes, CC, fracción difusa, D, índice de claridad, k_t, temperatura, T, altura solar , α, y el índice de claridad, ε, e índice de brillo de Pérez, Δ, todas descritas en la Tabla 2. La Figura 15 resume los resultados de coeficiente de correlación de Pearson entre las variables utilizadas.

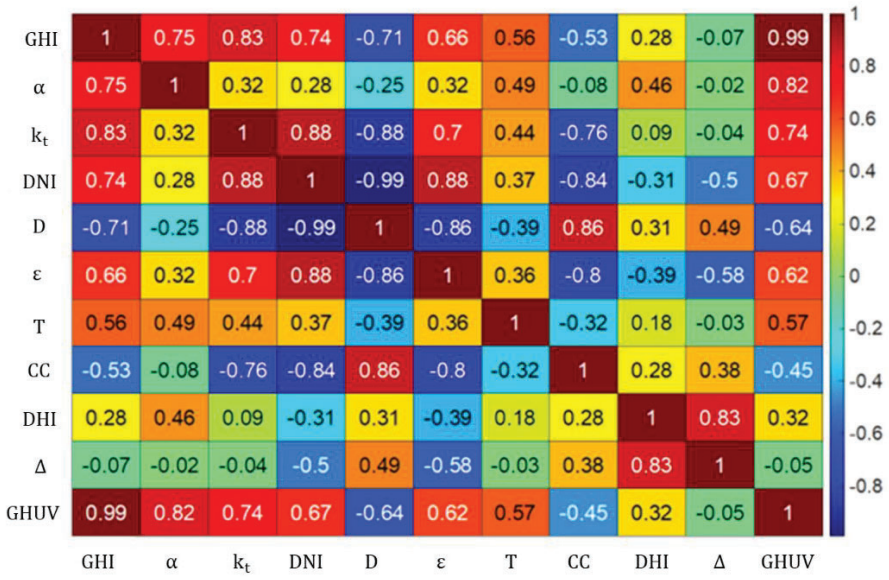

Figura 15. Matriz de los coeficientes de correlación de Pearson de todas las variables meteorológicas consideradas en este estudio. (Fuente: Adaptada de [102])

Las correlaciones de las variables meteorológicas con GHUV se muestran en la Tabla 7. Se observa que los mayores valores se han obtenido para GHI , α y k_t , con unos valores del coeficiente de correlación de Pearson de 0.99, 0.82 y 0.74 respectivamente.

Tabla 7. Selección de las variables meteorológicas a considerar, en función del coeficiente de correlación de Pearson $r(\mathrm{GHUV}, \mathrm{variable})$. (Fuente: Adaptada de [102])

Variable	**GHI**	**α**	**k_t**	**DNI**	**D**	**ε**	**T**	**CC**
$\mathbf{r(GHUV, Variable)}$	0.99	0.82	0.74	0.67	-0.64	0.62	0.57	-0.45

Una vez conocidas las variables que mayor influencia tienen sobre GHUV, se ha realizado el modelado mediante redes neuronales de la radiación ultravioleta. GHI ha sido la variable con mayor correlación sobre GHUV, y se ha incluido como primera entrada en dichos modelos. En la Tabla 8 se recogen los 18 modelos desarrollados, junto con los valores de nRMSE, nMBE y R^2 obtenidos, en la fase de entrenamiento y en la fase de validación. La eliminación de la altura solar y de la cobertura nubosa en los modelos, empeoran los resultados. Además, en los modelos en los que se ha incluido DNI, en lugar de GHI o $\mathrm{k_t}$, los resultados obtenidos han sido notablemente peores. Por todo ello, se ha considerado que el modelo más adecuado es el modelo 9 (GHI, α, CC) ya que está formado por un número reducido de variables, y los resultados obtenidos han sido ligeramente superiores a los que ha presentado el modelo 13 ($\mathrm{k_t}$, α, CC), que emplea $\mathrm{k_t}$ en lugar de GHI. El modelo 9 ha presentado un valor de R^2 del 99.59% para los datos de entrenamiento y del 99.61% para los datos de prueba.

Tabla 8. Resultados de los modelos $\mathrm{GHUV\ ANN}$. (Fuente: Adaptada de [102])

Número de modelo y variables		Entrenamiento			Validación		
#	**Variables**	**nRMSE** (%)	**nMBE** (%)	$\mathbf{R^2}$	**nRMSE** (%)	**nMBE** (%)	$\mathbf{R^2}$
1	$\mathrm{GHI, k_t, \alpha, DNI, D, \varepsilon, T, CC}$	3.82	0.00	99.68	3.77	−0.01	99.69
2	$\mathrm{GHI, \alpha, DNI, D, \varepsilon, T, CC}$	3.87	0.00	99.67	3.83	−0.01	99.68
3	$\mathrm{GHI, DNI, D, \varepsilon, T, CC}$	4.26	−0.01	99.60	4.21	−0.01	99.62
4	$\mathrm{GHI, \alpha, D, \varepsilon, T, CC}$	3.89	0.00	99.67	3.86	−0.02	99.68
5	$\mathrm{GHI, \alpha, \varepsilon, T, CC}$	3.91	−0.02	99.66	3.88	−0.03	99.67
6	$\mathrm{GHI, \alpha, T, CC}$	4.04	0.00	99.64	4.01	−0.01	99.65
7	$\mathrm{GHI, \alpha, \varepsilon, CC}$	4.15	0.00	99.62	4.09	0.00	99.64
8	$\mathrm{GHI, \alpha, T}$	4.85	0.00	99.48	4.82	0.04	99.49
9	$\mathrm{GHI, \alpha, CC}$	4.30	0.00	99.59	4.24	0.00	99.61
10	$\mathrm{GHI, \alpha, \varepsilon}$	4.71	−0.01	99.51	4.67	0.02	99.53
11	$\mathrm{GHI, \alpha}$	5.13	0.01	99.42	5.09	0.07	99.44
12	GHI	10.30	0.00	97.66	10.29	0.19	97.70

13	k_t, α, CC	4.36	0.00	99.58	4.34	0.02	99.59
14	k_t, α	5.13	0.00	99.42	5.10	0.05	99.44
15	k_t	39.72	−0.05	65.26	40.08	0.58	65.14
16	DNI, α, CC	8.70	−0.01	98.33	8.55	0.08	98.41
17	DNI, α	11.94	0.00	96.86	12.03	−0.02	96.86
18	DNI	45.45	0.00	54.50	46.05	0.45	53.98

Implementados los modelos de redes neuronales, se han desarrollado los modelos de regresión de primer y segundo orden con las mismas variables empleadas en los modelos 9 y 13 (GHI, k_t, α, CC) anteriormente citados. Los modelos de primer orden se recogen en la Tabla 9, observándose que, al emplear la variable k_t en lugar de GHI, los resultados también empeoran, al igual que ha sucedido en los modelos derivados de redes neuronales. A la vista de estos resultados, se considera que es preferible utilizar el parámetro GHI en lugar de k_t. Los modelos de regresión multilineal han presentado mejores resultados $(R^2 > 98.8\%)$ que el de regresión lineal $(R^2 = 97.3\%)$.

Tabla 9. Modelos de primer orden realizados mediante regresiones multilineales. (Fuente: [102])

Modelos de primer orden	R^2	**nRMSE (%)**	**nMBE (%)**
$GHUV = 0.3676 + 0.0369 \cdot GHI$	97.33	11.02	$1 \cdot 10^{-3}$
$GHUV = -1.7224 + 0.0317 \cdot GHI + 6.9531 \cdot \alpha$	98.81	7.39	0.11
$GHUV = -1.9243 + 0.0323 \cdot GHI + 6.5892 \cdot \alpha + 0.0035 \cdot CC$	98.82	7.36	0.11
$GHUV = -11.1581 + 22.5424 \cdot k_t + 24.4465 \cdot \alpha$	93.01	17.95	0.11
$GHUV = -11.3956 + 22.8218 \cdot k_t + 24.3899 \cdot \alpha + 0.0021 \cdot CC$	93.01	17.95	0.11

Al analizar los modelos de segundo orden, recogidos en la Tabla 10, se comprueba que no ha habido diferencias significativas en los resultados al sustituir la variable k_t por GHI. En ambos casos, cuando se ha incluido la variable CC, los resultados han mejorado ligeramente.

Tabla 10. Modelos de segundo orden realizados mediante regresiones multilineales. (Fuente: [102])

Modelos de segundo orden	$\mathbf{R^2}$	**nRMSE (%)**	**nMBE (%)**
$\mathrm{GHUV} = -1.8212 + 0.0167 \cdot \mathrm{GHI} + 19.0462 \cdot \alpha + 0.0126 \cdot \mathrm{CC} - 9.29 \cdot 10^{-6} \cdot \mathrm{GHI}^2 + 0.0188 \cdot \mathrm{GHI} \cdot \alpha + 8.80 \cdot 10^{-5} \cdot \mathrm{GHI} \cdot \mathrm{CC} - 7.2559 \cdot \alpha^2 - 0.0958 \cdot \alpha \cdot \mathrm{CC} - 6.59 \cdot 10^{-5} \cdot \mathrm{CC}^2$	99.45	5.02	0.06
$\mathrm{GHUV} = -1.1625 + 0.0238 \cdot \mathrm{GHI} + 10.2243 \cdot \alpha - 1.27 \cdot 10^{-5} \cdot \mathrm{GHI}^2 + 0.0253 \cdot \mathrm{GHI} \cdot \alpha - 8.8361 \cdot \alpha^2$	99.32	5.60	0.07
$\mathrm{GHUV} = -0.3540 + 2.0833 \cdot \mathrm{k_t} + 14.0893 \cdot \alpha - 0.0165 \cdot \mathrm{CC} - 9.0813 \cdot \mathrm{k_t^2} + 40.7916 \cdot \mathrm{k_t} \cdot \alpha + 0.0405 \cdot \mathrm{k_t} \cdot \mathrm{CC} - 7.9650 \cdot \alpha^2 - 0.0170 \cdot \alpha \cdot \mathrm{CC} - 8.83 \cdot 10^{-5} \cdot \mathrm{CC}$	99.40	5.24	0.08
$\mathrm{GHUV} = -2.7058 + 7.3586 \cdot \mathrm{k_t} + 11.4945 \cdot \alpha - 10.8880 \cdot +42.6023 \cdot \mathrm{k_t} \cdot \alpha - 7.7515 \cdot \alpha^2$	99.32	5.62	0.08

En modelos de segundo orden, puede ser interesante emplear $\mathrm{k_t}$ en lugar de GHI, al ser $\mathrm{k_t}$ una variable que está relacionada con la claridad del cielo. Sin embargo, en los modelos de primer orden esta opción no es válida ya que los resultados empeoran significativamente como ya se ha visto.

4.2. Modelización de la irradiancia eritemática ultravioleta (UVER) bajo diferentes condiciones de cielo en Burgos, España, mediante modelos MLR y ANN.

En el tercer artículo de esta tesis [87], se ha aplicado el mismo procedimiento para modelar GHUVE utilizando modelos de regresiones multilineales y de redes neuronales artificiales. La campaña experimental para la obtención de los datos es la misma que la utilizada en el segundo de los artículos de la tesis, entre septiembre de 2020 y junio de 2022.

En ese caso, las variables disponibles fueron la irradiancia global horizontal, GHI, la irradiancia directa normal, DNI, la irradiancia difusa

horizontal, DHI, cobertura de nubes, CC, fracción difusa, D, índice de claridad, $\mathrm{k_t}$, temperatura del aire, T, humedad relativa, RH, velocidad del viento, WS, ángulo azimultal , ψ, ángulo cenital, θ_z, el índice de claridad, ε, e índice de brillo de Pérez, Δ, todas descritas en la Tabla 2. Nuevamente, el coeficiente de correlación de Pearson, ha determinado la correlación entre las variables meteorológicas y GHUVE. Los resultados, recogidos en la Tabla 11, muestran que las variables GHI y θ_z presentan una correlación muy fuerte o fuerte con GHUVE en condiciones de cielo claro, intermedio, cubierto y para todos los tipos de cielo. Estos resultados concuerdan con los obtenidos por otros autores [44,46,48].

Tabla 11. Coeficientes de Pearson calculados para las distintas variables (Fuente: [87])

	$\lvert\mathbf{r(GHUVE, variable)}\rvert$				
Tipo de Cielo CIE	$[\mathbf{1-0.9}]$	$(\mathbf{0.9-0.7}]$	$(\mathbf{0.7-0.5}]$	$(\mathbf{0.5-0.3}]$	$(\mathbf{0.3-0}]$
Todo tipo de cielo	GHI	θ_z	$\mathrm{k_t, D, \varepsilon, RH, DNI, T}$	$\mathrm{k_d', DHI}$	$\Delta, \mathrm{WS}, \psi, \mathrm{CC}$
Cubierto	GHI	$\theta_z, \mathrm{k_d', DHI}$	$\mathrm{k_t, D, DNI}, \Delta$	$\varepsilon, \mathrm{RH, T}$	$\mathrm{WS}, \psi, \mathrm{CC}$
Intermedio	$-$	GHI, θ_z	$\mathrm{k_t, k_d', D, DHI, DNI}$	$\varepsilon, \mathrm{RH, T}$	$\Delta, \mathrm{WS}, \psi, \mathrm{CC}$
Claro	GHI, θ_z	$-$	T	$\mathrm{k_t, k_d', D}, \varepsilon, \mathrm{RH, DNI}$	$\Delta, \mathrm{DHI, WS}, \psi, \mathrm{CC}$

Se ha modelado GHUVE, a partir de las variables que han presentado una correlación moderada, fuerte y muy fuerte $(\mathrm{r} \geq 0.5)$ con esta variable.

En la Tabla 12 se muestran las expresiones matemáticas de los cuatro modelos de regresión junto con la bondad de ajuste de cada uno de ellos. En los cuatro casos, los resultados del ajuste de los modelos han presentado correlaciones elevadas con los datos experimentales $(\mathrm{R}^2 > 0{,}92)$. Sin embargo, en los cuatro casos el valor de nRMSE ha sido elevado, superando el 21%.

Tabla 12. Modelos de regresión multilineal (MLR) de GHUVE y bondad del ajuste (basado en el 85% de los datos) (Fuente: [87])

Condiciones de cielo	Modelos MLR	$\mathbf{R^2}$	nRMSE (%)	nMBE (%)
Todo tipo de cielo	$\mathrm{GHUVE} = 1.90 \cdot 10^{-2} + 2.35 \cdot 10^{-4} \cdot \mathrm{GHI} - 1.74 \cdot 10^{-2} \cdot \theta_z - 9.85 \cdot 10^{-2} \mathrm{k_t} + 7.44 \cdot 10^{-4} \mathrm{T}$	0.937	25.60	$-2.05 \cdot 10^{-12}$
Cubierto	$\mathrm{GHUVE} = 2.98 \cdot 10^{-2} + 1.61 \cdot 10^{-4} \cdot \mathrm{GHI} - 2.71 \cdot 10^{-2} \cdot \theta_z + 1.30 \cdot \mathrm{k_d'} - 9.89 \cdot 10^{-4} \cdot \mathrm{DHI}$	0.926	29.80	$6.92 \cdot 10^{-13}$
Intermedio	$\mathrm{GHUVE} = 8.54 \cdot 10^{-2} + 2.59 \cdot 10^{-4} \cdot \mathrm{GHI} - 6.98 \cdot 10^{-2} \cdot \theta_z - 1.80 \cdot 10^{-4} \cdot \mathrm{DHI} - 9.91 \cdot 10^{-5} \cdot \mathrm{DNI}$	0.934	22.49	$3.23 \cdot 10^{-12}$
Claro	$\mathrm{GHUVE} = 1.75 \cdot 10^{-1} + 5.84 \cdot 10^{-5} \cdot \mathrm{GHI} - 1.52 \cdot 10^{-1} \cdot \theta_z + 6.89 \cdot 10^{-4} \cdot \mathrm{T}$	0.940	21.10	$9.87 \cdot 10^{-13}$

Para mejorar los resultados obtenidos mediante MLR se ha estimado GHUVE por medio de redes neuronales. Para ello se han generado y probado cuatro modelos (uno para cada tipo de cielo y un cuarto para todo tipo de cielo) utilizando las variables meteorológicas seleccionadas en la Tabla 11. El coeficiente de correlación obtenido, en los cuatro casos, ha sido elevado, $\mathrm{R}^2 > 0.95$. El valor de nRSME ha variado entre 11.9% y 21.3%.

La bondad de ajuste de la validación de los cuatro modelos, tanto para MLR como ANN, se muestra en la Tabla 13. Se observa que se han obtenido mejores resultados en los modelos ANN que en los modelos MLR. Los mejores resultados se han obtenido para cielos claros ($\mathrm{R}^2 > 0.97$ y $\mathrm{nRMSE} < 12.4\%$). Además, tanto para cielos claros como para todo tipo de cielo, el valor de nRMSE ha mejorado significativamente, disminuyendo más del 40% con respecto a los modelos MLR.

Tabla 13. Bondad de ajuste de los modelos MLR y ANN (basados en el 15% de los datos) (Fuente: [87])

Condiciones de cielo	$\mathbf{R^2}$	nRMSE (%)	nMBE (%)	Condiciones de cielo	$\mathbf{R^2}$	nRMSE (%)	nMBE (%)
Todo tipo de cielo (MLR1)	0.938	25.21	$1.41 \cdot 10^{-1}$	**Todo tipo de cielo (ANN1)**	0.979	14.63	$1.55 \cdot 10^{-1}$
Cubiertos (MLR2)	0.930	29.65	$6.28 \cdot 10^{-1}$	**Cubiertos (ANN2)**	0.965	21.06	$6.58 \cdot 10^{-1}$
Intermedios (MLR3)	0.923	23.57	$-5.75 \cdot 10^{-1}$	**Intermedios (ANN3)**	0.953	19.20	$3.38 \cdot 10^{-1}$
Claros (MLR4)	0.942	20.57	$-2.10 \cdot 10^{-1}$	**Claros (ANN4)**	0.979	12.35	$4.31 \cdot 10^{-1}$

En las regresiones multilineales, los valores de nRMSE y de nMBE obtenidos, han superado en todos los casos el 20%. Estos valores son similares a los que obtuvo González-Rodríguez et al. [2], empleando polinomios de segundo grado (nRMSE entre el 20% y el 54%).

En los modelos de redes neuronales, los valores de nRMSE han oscilado entre el 12% y el 21%, valores similares a los obtenidos por otros autores ([48,80,103–105]) que obtuvieron valores de nRMSE entre 14% y 21%.

A partir de los modelos de ANN para todo tipo de cielo, se ha buscado optimizar el número de variables y la estructura de la red neuronal que permita minimizar el valor de nRMSE. Para ello, se han utilizado como variables de referencia las identificadas como fuertemente correlacionadas con GHUVE, (GHI y θ_z) (Tabla 11). Esta combinación de variables, cuyo nRMSE ha sido de 17.02% (calculado con 2 neuronas) se ha combinado con el resto de variables, aumentando una a una tanto el número de variables como el número de neuronas, de tal forma que el número de neuronas en la capa oculta siempre sea igual o inferior al número de variables de entrada. Los mejores resultados se han obtenido para la combinación de 5 y 6 variables y redes neuronales con hasta 6 neuronas en la capa oculta. En la Tabla 14 se muestran las

combinaciones que han estimado el menor valor de nRMSE, utilizando 5 y 6 variables en combinación, variando de 2 hasta 6 el número de neuronas en la capa oculta. Un análisis pormenorizado de los resultados obtenidos ha considerado el modelo 2, cuyas variables de entrada fueron $\mathrm{GHI}, \theta_z, \mathrm{T}, \mathrm{k_t}, \psi$, como el modelo óptimo, debido a que está formado por variables que se miden habitualmente en las estaciones radiométricas, permitiendo su aplicación en escenarios reales sin necesidad de sensores especializados adicionales.

Tabla 14. $\mathrm{nRMSE}\ (\%)$ para combinaciones de 5 y 6 variables con 2 a 6 neuronas (Fuente:[87])

Número modelo	Número de variables/ número de neuronas	Variables meteorológicas	**nRMSE** (%)
1	$5/2$	$\mathrm{GHI}, \theta_z, \varepsilon, \mathrm{T}, \mathrm{k_t}$	14.49
2	$5/3$	$\mathrm{GHI}, \theta_z, \mathrm{T}, \mathrm{k_t}, \psi$	14.16
3	$5/4$	$\mathrm{GHI}, \theta_z, \mathrm{T}, \mathrm{CC}, \psi$	13.34
4	$5/5$	$\mathrm{GHI}, \theta_z, \mathrm{T}, \Delta, \psi$	13.01
5	$6/2$	$\mathrm{GHI}, \theta_z, \varepsilon, \mathrm{T}, \mathrm{k_t}, \mathrm{RH}$	14.11
6	$6/3$	$\mathrm{GHI}, \theta_z, \mathrm{DHI}, \mathrm{T}, \mathrm{RH}, \psi$	13.59
7	$6/4$	$\mathrm{GHI}, \theta_z, \mathrm{T}, \mathrm{RH}, \mathrm{CC}, \psi$	12.94
8	$6/5$	$\mathrm{GHI}, \theta_z, \mathrm{T}, \mathrm{RH}, \mathrm{CC}, \psi$	12.53
9	$6/6$	$\mathrm{GHI}, \theta_z, \mathrm{T}, \mathrm{k_t}, \mathrm{CC}, \psi$	12.16

Capítulo 5. Aspectos Sociales y de la Salud

En los Juegos Olímpicos de Tokio 2020, el índice UVI superó el nivel 8 durante 4 de los 5 días que duró la competición. Un alto porcentaje de los componentes de la Selección Española de Vela presentaron síntomas de haber recibido altas dosis de radiación UV, que les provocaron quemaduras solares [106].

Debido a la gran influencia que tiene la exposición a la radiación solar ultravioleta sobre la salud, es fundamental promover una conciencia social en el uso de fotoprotectores solares, que permitan disfrutar de los beneficios que ofrece la radiación UV minimizando los efectos nocivos de la misma. Un ejemplo de esta política, es la promovida por la OMS, la OIT, la Organización Meteorológica Mundial (OMM) y el Programa de las Naciones Unidas para el Medio Ambiente (PNUMA), mediante la creación de una aplicación para teléfonos móviles (SunSmart Global UV) que permite conocer tanto la predicción meteorológica como el UVI de los próximos cinco días en distintas ubicaciones [107].

En la exposición a la irradiación ultravioleta en el trabajo, un factor importante del riesgo viene determinado por la actividad en la que se engloba el trabajo. Wittlich et al. [13] hace una clasificación de los trabajos según la cantidad de SED anual que reciben los trabajadores. Es evidente, que la cantidad de radiación es muy distinta de unos sectores ocupacionales a otros pero, dentro del mismo sector, lo que determina el riesgo es la subocupación que se realiza. Ejemplos de estas variaciones los explicita [13] distinguiendo entre el trabajo de los estibadores portuarios según que se dediquen a cargar un tren o un barco, o el de las maestras de preescolar frente a las de guardería. En el mismo sentido [51] distingue entre diferentes tipos de carteros o [108] entre los trabajadores portuarios y los estibadores.

Como respuesta a la preocupación de dermatólogos y pacientes ante la frecuencia del cáncer de piel no melanoma de los trabajadores, en la 1ª Cumbre Multilateral sobre el Cáncer de Piel Ocupacional, que tuvo lugar en el 15º Congreso de la Asociación Europea de Dermatología Oncológica en 2019, se estableció una llamada a la acción para luchar contra este tipo de cáncer en los trabajadores al aire libre [109]. Entre las acciones propuestas se pueden destacar las siguientes:

- Se debería mejorar el marco legislativo que permite proteger a los trabajadores al aire libre, para que lo haga de forma más eficaz. El cáncer de piel no melanoma debería ser reconocida como enfermedad profesional en toda la Unión Europea.

- Los lugares de trabajo deberían de estar provistos de herramientas que permitan monitorizar la exposición a la radiación UV, y se deberían emplear recursos rentables que protegiesen a los trabajadores.

- Los trabajadores sanitarios y los empleadores deberían trabajar conjuntamente para fomentar la prevención del cáncer de piel.

Esta iniciativa se puede considerar heredera de la campaña “Slip, Slop, Slap”, para la prevención del cáncer de piel, promovida en Australia en el verano de 1980-81, que le convirtió en el país líder en la prevención de este tipo de cáncer. La campaña tuvo su continuación en 1988 con el programa SunSmart, que empezó en Melbourne durante los fines de semana de verano [110], y se extendió a todo el país, incluyendo campañas en los medios de comunicación, programas para escuelas y lugares de trabajo y formación para el personal sanitario. Además, la adopción de medidas fiscales como la eliminación de impuestos para los protectores solares, o las deducciones fiscales por el uso de estos productos que tienen los trabajadores al aire libre, así como la prohibición en todo el país de los soláriums comerciales, son medidas

que han mejorado los hábitos de protección de la población de Australia. La concienciación de la necesidad de protección en actividades de ocio, junto con la política de protección en escuelas y lugares de trabajo, ha conseguido la disminución de la incidencia del cáncer de piel entre la población australiana, mientras que en otros muchos países del mundo sigue en aumento [111]. Este es un ejemplo de cómo la realización de campañas de protección gubernamental puede ayudar a una mejor concienciación de la necesidad de protección frente a los peligros de la radiación UV.

Teniendo en cuenta la conveniencia de evitar los efectos no deseados de la radiación, es necesario, fundamentalmente en personas con fototipos bajos, con múltiples lunares, pacientes con cáncer, y en general personas que se encuentran expuestas de manera prolongada o intensa a la radiación UV, proteger la piel mediante el uso de protectores solares de amplio espectro y mediante el empleo de sombreros, gafas de sol y ropa [112]. Los sombreros permiten proteger la cabeza, la frente y el cuello, mientras que el uso de gafas de sol con protección UVA ayuda a prevenir la aparición de lesiones en los ojos. Los guantes son útiles para evitar los signos de fotoenvejecimiento en las manos [113]. La protección que proporciona la ropa frente a la radiación UV se ve influenciada por el grosor, el color (los colores oscuros protegen más eficientemente), la trama y el tamaño del poro, la humedad y la estanqueidad del tejido [113], y su grado de fotoprotección se indica a través del factor de protección UV (UPF) y se mide con un espectofotómetro, que indica la cantidad de transmisión de radiación UV [114].

En esta sección se introduce un estudio acerca de la percepción del riesgo solar y la inducción al uso de vestimenta con protección solar en un grupo específico de población que es el de los estudiantes del Centro Universitario de la Defensa (CUD) de Marín, Pontevedra. Este estudio

se ha podido llevar a cabo gracias al trabajo de profesores de la mencionada Escuela, habituales colaboradores con el grupo de investigación. El estudio se ha realizado a través de encuestas a los alumnos del CUD, analizadas mediante Modelos de Ecuaciones Estructurales. El trabajo constituye la cuarta aportación a la tesis.

5.1. Modelos de ecuaciones estructurales

Los modelos de ecuaciones estructurales (SEM), combinan el análisis de ruta con el análisis factorial [115,116], permitiendo comprender los patrones complejos de las interrelaciones. El análisis de ruta se centra en la trayectoria causal de las variables observadas [117,118]. Las variables latentes son las variables que no se miden directamente, siendo los factores que hacen que un conjunto de variables observadas, medidas o indicadores, varíen. Al no ser medibles, se les debe asignar una métrica, asignándoles el valor 1 a una de las trayectorias dirigidas hacia una de las variables observadas sobre las que influye, y, a partir de esta restricción se estiman el resto de trayectorias. El interés de un SEM completo es conocer la trayectoria causal de las variables latentes.

Cuando cada variable latente sólo tiene un indicador, un modelo de ecuación estructural realiza un análisis de trayectorias. Sin embargo, cuando cada variable tiene varios indicadores, pero no hay efectos directos que los conecten, se realiza un análisis factorial. Cuando cada variable tiene varios indicadores y caminos que los conectan, se construyen modelos estructurales completos.

Mientras que el análisis factorial describe la relación entre las variables latentes y las variables observadas, el análisis de trayectorias representa los efectos directos e indirectos de las variables latentes entre sí. En el análisis de trayectorias tradicional, los efectos mencionados se producen entre variables observadas. En un modelo

de ecuaciones estructurales, el análisis de trayectorias se realiza fundamentalmente entre variables latentes [119].

En los gráficos SEM , el modelo de regresión lineal supone implícitamente un error de medición cero y los términos de error de las variables observadas se modelan explícitamente en los modelos de ecuaciones estructurales. En estos modelos también se incluyen posibles efectos directos e indirectos entre sus variables [120].

Varios autores, en diferentes campos científicos, han empleado los modelos de ecuaciones estructurales en sus investigaciones. Liu et al. [121] ha utilizado un SEM para estudiar cómo afectan, directa o indirectamente, el cambio climático y el desarrollo socioeconómico en el agua subterránea, y cómo puede influir el cambio de uso de la tierra en el reequilibrio del déficit de agua subterránea producido. Zhu et al. [122] ha estudiado la previsión de generación de energía de una planta fotovoltaica, analizando la influencia de determinados factores meteorológicos en la generación de energía. Ha tenido en cuenta que, el entorno en el que se encuentra la planta presenta características meteorológicas complejas, y ha utilizado un modelo de ecuaciones estructurales para evaluar qué factores son los que más influyen. Las variables que ha considerado han sido la intensidad de la irradiancia solar, la velocidad del viento, la densidad atmosférica, la nubosidad, la humedad relativa y la temperatura ambiente, obteniendo que la potencia de la planta está directamente relacionada con la intensidad de la radiación solar y con la temperatura ambiente, y con menor influencia de la densidad atmosférica. Shi et al. [123] ha utilizado un SEM para analizar los factores que están implicados en las reservas de carbono de los bosques de bambú en China. Entre las variables estudiadas, las que han sido decisivas para las reservas de carbono en los bosques de bambú han sido la densidad de los tallos, la edad media de las plantas, su diámetro a la altura del pecho, la temperatura media

anual y la precipitación media anual. Un campo habitual de utilización de modelos de ecuaciones estructurales en el ámbito de las ciencias sociales y de la conducta, donde permiten contribuir a generar modelos complejos que incorporan múltiples indicadores, mejorando la comprensión de cómo diversas variables o factores se interrelacionan entre sí y explican desenlaces o comportamientos [124,125].

5.2. Una evaluación sobre la eficiencia de la ropa con protección UV entre los alumnos de la Escuela de la Armada Española.

En el cuarto artículo de esta tesis [126] se han analizado, mediante el empleo de SEM, las variables de comportamiento que están asociadas a los efectos de los rayos UV sobre la piel, denotados por los efectos combinados de las variables exógenas, sobre la decisión de compra y empleo de ropa con protección UV.

Este estudio se ha llevado a cabo a partir de un cuestionario realizado a alumnos de la Escuela Naval Militar de Marín (España) que realizan entrenamientos al aire libre. Está formado por preguntas que contienen variables observadas relacionadas con la adquisición y uso de ropa militar con protección frente a los rayos UV (Tabla 15), en un cuestionario con respuestas en escala tipo Likert.

Tabla 15. Cuestionario realizado a alumnos de la Escuela Naval Militar de Marín (España). (Fuente: Adaptada de [126])

1	Si un miembro de las fuerzas armadas no se protege del sol, el riesgo de padecer cáncer de piel en el futuro es: (1 = no bajo a 5 = muy alto)
2	Si a un miembro de las fuerzas armadas le diagnosticaran cáncer de piel en el futuro, lo consideraría: (1 = no grave a 5 = muy grave)
3	Usar ropa de protección solar durante las maniobras es una forma cómoda de proteger a los miembros de las fuerzas armadas del sol. (1 = nada agradable a 4 = muy agradable)
4	Usar ropa de protección solar para la salud de un miembro de las fuerzas armadas es:

	(1 = nada importante a 4 = muy importante)
5	Usar ropa de protección solar es molesto durante la vida diaria en el ejército. (1 = muy molesto a 4 = nada molesto)
6	Usar ropa de protección solar es inconveniente, porque tiendo a olvidarla. (1 = muy inconveniente a 5 = nada inconveniente)
7	Usar ropa de protección solar es innecesario. (1 = muy innecesario a 4 = necesario)
8	¿Con qué frecuencia los militares usan ropa de protección solar? (1 = casi nunca a 4 = siempre)
9	¿Qué importancia tiene para los superiores militares de su entorno el uso de ropa de protección solar para su propia protección? (1 = nada importante a 4 = muy importante)
10	¿Qué importancia tiene para los superiores militares de su entorno el uso de ropa de protección solar para tu protección? (1 = nada importante a 4 = muy importante)
11	¿Crees que podrás utilizar ropa de protección solar adecuada para protegerte del sol? (1 = definitivamente no 7 = definitivamente sí)
12	¿Tienes intención de utilizar adecuadamente ropa de protección solar para protegerte del sol? (1 = definitivamente no 7 = definitivamente sí)
13	¿Planeas comprar ropa con protección solar?
14	¿Planeas llevar ropa con protección solar durante el entrenamiento en un día soleado?
15	¿Tienes previsto controlar la duración del entrenamiento para ponerte ropa de protección solar en función del tiempo que haga?
16	¿Planeas pedirle a otros militares que te recuerden usar ropa con protección solar? (1 = definitivamente no 7 = definitivamente sí)
17	¿Con qué frecuencia se protegió del sol usando ropa con protección solar cuando estuvo al aire libre en un día soleado durante ejercicios militares? (1 = nunca a 5 = siempre)

En la Figura 16 se muestra la hipótesis propuesta en el modelo de dependencias entre las variables utilizadas mediante el diagrama de flujo en el que se representan las variables latentes: actitud (ATT), influencia social (SOC) y la planificación de la acción (PLN) y cinco variables observadas: susceptibilidad percibida (SUS), gravedad percibida (SEV), autoeficacia (EFF), intención (INT) y hábito de uso de

ropa de protección solar (HAB). A continuación, en la Tabla 16, se muestran las hipótesis realizadas para el modelo propuesto.

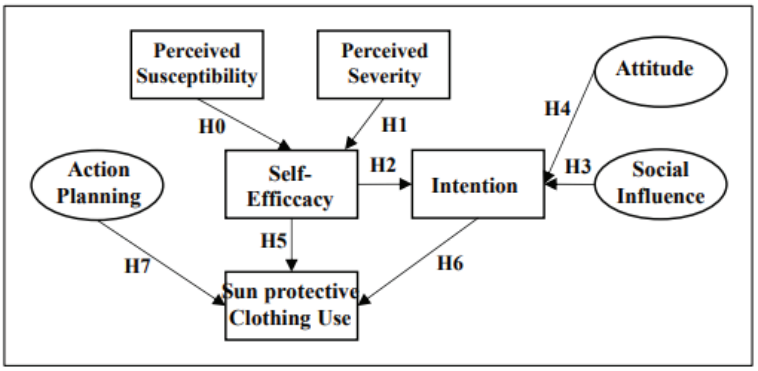

Figura 16. Modelo propuesto para el uso de textiles UV (Fuente: [126])

Tabla 16. Hipótesis realizadas. (Fuente: [126])

	Hipótesis
H0	Percepción de que protegerse del sol previene el riesgo de desarrollar cáncer de piel en el futuro.
H1	Percepción de que ante un diagnóstico de cáncer de piel, una forma eficaz de protegerse del sol sería llevar ropa con protección solar.
H2	Actitud positiva hacia la intención del uso de ropa con protección UV para protegerse del sol.
H3	Influencia de las normas sociales en la intención de usar ropa con protección UV.
H4	Predisposición a llevar ropa con protección solar para protegerse eficazmente del sol.
H5	Necesidad de refuerzo motivacional para usar ropa con protección solar, teniendo dicho hábito ya adquirido.
H6	Intencionalidad de vestir ropa con protección solar sobre el hábito de uso de esta.
H7	Planteamiento del uso de ropa con protección solar que puede convertirse en un hábito de uso.

Inicialmente, todas las mediciones se han sometido a las pruebas de suposición características de los estudios que implican análisis multivariante [119]. Las variables exógenas observadas (susceptibilidad

percibida, SUS, y gravedad percibida, SEV), y las variables latentes (actitud, ATT, planificación de acciones, PLN, e influencia social, SOC) han revelado ausencia de multicolinealidad. Los supuestos de normalidad y linealidad multivariante resultantes de las combinaciones dos a dos de las variables métricas, se han cumplido.

Para preservar la consistencia del modelo, ha sido necesario verificar la robustez entre las variables latentes (o constructos) ATT, PLN y SOC. A partir del alfa de Cronbach [127,128] se ha medido la fiabilidad de las tres variables latentes (ATT, PLN y SOC), obteniéndose valores de 0.733, 0.866 y 0.558, respectivamente. Todas las variables, menos SOC, han superado el valor mínimo de 0.70, y por lo tanto cumplen los requisitos de fiabilidad [129]. Una vez que se ha comprobado que no existe multicolinealidad entre ATT, PLN y SOC se ha llevado a cabo, mediante el empleo de SEM ajustado a las variables latentes, la estimación de las relaciones teóricas hipotéticas, H0 a H7 definidas en la Tabla 16.

Analizada la relación causal de las variables exógenas susceptibilidad (SUS) y severidad (SEV) sobre la variable eficiencia (EFF), se han confirmado las hipótesis H0 (protegerse del sol previene el riesgo de desarrollar cáncer de piel en el futuro) y H1 (en caso de ser diagnosticado de cáncer de piel, una forma eficaz de protegerse del sol sería llevar ropa con protección solar), a un nivel de significancia del 10%. También se ha evaluado la relación entre las variables EFF y las variables latentes actitud e influencia social sobre la intención, aceptando que las hipótesis H2 (actitud positiva hacia el uso de ropa con protección UV para protegerse del sol) y H4 (percepción de que llevar ropa con protección solar sería eficaz) influirían positivamente en la disposición a llevar ropa con protección solar para protegerse del sol en actividades militares al aire libre. Sin embargo, la hipótesis H3 ha sido rechazada, lo que supone que las normas sociales que

recomiendan el uso de ropa con protección UV no influyen en la intención de un militar de utilizar este tipo de ropa. Por último, se ha analizado la influencia que tienen las variables EFF, y las variables latentes planificación de la acción e intención sobre el hábito de llevar ropa con protección solar. Se han confirmado las hipótesis H6 (la intención que tiene una persona de vestir ropa con protección solar está relacionada con el hábito de uso) y H7 (si una persona se plantea vestir ropa con protección solar, es posible que esta idea se convierta en un hábito de uso). Además, también se ha determinado que la variable mediadora EFF no ha mostrado diferencias significativas con la variable hábito, por lo que la hipótesis H5 (si una persona necesita un refuerzo motivacional para usar ropa con protección solar, teniendo dicho hábito ya adquirido) se ha rechazado.

Con los resultados obtenidos, se puede concluir que los estudiantes han mostrado una actitud positiva frente a la decisión de compra y uso de uniformes con protección ultravioleta.

Este trabajo ha permitido demostrar la utilidad de los modelos de ecuaciones estructurales en el análisis de encuestas para analizar el comportamiento humano. Estos modelos constituyen una herramienta potente para formular de manera explícita y contrastar teorías complejas, incluyendo relaciones profundas y/o jerárquicas entre muchas variables.

Capítulo 6. Conclusiones y Líneas de Futuro.

6.1. Conclusiones

El objetivo de esta Tesis es modelar matemáticamente la radiación ultravioleta, lo que se ha logrado a través de la consecución de los objetivos parciales concretados en 4 artículos publicados en revistas científicas indexadas en JCR.

El análisis de los datos experimentales del ratio GHUV/GHI ha mostrado una gran dependencia de las condiciones del tipo cielo, ya se haya clasificado este a partir de la norma ISO/CIE o del parámetro k_t. Los valores más altos de GHUV/GHI se han obtenido para cielos cubiertos, y los valores más bajos para cielos claros. No se observa en la práctica ninguna tendencia ni horaria, ni mensual ni estacional, salvo la relacionada con el predominio de un tipo de cielo sobre otro. Los valores de GHUV/GHI alcanzados representan aproximadamente el 4%, resultado que concuerda con los obtenidos en otras localizaciones, de donde se deduce la posibilidad de modelar con relativa precisión GHUV a partir de GHI.

Analizada la relación entre GHUV y las variables disponibles, se ha observado que, según el coeficiente de Pearson, las más influyentes son GHI, α y k_t. A partir de los modelos desarrollados mediante ANN se ha concluido que el modelo con mejores resultados ha sido el formado por GHI , α y CC (con un R^2 de 99.61% y un nRMSE de 4.24%). Utilizando modelos de regresión, los modelos de segundo orden obtuvieron mejores resultados que los modelos de primer orden. Se puede concluir que para modelar GHUV no existe gran diferencia entre el empleo de redes neuronales y regresiones multilineales de segundo orden.

Analizados los datos experimentales del ratio $\mathrm{GHUVE/GHI}$ se ha observado que, a diferencia del comportamiento de $\mathrm{GHUV/GHI}$, este presenta variabilidad en todos los intervalos temporales considerados (horario, mensual y estacional). Comparando los resultados obtenidos al modelar GHUVE empleando regresiones multilineales y redes neuronales, se han obtenido mejores resultados cuando se han empleado ANN. Para todo tipo de cielo el modelo que mejores resultados ha presentado ha sido el que incluía como variables $\mathrm{GHI}, \theta_z, \mathrm{T}, \mathrm{k_t}$.

En cualquier caso, los modelos desarrollados son modelos locales cuya extrapolación a otras localizaciones y climas diferentes a los de la ciudad de Burgos, arrojarán resultados diferentes. Para la obtención de modelos universales válidos en cualquier localización es imprescindible la utilización de datos procedentes de diferentes localizaciones y la utilización de algoritmos de interpolación que permitan la generación de mapas de radiación UV y UVER con una adecuada resolución espacial y temporal.

A partir de modelos de ecuaciones estructurales se ha analizado la percepción que un grupo de alumnos, que realizan entrenamientos al aire libre de la Escuela Naval Militar de Marín, tiene del riesgo para la salud la exposición a la radiación ultravioleta. Para ello, se ha estudiado la relación entre las variables observadas (susceptibilidad percibida, gravedad percibida, autoeficacia, intención y hábito de uso de ropa de protección solar) y las variables latentes (actitud, influencia social y la planificación de la acción) del modelo. Se ha concluido que los alumnos han presentado una actitud positiva frente a la compra y al uso de ropa con protección UV.

6.2. Líneas de futuro

Esta tesis contribuye, con el análisis y modelado de la irradiancia UV y eritemática, a la línea de trabajo fundamental del grupo de investigación Solar and Wind Feasibility Technologies de la Universidad de Burgos, el análisis espectral de la radiación solar: aplicaciones climáticas, energéticas y biológicas. Pero no es, en absoluto un trabajo cerrado. La tesis ha abierto otras líneas de investigación que permitirán un mayor conocimiento de la radiación UV, una de las bandas del espectro solar con más influencia en la vida en la Tierra y en la salud humana. Entre ellas, distinguimos las siguientes:

Línea 1: Aunque en el trabajo se han utilizado exclusivamente variables meteorológicas obtenidas de instalaciones terrestres, la influencia de otras magnitudes, como el ozono atmosférico (TOM) o la presencia de aerosoles sobre la radiación UV global, A, B y eritemática hace conveniente la inclusión de estas variables en los modelos. Se plantea la obtención de estos datos a través de estaciones de la Agencia Estatal de Meteorología y medidas de satélite, lo que obligará a la modificación de la granularidad de los datos para adaptar las series de medidas a la disponibilidad de los datos externos.

Línea 2: Diferentes estudios afirman que la contribución de la componente difusa de la radiación UV, DHUV, a la cantidad global de radiación UV es superior al 50%, resultando por tanto muy importante la modelización de esta variable. La modelización de esta componente de la radiación UV se ve además complicada, por la escasez de datos experimentales que permitan construir y validar los modelos. Esta es una de las líneas de trabajo futuro propuesta como continuidad de esta tesis.

Línea 3: Para que se apliquen de forma efectiva, medidas de protección solar para la realización de actividades realizadas en exterior, laborales

o de ocio, es preciso que los afectados perciban este riesgo. Las actividades de concienciación requieren datos precisos de las dosis exactas de radiación UV y UVE absorbidas durante estas actividades. La determinación de estos niveles en unidades MED y/o SED a partir de modelos validados frente a dispositivos calibrados será imprescindible para llevar a cabo este objetivo.

Línea 4: El diseño y calibrado de dispositivos de bajo coste destinados a la determinación de la dosis de radiación UV permitirá la democratización de estos sistemas para la protección de la población en wearables y aplicaciones móviles. Esta línea ha permitido ya la publicación de un artículo científico [130].

Línea 5: Para la obtención de las dosis totales de radiación UV recibidas en entornos complejos, como, por ejemplo, las ciudades, es preciso el conocimiento de la interacción de esta banda del espectro con las diferentes superficies que conforman estos entornos. La determinación de la reflectividad de las superficies en función de la longitud de onda es fundamental para este análisis y permitirá el estudio de la trayectoria de la radiación en ambientes con gran número de obstáculos y el diseño de ciudades y espacios más seguros desde el punto de vista de la radiación UV . Esta línea de investigación se está actualmente desarrollando a través del proyecto recientemente financiado PID2022-139477OB-I00

Línea 6: Los modelos de ecuaciones estructurales se han mostrado como herramientas útiles en la evaluación de variables latentes relacionadas con el comportamiento humano. La utilización de estos modelos en el análisis de encuestas relacionadas con la percepción del riesgo solar puede contribuir al diseño de campañas de concienciación más efectivas para grupos especialmente afectados, como pueden ser los trabajadores de exterior en ciudades, sector agrícola y ganadero,

juventud y deportistas. Esta línea de investigación continuará con el análisis de las encuestas ya realizadas a estos grupos de riesgo.

Línea 7: Los modelos dirigidos por datos (data-driven models) determinados mediante algoritmos de inteligencia artificial se han mostrado muy efectivos para el estudio de variables climáticas como la radiación solar en todas las bandas del espectro. El empleo de algoritmos distintos a las redes neuronales tradicionales, como las máquinas de soporte de vectores, árboles de decisión, redes neuronales convolucionales, transformadores de visión, etc, serán herramientas útiles para la obtención de nuevos modelos para las diferentes componentes de la radiación UV a partir de variables más fácilmente obtenidas en instalaciones terrestres o imágenes de cielo.

Línea 8: La ingente cantidad de datos meteorológicos de gran calidad registrados en las instalaciones del grupo de investigación, podrán ser analizados y modelados mediante herramientas tradicionales englobadas en Data Science: regresiones, técnicas bayesianas, análisis de componentes principales…

Línea 9: De igual manera, la combinación de las bases de datos del grupo de investigación, con las de otros grupos o la AEMET, red MESOR, y otras, permitirá la extrapolación e interpolación de datos y modelos a otras localizaciones y el análisis y desarrollo de técnicas matemáticas de interpolación y extrapolación específicas para este tipo de datos.

Línea 10: Desde el punto de vista experimental, la obtención de modelos avanzados de radiación UV que permitan la determinación de la distribución angular de la misma en toda la bóveda celeste precisará del diseño y calibración de escáneres de cielo en esta banda del espectro.

Línea 11: Este mismo objetivo deberá intentarse mediante imágenes de cielo HDR realizados con cámaras de bajo coste calibradas también

en esta banda del espectro. Estos dos últimos objetivos están siendo desarrollados mediante el proyecto TED2021-131563B-I00.

Bibliografía

[1] A.A.M. Ahmed, M.H. Ahmed, S.K. Saha, O. Ahmed, A. Sutradhar, Optimization algorithms as training approach with hybrid deep learning methods to develop an ultraviolet index forecasting model, Stoch. Environ. Res. Risk Assess. 36 (2022) 3011–3039. https://doi.org/10.1007/s00477-022-02177-3.

[2] L. González-Rodríguez, A.P. de Oliveira, L. Rodríguez-López, J. Rosas, D. Contreras, A.C. Baeza, A study of Uver in Santiago, Chile based on Long-Term in Situ Measurements (Five Years) and Empirical Modelling, Energies. 14 (2021) 368. https://doi.org/10.3390/en14020368.

[3] G. Salvadori, D. Lista, C. Burattini, L. Gugliermetti, F. Leccese, F. Bisegna, Sun Exposure of Body Districts: Development and Validation of an Algorithm to Predict the Erythemal Ultra Violet Dose, Int. J. Environ. Res. Public Health. 16 (2019) 3632. https://doi.org/10.3390/ijerph16193632.

[4] A. Serrano, M. Antón, M.L. Cancillo, V.L. Mateos, Daily and annual variations of erythemal ultraviolet radiation in Southwestern Spain, Ann. Geophys. 24 (2006) 427–441. https://doi.org/10.5194/angeo-24-427-2006.

[5] L. Alados-Arboledas, I. Alados, I. Foyo-Moreno, F.J. Olmo, A. Alcántara, The influence of clouds on surface UV erythemal irradiance, Atmos. Res. 66 (2003) 273–290. https://doi.org/10.1016/S0169-8095(03)00027-9.

[6] I. Foyo-Moreno, I. Alados, F.J. Olmo, L. Alados-Arboledas, The influence of cloudiness on UV global irradiance (295-385 nm), Agric. For. Meteorol. 120 (2003) 101–111. https://doi.org/10.1016/j.agrformet.2003.08.023.

[7] L. Wang, W. Gong, A. Lin, B. Hu, Measurements and cloudiness

influence on UV radiation in Central China, Int. J. Climatol. 34 (2014) 3417–3425. https://doi.org/10.1002/joc.3918.

[8] D. Mateos, R. Román, J. Bilbao, A. de Miguel, A. Pérez-Burgos, Cloud modulation of shortwave and ultraviolet solar irradiances at surface, Opt. Pura y Apl. 45 (2012) 29–32. https://doi.org/10.7149/OPA.45.1.29.

[9] K.O. Ogunjobi, Y.J. Kim, Ultraviolet (0.280-0.400 μm) and broadband solar hourly radiation at Kwangju, South Korea: Analysis of their correlation with aerosol optical depth and clearness index, Atmos. Res. 71 (2004) 193–214. https://doi.org/10.1016/j.atmosres.2004.05.001.

[10] C.M. Lerche, P.A. Philipsen, H.C. Wulf, UVR: sun, lamps, pigmentation and Vitamin D, Photochem. Photobiol. Sci. 16 (2017) 291–301. https://doi.org/10.1039/c6pp00277c.

[11] J.W. Cherrie, M.P.C. Cherrie, Workplace exposure to UV radiation and strategies to minimize cancer risk, Br. Med. Bull. 144 (2022) 45–56. https://doi.org/10.1093/bmb/ldac019.

[12] K. Lamy, T. Portafaix, C. Brogniez, S. Godin-Beekmann, H. Bencherif, B. Morel, A. Pazmino, J.M. Metzger, F. Auriol, C. Deroo, V. Duflot, P. Goloub, C.N. Long, Ultraviolet radiation modelling from ground-based and satellite measurements on Reunion Island, southern tropics, Atmos. Chem. Phys. 18 (2018) 227–246. https://doi.org/10.5194/acp-18-227-2018.

[13] M. Wittlich, S. Westerhausen, B. Strehl, H. Versteeg, W. Stöppelmann, The GENESIS-UV study on ultraviolet radiation exposure levels in 250 occupations to foster epidemiological and legislative efforts to combat nonmelanoma skin cancer, Br. J. Dermatol. 188 (2023) 350–360. https://doi.org/10.1093/bjd/ljac093.

[14] I. V. Ivanov, T. Mappes, P. Schaupp, C. Lappe, S. Wahl,

Ultraviolet radiation oxidative stress affects eye health, J. Biophotonics. 11 (2018) 1–13. https://doi.org/10.1002/jbio.201700377.

[15] N. Khanjani, A. Moradabadi, E. Najafi, B. Hayati, R. Abdollahi, Geographic variation in urinary tract and genital cancers in Iran: a hypothesis involving exposure to solar radiation, BMC Res. Notes. 16 (2023) 1–6. https://doi.org/10.1186/s13104-023-06334-x.

[16] P.H. Hart, M. Norval, S.N. Byrne, L.E. Rhodes, Exposure to Ultraviolet Radiation in the Modulation of Human Diseases, Annu. Rev. Pathol. Mech. Dis. 14 (2019) 55–81. https://doi.org/10.1146/annurev-pathmechdis-012418-012809.

[17] G.E. Davis, M.J. Davis, W.E. Lowell, The effect of ultraviolet radiation on the incidence and severity of major mental illness using birth month, birth year, and sunspot data, Heliyon. 8 (2022) e09197. https://doi.org/10.1016/j.heliyon.2022.e09197.

[18] M.F. Holick, Biological effects of sunlight, ultraviolet radiation, visible light, infrared radiation and Vitamin D for health, Anticancer Res. 36 (2016) 1345–1356.

[19] D.M.A, Mohamed, et al F.M., Okeil, Effect of ultraviolet on vitamin D and quality of life in postmenopausal women: a randomized controlled study, Physiother. Q. 27 (2019) 6–11. https://doi.org/10.5114/pq.2019.84272.

[20] B.N. Ames, W.B. Grant, W.C. Willett, Does the High Prevalence of Vitamin D Deficiency in African Americans Contribute to Health Disparities?, Nutrients. 13 (2021) 1–25. https://doi.org/10.3390/nu13020499.

[21] J.L. Sagripanti, C.D. Lytle, Estimated Inactivation of Coronaviruses by Solar Radiation With Special Reference to COVID-19, Photochem. Photobiol. 96 (2020) 731–737.

https://doi.org/10.1111/php.13293.

[22] J.B. Pérez-Gilaberte, N. Martín-Iranzo, J. Aguilera, M. Almenara-Blasco, M.V. de Gálvez, Y. Gilaberte, Correlation between UV Index, Temperature and Humidity with Respect to Incidence and Severity of COVID 19 in Spain, Int. J. Environ. Res. Public Health. 20 (2023). https://doi.org/10.3390/ijerph20031973.

[23] G.H. Bernhard, S. Madronich, R.M. Lucas, S.N. Byrne, T. Schikowski, R.E. Neale, Linkages between COVID-19, solar UV radiation, and the Montreal Protocol, Photochem. Photobiol. Sci. 22 (2023) 991–1009. https://doi.org/10.1007/s43630-023-00373-w.

[24] H. Nandin de Carvalho, Latitude impact on pandemic Sars-Cov-2 2020 outbreaks and possible utility of UV indexes in predictions of regional daily infections and deaths, J. Photochem. Photobiol. 10 (2022). https://doi.org/10.1016/j.jpap.2022.100108.

[25] L. Wang, W. Gong, J. Li, Y. Ma, B. Hu, Empirical studies of cloud effects on ultraviolet radiation in Central China, Int. J. Climatol. 34 (2014) 2218–2228. https://doi.org/10.1002/joc.3832.

[26] L. Feng, L. Wang, W. Gong, A. Lin, B. Hu, Estimation of hourly and daily ultraviolet solar irradiation under various sky conditions at Sanya, Southern China, Theor. Appl. Climatol. 121 (2015) 187–198. https://doi.org/10.1007/s00704-014-1239-3.

[27] S.S. Leal, C. Tíba, R. Piacentini, Daily UV radiation modeling with the usage of statistical correlations and artificial neural networks, Renew. Energy. 36 (2011) 3337–3344. https://doi.org/10.1016/j.renene.2011.05.007.

[28] A.C.S. Porfirio, J.L. De Souza, G.B. Lyra, M.A. Maringolo Lemes, An assessment of the global UV solar radiation under various sky conditions in Maceió-Northeastern Brazil, Energy. 44 (2012) 584–592. https://doi.org/10.1016/j.energy.2012.05.042.

[29] I. Foyo-Moreno, I. Alados, F.J. Olmo, L. Alados-Arboledas, The influence of cloudiness on UV global irradiance (295-385 nm), Agric. For. Meteorol. 120 (2003) 101–111. https://doi.org/10.1016/j.agrformet.2003.08.023.

[30] J. Bilbao, D. Mateos, A. de Miguel, Analysis and cloudiness influence on UV total irradiation, Int. J. Climatol. 31 (2011) 451–460. https://doi.org/10.1002/joc.2072.

[31] I. Foyo-Moreno, J. Vida, L. Alados-Arboledas, Ground based ultraviolet (290-385 nm) and broadband solar radiation measurements in south-eastern Spain, Int. J. Climatol. 18 (1998) 1389–1400. https://doi.org/10.1002/(SICI)1097-0088(1998100)18:12<1389::AID-JOC318>3.0.CO;2-N.

[32] I. Foyo-Moreno, J. Vida, L. Alados-Arboledas, A simple all weather model to estimate ultraviolet solar radiation (290-385 nm), J. Appl. Meteorol. 38 (1999) 1020–1026. https://doi.org/10.1175/1520-0450(1999)038<1020:ASAWMT>2.0.CO;2.

[33] J. Bilbao, D. Mateos, A. de Miguel, Analysis and cloudiness influence on UV total irradiation, Int. J. Climatol. 31 (2011) 451–460. https://doi.org/10.1002/joc.2072.

[34] B.L. Diffey, Sources and measurement of ultraviolet radiation, Methods. 28 (2002) 4–13. https://doi.org/10.1016/S1046-2023(02)00204-9.

[35] S.D. Al-Aruri, The empirical relationship between global radiation and global ultraviolet (0.290-0.385) $μ$m solar radiation components, Sol. Energy. 45 (1990) 61–64. https://doi.org/10.1016/0038-092X(90)90028-B.

[36] F.J. Barbero, G. López, F.J. Batlles, Determination of daily solar ultraviolet radiation using statistical models and artificial neural networks, Ann. Geophys. 24 (2006) 2105–2114.

https://doi.org/10.5194/angeo-24-2105-2006.

[37] B. Hu, Y. Wang, G. Liu, Variation characteristics of ultraviolet radiation derived from measurement and reconstruction in Beijing, China, Tellus, Ser. B Chem. Phys. Meteorol. 62 (2010) 100–108. https://doi.org/10.1111/j.1600-0889.2010.00452.x.

[38] A. Habte, M. Sengupta, C.A. Gueymard, R. Narasappa, O. Rosseler, D.M. Burns, Estimating Ultraviolet Radiation From Global Horizontal Irradiance, IEEE J. Photovoltaics. 9 (2019) 139–146. https://doi.org/10.1109/JPHOTOV.2018.2871780.

[39] L. Wang, W. Gong, M. Luo, W. Wang, B. Hu, M. Zhang, Comparison of different UV models for cloud effect study, Energy. 80 (2015) 695–705. https://doi.org/10.1016/j.energy.2014.12.026.

[40] H. Liu, B. Hu, L. Zhang, X.J. Zhao, K.Z. Shang, Y.S. Wang, J. Wang, Ultraviolet radiation over China: Spatial distribution and trends, Renew. Sustain. Energy Rev. 76 (2017) 1371–1383. https://doi.org/10.1016/j.rser.2017.03.102.

[41] C. Gueymard, SMARTS2, A Simple Model of the Atmospheric Radiative Transfer of Sunshine: Algorithms and performance assessment, Florida Sol. Energy Cent. (1995) 1–78.

[42] ISO/CIE 17166:2019(E), 2019. Erythema reference action spectrum and standard erythema dose. ISO: Geneva, CIE: Vienna., (2019).

[43] A.R. Esteve, M.J. Marín, F. Tena, M.P. Utrillas, J.A. Martinez-Lozano, Influence of cloudiness over the values of erythemal radiation in Valencia, Spain, Int. J. Climatol. (2010) 127–136. https://doi.org/10.1002/joc.1883.

[44] A. de Miguel, R. Román, J. Bilbao, D. Mateos, Evolution of erythemal and total shortwave solar radiation in Valladolid, Spain: Effects of atmospheric factors, J. Atmos. Solar-Terrestrial Phys.

73 (2011) 578–586. https://doi.org/10.1016/j.jastp.2010.11.021.

[45] G.H. Bernhard, A.F. Bais, P.J. Aucamp, A.R. Klekociuk, J.B. Liley, R.L. McKenzie, Stratospheric ozone, UV radiation, and climate interactions, Photochem. Photobiol. Sci. 22 (2023) 937–989. https://doi.org/10.1007/s43630-023-00371-y.

[46] J. Bilbao, R. Román, C. Yousif, A. Pérez-Burgos, D. Mateos, A. de Miguel, Global, diffuse, beam and ultraviolet solar irradiance recorded in Malta and atmospheric component influences under cloudless skies, Sol. Energy. 121 (2015) 131–138. https://doi.org/10.1016/j.solener.2015.04.048.

[47] S. Buntoung, S. Janjai, M. Nunez, P. Choosri, N. Pratummasoot, K. Chiwpreecha, Sensitivity of erythemal UV/global irradiance ratios to atmospheric parameters: Application for estimating erythemal radiation at four sites in Thailand, Atmos. Res. 148 (2014) 24–34. https://doi.org/10.1016/j.atmosres.2014.05.020.

[48] I. Alados, M.A. Gomera, I. Foyo-Moreno, L. Alados-Arboledas, Neural network for the estimation of UV erythemal irradiance using solar broadband irradiance, Int. J. Climatol. 27 (2007) 1791–1799. https://doi.org/10.1002/joc.1496.

[49] C.P. Jacovides, F.S. Tymvios, J. Boland, M. Tsitouri, Artificial Neural Network models for estimating daily solar global UV, PAR and broadband radiant fluxes in an eastern Mediterranean site, Atmos. Res. 152 (2015) 138–145. https://doi.org/10.1016/j.atmosres.2013.11.004.

[50] INTERNATIONAL COMMISSION ON NON-IONIZING RADIATION PROTECTION., ICNIRP STATEMENT ON PROTECTION OF WORKERS AGAINST ULTRAVIOLET RADIATION, Health Phys. 99 (2010) 66–87. https://doi.org/10.1097/HP.0b013e3181d85908.

[51] S.M. John, C. Garbe, L.E. French, J. Takala, W. Yared, A.

Cardone, R. Gehring, A. Spahn, A. Stratigos, Improved protection of outdoor workers from solar ultraviolet radiation: position statement, J. Eur. Acad. Dermatology Venereol. 35 (2021) 1278–1284. https://doi.org/10.1111/jdv.17011.

[52] Programa de las Naciones Unidas para el Desarrollo, Protocolo de Montreal relativo a las sustancias que agotan la capa de ozono, New York, NY, 2008.

[53] R.E. Neale, P.W. Barnes, T.M. Robson, P.J. Neale, C.E. Williamson, R.G. Zepp, S.R. Wilson, S. Madronich, A.L. Andrady, A.M. Heikkilä, G.H. Bernhard, A.F. Bais, P.J. Aucamp, A.T. Banaszak, J.F. Bornman, L.S. Bruckman, S.N. Byrne, B. Foereid, D.P. Häder, L.M. Hollestein, W.C. Hou, S. Hylander, M.A.K. Jansen, A.R. Klekociuk, J.B. Liley, J. Longstreth, R.M. Lucas, J. Martinez-Abaigar, K. McNeill, C.M. Olsen, K.K. Pandey, L.E. Rhodes, S.A. Robinson, K.C. Rose, T. Schikowski, K.R. Solomon, B. Sulzberger, J.E. Ukpebor, Q.W. Wang, S. Wängberg, C.C. White, S. Yazar, A.R. Young, P.J. Young, L. Zhu, M. Zhu, Environmental effects of stratospheric ozone depletion, UV radiation, and interactions with climate change: UNEP Environmental Effects Assessment Panel, Update 2020, Springer International Publishing, 2021. https://doi.org/10.1007/s43630-020-00001-x.

[54] A.L. Andrady, A.M. Heikkilä, K.K. Pandey, L.S. Bruckman, C.C. White, M. Zhu, L. Zhu, Effects of UV radiation on natural and synthetic materials, Photochem. Photobiol. Sci. 22 (2023) 1177–1202. https://doi.org/10.1007/s43630-023-00377-6.

[55] R.E. Neale, R.M. Lucas, S.N. Byrne, L. Hollestein, L.E. Rhodes, S. Yazar, A.R. Young, M. Berwick, R.A. Ireland, C.M. Olsen, The effects of exposure to solar radiation on human health, Photochem. Photobiol. Sci. 22 (2023) 1011–1047.

https://doi.org/10.1007/s43630-023-00375-8.

[56] F. Xie, Y. Xia, W. Feng, Y. Niu, Increasing Surface UV Radiation in the Tropics and Northern Mid-Latitudes due to Ozone Depletion after 2010, Adv. Atmos. Sci. 40 (2023) 1833–1843. https://doi.org/10.1007/s00376-023-2354-9.

[57] P.J. Neale, C.E. Williamson, A.T. Banaszak, D.P. Häder, S. Hylander, R. Ossola, K.C. Rose, S. Wängberg, R. Zepp, The response of aquatic ecosystems to the interactive effects of stratospheric ozone depletion, UV radiation, and climate change, Photochem. Photobiol. Sci. 22 (2023) 1093–1127. https://doi.org/10.1007/s43630-023-00370-z.

[58] A.L. Andrady, P.W. Barnes, J.F. Bornman, T. Gouin, S. Madronich, C.C. White, R.G. Zepp, M.A.K. Jansen, Oxidation and fragmentation of plastics in a changing environment; from UV-radiation to biological degradation, Sci. Total Environ. 851 (2022) 158022. https://doi.org/10.1016/j.scitotenv.2022.158022.

[59] P.W. Barnes, T.M. Robson, R.G. Zepp, J.F. Bornman, M.A.K. Jansen, R. Ossola, Q.W. Wang, S.A. Robinson, B. Foereid, A.R. Klekociuk, J. Martinez-Abaigar, W.C. Hou, R. Mackenzie, N.D. Paul, Interactive effects of changes in UV radiation and climate on terrestrial ecosystems, biogeochemical cycles, and feedbacks to the climate system, Springer International Publishing, 2023. https://doi.org/10.1007/s43630-023-00376-7.

[60] P.W. Barnes, T.M. Robson, R.G. Zepp, J.F. Bornman, M.A.K. Jansen, R. Ossola, Q.W. Wang, S.A. Robinson, B. Foereid, A.R. Klekociuk, J. Martinez-Abaigar, W.C. Hou, R. Mackenzie, N.D. Paul, Interactive effects of changes in UV radiation and climate on terrestrial ecosystems, biogeochemical cycles, and feedbacks to the climate system, Springer International Publishing, 2023. https://doi.org/10.1007/s43630-023-00376-7.

[61] S. García-Rodríguez, I. García, A. García-Rodríguez, M. Díez-Mediavilla, C. Alonso-Tristán, Solar Ultraviolet Irradiance Characterization under All Sky Conditions in Burgos, Spain, Appl. Sci. 12 (2022) 10407. https://doi.org/10.3390/app122010407.

[62] C.A. Gueymard, J.A. Ruiz-Arias, Extensive worldwide validation and climate sensitivity analysis of direct irradiance predictions from 1-min global irradiance, Sol. Energy. 128 (2016) 1–30. https://doi.org/10.1016/j.solener.2015.10.010.

[63] D. Granados-López, A. Suárez-García, M. Díez-Mediavilla, C. Alonso-Tristán, Feature selection for CIE standard sky classification, Sol. Energy. 218 (2021) 95–107. https://doi.org/10.1016/j.solener.2021.02.039.

[64] A. Suárez-García, D. Granados-López, D. González-Peña, M. Díez-Mediavilla, C. Alonso-Tristán, Seasonal caracterization of CIE standard sky types above Burgos, northwestern Spain, Sol. Energy. 169 (2018) 24–33. https://doi.org/10.1016/j.solener.2018.04.028.

[65] A. Suárez-García, M. Díez-Mediavilla, D. Granados-López, D. González-Peña, C. Alonso-Tristán, Benchmarking of meteorological indices for sky cloudiness classification, Sol. Energy. 195 (2020) 499–513. https://doi.org/10.1016/j.solener.2019.11.060.

[66] ISO 15469:2004(E)/CIE S 011/E:2003; Spatial Distribution of Daylight—CIE Standard General Sky. ISO: Geneva; CIE: Vienna, 2004.

[67] European Comission, Progress on Open Science: towards a shared research knowledge system, (2020) 1–65. https://doi.org/10.2777/00139.

[68] Jefatura del Estado, Ley 17/2022, de 5 de septiembre, por la que se modifica la Ley 14/2011, de 1 de junio, de la Ciencia, la

Tecnología y la Innovación. Boletín Oficial del Estado número 214, de 6 de septiembre de 2022, 2022.

[69] D.G. Erbs, S.A. Klein, J.A. Duffie, Estimation of the diffuse radiation fraction for hourly, daily and monthly-average global radiation, Sol. Energy. 28 (1982) 293–302. https://doi.org/10.1016/0038-092X(82)90302-4.

[70] M. Iqbal, An Introduction to Solar Radiation, Academic Press, New York, NY, USA, 1983.

[71] R. Perez, P. Ineichen, R. Seals, J. Michalsky, R. Stewart, Modeling daylight availability and irradiance components from direct and global irradiance, Sol. Energy. 44 (1990) 271–289. https://doi.org/10.1016/0038-092X(90)90055-H.

[72] C.A. Gueymard, A reevaluation of the solar constant based on a 42-year total solar irradiance time series and a reconciliation of spaceborne observations, Sol. Energy. 168 (2018) 2–9. https://doi.org/10.1016/j.solener.2018.04.001.

[73] C. Hoyer-Klick, D. Dumortier, A. Tsvetkov, J. Polo, J.L. Torres, C. Kurz, P. Ineichen, Management and Exploitation of Solar Resource Knowledge, Sixth Framew. Program. (2008) 1–20. https://www.mesor.org/docs/MESoR_D1.1.2_ExistingGroundData_v1.0.pdf.

[74] C.N. Long, E.G. Dutton, BSRN Global Network recommended QC tests, V2.0, Baseline Surf. Radiat. Netw. (2002) 1–3.

[75] R.E. Bird, R.L. Hulstrom, Simplified Clear Sky Model for Direct and Diffuse Insolation on Horizontal Surfaces, Solar Energy Research Institute, Golden, Colorado, 1981.

[76] R. Kittler, R. Perez, S. Darula, A set of standard skies. Characterizing daylight conditions for computer and energy conscious design. NASA LaRC Global Solar Mapping View project Calibration of an artificial sky with sun after refurbishment

View project, 1998. https://doi.org/10.13140/RG.2.1.4798.7048.

[77] D. Granados-López, M. Díez-Mediavilla, M.I. Dieste-Velasco, A. Suárez-García, C. Alonso-Tristán, Evaluation of the vertical sky component without obstructions for daylighting in Burgos, Spain, Appl. Sci. 10 (2020) 1–15. https://doi.org/10.3390/app10093095.

[78] A. García-Rodríguez, D. Granados-López, S. García-Rodríguez, M. Díez-Mediavilla, C. Alonso-Tristán, Modelling Photosynthetic Active Radiation (PAR) through meteorological indices under all sky conditions, Agric. For. Meteorol. 310 (2021) 108627. https://doi.org/10.1016/j.agrformet.2021.108627.

[79] C.P. Jacovides, F.S. Tymvios, D.N. Asimakopoulos, N.A. Kaltsounides, G.A. Theoharatos, M. Tsitouri, Solar global UVB (280-315 nm) and UVA (315-380 nm) radiant fluxes and their relationships with broadband global radiant flux at an eastern Mediterranean site, Agric. For. Meteorol. 149 (2009) 1188–1200. https://doi.org/10.1016/j.agrformet.2009.02.009.

[80] J. Junk, U. Feister, A. Helbig, Reconstruction of daily solar UV irradiation from 1893 to 2002 in Potsdam, Germany, Int. J. Biometeorol. 51 (2007) 505–512. https://doi.org/10.1007/s00484-007-0089-4.

[81] K. Sudhakar, T. Srivastava, et al., Modelling and Estimation of Photosynthetically Active Incident Radiation Based on Global Irradiance in Indian Latitudes, Int. J. Energy Environ. Eng. 4 (2013).

[82] A. García-Rodríguez, S. García-Rodríguez, D. Granados-López, M. Díez-Mediavilla, C. Alonso-Tristán, Extension of PAR Models under Local All-Sky Conditions to Different Climatic Zones, Appl. Sci. 12 (2022). https://doi.org/10.3390/app12052372.

[83] I. Foyo-Moreno, I. Alados, L. Alados-Arboledas, A new empirical model to estimate hourly diffuse photosynthetic photon flux

density, Atmos. Res. 203 (2018) 189–196. https://doi.org/10.1016/j.atmosres.2017.12.012.

[84] Q. Duan, Y. Feng, J. Wang, Estimating hourly solar near-infrared irradiance using meteorological data for sustainable building design and engineering, in: Am. Sol. Energy Soc. Natl. Sol. Conf. 2020 Proc., 2020: pp. 80–85. https://doi.org/10.18086/solar.2020.01.12.

[85] S. García-Rodríguez, I. García, A. García-Rodríguez, M. Díez-Mediavilla, C. Alonso-Tristán, Solar Ultraviolet Irradiance Characterization under All Sky Conditions in Burgos, Spain, Appl. Sci. 12 (2022) 10407. https://doi.org/10.3390/app122010407.

[86] N. Proutsos, S. Alexandris, A. Liakatas, P. Nastos, I.X. Tsiros, PAR and UVA composition of global solar radiation at a high altitude Mediterranean forest site, Atmos. Res. 269 (2022) 106039. https://doi.org/10.1016/j.atmosres.2022.106039.

[87] S. Garcia-Rodriguez, A. Garcia-Rodriguez, D. Granados-Lopez, I. Garcia, Ultraviolet Erythemal Irradiance (UVER) under Different Sky Conditions in Burgos , Spain: Multilinear Regression and Artificial Neural Network Models, Appl. Sci. 13 (2023). https://doi.org/10.3390/app131910979.

[88] M. Verbeek, Using linear regression to establish empirical relationships, IZA World Labor. (2017) 1–11. https://doi.org/10.15185/izawol.336.

[89] D. C., Montgomery, G.C. Runger, Probabilidad y Estadística aplicadas a la Ingeniería, 2ª, McGraw-Hill, México: Limusa-Willey, 2010.

[90] J. Jeon, The Strengths and Limitations of the Statistical Modeling of Complex Social Phenomenon: Focusing on SEM, Path Analysis, or Multiple Regression Models, Int. J. Soc. Behav. Educ. Econ. Bus. Ind. Eng. 9 (2015) 1604–1612.

[91] F. Villada, N. Muñoz, E. García, Aplicación de las Redes Neuronales al Pronóstico de Precios en el Mercado de Valores, Inf. Tecnol. 23 (2012) 11–20. https://doi.org/10.4067/S0718-07642012000400003.

[92] E. Rivera, Introduccion a redes neuronales artificiales, Científica 6. (2007) 11.

[93] F. Pérez, H. Fernández, Las redes neuronales y la evaluación del Riesgo de Crédito, Rev. Ing. Univ. Medellín. 6 (2007) 77–91.

[94] C. Ovalle, W. Auccahuasi, S. Meza, Franklin-Cordova-Buiza, K. Rojas, M. Cosme, M. Inciso-Rojas, G. Aiquipa, H.M.C. Martínez, A. Fuentes, A. Auccahuasi, Application of neural networks in the teacher selection process, Procedia Comput. Sci. 218 (2022) 1132–1143. https://doi.org/10.1016/j.procs.2023.01.092.

[95] W. Campos, Y. Trujillo, Redes Neuronales Artificiales en la estimación del esfuerzo, Rev. Cuba. Ciencias Informáticas. 15 (2021) 183–198. http://scielo.sld.cu/scielo.php?script=sci_abstract&pid=S2227-18992021000200183&lng=es&nrm=iso.

[96] S. Nembrini, On the behaviour of permutation-based variable importance measures in random forest clustering, J. Chemom. 33 (2019) 1–5. https://doi.org/10.1002/cem.3135.

[97] A. Bommert, X. Sun, B. Bischl, J. Rahnenführer, M. Lang, Benchmark for filter methods for feature selection in high-dimensional classification data, Comput. Stat. Data Anal. 143 (2020) 106839. https://doi.org/10.1016/j.csda.2019.106839.

[98] V.V. J. Weston, S. Mukherjee, O. Chapelle, M. Pontil, T. Poggio, Feature selection for SVMs, in: 14 Th Annu. Neural Inf. Process. Syst. Conf., Neural information processing systems foundation, n.d.

[99] R. Díaz-Uriarte, S. Alvarez de Andrés, Gene selection and

classification of microarray data using random forest, BMC Bioinformatics. 7 (2006) 1–13. https://doi.org/10.1186/1471-2105-7-3.

[100] M.B. Kursa, W.R. Rudnicki, Feature selection with the boruta package, J. Stat. Softw. 36 (2010) 1–13. https://doi.org/10.18637/jss.v036.i11.

[101] M. Mukaka, Statistics corner: A guide to appropriate use of correlation in medical research, Malawi MesicL J. 24 (3) (2012) 69–71.

[102] M.I. Dieste-Velasco, S. García-Rodríguez, A. García-Rodríguez, M. Díez-Mediavilla, C. Alonso-Tristán, Modeling Horizontal Ultraviolet Irradiance for All Sky Conditions by Using Artificial Neural Networks and Regression Models, Appl. Sci. 13 (2023) 1473. https://doi.org/10.3390/app13031473.

[103] U. Feister, J. Junk, M. Woldt, A. Bais, A. Helbig, M. Janouch, W. Josefsson, A. Kazantzidis, A. Lindfors, P.N. Den Outer, H. Slaper, Long-term solar UV radiation reconstructed by ANN modelling with emphasis on spatial characteristics of input data, Atmos. Chem. Phys. 8 (2008) 3107–3118. https://doi.org/10.5194/acp-8-3107-2008.

[104] S. Malinovic-Milicevic, Y. Vyklyuk, M.M. Radovanovic, M.D. Petrovic, Long-term erythemal ultraviolet radiation in Novi Sad (Serbia) reconstructed by neural network modelling, Int. J. Climatol. 38 (2018) 3264–3272. https://doi.org/10.1002/joc.5499.

[105] I. Alados, J.A. Mellado, F. Ramos, L. Alados-Arboledas, Estimating UV Erythemal Irradiance by Means of Neural Networks, Photochem. Photobiol. 80 (2004) 351–358. https://doi.org/10.1562/2004-03-12-RA-111.1.

[106] J.V. Gutiérrez-Manzanedo, C. Vaz Pardal, N. Blázquez-Sánchez, M.V. De Gálvez, J. Aguilera-Arjona, J.L. González-Montesinos,

F. Rivas Ruiz, M. De Troya-Martín, Ultraviolet exposure of competitors during a Tokyo Olympic Sailing Regatta Test Event, Photodermatol. Photoimmunol. Photomed. 39 (2023) 325–331. https://doi.org/10.1111/phpp.12839.

[107] World Health Organization, SunSmart Global UV App helps protect you from the dangers of the sun and promotes public health, (2022). https://www.who.int/es/news/item/21-06-2022-sunsmart-global-uv-app-helps-protect-you-from-the-dangers-of-the-sun-and-promotes-public-health.

[108] A. Modenese, F. Bisegna, M. Borra, C. Burattini, L. Gugliermetti, F.L. Filon, A. Militello, P. Toffanin, F. Gobba, Occupational Exposure to Solar UV Radiation in a Group of Dock-workers in North-East Italy, Proc. - 2020 IEEE Int. Conf. Environ. Electr. Eng. 2020 IEEE Ind. Commer. Power Syst. Eur. EEEIC / I CPS Eur. 2020. (2020) 16–21. https://doi.org/10.1109/EEEIC/ICPSEurope49358.2020.9160703.

[109] European Cancer Patient Coalition, Global Call to Action to End the Non-Melanoma Skin Cancer Epidemic in Outdoor Workers, 30 (2019).

[110] S.I. Henderson, K.L. King, K.K. Karipidis, R.A. Tinker, A.C. Green, Effectiveness, compliance and application of sunscreen for solar ultraviolet radiation protection in Australia, Public Heal. Res. Pract. 32 (2022) 1–7. https://doi.org/10.17061/phrp3212205.

[111] H. Walker, C. Maitland, T. Tabbakh, P. Preston, M. Wakefield, C. Sinclair, Forty years of Slip! Slop! Slap! A call to action on skin cancer prevention for Australia, Public Heal. Res. Pract. 32 (2022) 1–7. https://doi.org/10.17061/phrp31452117.

[112] S.Q. Wang, Y. Balagula, U. Osterwalder, Photoprotection: A

Review of the current and future technologies, Dermatol. Ther. 23 (2010) 31–47. https://doi.org/10.1111/j.1529-8019.2009.01289.x.

[113] S. González, M. Fernández-Lorente, Y. Gilaberte-Calzada, The latest on skin photoprotection, Clin. Dermatol. 26 (2008) 614–626. https://doi.org/10.1016/j.clindermatol.2007.09.010.

[114] H.P. Gies, C.R. Roy, G. Elliot, W. Zongli, Ultraviolet radiation protection factors for clothing, Health Phys. 1994 (n.d.) 131–139.

[115] Y. Fan, J. Chen, G. Shirkey, R. John, S.R. Wu, H. Park, C. Shao, Applications of structural equation modeling (SEM) in ecological studies: an updated review, Ecol. Process. 5 (2016). https://doi.org/10.1186/s13717-016-0063-3.

[116] R.O. Mueller, G. R. Hancock, Structural equation modeling. In The Reviewer's Guide to Quantitative Methods in the Social Sciences, Routledge, London, UK, 2018.

[117] R.O. Mueller, Structural equation modeling: Back to basics, Struct. Equ. Model. 4 (1997) 353–369. https://doi.org/10.1080/10705519709540081.

[118] S.M. Noar, J.G. Myrick, A. Zeitany, D. Kelley, B. Morales-Pico, N.E. Thomas, Testing a Social Cognitive Theory-Based Model of Indoor Tanning: Implications for Skin Cancer Prevention Messages, Health Commun. 30 (2015) 164–174. https://doi.org/10.1080/10410236.2014.974125.

[119] J.F. Hair, R. Anderson, R. Tatham, W. Black, Multivariate Data Analysis, Pearson, New York, NY, USA, 2009.

[120] M.M., Abdalla, J.R., Ribas, P.R., da Costa Vieria, The antecedents of word of mouth intentions about a Brazilian tourist destination, Tour. Manag. Stud. 10 (2014) 104–111.

[121] K. Liu, J. Zhang, M. Wang, Drivers of Groundwater Change in China and Future Projections, Remote Sens. 14 (2022) 1–13. https://doi.org/10.3390/rs14194825.

[122] H. Zhu, B. Zhang, W. Song, J. Dai, X. Lan, X. Chang, Power-Weighted Prediction of Photovoltaic Power Generation in the Context of Structural Equation Modeling, Sustain. 15 (2023). https://doi.org/10.3390/su151410808.

[123] Y. Shi, L. Xu, Y. Zhou, B. Ji, G. Zhou, H. Fang, J. Yin, X. Deng, Quantifying driving factors of vegetation carbon stocks of Moso bamboo forests using machine learning algorithm combined with structural equation model, For. Ecol. Manage. 429 (2018) 406–413. https://doi.org/10.1016/j.foreco.2018.07.035.

[124] M.A. Ruiz, A. Pardo, R. San Martín, Models of equations structural (Modelos de ecuaciones estructurales), Papeles Del Psicólogo. 31 (2010) 34–45.

[125] M.S. Ortiz, M. Fernández-Pera, Modelo de Ecuaciones Estructurales: Una guía para ciencias médicas y ciencias de la salud - Structural Equation modeling: A guide for Medical and Health sciences, Ter. Psicológica. 36 (2018) 51–57. https://doi.org/10.4067/s0718-48082017000300047.

[126] J.R. Ribas, S.G. Rodríguez, E.A. Fariña, A. Suárez-García, An Assessment on the Efficiency of Clothing with UV Protection among the Spanish Navy School Students, Materials (Basel). 15 (2022) 1–10. https://doi.org/10.3390/ma15186227.

[127] J.M. Cortina, What Is Coefficient Alpha? An Examination of Theory and Applications, J. Appl. Psychol. 78 (1993) 98–104.

[128] J. Rodríguez-Rodríguez, M. Reguant-Álvarez, Calcular la fiabilidad de un cuestionario o escala mediante el SPSS: el coeficiente alfa de Cronbach, REIRE Rev. d Innovaci i Recer. En Educ. 13 (2020) 1–13. https://doi.org/10.1344/reire2020.13.230048.

[129] C. Fornell, D.F. Larcker, Structural Equation Models with Unobservable Variables and Measurement Error: Algebra and

Statistics, J. Mark. Res. 18 (1981). https://doi.org/10.1177/002224378101800313.

[130] O. Guillán Lorenzo, A. Suárez-García, D. Gonzalez Peña, M. Garcia Fuente, D. Granados-Lopez, A Low-Cost Luxometer Benchmark for Solar Illuminance Measurement System Based on the Internet of Things, Sensors. 22 (2022). https://doi.org/10.3390/s22197107.

Artículos

applied sciences

MDPI

Article

Solar Ultraviolet Irradiance Characterization under All Sky Conditions in Burgos, Spain

Sol García-Rodríguez [1], Ignacio García [1,2], Ana García-Rodríguez [1], Montserrat Díez-Mediavilla [1] and Cristina Alonso-Tristán [1,*]

[1] Research Group Solar and Wind Feasibility Technologies (SWIFT), Electromechanical Engineering Department, Universidad de Burgos, 09006 Burgos, Spain
[2] Institute of Smart Cities (ISC), Department of Engineering, Public University of Navarre, Campus Arrosadía, 31006 Pamplona, Spain
* Correspondence: catristan@ubu.es or cristinaalonso.tristan@gmail.com; Tel.: +34-947-258853

Featured Application: The ratio between global horizontal ultraviolet irradiance and broadband solar horizontal irradiance is presented, and its dependency on sky cloudiness conditions, as defined by the CIE Standard sky classification and clearness index, is shown in this paper. A single pattern that is only dependent on sky conditions is discerned, regardless of the temporal basis of the study.

Abstract: Solar Ultraviolet Radiation (UVR), which is identified as a major environmental health hazard, is responsible for a variety of photochemical reactions with direct effects on urban and aquatic ecosystems, human health, plant growth, and the deterioration of industrial systems. Ground measurements of total solar UVR are scarce, with low spatial and temporal coverage around the world, which is mainly due to measurement equipment maintenance costs and the complexities of equipment calibration routines; however, models designed to estimate ultraviolet rays from global radiation measurements are frequently used alternatives. In an experimental campaign in Burgos, Spain, between September 2020 and June 2022, average values of the ratio between horizontal global ultraviolet irradiance (*GHUV*) and global horizontal irradiance (*GHI*) were determined, based on measurements at ten-minute intervals. Sky cloudiness was the most influential factor in the ratio, more so than any daily, monthly, or seasonal pattern. Both the CIE standard sky classification and the clearness index were used to characterize the cloudiness conditions of homogeneous skies. Overcast sky types presented the highest values of the ratio, whereas the clear sky categories presented the lowest and most dispersed values, regardless of the criteria used for sky classification. The main conclusion, for practical purposes, was that the ratio between *GHUV* and *GHI* can be used to model *GHUV*.

Keywords: UV; global irradiance; sky conditions; CIE standard sky classification; k_t; statistical analysis

Citation: García-Rodríguez, S.; García, I.; García-Rodríguez, A.; Díez-Mediavilla, M.; Alonso-Tristán, C. Solar Ultraviolet Irradiance Characterization under All Sky Conditions in Burgos, Spain. *Appl. Sci.* **2022**, *12*, 10407. https://doi.org/10.3390/app122010407

Academic Editors: Harry D. Kambezidis and Basil Psiloglou

Received: 19 September 2022
Accepted: 11 October 2022
Published: 15 October 2022

1. Introduction

Although Solar Ultraviolet Radiation (UVR) comprises only 8.73% of the solar radiation spectrum [1], its study is of great interest, due to its direct consequences for life on Earth. UVR is a major environmental hazard that causes health problems such as sunburn, skin cancer, photokeratitis, and ocular diseases, among others [2]; however, the natural synthesis of Vitamin D requires exposure to UVR [3]. UVR is also responsible for a variety of photochemical reactions, with direct effects on urban ecosystems [4]; for instance, the degradation of photovoltaic systems [5], stunted plant growth and morphology [6], and the equilibrium of aquatic ecosystems [7]. The spread and seasonality of several diseases have been linked to solar UVR [8–10]. UVR ground measurements are key to the analysis of its spatial and temporal distributions under different atmospheric conditions, and for public information campaigns on protection against UVR damage [11].

UVR is divided into three wavebands: UV-C (100–280 nm), UV-B (280–315 nm), and UV-A (315–400 nm). UV-C is absorbed in the stratosphere, whereas both the UV-A and the UV-B bands reach ground level in amounts that depend on several factors. Column ozone content, atmospheric composition [12] (aerosols, water vapor, and other gases), cloud type and distribution [13,14], and geometrical and geographic variables, such as solar zenith angle, and surface albedo [15,16], all contribute to UVR variability; however, it is difficult to evaluate the individual role of each variable, due to their combined effects with other variables under different atmospheric conditions [17].

UVR ground measurements are scarce, and spatial and temporal coverage around the globe is limited, which is mainly due to equipment maintenance costs and the complexities of measurement equipment calibration routines [17–19]; however, the models used to estimate solar UVR from global radiation measurements, with relatively few data inputs, are frequently used alternatives [11,12,15,20–36].

Several authors have studied the influence of clouds and sky conditions on surface UV measurements [12,13,17,22,33,37,38]. The presence of cloud cover and its type and distribution can both enhance total solar UVR by as much as 15% and reduce it by over 50%; this is due to the superposition of the albedo reflection, and distribution and extinction effects [39]. Conversely, atmospheric pollution and dust can drastically reduce total solar UV irradiance [33,40,41].

The ratio of global horizontal ultraviolet irradiance (*GHUV*) and global horizontal irradiance *(GHI)*, measured using different (ten-minute data intervals, hourly and daily values, and monthly and annual averages) time scales around the world and under different sky conditions, has been widely studied, as shown in the literature review summarized in Table 1. As is evident, the *GHUV*:*GHI* ratio ranges between 2.9 and 7%, with the highest values of the ratio corresponding to cloudy days, regardless of the index used for sky condition classification. The scattering effects on the UVR band caused by cloud cover increases the intensity of the *GHUV*, whereas the stronger absorption effect of water vapor on the infrared band contributes to lower levels of *GHI* [33]. The location of the measurement site is another important factor: *GHUV* at ground level increases when the site is closer to the Equator [42] and at a higher height above sea level (h.a.s.l.), due to the shorter optical length of rays through the atmosphere [43–45]. On a summer's day, *GHUV* is strongest at around noon when 50–60% of solar UVR can be measured. The solar zenith angle also affects the intensity of UVR: *GHUV* increases with the solar zenith angle, because solar UV rays, perceived as solid angles, are distributed over larger surface areas of the globe [16].

Table 1. Experimental measurements of the *GHUV*:*GHI* ratio around the world.

Ref.	Experimental Campaign	Location	Geographical Data	Height above Sea Level	*GHUV*/*GHI*	Comments
[46]	Austral summers 1978–1981	Amundsen-Scott South Pole Station	lat. 90° S	2835 m	4–4.3% (hourly av.)	Sun elevation > 17° Clear skies
[47]	30 min 1985–1987	Safat (Kuwait)	lat. 29°20′ N long. 47°57′ E	0 m	4.2–5.2% (monthly av.)	No sky classification
[48]	60 min 1985–1987	Dhahran (Saudi Arabia)	lat. 26°32′ N long. 50°13′ E	17 m	3.3–3.7% (monthly av.)	Sky conditions classified by k_t
[49]	60 min 01/01/1987–31/05/1988	Makkah (Saudi Arabia)	lat. 21.5° N long. 39.8° E	277 m	2.8–4.3% (monthly av.)	Sky conditions classified by k_t
[50]	2 min 01/04/1985–31/04/1988	Potsdam 1 (Germany)	lat. 52°22′ N long. 13°5′ E	35 m	3–4% (2 min av.)	No sky classification
[51]	10 min 03/1991–09/1991	Valencia (Spain)	lat. 39°28′00″ Nlong. 0°22′30″ W	40 m	2.7–3.2% (monthly av.)	Sky conditions classified by k_t

Table 1. *Cont.*

Ref.	Experimental Campaign	Location	Geographical Data	Height above Sea Level	*GHUV*/*GHI*	Comments
[52]	1990–1992	Cairo (Egypt)	lat. 30°05′ N long. 31°17′ E	23 m	2.7–3.4% (monthly av.)	All sky conditions
		Aswan (Egypt)	lat. 23°58′ N long. 32°47′ E	106 m	3.5–3.9% (monthly av.)	
[12,25,53]	1 min 1994–1995	Granada (Spain)	lat. 37.18° N long. 3.58° W	600 m	3–5% (monthly and hourly av.)	Sky conditions classified by k_t
					3.7–4% (1 min and 5 min av.) 4% (hourly av.) 3.4–4.6% (hourly av.)	Sky conditions classified by cloud cover (octas) All sky types
[53]	5 min 1993–1995	Almería (Spain)	lat. 36.83° N long. 2.41° W	0 m	3.7% (hourly av.)	All sky types
[30,54]	10 min 1991–1996 5 min 1996–1998	Valencia (Spain)	lat. 39°30′ N long. 0°25′ W	40 m	3.2% (10 min av.) 2.9–2.5% (hourly av.) 2.9–3.4% (daily av.)	Sky conditions classified by k_t
					4.4–5.6% (monthly av.)	
[23]	5 min 1996–1998	Cordoba (Spain)	lat. 37° 51′ N long. 4°48′ W	125 m	3.9–4.5% (monthly av.)	
[55]	60 min 03/1996–12/2000	Athens (Greece)	lat. 37.97° N long. 23.67° E	20 m	4.06% (monthly av.)	
[15]	1 min 06/1998–08/2001	Kwangju (South Korea)	lat. 35°10′ N long. 126°53′ E	90 m	7–9.4% (monthly av.)	Sky conditions classified by k_t
[56]	10 min 2004	Athalassa (Cyprus)	lat. 35°15′ N long. 33°40′ E	165 m	2.92–3.95% (hourly av.) 2.85–3.68% (daily av.)	Sky conditions classified by k_t
[57]	1 min 2005–2006	Lhasa (China)	lat. 29°30′ N long. 91°6′ E	3668 m	3.9–5% (monthly and daily av.)	Sky conditions classified by k_t
		Haibei (China)	lat. 37°37′ N long.101°19′ E	3230 m	3.7–4.6% (monthly and daily av.)	
[24,58,59]	5 min 2001–2005	Botucatu (Brazil)	lat. 22°530 S long.48°260′ W	786 m	4–4.9% (hourly av.) 4–4.8% (daily av.)	Sky conditions classified by k_t (four intervals)
[11]	5 min 2008	Maceió (Brazil)	lat. 9°280′ S long. 35°490′ W	127 m	2.3–3.6% (daily av.)	Sky conditions classified by k_t
[22]	10 min 02/2001–06/2008	Valladolid (Spain)	lat.41°40′ N long. 4°50′ W	840 m	3.8–4.4% (monthly and hourly av.) 3.8–4.2% (monthly and daily av.)	Sky conditions classified by cloud cover
[13,60]	1 min 2006–2012	Wuhan (China)	lat. 30°32′ N long. 114°21′ E	30 m	3.9–4.4% (daily av.) 3.8–4.3% (hourly av.) 3.96–4.94% (monthly av.)	Sky conditions classified by k_t
[18]	2005–2012	Sanya (China)	lat. 18°13′ N long. 109°28′ E	1.5 m	4.2–4.7% (monthly and hourly av.) 4.1–4.6% (monthly and daily av.)	Sky conditions classified by k_t

This study focuses on the determination of the *GHUV*/*GHI* ratio in Burgos (Spain), and its dependency on sky conditions, which is classified using different criteria. Experimental data of *GHUV*, *GHI*, and the sky luminance distribution were compiled from experimental sky scanner measurements. A complete statistical analysis of the results over different time scales (10 min, hourly, daily, monthly, and seasonal intervals) was completed. The results collected under different sky conditions, classified in accordance with the CIE standard sky taxonomy [61] and clearness index (k_t), were tested during a 22 month experimental test campaign.

The experimental facility, the measurement campaign, and the quality filters applied to the experimental data are described in Section 2. In Section 3, the description of the sky conditions in Burgos during the experimental campaign is presented, as well as a complete analysis of the quality of the experimental data and an analysis of the *GHUV*/*GHI* ratio over different temporal intervals and against sky classification criteria. Finally, the main results and the conclusions of the study are summarized in Section 4.

2. Experimental Data

All meteorological and radiometric experimental data used in this study were recorded at the weather station of the SWIFT Research Group, located on the roof of the Higher Polytechnic School building (EPS) of Burgos University (42°21′04″ N, 3°41′20″ W, 856 m above mean sea level). Figure 1 shows the location of the meteorological station on the flat roof of the EPS building, which is where the climatic parameters were measured. These parameters were as follows: ambient temperature, relative humidity, atmospheric pressure, wind speed and direction, and rainfall. A Kipp & Zonen CUV5 sensor was used to measure *GHUV*. *GHI* data were measured with a (Hulseflux, model SR11) pyranometer. Sky luminance and radiance distributions were determined with a commercial MS-321LR sky scanner manufactured by EKO Instruments (EKO Instruments Europe B.V. Den Haag, The Netherlands). The technical specifications of the various measurement instruments are shown in Tables 2–4. A complete description of the experimental facility and its location can be found in previous papers [62,63].

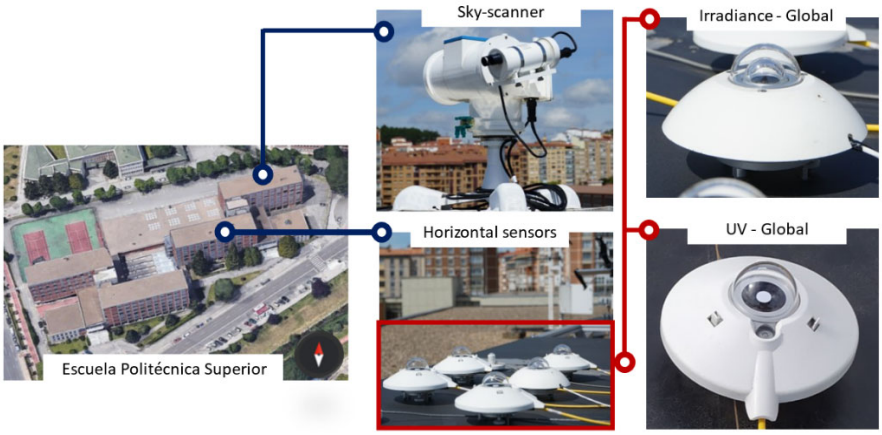

Figure 1. Location of the experimental equipment on the roof of the Higher Polytechnic School building at the University of Burgos (Spain).

Table 2. UV Radiometer technical specifications.

Model	CUV5
Spectral Range (Nominal passband 50% point)	300–385 nm
Spectral range (Overall)	280 to 400 nm
Sensitivity	300–500 $\mu V/(W/m^2)$
Temperature response (−40 °C–80 °C)	<−0.3%/°C
Directional response (up to 70° with 100 W/m^2 UV beam)	$< 5\ W/m^2$

Table 3. Pyranometer technical specifications.

Model	SR11
ISO classification	first class
Spectral range	285 to 3000 nm
Irradiance range	0 to 2000 W/m^2
Sensitivity	15 $\mu V/(W/m^2)$
Temperature response (−10 °C–40 °C)	±2%
Directional error	±20 W/m^2
Calibration uncertainty	<1.8%
Non-Stability	<±1% change per year
Tilt Error (0 to 90° at 1000 W m^{-2})	<±2%
Level Accuracy	<1%

Table 4. Sky scanner technical specifications.

Model	MS-321LR Sky Scanner
FOV	11°
Luminance	0 to 50 kcd/m^2
Radiance	0 to 300 W/m^2
A/D Convertor	16 bits
Calibration Error	2%

The experimental campaign ran from 14 September 2020 to 6 June 2022. *GHI* and *GHUV* data were recorded every 10 min (average recorded scans of 30 s). Experimental *GHI* data were subjected to the Quality Control (QC) procedure proposed for the MESoR project [64]. Regarding UV data, it was established that *GHUV* could not be higher than the extraterrestrial UV on the horizontal plane (UVH_0) that corresponded with the same time frame. UVH_0 was calculated with the correction factor (f_c) applied to the UV solar constant (UV_{sc}); this is based on the estimated orbital eccentricity multiplied by the cosine of the solar zenith angle, as shown in Equation (1).

$$UVH_0 = f_c UV_{sc} \cos\theta_z. \quad (1)$$

In the absence of a standardized value, the UV_{sc} was obtained from the integration of the solar spectrum, as revised by Gueymard [65], between 280 and 400 nm, subsequently obtaining a value of 102.15 W·m^{-2}. Data corresponding to solar elevation angles lower than 5° were discarded, in order to avoid the cosine response problems of the *GHI* and *GHUV* measurement instruments.

The sky scanner was adjusted monthly so that it could take measurements from sunrise to sunset. It completed a full scan in four minutes and started a new scan every ten minutes. Data that were not within the specifications (i.e., $\alpha_s \leq 7.5°, > 50$ kcd·m^{-2} and < 0.1 kcd·m^{-2}) were discarded. If a dataset (*GHI*, *GHUV*, or sky scanner measurement) failed to pass the QC, then all the simultaneous datasets were rejected; thus, 24.9% of the data recorded during the 22 month experimental campaign were rejected after failing the quality control tests, resulting in 34,270 valid 10 min data points. The seasonal data distribution was 22.8% in winter, 30.5% in spring, 20.3% in summer, and 26.3% in autumn.

Table 5 shows the annual and seasonal mean values of *GHI*, *GHUV*, temperature (*T*), relative humidity (*RH*), and wind speed (*WS*), which were calculated from the 10 min records. These values were obtained for the whole year and they were classified according to each sky type, k_t (overcast $0 \leq k_t \leq 0.35$, partly cloudy $0.35 < k_t \leq 0.65$, clear sky $0.65 < k_t \leq 1$) [66].

Table 5. Seasonal 10 min mean values (N) between 14 September 2020 and 6 June 2022 for global solar irradiance (*GHI*), global ultraviolet irradiance (*GHUV*), air temperature (*T*), relative humidity (*RH*), and wind speed (*WS*), for overcast, intermediate, and clear sky conditions classified in accordance with the k_t criteria.

Sky Type	Parameter	All Data	Season			
			Winter	Spring	Summer	Autumn
All Sky	N	34,270	7,824	10,458	6,972	9,016
	GHI (W·m^{-2})	353.27	258.17	412.21	499.63	254.23
	GHUV (W·m^{-2})	13.33	9.36	15.83	19.09	9.41
	T (°C)	13.20	7.44	13.68	21.51	11.21
	RH (%)	67.96	75.31	65.40	54.82	74.72
	WS (m·s^{-1})	2.15	2.37	2.17	1.97	2.09

Table 5. *Cont.*

Sky Type	Parameter	All Data	Season			
			Winter	Spring	Summer	Autumn
Overcast skies ($0 \leq k_t \leq 0.35$)	N	11,971	3,281	3,584	1,314	3,792
	GHI ($W \cdot m^{-2}$)	120.31	108.32	142.60	140.64	102.56
	GHUV ($W \cdot m^{-2}$)	5.51	4.86	6.54	6.60	4.73
	T (°C)	9.87	6.10	11.24	17.33	9.24
	RH (%)	82.41	85.64	79.15	71.97	86.30
	WS ($m \cdot s^{-1}$)	2.26	2.53	2.15	1.74	2.31
Intermediate skies ($0.35 < k_t \leq 0.65$)	N	9,579	2,240	2,916	1,885	2,538
	GHI ($W \cdot m^{-2}$)	312.54	278.81	361.07	335.61	269.44
	GHUV ($W \cdot m^{-2}$)	12.08	10.43	14.22	13.20	10.25
	T (°C)	12.97	7.75	13.78	20.27	11.24
	RH (%)	68.20	74.07	64.99	59.38	73.27
	WS ($m \cdot s^{-1}$)	2.11	2.43	2.09	1.83	2.05
Clear skies ($0.65 < k_t \leq 1$)	N	12,720	2,303	3,958	3,773	2,686
	GHI ($W \cdot m^{-2}$)	603.17	451.58	694.03	706.59	454.00
	GHUV ($W \cdot m^{-2}$)	21.63	14.75	25.43	26.40	15.22
	T (°C)	16.51	9.05	15.83	23.59	13.97
	RH (%)	54.18	61.80	53.24	46.56	59.74
	WS ($m \cdot s^{-1}$)	2.08	2.08	2.24	2.11	1.82

3. Results and Discussion

3.1. Sky Classification

Definition of (clear, intermediate, and overcast) sky types is usually achieved through meteorological and climate indices. Among others, the clearness index, k_t (ratio of global solar irradiation to extraterrestrial solar irradiation) [67–70], relative sunshine, S, [71,72], Perez's clearness index, ε, and sky brightness, Δ, [73,74], have been proposed as sky type classifiers. A previous study concluded [66] that limited results for sky classification can be obtained using meteorological indices. In 2003, the CIE adopted 15 standard sky types (five clear, five intermediate, and five overcast skies) in order to create a standard for sky classification [61]; these were defined by the International Commission on Illumination (*Commission Internationale de L'Éclairage* or CIE), and each one was perfectly characterized in terms of energy and daylight, and widely considered as an adequate representation of empirical sky conditions [75–80]. Therefore, the CIE standard for sky taxonomy was selected as the reference for atmospheric conditions. A complete description of the CIE standard sky classification model and the procedure for obtaining a CIE standard sky classification from sky scanner measurements can be found in previous works [62,63,81,82].

Figure 2 shows the frequency of occurrence of each CIE standard sky type in Burgos, Spain, during the experimental campaign. Skies in Burgos are predominantly clear, the most frequent sky type in the city being CIE standard sky type 13 (cloudless polluted with a broader solar corona), with a Frequency of Occurrence (FOC) higher than 18%. As can be observed in Figure 3, the fifteen CIE categories are grouped into overcast (CIE categories 1 to 5), partly cloudy (6 to 10), and clear skies (11 to 15); the clear sky conditions have the highest FOC (44.63%). This result concurs with previous experimental campaigns developed in Burgos between 2016 and 2022 [82,83]. As CIE standard sky classification data around the world are quite scarce, an alternative sky classification model, based on the k_t classification, was prepared. A comparison with CIE taxonomy is shown in Figure 3.

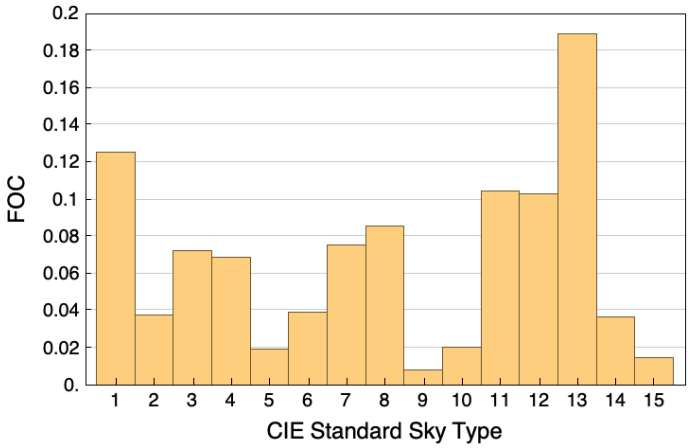

Figure 2. Frequency of Occurrence (FOC) of each CIE standard sky type in Burgos (Spain) from 14 September 2020 to 6 June 2022.

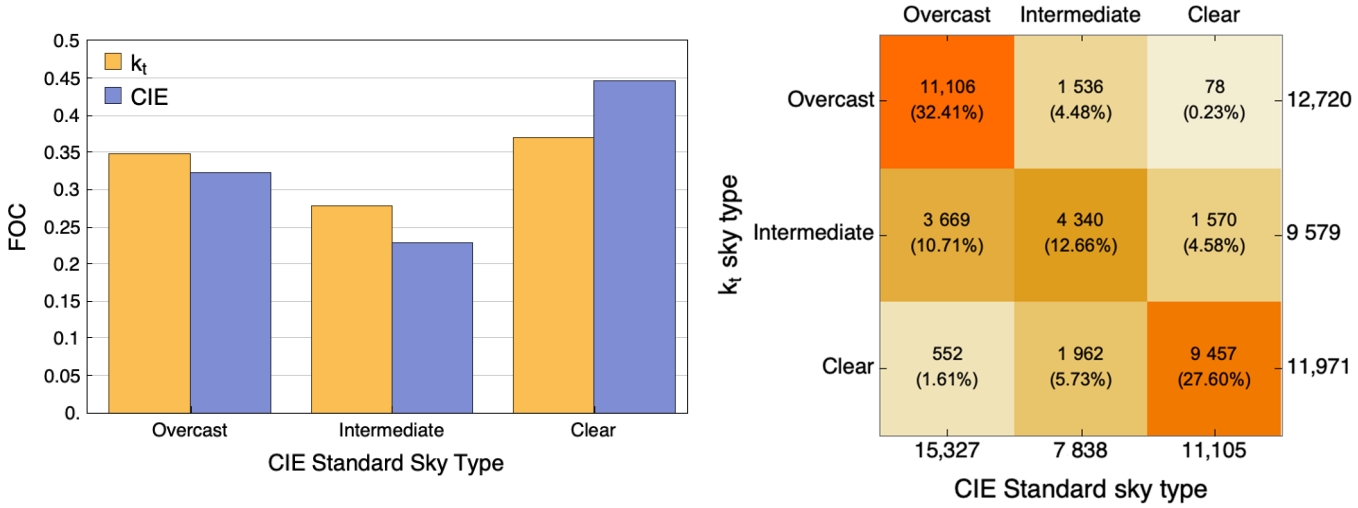

(**a**) (**b**)

Figure 3. (**a**) Frequency of occurrence (FOC) of the CIE and k_t sky classifications in Burgos (Spain) from 14 September 2020 to 6 June 2022; and (**b**) confusion matrix showing the coincidences in the classifications obtained according to both criteria.

The number of experimental data classified in each sky type category is shown in Figure 3a. The CIE classifies sky conditions as being clear more frequently than k_t, and as overcast or an intermediate sky type less frequently than k_t. The number of classification matches obtained, according to the CIE and k_t classifications, can be seen in the confusion matrix in Figure 3b.

k_t is closely linked to the irradiance value [1], whereas the CIE classification considers the angular distribution of sky radiance and luminance. In this sense, some of the CIE sky types included in the clear category are described as skies with a certain degree of turbidity or pollution, such as CIE sky type 13 (cloudless polluted with a broader solar corona), CIE sky type 14 (cloudless turbid with a broader solar corona), and CIE sky type 15 (white-blue turbid sky with a wide solar corona effect). This is linked to relatively low k_t values [66]. In any case, there is good agreement between the two classification criteria, as can be seen in Figure 3b.

3.2. Analysis of the 10 min GHUV/GHI Ratio

Figure 4 shows the evolution of the 10 min values of *GHUV*, *GHI*, and its ratio (*GHUV/GHI*), which were measured in Burgos throughout the experimental campaign. It should be noted that the gray areas that appear in the three plots in Figure 4, for each day between sunrise and sunset, correspond to missing data, either because they were not recorded or because they did not pass the QC described in Section 2. With regard to Figure 4c, the *GHUV/GHI* ratios assume values between 1% and 10%; however, the highest values are clearly concentrated in the early hours of the day, and they decrease significantly during the central hours, although there is no clear trend throughout the day. This evolution is analyzed in detail in Section 3.3.

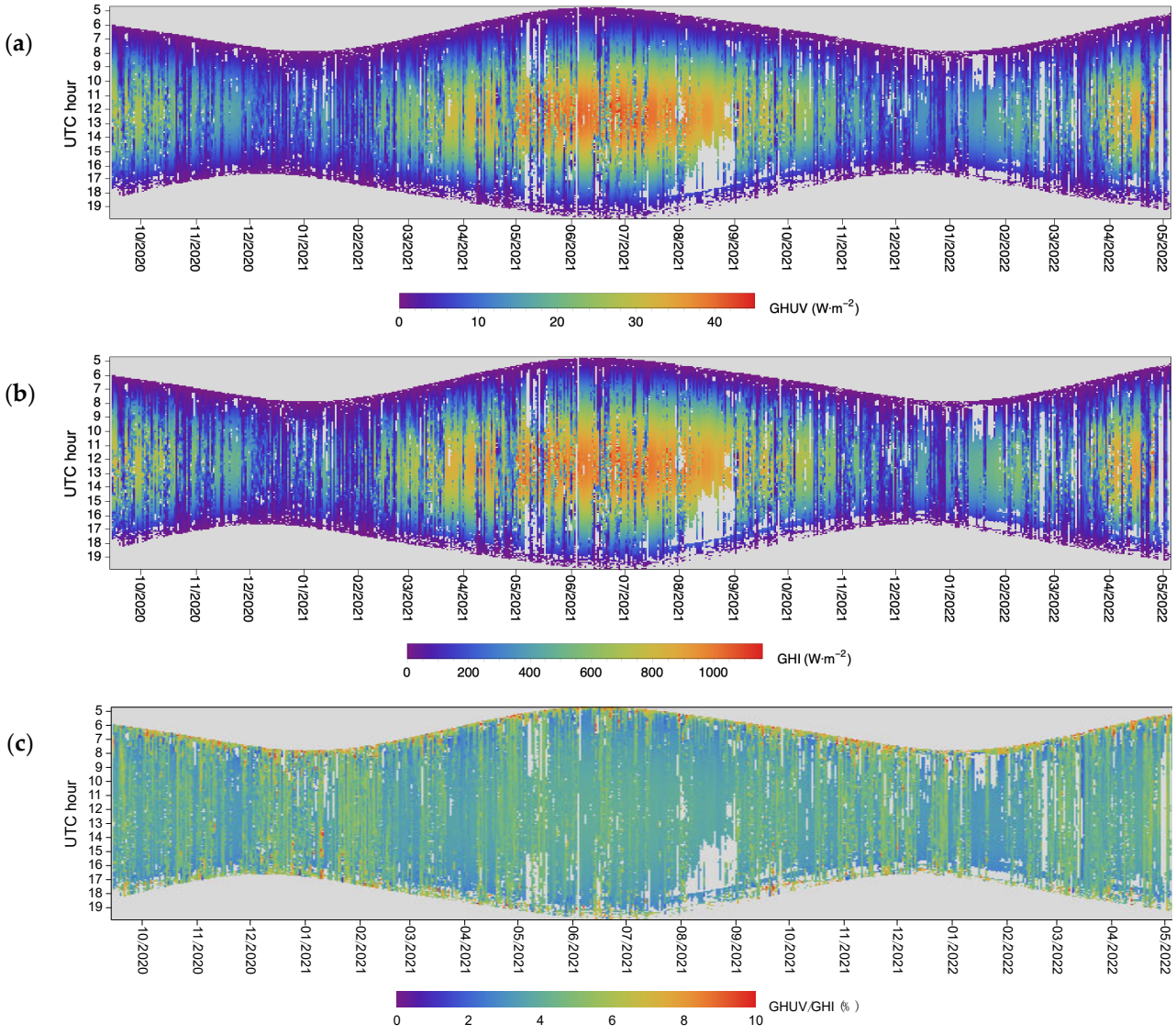

Figure 4. Ten minute experimental data of (**a**) *GHUV* (W·m^{-2}), (**b**) *GHI* (W·m^{-2}), and (**c**) the *GHUV/GHI* ratio (%) throughout the experimental campaign.

Although the scale used to represent the *GHUV/GHI* ratio values in Figure 4c reaches up to 10%, there are some values that considerably exceed this threshold (up to 15.21%): however, as can be seen in Figure 5a, which shows the Cumulative Distribution Function (CDF) of the 10 min *GHUV/GHI* ratios, the probability of this ratio exceeding 10% is extremely low (less than 0.05%). Figure 5a also shows the good fit between the empirical CDF (blue line) and the CDF adjusted to a normal distribution function (yellow line).

This can also be seen in Figure 5b, which shows the empirical Probability Distribution Function (PDF) of the 10 min *GHUV/GHI* ratios, and the adjusted PDF that shows a normal distribution.

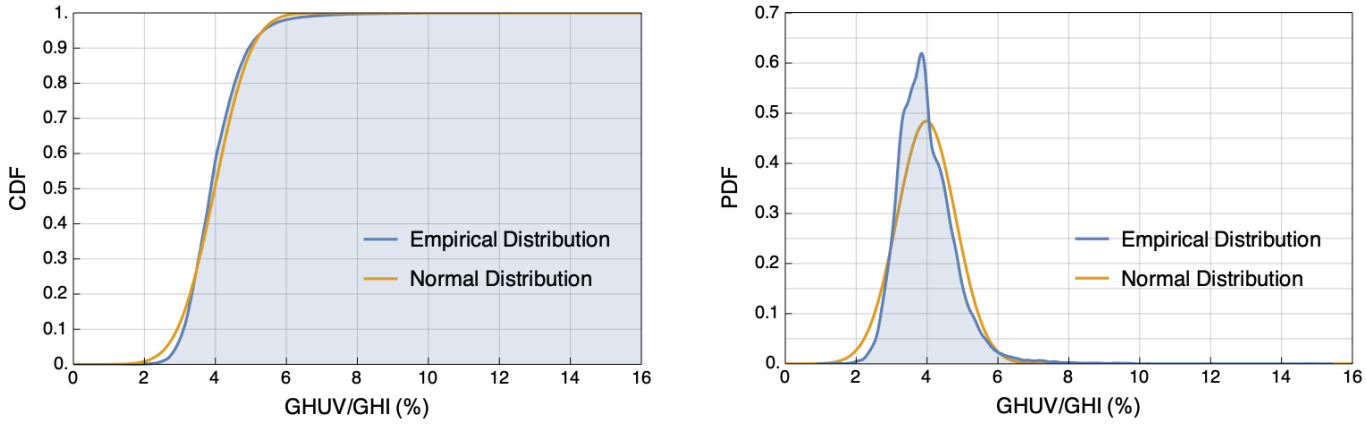

(**a**) (**b**)

Figure 5. Cumulative distribution function (**a**) and probability distribution function (**b**) of the 10 min data measured during the experimental campaign. Both the empirical CDF and PDF (blue line), and the CDF and PDF that were adjusted to a normal distribution function (yellow line), are plotted.

3.3. Hourly, Monthly, and Seasonal Analysis of the GHUV/GHI Ratio

Figure 6 shows the boxplot of the mean hourly values of the *GHUV/GHI* ratio, calculated from the average of the 10 min data, from sunrise to sunset, using the whole database. The graph represents the mean value (gray crosses), the median (white lines), the three quartiles, and both the maximum and minimum data values, as well as the outlier values. The mean hourly value of *GHUV/GHI* remained almost constant throughout the day. As previously noted, a small increase can be seen in the early hours of the day, which tends to stabilize during the central hours, and increases again at sunset. As the interquartile range shows, a greater dispersion of values in the first and last hours (1.9% at 5:00 h and 19:00 h), than in the central hours (0.75% at 12:00 h), of the day is observable. The average values were higher than the median values across all hours of the day. The hourly average of the ratio was 3.98 ± 0.82%, with maximum and minimum values of 4.25 ± 1.49% and 3.80 ± 1.14%, at 19:00 and at 18:00 h, respectively. These data, shown in Table 1, are comparable with other data from different locations in Spain. The hourly *GHUV/GHI* ratio in Burgos is higher than the ratio recorded at Almería (3.7%) [53], and lower than the ratios recorded at Granada (4%) [53], Valladolid (4.1%) [22], Valencia (4.2%), and Cordoba (4.9%) [23]; this is mainly due to each location's different sky conditions and their various heights above sea level.

Figures 7 and 8 show the statistical analysis of the monthly and seasonal averages of the *GHUV/GHI* ratio, which was calculated using the averages of the 10 min dataset, using the whole database. Figure 7 shows that the monthly data were almost constant throughout the year, with a small decrease in July and August. The standard deviation fluctuated between 0.69 and 1.23%, and the interquartile range was between 0.44% and 1.56%. December and January were the measurement campaign months with the highest data dispersion: the interquartile ranges were 1.51% and 1.56% with standard deviations of 1.29% and 1.27%, respectively. The maximum value was recorded in December (4.35% ± 1.29%), whereas the minimum was reached in July (3.82% ± 0.69%). A greater dispersion of values is observable in Figure 8 for the winter and autumn months, whereas the values in the summer months were closer, and therefore, they presented a smaller dispersion. These results are similar to the results obtained at other locations around the world (see Table 1), and the main differences between them can be attributed to the specific sky conditions, rather than the temporal variability of the ratio.

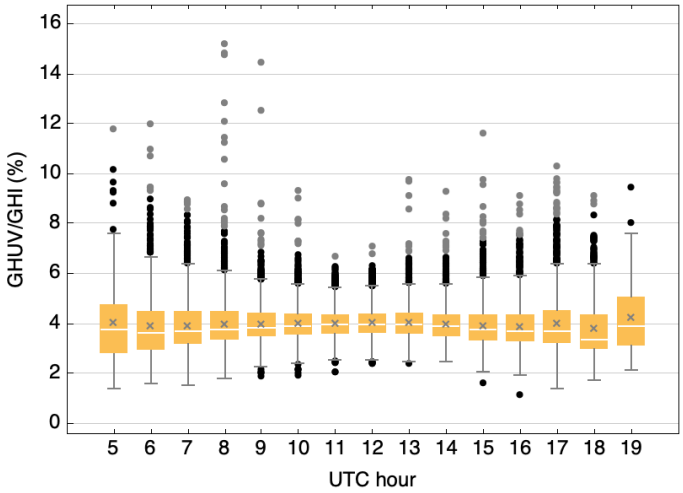

Figure 6. Boxplot of the *GHUV/GHI* hourly averages using the 10 min data. Gray crosses indicate the mean, and the white lines inside the box indicate the median. The limits of the boxes define the first, second, and third quartiles, whereas the extreme whiskers show the minimum and the maximum points. Black and gray circles represent outliers.

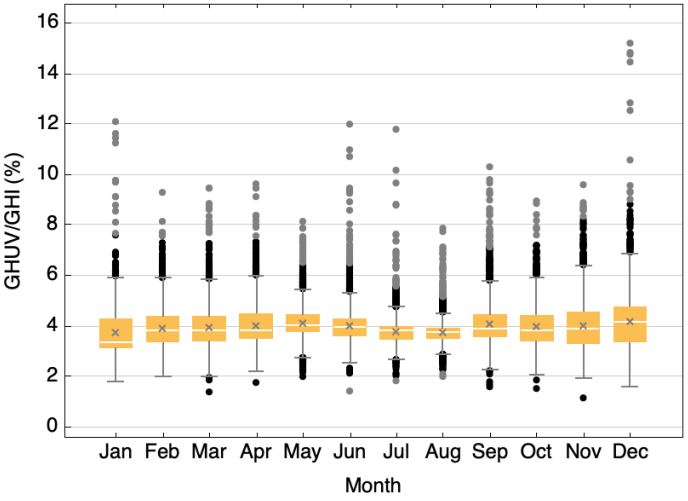

Figure 7. Boxplot of the *GHUV/GHI* monthly averages based on 10 min datasets.

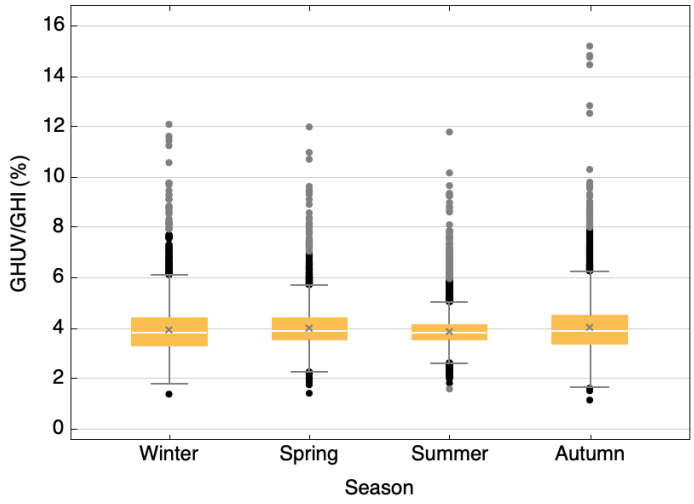

Figure 8. Boxplot of the *GHUV/GHI* seasonal averages based on the 10 min datasets.

3.4. GHUV/GHI Ratio and Sky Conditions

As explained in Section 3.1, during the experimental campaign, sky conditions were determined in Burgos using the CIE standard sky classification, or alternatively, the k_t criteria. Figure 9 shows the results of the statistical analysis of the average *GHUV/GHI* ratio, calculated using 10 min intervals, for each CIE standard sky type. The highest ratio values were obtained for sky types 5 (4.85 ± 0.92%) and 1 (4.73 ± 0.76%), which corresponded with the overcast sky conditions.

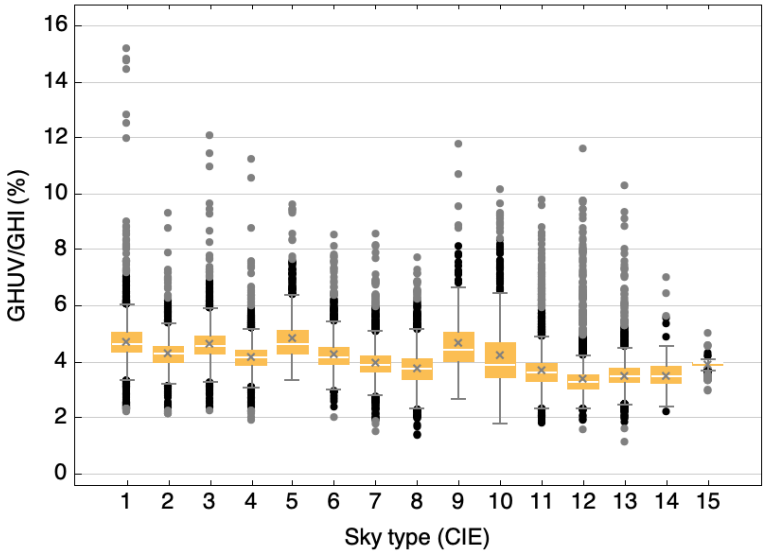

Figure 9. Boxplot of the average *GHUV/GHI* ratios for each CIE sky type using the 10 min data.

Figure 10 presents a comparison of the statistical analyses of the aggregated CIE sky types and the data classifications according to k_t. The same trend can be observed in both cases (i.e., the *GHUV/GHI* ratio was higher for overcast skies and lower for clearer skies). The mean values obtained in both cases, as well as their dispersion values, were similar; they were slightly higher for the overcast and intermediate sky types that were classified using the k_t taxonomy, and the results for the clear sky type were similar, as Table 6 shows.

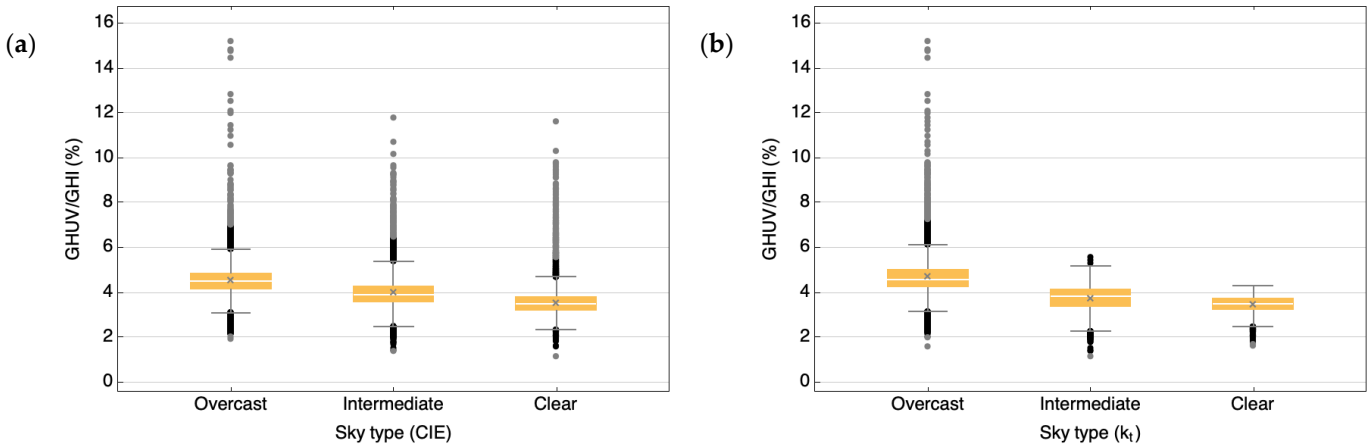

Figure 10. Boxplot of the *GHUV/GHI* average values for (**a**) each CIE sky type group and (**b**) for each sky type classification according to k_t, based on the 10 min datasets.

Table 6. Mean, standard deviation (STD), and interquartile range (IQR) of the *GHUV/GHI* average values (%), based on the 10 min datasets for clear, intermediate, and overcast sky types, which were classified according to the k_t and CIE criteria.

	Mean (%)		**STD (%)**		**IQR (%)**	
Sky classification	k_t	CIE	k_t	CIE	k_t	CIE
Overcast	4.719	4.562	0.844	0.737	0.751	0.711
Intermediate	3.740	4.007	0.542	0.780	0.745	0.725
Clear	3.469	3.547	0.350	0.619	0.507	0.589

The main characteristics of the monthly and seasonal *GHUV* and *GHI* ratios, based on the 10 min, hourly, and daily averages, were studied. The linear trend lines of both formulations ($GHUV = a{\cdot}GHI + b$, and $GHUV = a{\cdot}GHI$) were employed. According to several works, the formulation of the equation affects the quality of the results, due to errors induced by forcing the intercept to zero [34]. The temporal changes were examined, together with the effect of cloudiness; therefore, the k_t cloudiness classification was used to characterize the sky conditions. The results of these studies are depicted in Tables 7–9.

Table 7. Monthly, seasonal, and total averages of the *GHUV/GHI* ratio, number of 10 min values (N) and standard deviations (SD) under different sky conditions, together with the slope (a), offset (b), and R^2 values of the linear regressions $GHUV = a{\cdot}GHI + b$ and $GHUV = a{\cdot}GHI$.

Month/ Season	**All Skies**								**Overcast Skies(k_t<0.35)**			**Intermediate Skies(0.35≤k_t≤0.65)**			**Clear Skies(k_t>0.65)**		
	Σ(GHUV/GHI)/N			***GHUV=a·GHRa+b***			***GHUV=a·GHRa***		**Σ(GHUV/GHI)/N**			**Σ(GHUV/GHI)/N**			**Σ(GHUV/GHI)/N**		
	Value	***SD***	***N***	***a***	***b***	R^2	***a***	R^2	**Value**	***SD***	***N***	**Value**	***SD***	***N***	**Value**	***SD***	***N***
January	0.0375	0.0096	2026	0.0301	1.0802	0.9548	0.0331	0.9868	0.0477	0.0100	640	0.0365	0.0057	411	0.0312	0.0022	975
February	0.0393	0.0077	2862	0.0328	0.9594	0.9673	0.0352	0.9883	0.0461	0.0069	1132	0.0369	0.0045	943	0.0325	0.0026	787
March	0.0394	0.0080	3830	0.0341	0.9029	0.9689	0.0359	0.9885	0.0448	0.0082	1678	0.0367	0.0056	1107	0.0335	0.0027	1045
April	0.0401	0.0077	4213	0.0361	0.7294	0.9750	0.0373	0.9917	0.0473	0.0071	1509	0.0377	0.0054	1115	0.0349	0.0031	1589
May	0.0413	0.0072	3213	0.0383	0.5646	0.9831	0.0392	0.9938	0.0471	0.0072	1179	0.0388	0.0054	1073	0.0369	0.0032	961
June	0.0402	0.0078	2381	0.0392	−0.0572	0.9833	0.0391	0.9951	0.0487	0.0102	559	0.0384	0.0062	554	0.0372	0.0030	1268
July	0.0380	0.0063	2459	0.0394	−0.7329	0.9844	0.0384	0.9959	0.0477	0.0097	302	0.0364	0.0061	602	0.0367	0.0031	1555
August	0.0376	0.0057	1865	0.0383	−0.4667	0.9845	0.0376	0.9962	0.0468	0.0082	226	0.0356	0.0057	443	0.0365	0.0027	1196
September	0.0409	0.0084	3023	0.0362	0.8783	0.9697	0.0378	0.9907	0.0488	0.0092	973	0.0388	0.0051	1026	0.0354	0.0029	1024
October	0.0399	0.0080	2983	0.0340	0.8853	0.9682	0.0360	0.9891	0.0470	0.0073	1154	0.0377	0.0051	831	0.0335	0.0025	998
November	0.0401	0.0090	2993	0.0312	1.1881	0.9475	0.0348	0.9815	0.0474	0.0077	1336	0.0369	0.0050	785	0.0317	0.0023	872
December	0.0420	0.0112	2422	0.0303	1.1408	0.9383	0.0348	0.9747	0.0490	0.0105	1283	0.0363	0.0049	689	0.0309	0.0025	450
Winter	0.0394	0.0088	7824	0.0327	0.9126	0.9557	0.0351	0.9845	0.0463	0.0086	3281	0.0368	0.0052	2240	0.0320	0.0026	2303
Spring	0.0402	0.0076	10,458	0.0373	0.4694	0.9772	0.0380	0.9923	0.0471	0.0077	3584	0.0379	0.0055	2916	0.0358	0.0033	3958
Summer	0.0390	0.0069	6972	0.0383	−0.0557	0.9812	0.0382	0.9949	0.0480	0.0088	1314	0.0374	0.0059	1885	0.0366	0.0029	3773
Autumn	0.0404	0.0092	9016	0.0338	0.8111	0.9615	0.0359	0.9859	0.0478	0.0088	3792	0.0373	0.0051	2538	0.0327	0.0028	2686
All data	0.0398	0.0082	34,270	0.0370	0.2455	0.9746	0.0375	0.9907	0.0472	0.0084	11,971	0.0374	0.0054	9579	0.0347	0.0035	12,720

Table 8. Monthly, seasonal, and total *GHUV/GHI* average values, number of hourly values (N) and standard deviations (SD) under different sky conditions, together with the slope (a), offset (b), and R^2 values of the linear regressions $GHUV = a{\cdot}GHI + b$ and $GHUV = a{\cdot}GHI$.

Month/ Season	**All Skies**								**Overcast Skies(k_t<0.35)**			**Intermediate Skies(0.35≤k_t≤0.65)**			**Clear Skies(k_t>0.65)**		
	Σ(GHUV/GHI)/N			***GHUV=a·GHRa+b***			***GHUV=a·GHRa***		**Σ(GHUV/GHI)/N**			**Σ(GHUV/GHI)/N**			**Σ(GHUV/GHI)/N**		
	Value	***SD***	***N***	***a***	***b***	R^2	***a***	R^2	**Value**	***SD***	***N***	**Value**	***SD***	***N***	**Value**	***SD***	***N***
January	0.0420	0.0133	632	0.0316	0.6390	0.9702	0.0336	0.9858	0.0512	0.0124	255	0.0391	0.0109	176	0.0331	0.0079	201
February	0.0400	0.0089	591	0.0339	0.5703	0.9776	0.0354	0.9907	0.0466	0.0089	237	0.0373	0.0060	223	0.0329	0.0033	131
March	0.0410	0.0103	786	0.0350	0.5476	0.9777	0.0362	0.9902	0.0458	0.0111	345	0.0380	0.0075	270	0.0358	0.0077	171
April	0.0409	0.0096	827	0.0368	0.3907	0.9831	0.0375	0.9934	0.0480	0.0105	290	0.0377	0.0057	270	0.0364	0.0070	267
May	0.0425	0.0100	735	0.0390	0.3015	0.9882	0.0395	0.9948	0.0485	0.0110	265	0.0394	0.0079	299	0.0386	0.0069	171
June	0.0413	0.0099	477	0.0396	−0.1978	0.9904	0.0393	0.9963	0.0510	0.0134	116	0.0384	0.0072	157	0.0381	0.0042	204
July	0.0390	0.0092	474	0.0393	−0.6195	0.9902	0.0385	0.9966	0.0504	0.0156	68	0.0370	0.0083	144	0.0371	0.0034	262
August	0.0379	0.0064	399	0.0383	−0.4445	0.9900	0.0377	0.9966	0.0469	0.0087	57	0.0357	0.0059	120	0.0367	0.0032	222
September	0.0409	0.0086	592	0.0374	0.3882	0.9825	0.0382	0.9940	0.0474	0.0102	179	0.0391	0.0064	251	0.0363	0.0044	162
October	0.0411	0.0105	739	0.0350	0.4568	0.9823	0.0361	0.9928	0.0492	0.0114	264	0.0386	0.0077	246	0.0345	0.0044	229
November	0.0407	0.0097	605	0.0329	0.7094	0.9672	0.0352	0.9863	0.0474	0.0087	263	0.0376	0.0075	205	0.0326	0.0048	137
December	0.0433	0.0125	614	0.0324	0.6349	0.9635	0.0351	0.9813	0.0503	0.0117	314	0.0370	0.0066	198	0.0339	0.0109	102
Winter	0.0418	0.0117	1933	0.0338	0.5313	0.9695	0.0353	0.9862	0.0486	0.0117	848	0.0383	0.0084	644	0.0338	0.0075	441
Spring	0.0412	0.0097	2164	0.0379	0.2326	0.9843	0.0383	0.9936	0.0480	0.0108	744	0.0382	0.0069	756	0.0371	0.0064	664
Summer	0.0396	0.0086	1396	0.0387	−0.2087	0.9883	0.0384	0.9960	0.0489	0.0124	275	0.0377	0.0072	471	0.0371	0.0035	650
Autumn	0.0411	0.0104	1978	0.0350	0.4390	0.9776	0.0361	0.9903	0.0485	0.0103	786	0.0379	0.0071	688	0.0339	0.0061	504
All data	0.0410	0.0102	7471	0.0375	0.0857	0.9827	0.0376	0.9923	0.0484	0.0111	2653	0.0381	0.0074	2559	0.0358	0.0061	2259

Table 9. Monthly, seasonal, and total *GHUV/GHI* average values, number of daily values (N) and standard deviations (SD) under different sky conditions, together with the slope (a), offset (b), and R^2 values of the linear regressions $GHUV = a{\cdot}GHI + b$ and $GHUV = a{\cdot}GHI$.

Month/ Season	All Skies								Overcast Skies(k_t<0.35)			Intermediate Skies(0.35≤k_t≤0.65)			Clear Skies(k_t>0.65)		
	Σ(GHUV/GHI)/N			*GHUV=a·GHRa+b*			*GHUV=a·GHRa*		Σ(GHUV/GHI)/N			Σ(GHUV/GHI)/N			Σ(GHUV/GHI)/N		
	Value	*SD*	*N*	*a*	*b*	R^2	*a*	R^2	Value	*SD*	*N*	Value	*SD*	*N*	Value	*SD*	*N*
January	0.0376	0.0061	62	0.0271	1.7037	0.9851	0.0335	0.9897	0.0447	0.0043	19	0.0367	0.0038	24	0.0318	0.0007	19
February	0.0375	0.0043	56	0.0306	1.3763	0.9765	0.0354	0.9944	0.0432	0.0036	14	0.0361	0.0025	36	0.0330	0.0007	6
March	0.0382	0.0048	62	0.0314	1.6457	0.9663	0.0362	0.9929	0.0422	0.0050	20	0.0368	0.0034	31	0.0349	0.0026	11
April	0.0391	0.0039	60	0.0325	1.9853	0.9842	0.0371	0.9959	0.0438	0.0028	19	0.0377	0.0021	23	0.0358	0.0009	18
May	0.0398	0.0046	62	0.0380	0.4841	0.9907	0.0391	0.9975	0.0451	0.0039	15	0.0382	0.0036	39	0.0379	0.0010	8
June	0.0386	0.0038	34	0.0376	0.6227	0.9938	0.0388	0.9988	0.0421	0.0035	5	0.0378	0.0051	15	0.0381	0.0005	14
July	0.0383	0.0016	31	0.0334	2.4846	0.9712	0.0379	0.9989	-	-	0	0.0392	0.0020	13	0.0376	0.0007	18
August	0.0374	0.0014	31	0.0353	1.0985	0.9540	0.0373	0.9990	-	-	0	0.0376	0.0016	19	0.0372	0.0010	12
September	0.0392	0.0025	47	0.0325	2.1721	0.9736	0.0381	0.9966	0.0427	0.0015	8	0.0390	0.0018	32	0.0359	0.0013	7
October	0.0383	0.0044	62	0.0313	1.6001	0.9835	0.0359	0.9954	0.0442	0.0044	15	0.0373	0.0021	33	0.0343	0.0011	14
November	0.0383	0.0048	60	0.0279	1.7580	0.9734	0.0353	0.9903	0.0432	0.0031	22	0.0364	0.0025	29	0.0323	0.0012	9
December	0.0398	0.0055	62	0.0284	1.3206	0.9830	0.0353	0.9876	0.0442	0.0033	27	0.0371	0.0034	27	0.0338	0.0061	8
Winter	0.0382	0.0055	179	0.0302	1.3644	0.9613	0.0351	0.9900	0.0438	0.0044	59	0.0366	0.0035	88	0.0326	0.0021	32
Spring	0.0389	0.0042	168	0.0358	0.9105	0.9810	0.0379	0.9960	0.0438	0.0034	41	0.0378	0.0035	86	0.0365	0.0016	41
Summer	0.0386	0.0021	100	0.0342	1.9054	0.9811	0.0379	0.9984	0.0430	0.0014	8	0.0387	0.0019	53	0.0375	0.0008	39
Autumn	0.0385	0.0046	182	0.0325	1.0597	0.9721	0.0360	0.9933	0.0436	0.0035	56	0.0371	0.0023	94	0.0338	0.0031	32
All data	0.0386	0.0045	629	0.0358	0.5145	0.9763	0.0372	0.9947	0.0437	0.0037	164	0.0374	0.0030	321	0.0353	0.0028	144

Figure 11 shows the high positive correlation between both magnitudes, at 10 min, hourly, and daily intervals. Better fitting was obtained using no intercept linear regression models rather than linear regression models with an intercept, and the R^2 statistic increased as the time intervals lengthened; however, as is evident, both regressions were very similar. No significant differences were found for the slope and standard deviation values of the fitted data for the different considered time intervals.

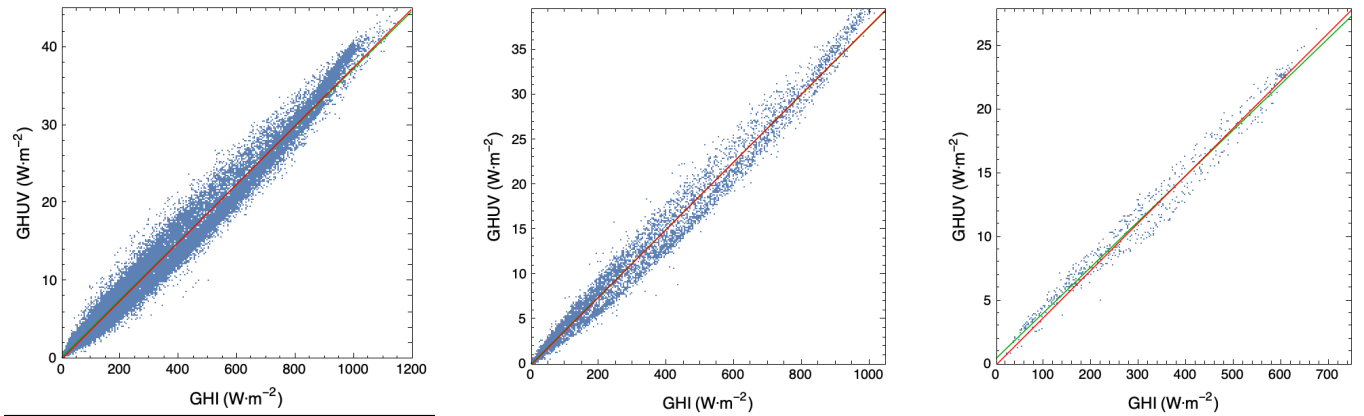

(**a**) (**b**) (**c**)

Figure 11. *GHUV* and *GHI* (W·m^{-2}) values recorded in Burgos (Spain) from 14 September 2020 to 6 June 2022: (**a**) 10 min data; (**b**) hourly average of 10 min data; (**c**) daily average of 10 min data. Tables below each plot show the two linear regressions (with and without constant), as well as the R^2 value and the 95% confidence interval (CI).

4. Conclusions

High quality *GHUV* and *GHI* datasets were recorded at 10 min intervals and analyzed in Burgos, Spain, between September 2020 and June 2022. The analysis of the experimental data has shown a representative dependency on the sky type conditions, classified with both the CIE and k_t taxonomies. The *GHUV/GHI* ratio yielded higher values for overcast sky types, and lower values with a higher scatter under clear sky conditions. A global

review of some *GHUV/GHI* ratios around the world has shown that *GHUV*, regardless of the temporal basis of the recorded data, accounts for up to 4% of the total incidence of *GHI* measured at the same location; the location's height above sea level and the sky conditions were the most influential parameters for the absolute value of the ratio. The value of the ratio increased in the categories which represented cloudier skies.

During this exhaustive analysis, the ratio did not exhibit any seasonal, monthly, or daily dependency, other than the predominance of one type of sky over another, in the period being analyzed.

Slight differences in the value of the ratio (mean and standard deviation) were detected depending on the sky classification criteria that was being used; the main difference between the values was the number of data that were classified as outliers. The fact that there was a higher number of outliers that corresponded with the CIE clear skies categories could be explained by the presence of aerosols or atmospheric turbidity; these factors are characteristic of clear sky types 13, 14, and 15, with a FOC of 19%, 3.8%, and 1.6% respectively.

The main conclusion, for practical purposes, is that the proportional relation between *GHUV* and *GHI* can be used for modelling *GHUV*.

Author Contributions: S.G.-R.: methodology, software, formal analysis, investigation, visualization. I.G.: methodology, software, formal analysis, investigation, original draft preparation, writing-review and editing, visualization; A.G.-R.: methodology, software, visualization; M.D.-M.: conceptualization, validation, original draft preparation, supervision, project administration; C.A.-T.: conceptualization, writing—review and editing; supervision, funding acquisition. All authors have read and agreed to the published version of the manuscript.

Funding: This research was funded by the Spanish Ministry of Science and Innovation, grant numbers RTI2018-098900-B-I00 and TED2021-131563B-I00, and Junta de Castilla y León, grant numbers INVESTUN/19/BU/0004 and INVESTUN/22/BU/0001.

Institutional Review Board Statement: Not applicable.

Informed Consent Statement: Not applicable.

Data Availability Statement: Copies of the original dataset used in this work can be downloaded from https://riubu.ubu.es/handle/10259/5512 (accessed on 10 October 2022).

Acknowledgments: Ignacio Garcia thanks the Spanish Ministry of Universities and the European Union-Next Generation EU for their financial support (program for the requalification of the Spanish university system 2021–2023, Resolution 14 February 2021).

Conflicts of Interest: The authors declare no conflict of interest.

References

1. Iqbal, M. *An Introduction to Solar Radiation*; Academic Press: Cambridge, MA, USA, 1983.
2. Soueid, L.; Triguero-Mas, M.; Dalmau, A.; Barrera-Gómez, J.; Alonso, L.; Basagaña, X.; Thieden, E.; Wulf, H.C.; Diffey, B.; Young, A.R.; et al. Estimating personal solar ultraviolet radiation exposure through time spent outdoors, ambient levels and modelling approaches*. *Br. J. Dermatol.* **2022**, *186*, 266–273. [CrossRef] [PubMed]
3. Vuilleumier, L.; Harris, T.; Nenes, A.; Backes, C.; Vernez, D. Developing a UV climatology for public health purposes using satellite data. *Environ. Int.* **2021**, *146*, 106177. [CrossRef] [PubMed]
4. Heisler, G.M.; Grant, R.H. Ultraviolet radiation in urban ecosystems with consideration of effects on human health. *Urban Ecosyst.* **2000**, *4*, 193–229. [CrossRef]
5. Ndiaye, A.; Charki, A.; Kobi, A.; Kébé, C.M.F.; Ndiaye, P.A.; Sambou, V. Degradations of silicon photovoltaic modules: A literature review. *Sol. Energy* **2013**, *96*, 140–151. [CrossRef]
6. Zhang, Y.; Kaiser, E.; Zhang, Y.; Zou, J.; Bian, Z.; Yang, Q.; Li, T. UVA radiation promotes tomato growth through morphological adaptation leading to increased light interception. *Environ. Exp. Bot.* **2020**, *176*, 104073. [CrossRef]
7. Häder, D.P.; Williamson, C.E.; Wängberg, S.Å.; Rautio, M.; Rose, K.C.; Gao, K.; Helbling, E.W.; Sinha, R.P.; Worrest, R. Effects of UV radiation on aquatic ecosystems and interactions with other environmental factors. *Photochem. Photobiol. Sci.* **2015**, *14*, 108–126. [CrossRef]
8. Grant, W.B.; Boucher, B.J. An Exploration of How Solar Radiation Affects the Seasonal Variation of Human Mortality Rates and the Seasonal Variation in Some Other Common Disorders. *Nutrients* **2022**, *14*, 2519. [CrossRef]

9. Nandin de Carvalho, H. Latitude impact on pandemic SARS-CoV-2 2020 outbreaks and possible utility of UV indexes in predictions of regional daily infections and deaths. *J. Photochem. Photobiol.* **2022**, *10*, 100108. [CrossRef]
10. Nicastro, F.; Sironi, G.; Antonello, E.; Bianco, A.; Biasin, M.; Brucato, J.R.; Ermolli, I.; Pareschi, G.; Salvati, M.; Tozzi, P.; et al. Solar UV-B/A radiation is highly effective in inactivating SARS-CoV-2. *Sci. Rep.* **2021**, *11*, 14805. [CrossRef]
11. Porfirio, A.C.S.; De Souza, J.L.; Lyra, G.B.; Maringolo Lemes, M.A. An assessment of the global UV solar radiation under various sky conditions in Maceió-Northeastern Brazil. *Energy* **2012**, *44*, 584–592. [CrossRef]
12. Foyo-Moreno, I.; Alados, I.; Olmo, F.J.; Alados-Arboledas, L. The influence of cloudiness on UV global irradiance (295–385 nm). *Agric. For. Meteorol.* **2003**, *120*, 101–111. [CrossRef]
13. Wang, L.; Gong, W.; Lin, A.; Hu, B. Measurements and cloudiness influence on UV radiation in Central China. *Int. J. Climatol.* **2014**, *34*, 3417–3425. [CrossRef]
14. Mateos, D.; Román, R.; Bilbao, J.; de Miguel, A.; Pérez-Burgos, A. Cloud modulation of shortwave and ultraviolet solar irradiances at surface. *Opt. Pura Apl.* **2012**, *45*, 29–32. [CrossRef]
15. Ogunjobi, K.O.; Kim, Y.J. Ultraviolet (0.280–0.400 μm) and broadband solar hourly radiation at Kwangju, South Korea: Analysis of their correlation with aerosol optical depth and clearness index. *Atmos. Res.* **2004**, *71*, 193–214. [CrossRef]
16. Lerche, C.M.; Philipsen, P.A.; Wulf, H.C. UVR: Sun, lamps, pigmentation and vitamin D. *Photochem. Photobiol. Sci.* **2017**, *16*, 291–301. [CrossRef]
17. Wang, L.; Gong, W.; Li, J.; Ma, Y.; Hu, B. Empirical studies of cloud effects on ultraviolet radiation in Central China. *Int. J. Climatol.* **2014**, *34*, 2218–2228. [CrossRef]
18. Feng, L.; Wang, L.; Gong, W.; Lin, A.; Hu, B. Estimation of hourly and daily ultraviolet solar irradiation under various sky conditions at Sanya, Southern China. *Theor. Appl. Climatol.* **2015**, *121*, 187–198. [CrossRef]
19. Leal, S.S.; Tíba, C.; Piacentini, R. Daily UV radiation modeling with the usage of statistical correlations and artificial neural networks. *Renew. Energy* **2011**, *36*, 3337–3344. [CrossRef]
20. Al-Aruri, S.D. The empirical relationship between global radiation and global ultraviolet (0.290–0.385) μm solar radiation components. *Sol. Energy* **1990**, *45*, 61–64. [CrossRef]
21. Barbero, F.J.; López, G.; Batlles, F.J. Determination of daily solar ultraviolet radiation using statistical models and artificial neural networks. *Ann. Geophys.* **2006**, *24*, 2105–2114. [CrossRef]
22. Bilbao, J.; Mateos, D.; de Miguel, A. Analysis and cloudiness influence on UV total irradiation. *Int. J. Climatol.* **2011**, *31*, 451–460. [CrossRef]
23. Canada, J.; Pedros, G.; Bosca, J.V. Relationships between UV (0.290–0.385 μm) and broad band solar radiation hourly values in Valencia and Córdoba, Spain. *Energy* **2003**, *28*, 199–217. [CrossRef]
24. Escobedo, J.F.; Gomes, E.N.; Oliveira, A.P.; Soares, J. Modeling hourly and daily fractions of UV, PAR and NIR to global solar radiation under various sky conditions at Botucatu, Brazil. *Appl. Energy* **2009**, *86*, 299–309. [CrossRef]
25. Foyo-Moreno, I.; Vida, J.; Alados-Arboledas, L. Ground based ultraviolet (290–385 nm) and broadband solar radiation measurements in south-eastern Spain. *Int. J. Climatol.* **1998**, *18*, 1389–1400. [CrossRef]
26. Habte, A.; Sengupta, M.; Gueymard, C.A.; Narasappa, R.; Rosseler, O.; Burns, D.M. Estimating ultraviolet radiation from global horizontal irradiance. *IEEE J. Photovolt.* **2018**, *9*, 139–146. [CrossRef]
27. Jacovides, C.P.; Tymvios, F.S.; Asimakopoulos, D.N.; Kaltsounides, N.A.; Theoharatos, G.A.; Tsitouri, M. Solar global UVB (280–315nm) and UVA (315–380nm) radiant fluxes and their relationships with broadband global radiant flux at an eastern Mediterranean site. *Agric. For. Meteorol.* **2009**, *149*, 1188–1200. [CrossRef]
28. Lamy, K.; Portafaix, T.; Brogniez, C.; Godin-Beekmann, S.; Bencherif, H.; Morel, B.; Pazmino, A.; Metzger, J.M.; Auriol, F.; Deroo, C.; et al. Ultraviolet radiation modelling from ground-based and satellite measurements on Reunion Island, southern tropics. *Atmos. Chem. Phys.* **2018**, *18*, 227–246. [CrossRef]
29. Liu, H.; Hu, B.; Zhang, L.; Zhao, X.J.; Shang, K.Z.; Wang, Y.S.; Wang, J. Ultraviolet radiation over China: Spatial distribution and trends. *Renew. Sustain. Energy Rev.* **2017**, *76*, 1371–1383. [CrossRef]
30. Martinez-Lozano, J.A.; Tena, F.; Utrillas, M.P. Ratio of UV to global broad band irradiation in Valencia, Spain. *Int. J. Climatol.* **1999**, *19*, 903–911. [CrossRef]
31. Murillo, W.; Cañada, J.; Pedrós, G. Correlation between global ultraviolet (290-385nm) and global irradiation in Valencia and Cordoba (Spain). *Renew. Energy* **2003**, *28*, 409–418. [CrossRef]
32. Paulescu, M.; Stefu, N.; Tulcan-Paulescu, E.; Calinoiu, D.; Neculae, A.; Gravila, P. UV solar irradiance from broadband radiation and other meteorological data. *Atmos. Res.* **2010**, *96*, 141–148. [CrossRef]
33. Podstawczyńska, A. UV and global solar radiation in Łódź, Central Poland. *Int. J. Climatol. A J. R. Meteorol. Soc.* **2010**, *30*, 1–10.
34. Proutsos, N.; Alexandris, S.; Liakatas, A.; Nastos, P.; Tsiros, I.X. PAR and UVA composition of global solar radiation at a high altitude Mediterranean forest site. *Atmos. Res.* **2022**, *269*, 106039. [CrossRef]
35. Robaa, S.M. A study of ultraviolet solar radiation at Cairo urban area, Egypt. *Sol. Energy* **2004**, *77*, 251–259. [CrossRef]
36. Sahan, M. The measurements of the global solar radiation and solar ultraviolet radiation during 2018 year. In Proceedings of the Turkish Physical Society 35th International Physics Congress, TPS 2019, Bodrum, Turkey, 4–8 September 2019.
37. López, M.L.; Palancar, G.G.; Toselli, B.M. Effects of stratocumulus, cumulus, and cirrus clouds on the UV-B diffuse to global ratio: Experimental and modeling results. *J. Quant. Spectrosc. Radiat. Transf.* **2012**, *113*, 461–469. [CrossRef]

38. Calbó, J.; Pagès, D.; González, J.A. Empirical studies of cloud effects on UV radiation: A review. *Rev. Geophys.* **2005**, *43*, 1–28. [CrossRef]
39. Degünther, M.; Meerkötter, R. Effect of remote clouds on surface UV irradiance. In *Annales Geophysicae*; Springer: Berlin/Heidelberg, Germany, 2020; pp. 679–686.
40. Maghrabi, A.H.; Al-Dosari, A.F. Effects on surface meteorological parameters and radiation levels of a heavy dust storm occurred in Central Arabian Peninsula. *Atmos. Res.* **2016**, *182*, 30–35. [CrossRef]
41. Di Sarra, A.; Cacciani, M.; Chamard, P.; Cornwall, C.; Deluisi, J.J.; Di Iorio, T.; Disterhoft, P.; Fiocco, G.; Fuá, D.; Monteleone, F. Effects of desert dust and ozone on the ultraviolet irradiance: Observations at the Mediterranean island of Lampedusa during PAUR II. *J. Geophys. Res.* **2002**, *107*, PAU-2. [CrossRef]
42. Diffey, B.L. Sources and measurement of ultraviolet radiation. *Methods* **2002**, *28*, 4–13. [CrossRef]
43. Dvorkin, A.Y.; Steinberger, E.H. Modeling the altitude effect on solar UV radiation. *Sol. Energy* **1999**, *65*, 181–187. [CrossRef]
44. Singh, S.; Singh, R. High-altitude clear-sky direct solar ultraviolet irradiance at Leh and Hanle in the western Himalayas: Observations and model calculations. *J. Geophys. Res. D Atmos.* **2004**, *109*, D19201–D19212. [CrossRef]
45. Sola, Y.; Lorente, J.; Campmany, E.; de Cabo, X.; Bech, J.; Redaño, A.; Martínez-Lozano, J.A.; Utrillas, M.P.; Alados-Arboledas, L.; Olmo, F.J.; et al. Altitude effect in UV radiation during the Evaluation of the Effects of Elevation and Aerosols on the Ultraviolet Radiation 2002 (VELETA-2002) field campaign. *J. Geophys. Res. Atmos.* **2008**, *113*, D23. [CrossRef]
46. Baker-Blocker, A.; DeLuisi, J.J.; Dutton, E.G. Received ultraviolet radiation at the South Pole. *Sol. Energy* **1984**, *32*, 659–662. [CrossRef]
47. Al-Aruri, S.; Rasas, M.; Al-Jamal, K.; Shaban, N. An assessment of global ultraviolet solar radiation in the range (0.290–0.385 μm) in Kuwait. *Sol. Energy* **1988**, *41*, 159–162. [CrossRef]
48. Elhadidy, M.A.; Abdel-Nabi, D.Y.; Kruss, P.D. Ultraviolet solar radiation at Dhahran, Saudi Arabia. *Sol. Energy* **1990**, *44*, 315–319. [CrossRef]
49. Khogali, A.; Al-Bar, O.F. A study of solar ultraviolet radiation at Makkah solar station. *Sol. Energy* **1992**, *48*, 79–87. [CrossRef]
50. Feister, U.; Grasnick, K.H. Solar UV radiation measurements at Potsdam (52°22′ N, 13°5′ E). *Sol. Energy* **1992**, *49*, 541–548. [CrossRef]
51. Martinez-Lozano, J.A.; Casanovas, A.J.; Utrillas, M.P. Comparison of global ultraviolet (290–385 nm) and global irradiation measured during the warm season in valencia, spain. *Int. J. Climatol.* **1994**, *14*, 93–102. [CrossRef]
52. Shaltout, M.A.; Ghonim, M.M.; Trabea, A.A.; Allam, H. Ultraviolt solar radiation over Egypt. *Renew. Energy* **1994**, *5*, 1506–1508. [CrossRef]
53. Foyo-Moreno, I.; Vida, J.; Alados-Arboledas, L. A simple all weather model to estimate ultraviolet solar radiation (290–385 nm). *J. Appl. Meteorol.* **1999**, *38*, 1020–1026. [CrossRef]
54. Cañada, J.; Pedrós, G.; López, A.; Boscá, J.V. Influences of the clearness index for the whole spectrum and of the relative optical air mass on UV solar irradiance for two locations in the Mediterranean area, Valencia and Cordoba. *J. Geophys. Res. Atmos.* **2000**, *105*, 4759–4766. [CrossRef]
55. Koronakis, P.S.; Sfantos, G.K.; Paliatsos, A.G.; Kaldellis, J.K.; Garofalakis, J.E.; Koronaki, I.P. Interrelations of UV-global/global/diffuse solar irradiance components and UV-global attenuation on air pollution episode days in Athens, Greece. *Atmos. Environ.* **2002**, *36*, 3173–3181. [CrossRef]
56. Jacovides, C.P.; Assimakopoulos, V.D.; Tymvios, F.S.; Theophilou, K.; Asimakopoulos, D.N. Solar global UV (280–380 nm) radiation and its relationship with solar global radiation measured on the island of Cyprus. *Energy* **2006**, *31*, 2728–2738. [CrossRef]
57. Hu, B.; Wang, Y.; Liu, G. Influences of the clearness index on UV solar radiation for two locations in the Tibetan Plateau-Lhasa and Haibei. *Adv. Atmos. Sci.* **2008**, *25*, 885–896. [CrossRef]
58. Escobedo, J.F.; Gomes, E.N.; Oliveira, A.P.; Soares, J. Ratios of UV, PAR and NIR components to global solar radiation measured at Botucatu site in Brazil. *Renew. Energy* **2011**, *36*, 169–178. [CrossRef]
59. Escobedo, J.F.; Dal Pai, A.; de Oliveira, A.P.; Soares, J.; Dal Pai, E. Diurnal and Annual Evolution of UV, PAR and NIR Irradiations in Botucatu/Brazil. *Energy Procedia* **2014**, *57*, 1130–1139. [CrossRef]
60. Wang, L.; Gong, W.; Ma, Y.; Hu, B.; Wang, W.; Zhang, M. Analysis of ultraviolet radiation in Central China from observation and estimation. *Energy* **2013**, *59*, 764–774. [CrossRef]
61. *ISO 15469:2004(E)/CIE S 011/E:2003*; Spatial Distribution of Daylight—CIE Standard General Sky. ISO: Geneva, Switzerland; CIE: Vienna, Austria, 2004.
62. García-Rodríguez, A.; García-Rodríguez, S.; Granados-López, D.; Díez-Mediavilla, M.; Alonso-Tristán, C. Extension of PAR Models under Local All-Sky Conditions to Different Climatic Zones. *Appl. Sci.* **2022**, *12*, 2372. [CrossRef]
63. Granados-López, D.; Suárez-García, A.; Díez-Mediavilla, M.; Alonso-Tristán, C. Feature selection for CIE standard sky classification. *Sol. Energy* **2021**, *218*, 95–107. [CrossRef]
64. Hoyer-Klick, C.; Schillings, C.; Schroedter Homscheidt, M.; Beyer, H.G.; Dumortier, D.; Wald, L.; Ménard, L.; Gschwind, B.; Martinoli, M.; Gaboardi, E.; et al. Management and exploitation of solar resource knowledge. In Proceedings of the EUROSUN 2008, 1st International Congress on Heating, Cooling and Buildings, Lisbonne, Portugal, 7 October 2008; p. 405.
65. Gueymard, C.A. Revised composite extraterrestrial spectrum based on recent solar irradiance observations. *Sol. Energy* **2018**, *169*, 434–440. [CrossRef]

66. Suárez-García, A.; Díez-Mediavilla, M.; Granados-López, D.; González-Peña, D.; Alonso-Tristán, C. Benchmarking of meteorological indices for sky cloudiness classification. *J. Sol. Energy* **2020**, *195*, 499–513. [CrossRef]
67. Al-Shooshan, A.A. Estimation of photosynthetically active radiation under an arid climate. *J. Agric. Eng. Res.* **1997**, *66*, 9–13. [CrossRef]
68. Finch, D.A.; Bailey, W.G.; McArthur, L.J.B.; Nasitwitwi, M. Photosynthetically active radiation regimes in a southern African savanna environment. *Agric. For. Meteorol.* **2004**, *122*, 229–238. [CrossRef]
69. Jacovides, C.P.; Tymvios, F.S.; Assimakopoulos, V.D.; Kaltsounides, N.A. The dependence of global and diffuse PAR radiation components on sky conditions at Athens, Greece. *Agric. For. Meteorol.* **2007**, *143*, 277–287. [CrossRef]
70. Wang, L.; Gong, W.; Lin, A.; Hu, B. Analysis of photosynthetically active radiation under various sky conditions in Wuhan, Central China. *Int. J. Biometeorol.* **2014**, *58*, 1711–1720. [CrossRef]
71. Udo, S.O.; Aro, T.O. Global PAR related to global solar radiation for central Nigeria. *Agric. For. Meteorol.* **1999**, *97*, 21–31. [CrossRef]
72. Udo, S.O.; Aro, T.O. New empirical relationships for determining global PAR from measurements of global solar radiation, infrared radiation or sunshine duration. *Int. J. Climatol.* **2000**, *20*, 1265–1274. [CrossRef]
73. Alados, I.; Foyo-Moreno, I.y.; Alados-Arboledas, L. Photosynthetically active radiation: Measurements and modelling. *Agric. For. Meteorol.* **1996**, *78*, 121–131. [CrossRef]
74. Jacovides, C.P.; Timvios, F.S.; Papaioannou, G.; Asimakopoulos, D.N.; Theofilou, C.M. Ratio of PAR to broadband solar radiation measured in Cyprus. *Agric. For. Meteorol.* **2004**, *121*, 135–140. [CrossRef]
75. Alshaibani, K. Finding frequency distributions of CIE Standard General Skies from sky illuminance or irradiance. *Light. Res. Technol.* **2011**, *43*, 487–495. [CrossRef]
76. Li, D.H.W.; Cheung, G.H.W. Average daylight factor for the 15 CIE standard skies. *Light. Res. Technol.* **2006**, *38*, 137–152. [CrossRef]
77. Li, D.H.W.; Lam, T.N.T.; Cheung, K.L.; Tang, H.L. An analysis of luminous efficacies under the CIE standard skies. *Renew. Energy* **2008**, *33*, 2357–2365. [CrossRef]
78. Li, D.H.W.; Tang, H.L.; Wong, S.L.; Tsang, E.K.W.; Cheung, G.H.W.; Lam, T.N.T. Skies classification using artificial neural networks (ANN) techniques. In Proceedings of the 6th International Conference on Indoor Air Quality, Ventilation and Energy Conservation in Buildings: Sustainable Built Environment, IAQVEC 2007, Sendai, Japan, 28–31 October 2007; pp. 61–68.
79. Torres, J.L.; de Blas, M.; García, A.; Gracia, A.; de Francisco, A. Sky luminance distribution in the North of Iberian Peninsula during winter. *J. Atmos. Sol. Terr. Phys.* **2010**, *72*, 1147–1154. [CrossRef]
80. Tregenza, P.R. Analysing sky luminance scans to obtain frequency distributions of CIE Standard General Skies. *Light. Res. Technol.* **2004**, *36*, 271–279. [CrossRef]
81. Granados-López, D.; García-Rodríguez, A.; García-Rodríguez, S.; Suárez-García, A.; Díez-Mediavilla, M.; Alonso-Tristán, C. Pixel-based image processing for cie standard sky classification through ANN. *Complexity* **2021**, *310*, 108627. [CrossRef]
82. Suárez-García, A.; Granados-López, D.; González-Peña, D.; Díez-Mediavilla, M.; Alonso-Tristán, C. Seasonal caracterization of CIE standard sky types above Burgos, northwestern Spain. *Sol. Energy* **2018**, *169*, 24–33. [CrossRef]
83. García-Rodríguez, A.; Granados-López, D.; García-Rodríguez, S.; Díez-Mediavilla, M.; Alonso-Tristán, C. Modelling Photosynthetic Active Radiation (PAR) through meteorological indices under all sky conditions. *Agric. For. Meteorol.* **2021**, *310*, 108627. [CrossRef]

applied sciences

MDPI

Article

Modeling Horizontal Ultraviolet Irradiance for All Sky Conditions by Using Artificial Neural Networks and Regression Models

M. I. Dieste-Velasco, S. García-Rodríguez, A. García-Rodríguez, M. Díez-Mediavilla and C. Alonso-Tristán *

Research Group Solar and Wind Feasibility Technologies (SWIFT), Electromechanical Engineering Department, Universidad de Burgos, 09006 Burgos, Spain

* Correspondence: catristan@ubu.es or cristinaalonso.tristan@gmail.com; Tel.: +34-947-258853

Abstract: In the present study, different models constructed with meteorological variables are proposed for the determination of horizontal ultraviolet irradiance (I_{UV}), on the basis of data collected at Burgos (Spain) during an experimental campaign between March 2020 and May 2022. The aim is to explore the effectiveness of a range of variables for modelling horizontal ultraviolet irradiance through a comparison of supervised artificial neural network (ANN) and regression model results. A preliminary feature selection process using the Pearson correlation coefficient was sufficient to determine the variables for use in the models. The following variables and their influence on horizontal ultraviolet irradiance were analyzed: horizontal global irradiance (I_{GH}), clearness index (k_t), solar altitude angle (α), horizontal beam irradiance (I_{BH}), diffuse fraction (D), temperature (T), sky clearness (ε), cloud cover (Cc), horizontal diffuse irradiance (I_{DH}), and sky brightness (Δ). The ANN models yielded results of greater accuracy than the regression models.

Keywords: UV irradiance; ANN; modeling; multilinear regression models

Citation: Dieste-Velasco, M.I.; García-Rodríguez, S.; García-Rodríguez, A.; Díez-Mediavilla, M.; Alonso-Tristán, C. Modeling Horizontal Ultraviolet Irradiance for All Sky Conditions by Using Artificial Neural Networks and Regression Models. *Appl. Sci.* **2023**, *13*, 1473. https://doi.org/10.3390/app13031473

Academic Editors: Harry D. Kambezidis and Basil Psiloglou

Received: 2 December 2022
Revised: 18 January 2023
Accepted: 19 January 2023
Published: 22 January 2023

1. Introduction

Ultraviolet radiation is the region of the solar spectrum with wavelengths between 100 and 400 nm. It is usually divided into three spectral bands: UV-C (100–280 nm), completely absorbed in the Earth's atmosphere; UV-B (280–315 nm), partially absorbed by the stratospheric ozone; and UV-A (315–400 nm), weakly absorbed by ozone and therefore transmitted to the Earth's surface [1]. UV radiation varies greatly on the ground, depending mainly on latitude, solar elevation, temperature, cloud characteristics, total ozone, aerosol pollution, and surface albedo [2,3]. Ultraviolet radiation can induce serious adverse health effects and may be responsible for premature skin aging, proliferation of skin cancer [4–6], immune deficiencies and cataracts, as well as damage to ecosystems, crops [7,8], and the biosphere [9]. However, ultraviolet radiation in moderate doses has health benefits, can reduce blood pressure, has been linked to improvements in mental health, and promotes the synthesis of vitamin D, among other advantages [10].

As not all ground meteorological stations have sensors to measure ultraviolet irradiance [11], mathematical models are therefore usually developed to generate ultraviolet values based on experimental measurements of other meteorological data that are more frequently recorded at ground meteorological stations, such as horizontal global irradiance [12]. In many works, the ratio between the ultraviolet component and the horizontal global irradiance, (I_{UV}/I_{GH}), has been studied, obtaining values of between 2.5% and 6% [13]. A complete review of this relation can be found in [14]. The ratio between both magnitudes is location dependent and is influenced by the clearness index, k_t; when cloudiness increases, the ratio of I_{UV} to I_{GH} increases [15], i.e., the presence of clouds reduces the global horizontal irradiance to a greater extent than the UV component [16–18]. The dependence of solar UV irradiance on solar elevation has also been studied, observing that

when solar elevation increases, the levels of I_{UV} reaching the surface also increase. It can be concluded that solar elevation is one determining factor when modeling solar UV radiation under all sky conditions [18]. It has been found that the dependence of I_{UV} upon I_{GH} and the relative optical air mass can be parameterized with the brightness index on a daily basis [19,20], revealing a strong inverse linear dependence on the logarithm in relation to the optical air mass.

Several works have developed different mathematical models for obtaining UV values as a function of certain atmospheric parameters such as relative optical air mass, cloud modification factors [3,21,22], aerosols, different tilt angles and ozone as well as local surface characteristics (albedo) [23], cosine of the solar zenith angle [2], precipitable water content, total ozone column, aerosol optical depth, temperature, humidity and dew point temperature under all sky conditions [13]. Many other works observed that I_{UV} and I_{GH} are mainly affected by solar zenith angle [24]. Besides the variation in solar zenith angle, cloud cover is an important factor in UV levels [25]; however, under clear skies, the most important factor in the attenuation of solar radiation are aerosols [26]. The model is therefore often programmed to perform a preliminary classification of the atmospheric conditions, based on sky types, using the clearness index as a classifier with different time intervals [2,3,27]. The UV component has been modeled in China, using two input parameters: the effect of the comprehensive attenuation factors for assumed cloud-free conditions and the effect of the clouds; this has obtained good results at a different location from the one at which model was developed [28]. Other models were used to estimate I_{UV} under various sky conditions, analyzing the dependence of UV irradiance on the brightness index, Δ, and the solar elevation angle [27]. It has been shown, using the brightness index as a parameter to model cloudiness, that clouds hardly reduce the UV component, but the horizontal global component does [3]. If a specific brightness is used, it is observed that the UV component increases almost exponentially with the zenith angle [29]. In addition, different statistical models have been developed to estimate daily I_{UV} from I_{GH} through the linear correlation; these introduce a polynomial correction of the average ratio I_{UV}/I_{GH} as a function of the transmittance index of global solar irradiance and the UV atmospheric transmittance index by means of a multiple regression of the air mass and clearness index [11].

Other researchers have obtained semi-empirical models based on the SMARTS radiative transfer model [30], using atmospheric precipitable water, total ozone column, aerosol optical depth, daily temperature, relative humidity, atmospheric pressure, and dew point temperature as the input variables [13]. In this case, the I_{UV} as modeled is considered to be the product of the cloud modification factor of UV irradiance multiplied by the simulated UV irradiance under clear sky conditions. For a quantitative evaluation of the effect of clouds and aerosols on radiation, the so-called daily attenuation coefficients for cloud and aerosols were defined.

In recent years, the use of ANNs is becoming frequent for the calculation of UV component values because they possess some advantages over classic modeling. They do not require a user-specified problem-solving algorithm, and they can respond to patterns which are similar, but not identical, to that for which they were trained [31]. However, the ANN is often a "black box" system; its use is not a user-friendly task for a non-expert [20]. In all the works found in the literature in the field of ANN, I_{GH} has been used as input and its use is now the norm to obtain accurate results when modelling I_{UV}, regardless of the number and the characteristics of the other variables used as inputs and the architecture of the ANN [20,29,32,33]. In addition, other authors have developed UV estimation models through an empirical artificial neural network (ANN) and support vector machine (SVM), using different variables for each method in order to compare the results obtained for the modeled values of the UV component [34].

Moreover, other magnitudes related to UV radiation have also been modeled using ANNs, such as the ratio I_{UV}/I_{GH}, considering the transmittance index of I_{GH} and the atmospheric transmittance index as the inputs, or the UV atmospheric transmittance index,

using the air mass and the clearness index as the inputs [11]. Statistical models and ANNs showed good statistical performance with an RMS lower than 5% and an MBE between 0.4 and 2% [11]. All models can be used to estimate UV radiation at locations where only I_{GH} data are available [11]. ANN models have been developed to estimate solar UV erythemal irradiance (UVER), based on a combination of optical air mass, ozone column content, and I_{GH}. The input data were collected at different locations, obtaining a mean bias deviation of less than 1% and a root mean square deviation of less than 17% for all locations [35].

In this work, different models are proposed for the determination of the I_{UV} based on meteorological variables, using data collected at Burgos (Spain). To do so, supervised artificial neural networks (ANNs) are used and a comparison is also made with the results obtained through regression models. The following meteorological variables are included in the study: horizontal global irradiance, I_{GH}, clearness index, k_t, solar altitude angle, α, horizontal beam irradiance, I_{BH}, diffuse fraction, D, temperature, T, sky clearness, ε, cloud cover, Cc, horizontal diffuse irradiance, I_{DH}, and sky brightness, Δ. First, a feature selection procedure was applied to identify related features and to remove the irrelevant or less important ones. After the feature selection procedure, two different strategies were used for modelling I_{UV}: multilinear regression and ANN modelling. Analysis and comparisons of both models were conducted to study the influence of sky conditions on the accuracy of the model. The experimental data for this study were collected during an experimental campaign that ran from March 2020 to May 2022, in Burgos, Spain.

The paper is structured as follows: after the Introduction section, the characteristics of the measurement equipment and the experimental data in use are described in Section 2. In the same section, a methodology is also presented; this will be followed to obtain the independent variables (meteorological and radiation variables) that were used to develop the models. Then, in Section 3, the results of using the ANN models are shown. In Section 4, the results obtained with the regression models are analyzed. Finally, the main conclusions obtained in this work are presented in Section 5.

2. Equipment and Methodology

In this section, the measurement equipment used to determine the meteorological and radiation variables is detailed, as well as the methodology followed to develop the models that predict I_{UV} levels. In the present work, these models are developed for all-sky conditions.

2.1. Description of the Experimental Data

The data were collected at the weather station located on the flat roof of the Higher Polytechnic School of the University of Burgos (42°21′04″ N, 3°41′20″ W, 956 m above mean sea level), shown in Figure 1. The experimental campaign ran from March 2020 to May 2022. Data were collected every 30 s and averages were recorded every 5 min. The experimental data I_{GH}, I_{DH}, I_{BH} were subjected to the quality control (QC) procedure proposed in the MESoR project [36]. Regarding I_{UV} data, it has been established that it could not be higher than extraterrestrial UV on the horizontal plane, UVH_0 corresponding to the same time frame. UVH_0 was calculated using Equation (1):

$$UVH_0 = \varepsilon_0 UV_{sc} \cos Z \quad (1)$$

where UV_{sc} is the UV solar constant, and f_c is the correction factor based on estimated orbital eccentricity ($\varepsilon_0 = 1 + 0.033 \cdot \cos\left(\frac{2 \cdot \pi \cdot d_n}{365}\right)$) where d_n is the day of the year multiplied by the cosine of the solar zenith angle ($\cos Z$). UV_{sc} was obtained from the integration of the solar spectrum, revised by Gueymard [37] at between 280 and 400 nm, yielding a value of 102.15 $W \cdot m^{-2}$. Data corresponding to solar elevation angles lower than 5° were discarded in order to avoid the cosine response problems of the irradiance measurement instruments. After the filtering process, a total of 68,509 experimental measurement data were used in the study.

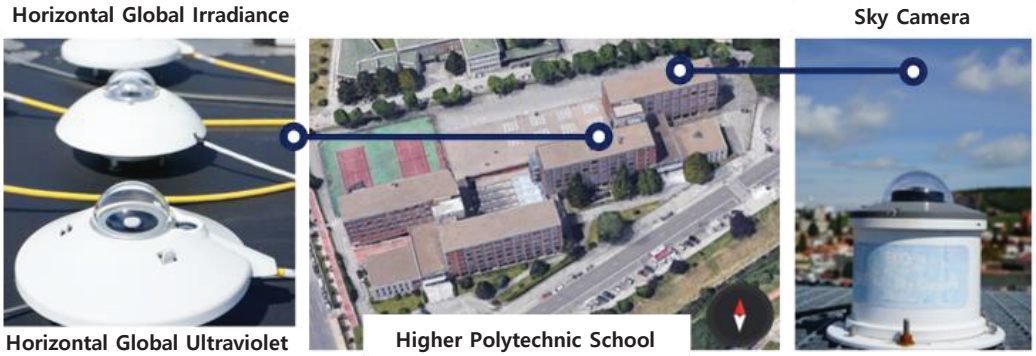

Figure 1. Experimental equipment.

I_{GH}, I_{DH}, and I_{BH} were measured with Hulseflux pyranometers (model SR11: sensitivity of 12.13 $\mu V/(W/m^2)$ and uncertainty of $\pm 1.8\%$) and a pyrheliometer (model DR01: sensitivity of 10×10^{-6} $V/(W/m^2)$ and uncertainty of $\pm 1.2\%$), respectively. For direct and diffuse radiation measurements, I_{DH} and I_{BH}, a GEONICA-SEMS-3000 sun tracker equipped with a shading disc has been used. A Kipp & Zonnen pyranometer (model CUV5: sensitivity of 300–500 $\mu V/(W/m^2)$ and uncertainty of $\pm 5\%$) was used to determine the I_{UV} values. The cloud cover was calculated with a commercial SONA201D all-sky camera (Sieltec Canary Islands, Spain). The trigger frequency of the camera was 1 s and its image resolution was 1158×1172 pixels, recorded with the RGB color model (8-bit pixels with integer values between 0 and 255 were used). A complete description of the experimental facility and instruments can be found in previous works [14,38,39].

2.2. Statistical Parameters and Estimators

In addition to the experimental measurements (I_{GH}, I_{DH}, and I_{BH}, as indicated above), other meteorological variables easily obtained from those values were used. Δ is the sky's brightness, as shown in Equation (2). It quantifies cloud thickness or aerosol loading.

$$\Delta = \frac{I_{DH} * m}{B_{sc} \cdot \varepsilon_0} \tag{2}$$

where B_{sc} is the extraterrestrial irradiance constant (=1361.1 W/m^2 [40]) and m is the relative optical air mass. The sky's clearness index, ε, predicts cloud conditions using the ratio between the diffuse horizontal irradiance and the direct one on the same plane, as shown in Equation (3), where $k = 1.041$ for Z in radians.

$$\varepsilon = \left(\frac{I_{DH} + I}{I_{DH}} + kZ^3 \right) / \left(1 + kZ^3 \right) \tag{3}$$

The clearness index, k_t, obtained with Equation (4), defined as the ratio of the global horizontal irradiance at ground level and the extra-terrestrial global solar irradiance, measures the fraction of the solar radiation transmitted through the atmosphere.

$$k_t = \frac{I_{GH}}{B_{sc} \cdot \varepsilon_0 \cdot \cos Z} \tag{4}$$

The sky ratio or diffuse fraction, D, as shown in Equation (5), is defined as the ratio of horizontal diffuse irradiance to horizontal global irradiance. It refers to the cloudiness of the sky and/or the turbidity of the atmosphere.

$$D = \frac{I_{DH}}{I_{GH}} \tag{5}$$

The goodness-of-fit of the models was calculated in terms of nMBE (%) (normalized mean bias error) and nRMSE (%) (normalized root mean square error). Equations (6) and (7) show the statistical estimators employed in this study.

$$\text{nMBE } (\%) = 100\frac{\sum_n (X_{\text{model}} - X_{\text{measured}})}{\sum_n X_{\text{measured}}} \quad (6)$$

$$\text{nRMSE } (\%) = 100\frac{\sqrt{\frac{\sum_n (X_{\text{model}} - X_{\text{measured}})^2}{n}}}{\frac{\sum_n X_{\text{measured}}}{n}} \quad (7)$$

The Pearson correlation coefficient was used to determine the degree of correlation between I_{UV} and the meteorological variables under study. The Pearson criterion is based on the Pearson correlation coefficient, r. If there is a strong correlation between I_{UV} and the selected variable, then the Pearson coefficient will be either 1 (direct correlation) or −1 (inverse correlation). However, a Pearson coefficient close to 0 implies a weak or null correlation. The rule of thumb [41] established five r intervals for the correlation: direct ($1 \geq |r| \geq 0.9$), strong ($0.9 > |r| \geq 0.7$), moderate ($0.7 > |r| \geq 0.5$), weak ($0.5 > |r| \geq 0.3$), and negligible ($|r| < 0.3$). Figure 2 shows the correlation between all variables considered in the study. The correlation of I_{UV} with the independent meteorological variables is obtained from the last row/column of the correlation matrix shown in Figure 2. The influence of these variables on I_{UV} can also be seen graphically in Figure 3, where the input variables have been ordered according to the correlation with I_{UV}.

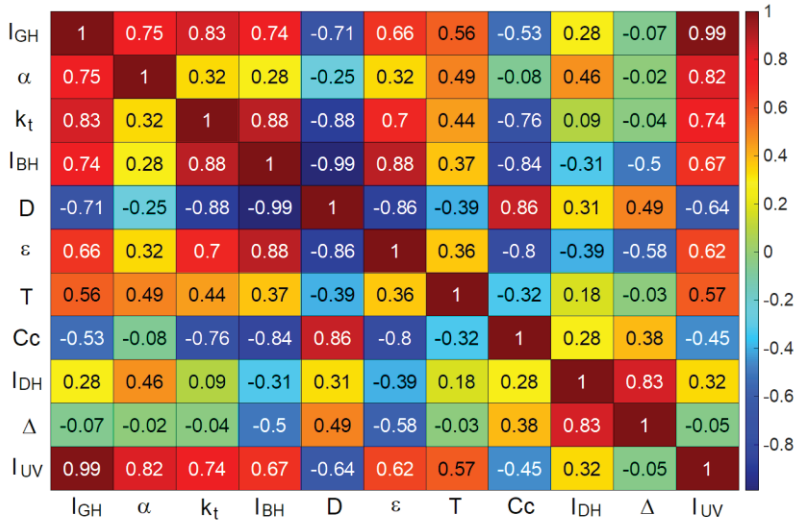

Figure 2. The Pearson correlation coefficient matrix of all meteorological variables considered in this study.

The meteorological variables with $r(I_{UV}, \text{variable}) < 0.4$ were discarded as inputs for the models, after which only the variables included in Table 1 were considered.

Table 1. Selection of meteorological variables to be considered, according to the Pearson correlation coefficient $r(I_{UV}, \text{variable})$.

Variable:	I_{GH}	α	k_t	I_{BH}	D	ε	T	Cc
$r_{(I_{UV}, \text{variable})}$:	0.99	0.82	0.74	0.67	−0.64	0.62	0.57	−0.45

As Figure 3 shows, I_{GH} has the strongest correlation with I_{UV}, followed by the solar altitude angle, α, and the clearness index, k_t. Only D and Cc presented weak inverse correlation with I_{UV}. The results were coherent with those in the literature review.

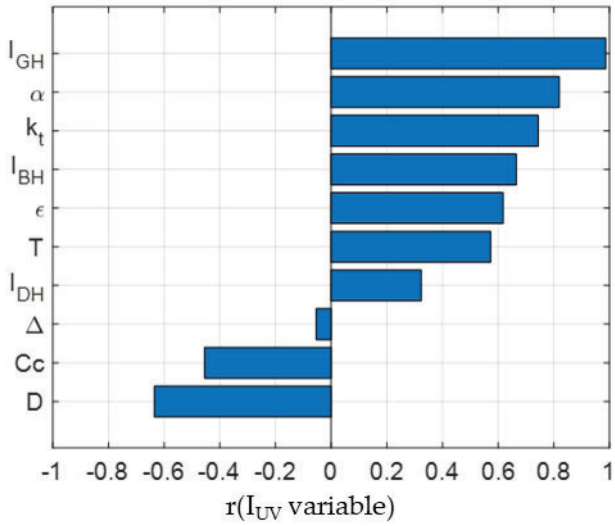

Figure 3. The Pearson correlation coefficient, r(I_{UV}, variable), between I_{UV} and the meteorological variables considered in the study.

3. Artificial Neural Network Models

A topology consisting of an input layer, a hidden layer, and an output layer was considered for the ANN, and the Levenberg–Marquardt algorithm was used to adjust both the weights and the bias of the network, in accordance with Equation (8). The transfer function in the hidden layer, f_1, was sigmoidal, and f_2 in the output layer was a linear function. W_1 and b_1 were the weights and biases of the hidden layer, and W_2 and b_2 were the weights and biases of the output layer, respectively.

$$I_{UV} = f_2(W_2 * f_1(W_1 * \text{Inputs} + b_1) + b_2) \quad (8)$$

All the meteorological variables indicated in Table 1 may be used to develop ANN-based models. As indicated above, I_{GH} is the variable with the greatest influence on I_{UV}. The Pearson correlation coefficient is 0.99, as shown in Figure 2. Therefore, I_{GH} must be included as a first input of the model. However, some of the variables are correlated between each other and their inclusion together in the ANN model increased the complexity of the model without significantly improving accuracy, both for the nRMSE and the nMBE values. As can be seen in Table 2, the Pearson coefficient r(I_{GH}variable) highlighted a high correlation between I_{GH} and k_t. On the other hand, as can be observed in Figure 2, a high correlation exits between I_{BH}, and D. To determine the optimal neural network, the goodness of fit of the models obtained with the combination of inputs shown in Table 3 was analyzed, using the previously defined indicators, nRMSE, and nMBE. In each combination, one of the variables was eliminated or substituted. For the analysis, the experimental data set was divided into three groups: 70% was used as a training set, 15% as a validation set, and the remaining 15% was used to test the model. The three (training, validation and test) data sets were the same in all the models that were developed.

Table 2. The Pearson correlation coefficient r(I_{GH}, variable) for detecting redundant information.

Variable:	k_t	α	I_{BH}	D	ε	T	Cc
$r_{(I_{GH}, \text{Variable})}$:	0.83	0.75	0.74	−0.71	0.66	0.56	−0.53

Table 3. Results of I_{UV} ANN models.

Model Number & Variables		Training			Test		
#	Variables	nRMSE (%)	nMBE (%)	R^2 (%)	nRMSE (%)	nMBE (%)	R^2 (%)
1	I_{GH}, k_t, α, I_{BH}, D, ε, T, Cc	3.82	0.00	99.68%	3.77	−0.01	99.69%
2	I_{GH}, α, I_{BH}, D, ε, T, Cc	3.87	0.00	99.67%	3.83	−0.01	99.68%
3	I_{GH}, I_{BH}, D, ε, T, Cc	4.26	−0.01	99.60%	4.21	−0.01	99.62%
4	I_{GH}, α, D, ε, T, Cc	3.89	0.00	99.67%	3.86	−0.02	99.68%
5	I_{GH}, α, ε, T, Cc	3.91	−0.02	99.66%	3.88	−0.03	99.67%
6	I_{GH}, α, T, Cc	4.04	0.00	99.64%	4.01	−0.01	99.65%
7	I_{GH}, α, ε, Cc	4.15	0.00	99.62%	4.09	0.00	99.64%
8	I_{GH}, α, T	4.85	0.00	99.48%	4.82	0.04	99.49%
9	I_{GH}, α, Cc	4.30	0.00	99.59%	4.24	0.00	99.61%
10	I_{GH}, α, ε	4.71	−0.01	99.51%	4.67	0.02	99.53%
11	I_{GH}, α	5.13	0.01	99.42%	5.09	0.07	99.44%
12	I_{GH}	10.30	0.00	97.66%	10.29	0.19	97.70%
13	k_t, α, Cc	4.36	0.00	99.58%	4.34	0.02	99.59%
14	k_t, α	5.13	0.00	99.42%	5.10	0.05	99.44%
15	k_t	39.72	−0.05	65.26%	40.08	0.58	65.14%
16	I_{BH}, α, Cc	8.70	−0.01	98.33%	8.55	0.08	98.41%
17	I_{BH}, α	11.94	0.00	96.86%	12.03	−0.02	96.86%
18	I_{BH}	45.45	0.00	54.50%	46.05	0.45	53.98%

Table 3 shows the 18 ANN models developed with the nRMSE, nMBE, and the corresponding R^2 values obtained for the data used in both the training and in the test models.

The results shown in Table 3 confirmed that the inclusion of meteorological variables with a high Pearson correlation coefficient in no way improved the accuracy of the ANN. On the one hand, considering I_{GH}, α, ε, T, Cc, ANN model number 5 might be more appropriate than models 1 to 4 listed in Table 3. On the other hand, eliminating solar height had a negative influence on the values of the statistics under analysis. Therefore, solar height was left as an independent variable in the models. Likewise, worse results were observed after removing cloud cover and leaving temperature. Based on the above, the model to be used was model number 9, from Table 3, as that model presented a reduced number of inputs (I_{GH}, α, Cc) and yielded adequate nRMSE and nMBE values. In addition, it was observed that model 9, which uses I_{GH}, yielded a somewhat lower nRMSE than model 13, obtained using k_t instead of I_{GH} and with the two other above-mentioned variables (α, Cc). However, both models could be used, as they yielded similar results. On the other hand, significantly worse statistics were observed when using I_{BH} instead of I_{GH} with the two previously mentioned variables (α, Cc). It can be seen that the selected model (model 9) presented an R^2 of 99.59% with the training dataset, and of 99.61% with the test dataset, and similar values were obtained with the model that used k_t instead of I_{GH}.

Figure 4 shows the relationship between I_{UV} and I_{GH} based on the data considered in this study. Both the training and the test datasets showed similar distributions.

Figure 5 also shows the relationship between solar height and ultraviolet radiation for both the training and test datasets. These figures are included because solar height will be a variable that will be part of the selected models, as can be seen in Table 3, while Figure 6 represents the ultraviolet radiation vs. cloud cover for both datasets.

Figure 7 shows the values predicted with ANN model number 9, where the "Output" corresponds to the neural network outputs and "Target" to the experimental values for both training and test dataset results.

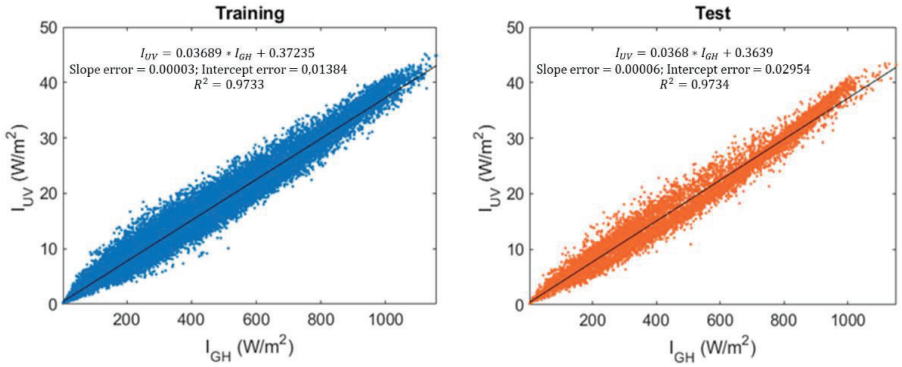

Figure 4. Ultraviolet irradiance, $I_{UV,}$ vs. global horizontal irradiance, I_{GH}.

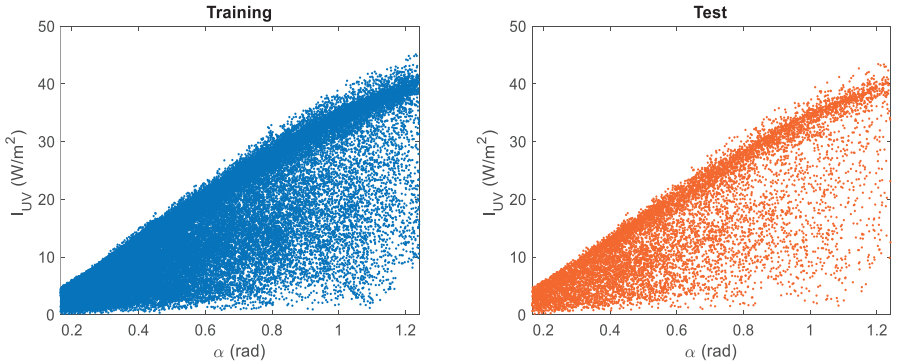

Figure 5. Ultraviolet irradiance, I_{UV}, vs. solar altitude, α.

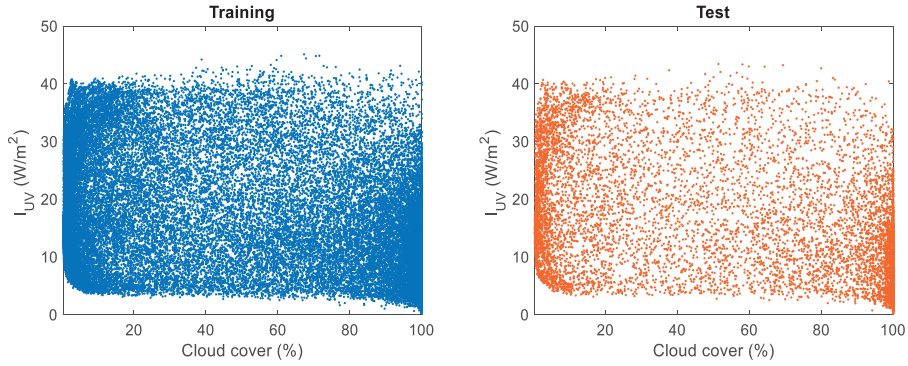

Figure 6. Ultraviolet irradiance, I_{UV}, vs. cloud cover, Cc.

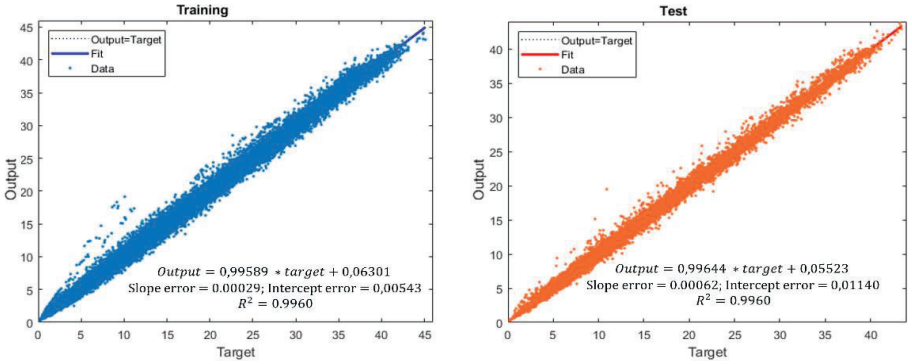

Figure 7. Results of $I_{UV} = f(I_{GH}, \alpha, Cc)$, using ANN model 9.

4. Regression Models

Having determined the ANN-based models, a regression fit was performed with the same selected variables (I_{GH}, α, and Cc) analyzing first and second-order models. A similar

study was also performed with (k_t, α, and Cc). The models were fitted with 85% of the data to generate the regression models, and the remaining 15% of the data were used to test the models. The data used for fitting and testing the regression models were the same as those used for the ANN models. It should be noted that when using I_{BH} instead of I_{GH} or k_t, the accuracy of the models worsened significantly, which could be expected a priori in view of the correlation matrix shown in Figure 2. Therefore, these models were not included in the present study.

From the data shown in Figure 4 an approximately linear relationship between I_{UV} and I_{GH} can be deduced after fitting a first-order model as a function of I_{GH}, $I_{UV} = 0.3676 + 0.0369 \cdot I_{GH}$. It could therefore be considered, as an approximate value, that I_{UV} was 3.7% of I_{GH}, for the data analyzed within the study period and in the locality of Burgos, Spain. The results with the linear model $R^2 = 97.32\%$, RSME = 11.02%, and nMBE = 0.00% were worse than those obtained with more complex models, which included a larger number of variables but had the advantage of simplicity.

The following linear regression models given by Equation (9) can be considered as a first option, in the case of preferring greater accuracy, than the linear model with I_{GH} without using ANNs:

$$I_{UV} = b_0 + \sum_{j=1}^{3} b_j * x_j \tag{9}$$

Although this means including more independent variables in the model. The use of a second-order regression model, such as the one shown in Equation (10), could also be considered, should greater precision be needed:

$$I_{UV} = b_0 + \sum_{j=1}^{3} b_j * x_j + \sum_{j=1}^{3} b_{jj} * x_j^2 + \sum_{\substack{k>j \\ j=1,2}}^{3} b_{jk} * x_j * x_k \tag{10}$$

Equations (9) and (10) show the first-order and the second-order models to be fitted to the ultraviolet irradiance model, considering $x_1 = I_{GH}$, $x_2 = \alpha$ and $x_3 = Cc$ both in the first-order and the second-order models. Equation (11) shows the first-order regression model fitted with the above three variables, and Equation (12) also shows the linear regression model fitted only for I_{GH} and solar altitude, i.e., eliminating cloud cover from the linear-regression model.

$$\begin{gathered} \mathbf{I_{UV} = -1.9243 + 0.0323 \cdot I_{GH} + 6.5892 * \alpha + 0.0035 \cdot Cc} \\ \left[\mathbf{R^2_{Training} = 98.83\%,\ nRMSE_{Training} = 7.29\%,\ nMBE_{Training} = 0.00\%}\right] \\ \left[R^2_{Test} = 98.82\%,\ nRMSE_{Test} = 7.36\%,\ nMBE_{Test} = 0.11\%\right] \end{gathered} \tag{11}$$

$$\begin{gathered} I_{UV} = -1.7224 + 0.0317 \cdot I_{GH} + 6.9531 \cdot \alpha \\ \left[R^2_{Training} = 98.82\%,\ nRMSE_{Training} = 7.32\%,\ nMBE_{Training} = 0.00\%\right] \\ \left[R^2_{Test} = 98.81\%,\ nRMSE_{Test} = 7.39\%,\ nMBE_{Test} = 0.11\%\right] \end{gathered} \tag{12}$$

Equation (13) shows the second-order model, with the three independent variables selected for ANN model 9, fitted to the data that are studied in this work.

$$\begin{gathered} I_{UV} = -1.8212 + 0.0167 \cdot I_{GH} + 19.0462 \cdot \alpha + 0.0126 \cdot Cc - 9.29 \cdot 10^{-6} \cdot I_{GH}^2 + 0.0188 \cdot I_{GH} \cdot \alpha + 8.80 \cdot 10^{-5} \\ \cdot I_{GH} \cdot Cc - 7.2559 \cdot \alpha^2 - 0.0958 \cdot \alpha \cdot Cc - 6.59 \cdot 10^{-5} \cdot Cc^2 \\ [R^2_{Training} = 99.43\%,\ nRMSE_{Training} = 5.06\%,\ nMBE_{Training} = 0.00\%] \\ [R^2_{Test} = 99.45\%, nRMSE_{Test} = 5.02\%,\ nMBE_{Test} = 0.06\%] \end{gathered} \tag{13}$$

A simpler model is shown in Equation (14), in which cloud cover is removed as an independent variable, which may be useful if cloud-cover data are unavailable.

$$\begin{array}{l} I_{UV} = -1.1625 + 0.0238 \cdot I_{GH} + 10.2243 \cdot \alpha - 1.27 \cdot 10^{-5} \cdot I_{GH}^2 + 0.0253 \cdot I_{GH} \cdot \alpha - 8.8361 \cdot \alpha^2 \\ [R^2_{Training} = 99.30\%,\ nRMSE_{Training} = 5.63\%,\ nMBE_{Training} = 0.00\%] \\ [R^2_{Test} = 99.32\%,\ nRMSE_{Test} = 5.60\%,\ nMBE_{Test} = 0.07\%] \end{array} \quad (14)$$

A study was also conducted on the use of k_t instead of I_{GH}. In this case, the values are shown below in Equations (15)–(18).

$$I_{UV} = -11.3956 + 22.8218 \cdot k_t + 24.3899 \cdot + 0.0021 \cdot Cc \quad (15)$$

$$\begin{array}{l} \left[\mathbf{R^2_{Training} = 93.18\%,\ nRMSE_{Training} = 17.57\%,\ nMBE_{Training} = 0.00\%}\right] \\ \left[\mathbf{R^2_{Test} = 93.01\%,\ nRMSE_{Test} = 17.95\%,\ nMBE_{Test} = 0.11\%}\right] \\ I_{UV} = -11.1581 + 22.5424 \cdot k_t + 24.4465 \cdot \alpha \end{array} \quad (16)$$

$$\begin{array}{l} \left[\mathbf{R^2_{Training} = 93.18\%,\ nRMSE_{Training} = 17.57\%,\ nMBE_{Training} = 0.00\%}\right] \\ \left[\mathbf{R^2_{Test} = 93.01\%,\ nRMSE_{Test} = 17.95\%,\ nMBE_{Test} = 0.11\%}\right] \\ \mathbf{I_{UV} = -0.3544 + 2.0833 \cdot k_t + 14.0893 \cdot \alpha - 0.0165 \cdot Cc - 9.0813 \cdot k_t^2 + 40.7916 \cdot k_t \cdot \alpha} \\ \mathbf{+ 0.0405 \cdot k_t \cdot Cc - 7.9650 \cdot \alpha^2 - 0.0170 \cdot \alpha \cdot Cc - 8.83 \cdot 10^{-5} \cdot Cc^2} \\ \left[\mathbf{R^2_{Training} = 99.39\%,\ nRMSE_{Training} = 5.26\%,\ nMBE_{Training} = 0.00\%}\right] \\ \left[\mathbf{R^2_{Test} = 99.40\%,\ nRMSE_{Test} = 5.24\%,\ nMBE_{Test} = 0.08\%}\right] \end{array} \quad (17)$$

Analogously to I_{GH}, the model in Equation (17), in which cloud cover as an independent variable is removed, is useful if the cloud-cover data are unavailable.

$$\begin{array}{l} \mathbf{I_{UV} = -2.7058 + 7.3586 \cdot k_t + 11.4945 \cdot \alpha - 10.8880 \cdot + 42.6023 \cdot k_t \cdot \alpha - 7.7515} \\ \mathbf{\cdot \alpha^2} \\ \left[\mathbf{R^2_{Training} = 99.30\%,\ nRMSE_{Training} = 5.63\%,\ nMBE_{Training}} = 0.00\%\right] \\ \left[R^2_{Test} = 99.32\%, nRMSE_{Test} = 5.62\%, nMBE_{Test} = 0.08\%\right] \end{array} \quad (18)$$

It can be observed that when quadratic terms are included in the regression models, the models containing k_t instead of I_{GH} led to similar results, with the models containing I_{GH} yielding somewhat better results. Therefore, in the case of using a second-order model, it may be preferable to use k_t in the formulation, as it gives an idea of the clearness of the sky, and the results are similar to using I_{GH}. The same is not true when using linear models, where the accuracy of considering k_t in the formulation worsens significantly, as can be seen when comparing Equations (15) and (16) with (11) and (12), which correspond to the first order models for k_t and I_{GH}, respectively. Therefore, the use of first-order models makes it preferable to introduce I_{GH} in the formulation, as the models with k_t yielded less accurate results.

Figures 8–10 show the response surfaces obtained with the second-order regression models shown in Equations (13) and (17), which correspond to the second-order regression models developed for I_{GH}, α, and cloud cover and for k_t, α, and cloud cover, respectively.

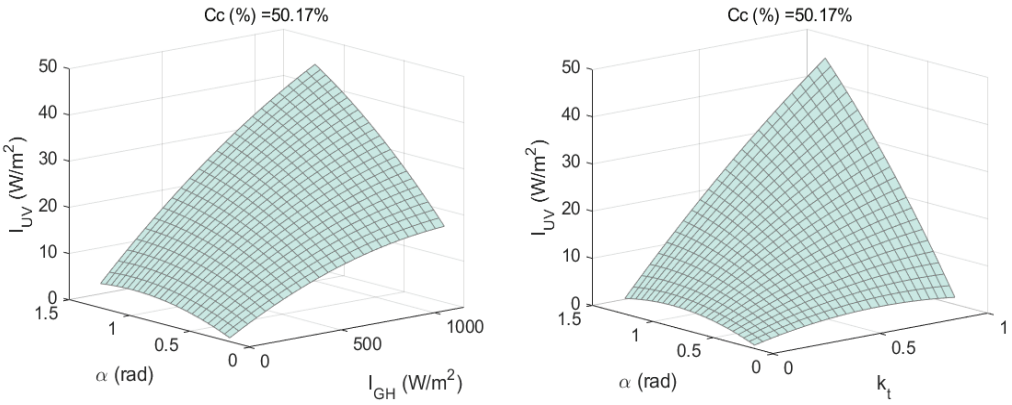

(**a**) (**b**)

Figure 8. (**a**) I_{UV} vs. $(\alpha, I_{GH})|_{Cc=constant}$ and (**b**) I_{UV} vs. $(\alpha, k_t)|_{Cc=constant}$.

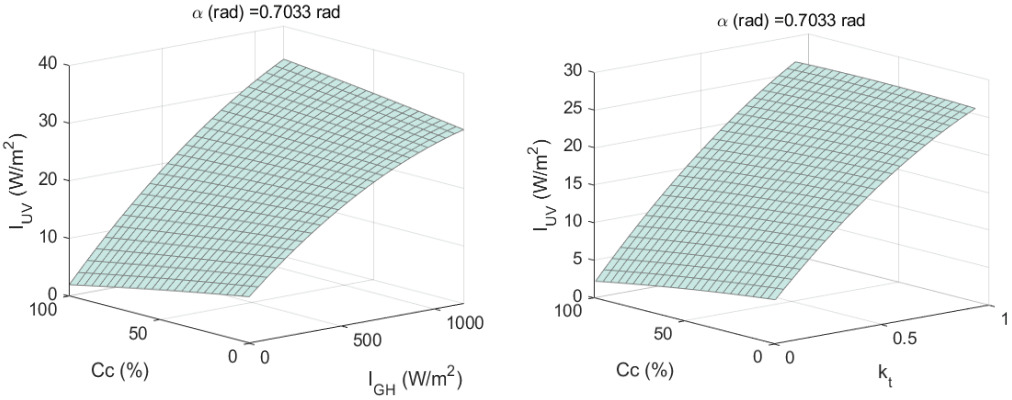

(**a**) (**b**)

Figure 9. (**a**) I_{UV} vs. $(Cc, I_{GH})|_{=constant}$ and (**b**) I_{UV} vs. $(Cc, k_t)|_{=constant}$.

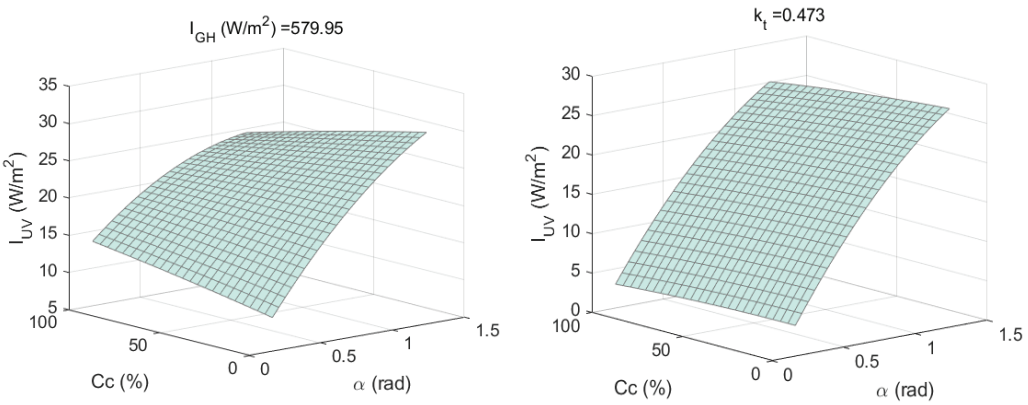

(**a**) (**b**)

Figure 10. (**a**) I_{UV} vs. $(Cc, \alpha)|_{I_{GH}=constant}$ and (**b**) I_{UV} vs. $(Cc, \alpha)|_{k_t=constant}$.

5. Conclusions

In the present work, different models have been analyzed for the determination of horizontal ultraviolet irradiance based on meteorological and radiative variables collected in Burgos (Spain), using supervised ANNs and regression models.

The ANN-based models presented higher accuracy in their predictions of horizontal ultraviolet irradiance than the regression-based models. Specifically, in the case of the selected model, which included I_{GH}, α, and Cc as independent variables, the datasets used to train the neural network and the test data yielded nRMSE readings of 4.30% and

4.24%, respectively. This ANN-based model was more accurate than the one obtained with the second-order regression model, which used the same variables and yielded nRMSE readings of 5.06% and 5.02% with the training and the test datasets, respectively.

It has also been observed that when quadratic terms were included in the regression models, the models containing k_t rather than I_{GH} yielded similar results, while the models containing I_{GH} were somewhat better. In the case of using the neural network with k_t, α and Cc as independent variables, nRMSE readings of 4.36% and 4.34% were obtained with the training and the test datasets, respectively. Analogously to the case of I_{GH}, the ANN-based model for k_t was more accurate than the model obtained for k_t with a second-order regression fit using the same variables yielding nRMSE readings of 5.26% and 5.24% for the training and the test datasets, respectively.

It may therefore be preferable to use k_t in the formulation in the case of using a second-order model, as it gives an idea of the clearness of the sky and the results are similar to those obtained when using I_{GH}. The same could not be said when using linear models, with which the accuracy when considering k_t in the formulation worsened significantly.

In the case that cloud cover measurements are not available, models 11 and 14 in Table 3, which have only two independent variables (α and I_{GH}) and (α and k_t), respectively, and which can be easily measured at most stations, present results with high nRMSE accuracy (5.13% in both cases); they can be useful for predicting ultraviolet radiation.The effectiveness of the above methods for modeling horizontal ultraviolet irradiance has been demonstrated, using a reduced number of variables, with the data analyzed in the present study.

Author Contributions: M.I.D.-V.: methodology, software, formal analysis, investigation, visualization. S.G.-R.: methodology, software, formal analysis, investigation, draft preparation; A.G.-R.: software, visualization; M.D.-M.: conceptualization, validation, original draft preparation, supervision, project administration; C.A.-T.: conceptualization, writing—review and editing; supervision, funding acquisition. All authors have read and agreed to the published version of the manuscript.

Funding: This research is a result of the project RTI2018-098900-B-I00 financed by the Spanish Ministry of Science and Innovation, project TED2021-131563B-I00 financed by MCIN/AEI/10.13039/501100011033 and the European Union "NextGenerationEU"/PRTR», and Junta de Castilla y León, under grant number INVESTUN/19/BU/0004.

Institutional Review Board Statement: Not applicable.

Informed Consent Statement: Not applicable.

Data Availability Statement: Copies of the original dataset used in this work can be downloaded from https://riubu.ubu.es/handle/10259/5512 (accessed on 11 November 2022).

Conflicts of Interest: The authors declare no conflict of interest.

Nomenclature

B_{sc}	Extraterrestrial irradiance constant (=1361.1 W/m^2)
Cc	Cloud cover (%)
D	Diffuse fraction
I_{BH}	Horizontal beam irradiance (W/m^2)
I_{DH}	Horizontal diffuse irradiance (W/m^2)
I_{GH}	Horizontal global irradiance (W/m^2)
I_{UV}	Horizontal ultraviolet irradiance (W/m^2)
k_t	Clearness index
m	Relative optical air mass
MBE	Mean bias error (%)
n	Number of data

RMSE	Root mean square error (%)
T	Temperature (°C)
$X_{measured}$	Measured variable
X_{model}	Predicted variable
Z	Solar zenith angle (rad)
α	Solar altitude angle (rad)
Δ	Sky brightness
ε	Sky clearness
ε_0	Average value of the orbital eccentricity of the Earth

References

1. Alados-Arboledas, L.; Alados, I.; Foyo-Moreno, I.; Olmo, F.J.; Alcántara, A. The Influence of Clouds on Surface UV Erythemal Irradiance. *Atmos. Res.* **2003**, *66*, 273–290. [CrossRef]
2. Hu, B.; Wang, Y.; Liu, G. Variation Characteristics of Ultraviolet Radiation Derived from Measurement and Reconstruction in Beijing, China. *Tellus Ser. B Chem. Phys. Meteorol.* **2010**, *62*, 100–108. [CrossRef]
3. Murillo, W.; Cañada, J.; Pedrós, G. Correlation between Global Ultraviolet (290–385 nm) and Global Irradiation in Valencia and Cordoba (Spain). *Renew. Energy* **2003**, *28*, 409–418. [CrossRef]
4. Human, S.; Bajic, V. Modelling Ultraviolet Irradiance in South Africa. *Radiat. Prot. Dosim.* **2000**, *91*, 181–183. [CrossRef]
5. Modenese, A.; Gobba, F.; Paolucci, V.; John, S.M.; Sartorelli, P.; Wittlich, M. Occupational Solar UV Exposure in Construction Workers in Italy: Results of a One-Month Monitoring with Personal Dosimeters. In Proceedings of the 2020 IEEE International Conference on Environment and Electrical Engineering and 2020 IEEE Industrial and Commercial Power Systems Europe (EEEIC/I&CPS Europe), Madrid, Spain, 9–12 June 2020; pp. 6–10. [CrossRef]
6. Ahmed, A.A.M.; Ahmed, M.H.; Saha, S.K.; Ahmed, O.; Sutradhar, A. Optimization Algorithms as Training Approach with Hybrid Deep Learning Methods to Develop an Ultraviolet Index Forecasting Model. *Stoch. Environ. Res. Risk Assess.* **2022**, *36*, 3011–3039. [CrossRef]
7. Al-Aruri, S.D. The Empirical Relationship between Global Radiation and Global Ultraviolet (0.290–0.385) μm Solar Radiation Components. *Sol. Energy* **1990**, *45*, 61–64. [CrossRef]
8. Modenese, A.; Bisegna, F.; Borra, M.; Burattini, C.; Gugliermetti, L.; Filon, F.L.; Militello, A.; Toffanin, P.; Gobba, F. Occupational Exposure to Solar UV Radiation in a Group of Dock-Workers in North-East Italy. In Proceedings of the 2020 IEEE International Conference on Environment and Electrical Engineering and 2020 IEEE Industrial and Commercial Power Systems Europe (EEEIC/I&CPS Europe), Madrid, Spain, 9–12 June 2020; pp. 16–21. [CrossRef]
9. Lamy, K.; Portafaix, T.; Brogniez, C.; Godin-Beekmann, S.; Bencherif, H.; Morel, B.; Pazmino, A.; Metzger, J.M.; Auriol, F.; Deroo, C.; et al. Ultraviolet Radiation Modelling from Ground-Based and Satellite Measurements on Reunion Island, Southern Tropics. *Atmos. Chem. Phys.* **2018**, *18*, 227–246. [CrossRef]
10. Serrano, M.A.; Cañada, J.; Moreno, J.C.; Gurrea, G. Solar Ultraviolet Doses and Vitamin D in a Northern Mid-Latitude. *Sci. Total Environ.* **2017**, *574*, 744–750. [CrossRef]
11. Leal, S.S.; Tíba, C.; Piacentini, R. Daily UV Radiation Modeling with the Usage of Statistical Correlations and Artificial Neural Networks. *Renew. Energy* **2011**, *36*, 3337–3344. [CrossRef]
12. Dahr, F.E.; Bah, A.; Ghennioui, A. Estimation of Ultraviolet Solar Irradiation of Semi-Arid Area—Case of Benguerir. In Proceedings of the 2020 International Conference on Electrical and Information Technologies (ICEIT), Rabat, Morocco, 4–7 March 2020; pp. 1–5. [CrossRef]
13. Zhang, X.; Hu, B.; Wang, Y.; Lu, J. Reconstruction of Daily Ultraviolet Radiation for Nine Observation Stations in China. *J. Atmos. Chem.* **2014**, *71*, 303–319. [CrossRef]
14. García-Rodríguez, S.; García, I.; García-Rodríguez, A.; Díez-Mediavilla, M.; Alonso-Tristán, C. Solar Ultraviolet Irradiance Characterization under All Sky Conditions in Burgos, Spain. *Appl. Sci.* **2022**, *12*, 10407. [CrossRef]
15. Foyo-Moreno, I.; Alados, I.; Olmo, F.J.; Alados-Arboledas, L. The Influence of Cloudiness on UV Global Irradiance (295–385 Nm). *Agric. For. Meteorol.* **2003**, *120*, 101–111. [CrossRef]
16. Foyo-Moreno, I.; Vida, J.; Alados-Arboledas, L. Ground Based Ultraviolet (290–385 Nm) and Broadband Solar Radiation Measurements in South-Eastern Spain. *Int. J. Climatol.* **1998**, *18*, 1389–1400. [CrossRef]
17. Foyo-Moreno, I.; Vida, J.; Alados-Arboledas, L. A Simple All Weather Model to Estimate Ultraviolet Solar Radiation (290–385 Nm). *J. Appl. Meteorol.* **1999**, *38*, 1020–1026. [CrossRef]
18. Bilbao, J.; Mateos, D.; de Miguel, A. Analysis and Cloudiness Influence on UV Total Irradiation. *Int. J. Climatol.* **2011**, *31*, 451–460. [CrossRef]
19. Barbero, F.J.; López, G.; Batlles, F.J. Determination of Daily Solar Ultraviolet Radiation Using Statistical Models and Artificial Neural Networks. *Ann. Geophys.* **2006**, *24*, 2105–2114. [CrossRef]
20. Jacovides, C.P.; Tymvios, F.S.; Boland, J.; Tsitouri, M. Artificial Neural Network Models for Estimating Daily Solar Global UV, PAR and Broadband Radiant Fluxes in an Eastern Mediterranean Site. *Atmos. Res.* **2015**, *152*, 138–145. [CrossRef]
21. Wang, L.; Gong, W.; Luo, M.; Wang, W.; Hu, B.; Zhang, M. Comparison of Different UV Models for Cloud Effect Study. *Energy* **2015**, *80*, 695–705. [CrossRef]

22. Wang, L.; Gong, W.; Li, J.; Ma, Y.; Hu, B. Empirical Studies of Cloud Effects on Ultraviolet Radiation in Central China. *Int. J. Climatol.* **2014**, *34*, 2218–2228. [CrossRef]
23. Habte, A.; Sengupta, M.; Gueymard, C.A.; Narasappa, R.; Rosseler, O.; Burns, D.M. Estimating Ultraviolet Radiation From Global Horizontal Irradiance. *IEEE J. Photovoltaics* **2019**, *9*, 139–146. [CrossRef]
24. Bilbao, J.; Román, R.; Yousif, C.; Pérez-Burgos, A.; Mateos, D.; de Miguel, A. Global, Diffuse, Beam and Ultraviolet Solar Irradiance Recorded in Malta and Atmospheric Component Influences under Cloudless Skies. *Sol. Energy* **2015**, *121*, 131–138. [CrossRef]
25. Antón, M.; Gil, J.E.; Cazorla, A.; Fernández-Gálvez, J.; Foyo-Moreno, I.; Olmo, F.J.; Alados-Arboledas, L. Short-Term Variability of Experimental Ultraviolet and Total Solar Irradiance in Southeastern Spain. *Atmos. Environ.* **2011**, *45*, 4815–4821. [CrossRef]
26. Lozano, I.L.; Sánchez-Hernández, G.; Guerrero-Rascado, J.L.; Alados, I.; Foyo-Moreno, I. Aerosol Radiative Effects in Photosynthetically Active Radiation and Total Irradiance at a Mediterranean Site from an 11-Year Database. *Atmos. Res.* **2021**, *255*, 105538. [CrossRef]
27. Liu, H.; Hu, B.; Zhang, L.; Zhao, X.J.; Shang, K.Z.; Wang, Y.S.; Wang, J. Ultraviolet Radiation over China: Spatial Distribution and Trends. *Renew. Sustain. Energy Rev.* **2017**, *76*, 1371–1383. [CrossRef]
28. Huang, M.; Jiang, H.; Ju, W.; Xiao, Z. Ultraviolet Radiation over Two Lakes in the Middle and Lower Reaches of the Yangtze River,,China: An Innovative Model for UV Estimation. *Terr. Atmos. Ocean. Sci.* **2011**, *22*, 491–506. [CrossRef]
29. Wang, L.; Gong, W.; Hu, B.; Feng, L.; Lin, A.; Zhang, M. Long-Term Variations of Ultraviolet Radiation in China from Measurements and Model Reconstructions. *Energy* **2014**, *78*, 928–938. [CrossRef]
30. Gueymard, C. *SMARTS2, A Simple Model of the Atmospheric Radiative Transfer of Sunshine: Algorithms and Performance Assessment*; Florida Solar Energy Center: Cocoa, FL, USA, 1995; pp. 1–78.
31. Behrang, M.A.; Assareh, E.; Ghanbarzadeh, A.; Noghrehabadi, A.R. The Potential of Different Artificial Neural Network (ANN) Techniques in Daily Global Solar Radiation Modeling Based on Meteorological Data. *Sol. Energy* **2010**, *84*, 1468–1480. [CrossRef]
32. Feister, U.; Junk, J.; Woldt, M.; Bais, A.; Helbig, A.; Janouch, M.; Josefsson, W.; Kazantzidis, A.; Lindfors, A.; Den Outer, P.N.; et al. Long-Term Solar UV Radiation Reconstructed by ANN Modelling with Emphasis on Spatial Characteristics of Input Data. *Atmos. Chem. Phys.* **2008**, *8*, 3107–3118. [CrossRef]
33. Junk, J.; Feister, U.; Helbig, A. Reconstruction of Daily Solar UV Irradiation from 1893 to 2002 in Potsdam, Germany. *Int. J. Biometeorol.* **2007**, *51*, 505–512. [CrossRef]
34. Teramoto, É.T.; Dos Santos, C.M.; Escobedo, J.F.; Dal Pai, A.; da Silva, S.H.M.G. Comparing Different Methods for Estimating Hourly Solar Ultraviolet Radiation: Empirical Models, Artificial Neural Network and Support Vector Machine. *Rev. Bras. Meteorol.* **2020**, *35*, 35–43. [CrossRef]
35. Alados, I.; Gomera, M.A.; Foyo-Moreno, I.; Alados-Arboledas, L. Neural Network for the Estimation of UV Erythemal Irradiance Using Solar Broadband Irradiance. *Int. J. Climatol.* **2007**, *27*, 1791–1799. [CrossRef]
36. Hoyer-Klick, C.; Beyer, H.G.; Dumortier, D.; Schroedter-Homscheidt, M.; Wald, L.; Martinoli, M.; Schillings, C.; Gschwind, B.; Menard, L.; Gaboardi, E.; et al. Management and Exploitation of Solar Resource Knowledge. In Proceeding of the EUROSUN 2008, 1st International Conference on Solar Heating, Cooling and Buildings, Lisbon, Portugal, 7–10 October 2008; pp. 1–7. [CrossRef]
37. Gueymard, C.A. Revised Composite Extraterrestrial Spectrum Based on Recent Solar Irradiance Observations. *Sol. Energy* **2018**, *169*, 434–440. [CrossRef]
38. Suárez-García, A.; Díez-Mediavilla, M.; Granados-López, D.; González-Peña, D.; Alonso-Tristán, C. Benchmarking of Meteorological Indices for Sky Cloudiness Classification. *Sol. Energy* **2020**, *195*, 499–513. [CrossRef]
39. Díez-Mediavilla, M.; Rodríguez-Amigo, M.C.; Dieste-Velasco, M.I.; García-Calderón, T.; Alonso-Tristán, C. The PV Potential of Vertical Façades: A Classic Approach Using Experimental Data from Burgos, Spain. *Sol. Energy* **2019**, *177*, 192–199. [CrossRef]
40. Gueymard, C.A. A Reevaluation of the Solar Constant Based on a 42-Year Total Solar Irradiance Time Series and a Reconciliation of Spaceborne Observations. *Sol. Energy* **2018**, *168*, 2–9. [CrossRef]
41. Mukaka, M. Statistics Corner: A Guide to Appropriate Use of Correlation in Medical Research. *Malawi Med. J.* **2012**, *24*, 69–71.

applied sciences

MDPI

Article

Ultraviolet Erythemal Irradiance (UVER) under Different Sky Conditions in Burgos, Spain: Multilinear Regression and Artificial Neural Network Models

S. García-Rodríguez [1], A. García-Rodríguez [1], D. Granados-López [1], I. García [1,2] and C. Alonso-Tristán [1,*]

[1] Research Group Solar and Wind Feasibility Technologies (SWIFT), Electromechanical Engineering Department, Universidad de Burgos, Escuela Politécnica Superior, 09006 Burgos, Spain; solgr@ubu.es (S.G.-R.); agrodriguez@ubu.es (A.G.-R.); dgranados@ubu.es (D.G.-L.); ignacio.garcia@unavarra.es (I.G.)

[2] Institute of Smart Cities (ISC), Engineering Department, Universidad Pública de Navarra, Campus Arrosadía, Pamplona 31006, Spain

* Correspondence: catristan@ubu.es or cristinaalonso.tristan@gmail.com; Tel.: +34-947-258853

Abstract: Different strategies for modeling Global Horizontal UltraViolet Erythemal irradiance (GHUVE) based on meteorological parameters measured in Burgos (Spain) have been developed. The experimental campaign ran from September 2020 to June 2022. The selection of relevant variables for modeling was based on Pearson's correlation coefficient. Multilinear Regression Model (MLR) and artificial neural network (ANN) techniques were employed to model GHUVE under different sky conditions (all skies, overcast, intermediate, and clear skies), classified according to the CIE standard on a 10 min basis. ANN models of GHUVE outperform those based on MLR according to the traditional statistical indices used in this study (R^2, MBE, and nRMSE). Moreover, the work proposes a simple all-sky ANN model of GHUVE based on usually recorded variables at ground meteorological stations.

Keywords: ultraviolet erythemal irradiance; UVER; statistical analysis; modeling; ANN; multilinear regression models

Citation: García-Rodríguez, S.; García-Rodríguez, A.; Granados-López, D.; García, I.; Alonso-Tristán, C. Ultraviolet Erythemal Irradiance (UVER) under Different Sky Conditions in Burgos, Spain: Multilinear Regression and Artificial Neural Network Models. *Appl. Sci.* **2023**, *13*, 10979. https://doi.org/10.3390/app131910979

Academic Editor: Harry Kambezidis

Received: 15 August 2023
Revised: 29 September 2023
Accepted: 2 October 2023
Published: 5 October 2023

1. Introduction

Ultraviolet radiation (UV) represents a small fraction of total solar radiation (5–7%) [1]. It is a highly energetic component of the solar spectrum that must be monitored as it can be detrimental to life on Earth [2], becoming the main risk factor for human health among photo-biological factors [3]. The UV region of the solar spectrum spans wavelengths between 100 and 400 nm, and it is divided into three components, i.e., UVA, UVB, and UVC. Although UVC radiation (100–280 nm) is entirely absorbed by atmospheric oxygen and ozone, a fraction of UVB (280–315 nm) and UVA (315–400 nm) reaches the Earth's surface as ozone partially absorbs these wavelengths [4]. Surface UV is also influenced by geographical parameters like altitude over the sea level and latitude [5].

UV radiation exerts significant effects on biological and photochemical processes [6], showing both beneficial and detrimental impacts. It has beneficial effects on humans, animals, plants, and the biosphere: while moderate doses of UV radiation enhance vitamin D synthesis, promote mental health, and reduce blood pressure [3,7,8], excessive exposure to UV radiation can cause cataracts, premature aging of the skin and skin cancer [1,9–11]. It also has negative effects on organisms, marine and terrestrial ecosystems, and certain building materials (paints and plastics) [12,13]. Ideally, there should be a balance in UV radiation exposure to reduce the adverse effects associated with too few or too high exposures [8].

The impacts of UV radiation on the skin have been commonly assessed using UV erythemal irradiance (UVER). In accordance with the ISO/CIE17166 : 2019(E) standard [14],

UVER is determined by applying a spectral weighting function known as the erythema spectral weighting function. This function quantifies the effectiveness of radiation at each wavelength (λ) to cause minimal erythema. The UVER value is obtained by weighting the spectral irradiance of the UV radiation at each wavelength using the corresponding erythema effectiveness factor and then summing up these weighted values for all wavelengths present in the source spectrum, as specified in the standard.

Due to the lack of UV and UVER sensors in many ground-based weather stations [15], these variables are often estimated from other radiometric or meteorological parameters. The effect of cloudiness on UVER has been analyzed for all-sky conditions. In overcast conditions and skies with low clouds, UVER decreases as cloudiness increases [16]. Cloud optical thickness and UVER radiation have an exponential dependence, with higher attenuation occurring in low clouds [17]. Therefore, the solar zenith angle (θ_z) is one of the most influential parameters in the variation of UVER [18]. As θ_z increases, there is a corresponding decrease in UVER [16,19]. Notably, a reduction of up to 40% is observed when the zenith angle increases from 20° to 50° [19].

The relationship between UVER, relative optical air mass, and atmospheric clearness has been analyzed, concluding that atmosphere transmissivity to UVER exhibits higher sensitivity to changes in atmospheric clearness compared to variations in the total ozone column (TOC) [20].

Previous research has assessed the effect of ozone on UVER, revealing that higher ozone levels lead to a decrease in UVER due to the ozone absorption band within the UV range [18,21]. The dependence of UVER on ozone is influenced by the variation of the zenith angle [13]. The influence of TOC on UVER is considerably smaller under overcast skies than under clear skies [22].

Different mathematical models have been developed to model UVER as a function of different meteorological variables. Empirical and radiative transfer models have been used to correlate UV radiation, solar broadband radiation, and atmospheric parameters (cloudiness, TOC, aerosols) [12,18,19,23–26]. Linear regressions (LR) have analyzed the effect of some geometric and atmospheric parameters on the ratio between global horizontal UV erythemal irradiance (GHUVE) and global horizontal irradiance (GHI). The aerosol load, TOC, and precipitable water exhibit a linear relationship with respect to GHUVE/GHI while θ_z and clearness index, k_t, defined as the ratio of GHI over the corresponding extraterrestrial irradiance, exhibit exponential and polynomial behaviors, respectively [27]. Additionally, LR was employed to analyze the GHUVE/GHI ratio at various altitudes, revealing a strong correlation between these variables. The determination coefficient (R^2) exhibits an increasing trend with higher altitudes [12].

In recent years, the use of machine learning (ML) algorithms for modeling climatic and meteorological data has become widespread [28]. These algorithms allow us to solve complex problems with higher performance than classical modeling [29]. Among the ML techniques, Artificial Neural Networks (ANN) are particularly noteworthy as they act as "black boxes" that establish mathematical relationships between the inputs and the output data without prior knowledge of the specific relationship (linear or nonlinear) existing between them [30]. Numerous researchers have used ANNs to calculate UVER, using GHI as main input [31–36] regardless of the characteristics of the other variables used. Table 1 shows an overview of the variables used in different studies to estimate UVER and the ratio UVER/GHI from ANN, LR, and multilinear regressions (MLR). Notably, GHI and TOC [31,34–36] have been used as the most used inputs in conjunction with other variables in all cases.

Table 1. Studies to estimate UVER ratio around the world.

Ref.	Location	Model	Meteorological Variables	Models	Data Granularity
[37]	Spain	UVER	m, TOC, VIS, latitude, cloudiness	ANN	3 h
[31]	Spain	UVER	m, TOC, k, k_b, k_t	ANN	30 min
[38]	Spain	UVER	TOC, cloudiness, AOD	MLR	1 min
[27]	Thailand	UVER/GHI	θ_z, AOD, TOC, k_t, precipitable water	LR	10 min
[39]	Korea	UVER/GHI	CC, AOD, SCD	MLR	10 min
[40]	Spain	UVER	m, TOC,k_t	LR	30 min
[34]	Germany	UVER	GHI, DHI, SD, TOC, VIS, θ_z	ANN	daily
[35]	European Sites	UVER UVER/GHI	SD, GHI, DHI, θ_z, CC, TOC,VIS, Month, snow weight, Albedo.	ANN	30 min
[36]	Serbia	UVER	GHI, cloudiness, m, k_t, TOC	ANN	10 min
[12]	Argentina	UVER/GHI	GHI, θ_z, k_t, altitude	LR	1 min

m : relative optical air mass, TOC: total ozone column, VIS: horizontal visibility, SCD : ozone slant column density, θ_z: solar zenith angle, AOD: aerosol optical depth, CC: cloud cover, GHI: global irradiation, DHI: diffuse irradiation, SD: sunshine duration

The main objective of this work is to develop mathematical models using different strategies for UVER from meteorological parameters measured in Burgos (Spain) during an extensive experimental campaign run from September 2020 to June 2022. After selecting the variables based on the Pearson correlation coefficient, both MLR and ANN techniques were employed to model GHUVE under different sky conditions, including all skies, overcast, intermediate, and clear skies, classified according to ISO/CIE standard sky classification [41]. It is important to highlight that the variables used in the models developed in this study were experimental variables typically recorded in terrestrial facilities that underwent the strictest quality controls. The use of variables from satellite observations or additional databases was discarded due to their different sampling frequency and to guarantee, as far as possible, the applicability of locally obtained models in other emplacements using only ground meteorological data.

The work is structured as follows: in Section 2, the experimental data used for modeling are described and analyzed, along with the criteria ensuring their quality. Section 3 presents the feature selection process based on the Pearson criterion. A complete discussion of the results is shown in Section 4. Finally, Section 5 presents the key findings and main conclusions obtained from this study.

2. Experimental Data and Quality Control

The SWIFT Research Group ground meteorological facility, located on the flat roof of the Higher Polytechnic School of the University of Burgos (42°21′04″ N, 3°41′20″ W, 856 m a.s.l.), and shown in Figure 1, has provided the experimental data used for this study, in a 10 min basis, with an average scanning granularity of 30 s, recorded from September 2020 to June 2022.

Various climatic parameters were recorded, including air temperature (T), relative humidity (RH), wind speed (WS), and direction. GHI and Diffuse Horizontal Irradiance (DHI) were measured with Hulseflux pyranometers (model SR11) and Direct Normal Irradiance (DNI) by means of a Hulseflux pyrheliometer (model DR01). A GEONICA-SEMS-3000 sun tracker equipped with a shading disc was employed for the measurement of DHI. Additionally, the pyrheliometer was mounted on the sun tracker to measure DNI. GHUVE values were obtained with a Kipp and Zonnen SUV-E radiometer. Sky luminance and radiance distributions, used to classify the sky condition, were determined with a sky-scanner EKO MS-321LR. The cloud cover (CC) was calculated with a commercial all-sky camera (SONAD201D) that records every 1 s an RGB color image with 1158 × 1172 pixels of resolution. A complete description of the experimental facility and instruments can be found in previous works [42,43].

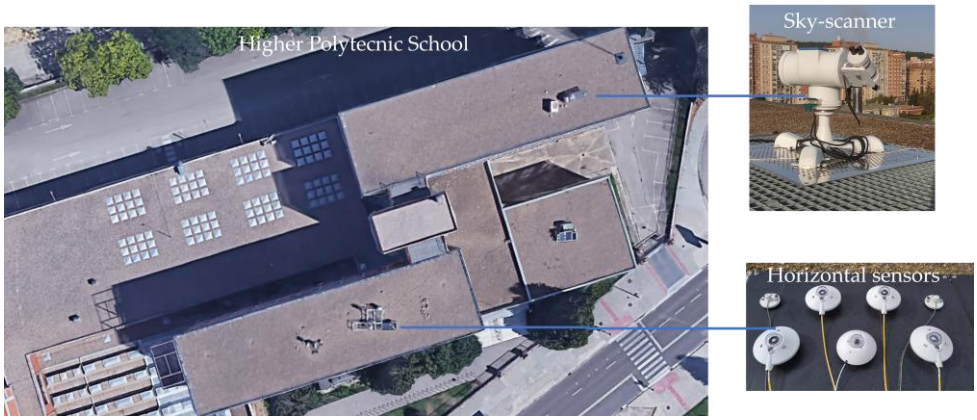

Figure 1. Experimental facility used in this study (Higher Polytechnic School, University of Burgos, Spain).

The collected GHI, GHUVE, DHI, and DNI data underwent the quality control procedure recommended by the MESoR project [44]. For the GHUVE data, it was determined that GHUVE values should not exceed the corresponding extraterrestrial UVER on the horizontal plane ($UVEH_0$). The calculation of $UVEH_0$ involved applying a correction factor (f_c), which considered the estimated orbital eccentricity to the UVER solar constant (UVE_{sc}) multiplied by the cosine of the solar zenith angle (θ_z), as described in Equation (1).

$$UVEH_0 = f_c \cdot UVE_{sc} \cdot \cos\theta_z \quad (1)$$

In the absence of a standardized value, UVE_{sc} was determined by integrating the product of the extraterrestrial solar spectrum [45] and the erythema spectral weighting function [14] over the wavelength range of 280 to 400 nm. This calculation yielded a value of 14.5 $W \cdot m^{-2}$. Data points corresponding to solar elevation angles below 5° were excluded from the analysis to mitigate the cosine response issues inherent to the GHI, and GHUVE measurement instruments.

A summary of the variables used in this study is shown in Table 2. Among these meteorological variables, the following were directly obtained from the experimental measurements: GHI, DHI, DNI, CC, RH, T, and WS. θ_z, and ψ were calculated. The remaining variables, including diffuse fraction, D [46], k_t [47], k'_d, Perez´s brightness factor (Δ) [48], and Perez´s clearness index, ε [48], were calculated using the equations described in Table 2.

The skies of the city of Burgos have been classified according to the ISO/CIE standard [41], which considers the angular distribution of luminance in the sky measured by the sky scanner. The sky is classified into 15 different types, where types 1 to 5 are considered overcast skies, types 6 to 10 are categorized as intermediate skies, and sky types 11 to 15 are identified as clear skies. A complete description of the ISO/CIE classification according to 15 types based on sky scanner measurements can be found in previous works [42,43].

Figure 2a illustrates the frequency of occurrence (FOC) of each ISO/CIE standard sky type during the experimental campaign. Clear skies predominate in Burgos, with the most frequent sky type being classified as 13 (cloudless polluted with a wider solar corona). This sky type exceeds the 20% of all observed skies. When only the three main sky categories are considered, as shown in Figure 2b (overcast, intermediate, and clear), clear skies have the highest FOC (higher than 45%). This fact concurs with findings from previous studies conducted in Burgos [28].

Table 2. Variables measured and calculated in Burgos.

Variables.	Meteorological Variables	Expression
GHI	Global Horizontal irradiance	measured
DHI	Diffuse Horizontal irradiance	measured
DNI	Direct Normal irradiance	measured
CC	Cloud cover	measured
RH	Relative Humidity	measured
T	Air temperature	measured
WS	Wind speed	measured
ψ	Solar azimuth angle	calculated
θ_z	Solar zenith angle	calculated
D	Diffuse fraction	$D = \frac{DHI}{GHI}$
k_t	Clearness index	$k_t = \frac{GHI}{B_{sc} f_c \cos\theta_z}$
k_d	Diffuse to extraterrestrial irradiance	$k_d = \frac{DHI}{B_{sc}}$
Δ	Perez´s brightness factor	$\Delta = \frac{m \cdot DHI}{B_{sc} \cdot f_c \cdot \cos\theta_z}$
ε	Perez´s clearness index	$\varepsilon = \frac{\frac{DHI+DNI}{DHI} + k(\theta_z)^3}{1+k(\theta_z)^3}$

B_{sc} is the solar constant (1361.1 W·m^{-2} [49]). f_c is the average value of the orbital eccentricity of the Earth. $k = 1.04$ (or $5.56 \cdot 10^{-6}$ if θ_z is expressed in degrees).

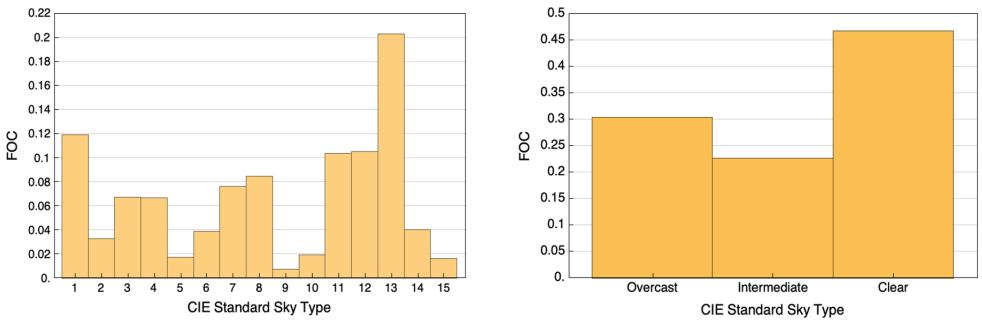

(**a**) (**b**)

Figure 2. Frequency of occurrence (FOC) in Burgos (Spain) (**a**) of each ISO/CIE standard sky type, and (**b**) for each ISO/CIE sky type group.

The box and whisker plot of Figure 3 shows the distribution of the GHUVE/GHI ratio based on 10 min data grouped by UTC hours, calculated from sunrise to sunset, using the complete database of the experimental campaign. The graph presents various statistical measures, including the mean value (gray crosses), the median (white lines inside the box), the interquartile range (the limits of the boxes), and both the maximum and minimum data values (the extreme whiskers), as well as the outlier values (black and gray circles). It can be observed that the hourly mean and median values of GHUVE/GHI gradually increased until noon (12 : 00 h) and then decreased until sunset. Higher dispersion of the values in the central hours of the day (10 : 00 h to 14 : 00 h) may be observed, as shown by the interquartile range (around $9 \cdot 10^{-3}$%). The maximum value ($4.2 \cdot 10^{-2}$%) is reached at 12 : 00 h UTC.

Figures 4 and 5 show the statistical analysis of the 10 min data of the GHUVE/GHI ratio grouped by month and season, respectively. Figure 4 reveals a gradual increase of GHUVE/GHI until May, followed by practically constant values until August, and then a decrease for the rest of the year. The interquartile range fluctuated between $3 \cdot 10^{-3}$% and $1.2 \cdot 10^{-2}$% and the standard deviation ranged between $3 \cdot 10^{-3}$% and $7 \cdot 10^{-3}$%. During the months from May to August, the ratio exhibited the greatest dispersion of the measurement campaign, with interquartile ranges around $1.1 \cdot 10^{-2}$% and standard

deviations around $6 \cdot 10^{-3}$%. The maximum value was recorded in July ($4.2 \cdot 10^{-2} \cdot$ %), while the minimum was reached in April ($1 \cdot 10^{-3}$%).

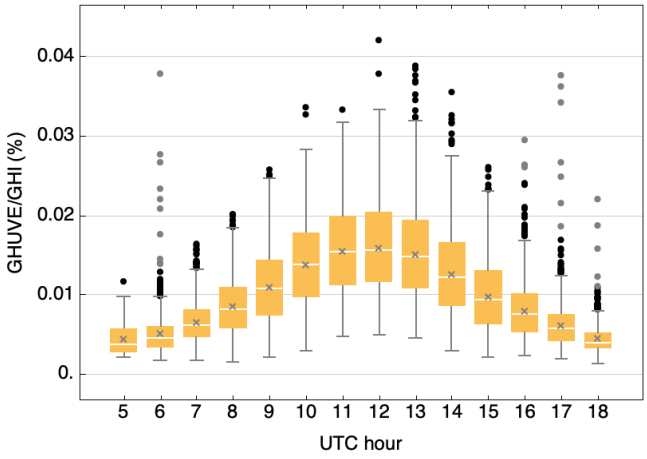

Figure 3. Box and whisker plot of the GHUVE/GHI ratio based on 10 min data grouped by UTC hours. Gray crosses indicate the mean, and the white lines inside the box indicate the median. The limits of the boxes define the first, second, and third quartiles, whereas the extreme whiskers show the minimum and the maximum points. Black and gray circles represent outliers.

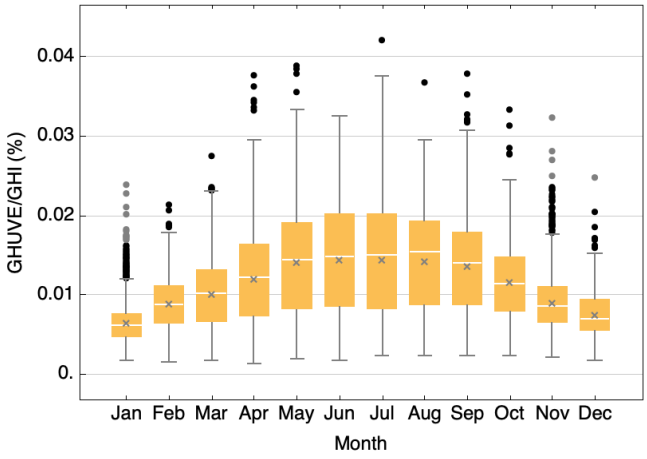

Figure 4. Box and whisker plot of the GHUVE/GHI ratio based on 10 min data grouped by months.

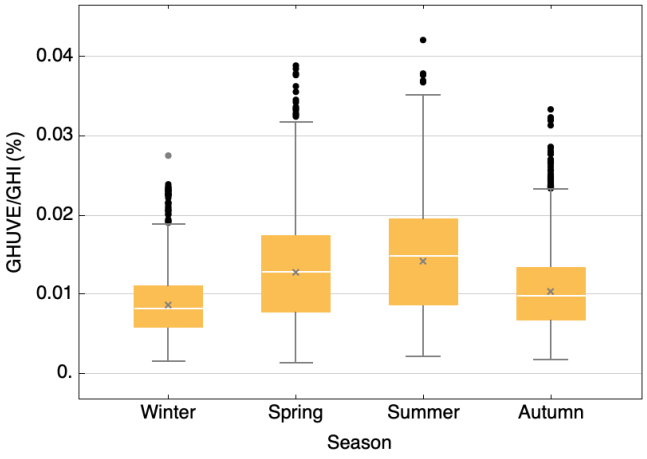

Figure 5. Box and whisker plot of the GHUVE/GHI ratio based on 10 min data grouped by seasons.

Figure 5 shows the greatest dispersion of values for the summer months and the highest value of the GHUVE/GHI ratio. Conversely, the dispersion of values in winter was relatively smaller. The interquartile ranges were $1.1 \cdot 10^{-2}$% and $5 \cdot 10^{-3}$% with standard deviations of $6 \cdot 10^{-3}$% and $4 \cdot 10^{-3}$%, respectively.

Upon analyzing the GHUVE/GHI ratio based on the 15 ISO/CIE sky types (Figure 6), it is evident that sky type 15 exhibits the highest ratio value and the lowest data dispersion. Conversely, sky type 12 demonstrates the lowest ratio value, with an average level of data dispersion. Notably, both sky types belong to the category of clear skies.

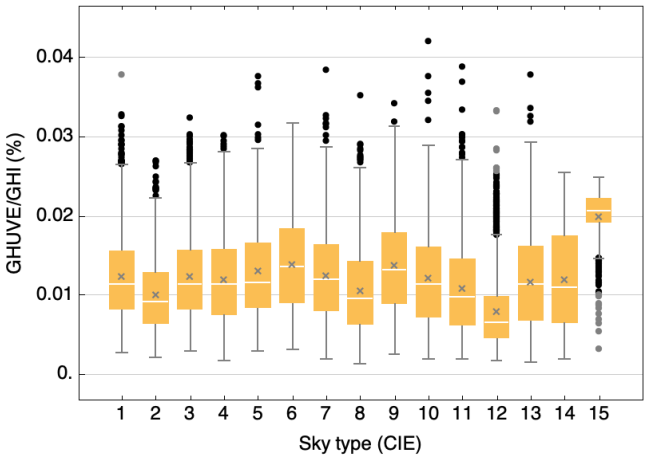

Figure 6. Box and whisker plot of the GHUVE/GHI standard sky type (1 to 15).

Figure 7 shows that the variation between the mean $\left(1.1 \cdot 10^{-2} - 1.2 \cdot 10^{-2}\%\right)$ and the dispersion (interquartile range: $8 \cdot 10^{-3} - 9 \cdot 10^{-3}$%, standard deviation: $5 \cdot 10^{-3} - 6 \cdot 10^{-3}\%$) of the three main ISO/CIE sky types is very similar.

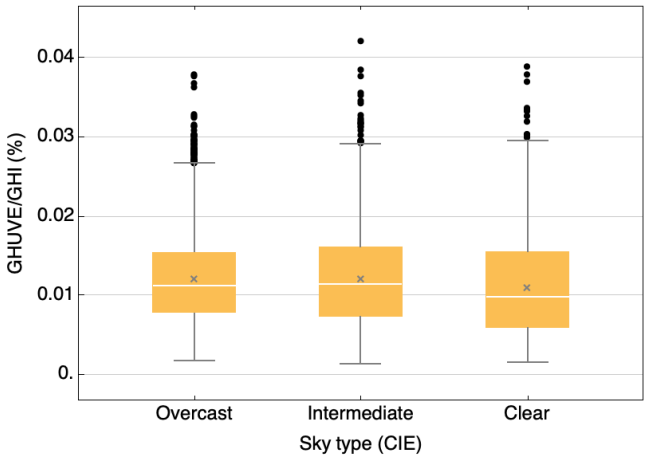

Figure 7. Box and whisker plot of the GHUVE/GHI ratio based on 10 min data grouped by sky type group (overcast, intermediate, clear).

3. Methodology

3.1. Feature Selection

Feature selection (FS) identifies the features that are related within a dataset, and it allows the elimination of irrelevant or unimportant features that contribute little or nothing to the definition of the target variable, providing more accurate models. This technique increases the performance of the developed model, improving its accuracy and reducing its complexity and overfitting, as well as its execution time.

In this study, to determine the most relevant meteorological variables for the estimation of UVER, a selection of variables was performed based on the Pearson correlation

coefficient (r), and the following rules: if GHUVE and one selected variable have a very weak relationship, the Pearson coefficient is 0; the relationship is very strong when r is close to 1 (direct correlation) or −1 (inverse correlation). To facilitate the assessment of correlation strength, the Thumb rule [50] established five r intervals for the correlation: direct $(1 \geq |r(\text{GHUVE, variable})| \geq 0.9)$, strong $(0.9 > |r(\text{GHUVE, variable})| \geq 0.7)$, moderate $(0.7 > |r(\text{GHUVE, variable})| \geq 0.5)$, weak $(0.5 > |r(\text{GHUVE, variable})| \geq 0.3)$, and negligible $(|r(\text{GHUVE, variable})| < 0.3)$.

Table 3 shows the various intervals of Pearson's coefficients calculated for the different meteorological variables. It can be observed that GHI exhibits a very strong and direct influence on GHUVE for all-skies, overcast, and clear skies, while for intermediate skies, GHI is strongly correlated. In clear skies, θ_z is also very strong and is inversely correlated with GHUVE, while for all-skies, overcast, and intermediate skies, this variable is strongly correlated. Likewise, in the case of all-sky types, k_t, D, ε, RH, DNI, and T have a moderate relationship with GHUVE. When analyzing overcast skies, a direct and strong relationship with k_d and DHI is observed, and a moderate relation with k_t, D, Δ, DNI. For intermediate skies, the relation between GHUVE and k_t, k_d, D, DHI, and DNI is moderate. WS, ψ, and CC present a negligible relation with GHUVE, so these meteorological variables were discarded as inputs for modeling GHUVE. These findings agree with the literature, which identifies GHI and θ_z as the two variables that strongly influence GHUVE measurements [18,19,31]. Meteorological variables whose relationship with GHUVE is moderate, strong, or very strong $(r \geq 0.5)$ have been selected.

Table 3. Pearson's coefficients were calculated for the different variables.

			|r(GHUVE,Variable)|.		
CIE Sky Type	**[1–0.9]**	**(0.9–0.7]**	**(0.7–0.5]**	**(0.5–0.3]**	**(0.3,0]**
All-sky	GHI	θ_z	k_t, D, ε, RH, DNI, T	k_d, DHI	Δ, WS, ψ, CC
Overcast	GHI	θ_z, k_d, DHI	k_t, D, DNI, Δ,	ε, RH, T	WS, ψ, CC
Intermediate	-	GHI, θ_z	k_t, k_d, D, DHI, DNI	ε, RH, T	Δ, WS, ψ, CC
Clear	GHI, θ_z	-	T	k_t, k_d, D, ε, RH, DNI	Δ, DHI, WS, ψ, CC

3.2. Multilinear Regression Model

Meteorological variables selected in Section 3.1 were used as input variables for both MLR and ANN models. Four MLR models were developed: one for all skies and three additional specific models for the clear, intermediate, and overcast sky types. To develop the MLR models, the data were divided into two groups: the first group, comprising 85% of the data, was used for model fitting, and the remaining 15% of the data was used for model validation. Conventional statistics were employed to evaluate the adequacy of fit for each model: coefficient of determination (R^2), normalized root mean square error (nRMSE) and normalized mean bias error (nMBE), calculated by Equations (2)–(4), respectively.

$$R^2 = \frac{\sum_{i=1}^{n} \left(GHUVE_{mod} - \overline{GHUVE}_{mod}\right) \cdot \left(GHUVE_{exp} - \overline{GHUVE}_{exp}\right)}{\sqrt{\sum_{i=1}^{n} \left[\left(GHUVE_{mod} - \overline{GHUVE_{mod}}\right)^2 \cdot \left(GHUVE_{exp} - \overline{GHUVE_{exp}}\right)^2\right]}} \quad (2)$$

$$nRMSE = \frac{1}{\overline{GHUVE}_{exp}} \sqrt{\frac{\sum_{i=1}^{n} \left(GHUVE_{mod} - GHUVE_{exp}\right)^2}{n}} 100(\%) \quad (3)$$

$$nMBE = \frac{1}{\overline{GHUVE}_{exp}} \frac{\sum_{i=1}^{n} \left(GHUVE_{mod} - GHUVE_{exp}\right)}{n} 100(\%) \quad (4)$$

where n represents the number of experimental data points used for model fitting and testing in each case; $GHUVE_{exp}$ is the experimental value of GHUVE, and $GHUVE_{mod}$ is the modeled GHUVE value.

The mathematical expressions of the four regression models and the goodness of fit of each one are shown in Table 4. The model's fitting results presented a high determination coefficient with the experimental data ($R^2 > 0.92$); however, the nRMSE values obtained through multilinear regressions exceeded 20% in all cases.

Table 4. Multilinear regression (MLR) models of GHUVE and goodness of fit (based on 85% of data).

Sky Types	MLR Model	R^2	nRSME(%)	nMBE (%)
All skies	$GHUVE = 1.90{\cdot}10^{-2} + 2.35{\cdot}10^{-4}GHI - 1.74{\cdot}10^{-2}\theta_z - 9.85{\cdot}10^{-2}k_t + 7.44{\cdot}10^{-4}T$	0.937	25.60	$-2.05{\cdot}10^{-1212}$
Overcast	$GHUVE = 2.98{\cdot}10^{-2} + 1.61{\cdot}10^{-4}GHI - 2.71{\cdot}10^{-2}\theta_z + 1.30k_d - 9.89{\cdot}10^{-4}DHI$	0.926	29.80	$6.92{\cdot}10^{-13}$
Intermediate	$GHUVE = 8.54{\cdot}10^{-2} + 2.59{\cdot}10^{-4}GHI - 6.98{\cdot}10^{-2}\theta_z - 1.80{\cdot}10^{-4}DHI - 9.91{\cdot}10^{-5}DNI$	0.934	22.49	$3.23{\cdot}10^{-12}$
Clear	$GHUVE = 1.75 \cdot 10^{-1} + 5.84 \cdot 10^{-5}GHI - 1.52 \cdot 10^{-1}\theta_z + 6.89 \cdot 10^{-4}T$	0.940	21.10	$9.87{\cdot}10^{-13}$

3.3. Artificial Neural Network Model

In this work, ANNs were used to estimate GHUVE through the Levenberg–Marquardt Back-Propagation (LMBP) algorithm. The ANN architecture adopted for this purpose consists of a single hidden layer and a single output, as outlined in a previous publication [28,29]. In the input layer, each neuron is a meteorological variable. Determining the optimal number of neurons in the hidden layer is currently unknown, but it is acknowledged that this number should not exceed the number of neurons in the preceding layer [51]. Therefore, if the input layer has only one variable and thus a single neuron, the hidden layer can have only one neuron. If the input layer has two meteorological variables, the hidden layer can have either one or two neurons. Similarly, if the input has three variables and, therefore, three neurons, the hidden layer can have three, two, or one neuron/s, and this trend continues for additional variables in the input layer. The iterative process and the fitting are explained elsewhere [28].

Four ANN models were generated and tested in this work, one for all skies and three for each sky type (clear, intermediate, and overcast), considering the selected meteorological variables shown in Table 3. Table 5 shows the goodness of fit for each ANN model according to the described statistics. It can be observed that in four cases, a good determination coefficient was obtained, $R^2 > 0.95$. The nRSME obtained varied between 11.9% and 21.3%. The best results were obtained for clear skies ($R^2 > 0.98$ and nRMSE < 12%).

Table 5. Goodness of fit of the ANN models (based on 85% of data).

Sky Condition	R^2	nRMSE (%)	nMBE (%)
All skies (MLR1)	0.988	14.36	$6.69 \cdot 10^{-2}$
Overcast	0.962	21.32	$6.69 \cdot 10^{-2}$
Intermediate	0.955	18.68	$9.09 \cdot 10^{-2}$
Clear	0.981	11.92	$7.59 \cdot 10^{-3}$

4. Results and Discussion

The remaining 15% of the data, not used previously for generating the MLR and ANN models, were used as a validation set for both MLR and ANN models. The results are shown in Table 6, with MLR outcomes on the left and ANN results on the right. The best results were obtained for clear skies ($R^2 > 0.97$, and nRMSE < 12.4%). Both nRMSE and nMBE values obtained through multilinear regressions exceeded 20% in all cases, results

close to those obtained by other authors [2] who performed models using second-degree polynomials, obtaining nRMSE values between 20% and 54%. Previous works modeled hourly [31] and daily [34–37] GHUVE values through ANN obtaining nRMSE ranging from 14 and 21%. Considerable improvement in performances occurred when the highly influential parameter TOC was introduced as ANN input.

Table 6. Goodness of fit of MLR and ANN models (based on 15% of data).

Sky Condition	R^2	nRSME (%)	nMBE (%)	Sky Condition	R^2	nRSME (%)	nMBE (%)
All skies (MLR1)	0.938	25.21	$1.41 \cdot 10^{-1}$	All skies (ANN1)	0.979	14.63	$1.55 \cdot 10^{-1}$
Overcast (MLR2)	0.930	29.65	$6.28 \cdot 10^{-1}$	Overcast (ANN2)	0.965	21.06	$6.58 \cdot 10^{-1}$
Intermediate (MLR3)	0.923	23.57	$-5.75 \cdot 10^{-1}$	Intermediate (ANN3)	0.953	19.20	$3.38 \cdot 10^{-1}$
Clear (MLR4)	0.942	20.57	$-2.10 \cdot 10^{-1}$	Clear (ANN4)	0.979	12.35	$4.31 \cdot 10^{-1}$

Table 6 comparison revealed that ANN models performed better than MLR models. For all skies and clear skies, the nRMSE value improved significantly, decreasing over 40% with respect to the MLR models. The nMBE value was overestimated for intermediate and clear skies.

Figures 8 and 9 compare the modeled GHUVE values from derived MLR models and ANN models, respectively, and the corresponding experimental GHUVE measurements obtained from the Burgos meteorological station using the referred validation data set. A good determination coefficient was obtained ($R^2 > 0.92$, MRL models, $R^2 > 0.95$ ANN models) both for all skies, overcast, intermediate, and clear sky conditions.

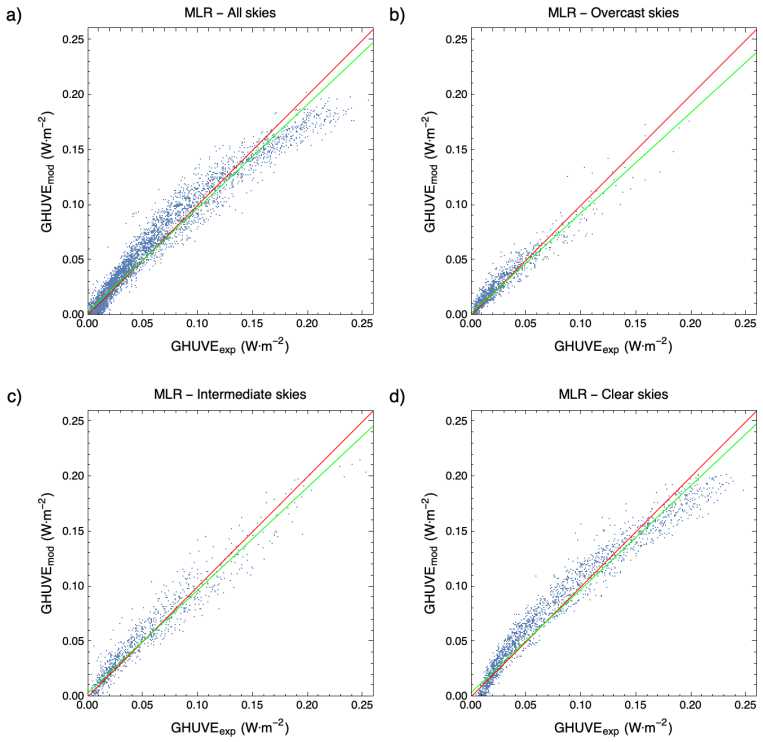

Figure 8. Comparison between calculated ($GHUVE_{mod}$) from MLR models and experimental $GHUVE_{exp}$ data under different sky conditions: (**a**) all skies, (**b**) overcast, (**c**) partial, and (**d**) clear skies. The green line represents the fitting line; the red line represents the x = y line.

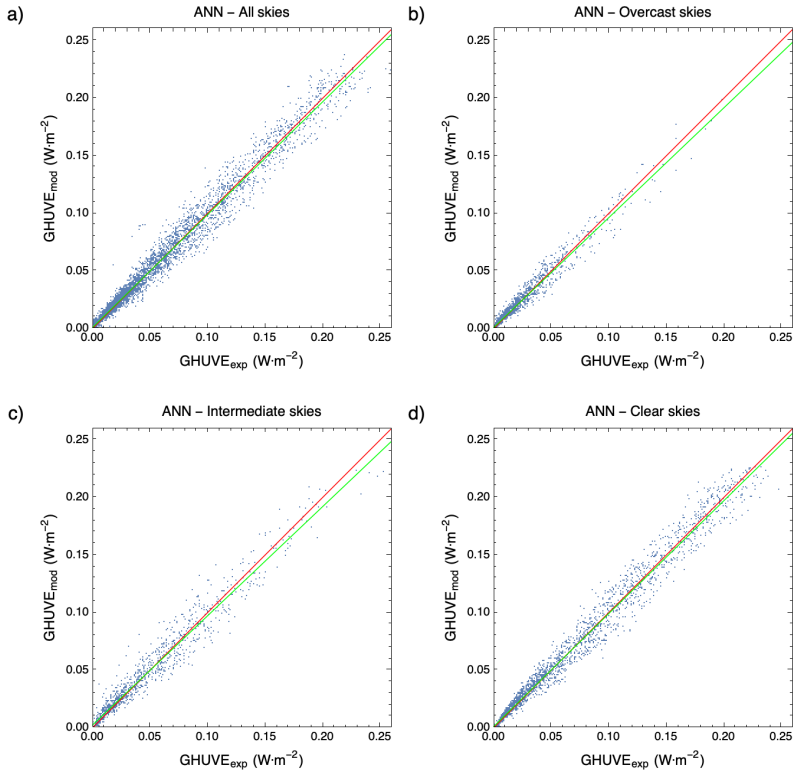

Figure 9. Comparison between calculated ($GHUVE_{mod}$) from ANN models and experimental $GHUVE_{exp}$ data under different sky conditions: (**a**) all skies, (**b**) overcast, (**c**) partial, and (**d**) clear skies. The green line represents the fitting line; the red line represents the x = y line.

To improve the previous results, a new approach was introduced to optimize the number of variables for minimizing nRMSE using ANN models for all-sky conditions. The number of neurons in the hidden layer can be adjusted accordingly to accommodate the complexity and dimensionality of the input data, from one neuron to the number of input variables of the ANN.

The two variables identified as strongly correlated to GHUVE based on Pearson's coefficient, as shown in Table 3, GHI and θ_z, were used as reference in this study. The ANN with two neurons in the hidden layer, with GHI and θ_z as input variables presented nRMSE of 17.02%, as shown in Table 7. By retaining GHI and θ_z as input variables, new ANN models were generated, increasing one by one the number of variables included in Table 2 and, consequently, the number of neurons in the hidden layer, from one neuron to as many neurons as the number of variables in each case.

Table 7. nRMSE for ANN model (GHI, θ_z) calculated with one and two neurons.

All-Skies	**nRMSE(%)**	
	One neuron	Two neurons
GHI, θ_z	18.65	17.02

Table 8 shows the percentage of GHUVE ANN models resulting from combinations of input variables out of the total of possible combinations for each case, whose nRMSE was below 15%. For the combination of five variables, with two to five neurons in the hidden layer, nRMSE $< 15\%$ was obtained for 5%, 25%, 28%, and 30% of the generated ANNs, respectively. For the combination of six variables, from two neurons to six neurons, nRMSE $< 15\%$ was obtained for the range $22 - 57\%$ of the generated ANN models.

Table 8. Percentage of generated GHUVE ANN models, according to number of input variables and number of neurons, with nRSME $< 15\%$..

	Number of Input Variables			
Number of neurons in the hidden layer	**3**	**4**	**5**	**6**
1	0	0	0	0
2	0	2	5	22
3	8	14	25	27
4		18	28	41
5			30	48
6				57

Table 9 shows the combinations of five and six input variables ranging from two to six neurons in the ANN hidden layer, which estimated the lowest nRMSE. Among the various ANN models considered, despite its slightly higher error, Model 2 was considered the optimal model due to the use as input data variables that are commonly measured at ground radiometric stations. The practical advantage of this model lies in the accessibility and availability of GHI, θ_z, T, k_t, and ψ data, making it easier to implement in real-world scenarios without the need for additional specialized measurements. In contrast, the other models are based on meteorological variables that are not frequently recorded at meteorological stations. ANN Models 3, 7, 8, and 9 depend on CC, which requires the use of a sky camera. Models 1, 4, 5, and 6 rely on DHI, thus requiring the use of a pyrheliometer and a solar tracker, elements of high cost and complex maintenance, and, therefore, scarce in meteorological ground facilities.

Table 9. Performance (nRSME (%)) of ANN models of GHUVE, generated from combinations of five and six experimental meteorological variables and from two to six neurons in the hidden layer.

ANN	Number of Variables/Neurons in the Hidden Layer	Meteorological Variables	RSME(%)
Model 1	5/2	GHI, θ_z, ε, T, k_t	14.49
Model 2	5/3	GHI, θ_z, T, k_t, ψ	14.16
Model 3	5/4	GHI, θ_z, T, CC, ψ	13.34
Model 4	5/5	GHI, θ_z, T, Δ, ψ	13.01
Model 5	6/2	GHI, θ_z, k_t, ε, T, RH	14.11
Model 6	6/3	GHI, θ_z, DHI, T, RH, ψ	13.59
Model 7	6/4	GHI, θ_z, T, RH, CC, ψ	12.94
Model 8	6/5	GHI, θ_z, T, RH, CC, ψ	12.53
Model 9	6/6	GHI, θ_z, k_t, T, CC, ψ	12.16

5. Conclusions

This study was based on the experimental data recorded and analyzed at 10 min intervals between September 2020 and June 2022 in Burgos (Spain). The GHUVE/GHI ratio was analyzed at different time intervals as a function of the sky type classified according to the ISO/CIE standard. The analysis of the GHUVE/GHI ratio yielded a gradual increase from dawn to noon (12:00 h) and a subsequent decrease until sunset. A greater dispersion of values was observed in the central hours of the day (10:00 a.m. to 2:00 p.m.). The relationship showed higher values with a higher dispersion for the months from May until August and lower values in December and January. The value of the ratio and the data dispersion into the three categories (overcast, intermediate, and clear skies) was very similar.

Different models were analyzed to determine GHUVE based on meteorological and radiative variables collected in Burgos, using multilinear regression models (MLR) and artificial neural network (ANN) for all skies, overcast, intermediate, and clear skies. The use of variables from databases or satellite observation was not considered to guarantee, as

far as possible, the applicability of locally obtained models in other locations using data from ground meteorological facilities.

The MLR model fitting results presented high determination coefficients with the experimental data ($R^2 > 0.92$) for all skies, overcast, intermediate, and clear skies. However, the nRMSE value was elevated, exceeding 20% in the four cases. Since the MLR models did not perform as expected, GHUVE was modeled by ANN models, considering the variables used for MLR modeling for each sky type. In all four cases, a good determination coefficient was obtained, $R^2 > 0.95$. The nRSME obtained varied between 12 and 21%. The best results were obtained for clear skies ($R^2 > 0.97$ and nRMSE $< 12.4\%$).

For all skies, the optimal number of variables was evaluated to achieve an nRMSE of less than 15% by means of ANN models. Through the derivation and analysis of multiple models, it was determined that the adequate choice was the model encompassing GHI, θ_z, T, k_t, ψ, due to its high performance and the availability of the required inputs from most ground meteorological facilities.

Future research endeavors should incorporate the deeply impactful total ozone column (TOC) variable among the model inputs. Addressing the scarcity of ground-based experimental TOC data could be achieved by using daily interpolated satellite observations. Incorporating other time scales (hourly and daily) and employing corrections based on site adaptation techniques will be imperative to extend the developed models to diverse locations accurately.

Author Contributions: Conceptualization, C.A.-T.; Formal analysis, S.G.-R., A.G.-R., D.G.-L. and I.G.; Funding acquisition, C.A.-T.; Investigation, S.G.-R., D.G.-L. and I.G.; Methodology, S.G.-R., A.G.-R. and I.G.; Software, S.G.-R., A.G.-R., D.G.-L. and I.G.; Supervision, C.A.-T.; Validation, C.A.-T.; Visualization, S.G.-R., A.G.-R. and I.G.; Writing—original draft, S.G.-R. and A.G.-R.; Writing—review and editing, C.A.-T. and I.G. All authors have read and agreed to the published version of the manuscript.

Funding: This research was funded by MCIN/AEI/ 10.13039/501100011033 and the "European Union Next Generation EU/PRTR grant numbers TED2021-131563B-I00 and PID2022-139477OB-I00 and Junta de Castilla y León, grant number INVESTUN/19/BU/0004.

Institutional Review Board Statement: Not applicable.

Informed Consent Statement: Not applicable.

Data Availability Statement: Copies of the original dataset used in this work can be downloaded from http://hdl.handle.net/10259/7778 (accessed on 18 September 2023).

Conflicts of Interest: The authors declare no conflict of interest.

Nomenclature

B_{sc}	Solar constant (=1361.1 W/m^2)
CC	Cloud cover (%)
D	Diffuse fraction
DHI	Diffuse horizontal irradiance (W/m^2)
DNI	Direct normal irradiance (W/m^2)
GHI	Global horizontal irradiance (W/m^2)
GHUVE	Global horizontal UV erythemal irradiance (W/m^2)
k_t	Clearness index
k'_d	Diffuse to extraterrestrial irradiance
n	Number of data points
nRMSE	Normalized root mean square error (%)
nMBE	Normalized mean bias error (%)
r	Pearson correlation coefficient
RH	Relative humidity (%)
R^2	Determination coefficient
T	Air temperature (°C)

TOC	Total ozone column
WS	Wind speed
Δ	Perez´s brightness factor
ε	Perez´s clearness index
f_c	The average value of the orbital eccentricity of the Earth
θ_z	Solar zenith angle (rad)
ψ	Solar azimuth angle (rad)

References

1. Ahmed, A.A.M.; Ahmed, M.H.; Saha, S.K.; Ahmed, O.; Sutradhar, A. Optimization algorithms as training approach with hybrid deep learning methods to develop an ultraviolet index forecasting model. *Stoch. Environ. Res. Risk Assess.* **2022**, *36*, 3011–3039. [CrossRef]
2. González-Rodríguez, L.; de Oliveira, A.P.; Rodríguez-López, L.; Rosas, J.; Contreras, D.; Baeza, A.C. A Study of UVER in Santiago, Chile Based on Long-Term In Situ Measurements (Five Years) and Empirical Modelling. *Energies* **2021**, *14*, 368. [CrossRef]
3. Salvadori, G.; Lista, D.; Burattini, C.; Gugliermetti, L.; Leccese, F.; Bisegna, F. Sun Exposure of Body Districts: Development and Validation of an Algorithm to Predict the Erythemal Ultra Violet Dose. *Int. J. Environ. Res. Public Heal.* **2019**, *16*, 3632. [CrossRef] [PubMed]
4. Alados-Arboledas, L.; Alados, I.; Foyo-Moreno, I.; Olmo, F.; Alcántara, A. The influence of clouds on surface UV erythemal irradiance. *Atmos. Res.* **2003**, *66*, 273–290. [CrossRef]
5. Cadet, J.-M.; Portafaix, T.; Bencherif, H.; Lamy, K.; Brogniez, C.; Auriol, F.; Metzger, J.-M.; Boudreault, L.-E.; Wright, C.Y. Inter-Comparison Campaign of Solar UVR Instruments under Clear Sky Conditions at Reunion Island (21° S, 55° E). *Int. J. Environ. Res. Public Health* **2020**, *17*, 2867. [CrossRef]
6. Serrano, A.; Antón, M.; Cancillo, M.L.; Mateos, V.L. Daily and annual variations of erythemal ultraviolet radiation in Southwestern Spain. *Ann. Geophys.* **2006**, *24*, 427–441. [CrossRef]
7. Serrano, M.-A.; Cañada, J.; Moreno, J.C.; Gurrea, G. Solar ultraviolet doses and vitamin D in a northern mid-latitude. *Sci. Total. Environ.* **2017**, *574*, 744–750. [CrossRef]
8. Vuilleumier, L.; Harris, T.; Nenes, A.; Backes, C.; Vernez, D. Developing a UV climatology for public health purposes using satellite data. *Environ. Int.* **2021**, *146*, 106177. [CrossRef]
9. Human, S.; Bajic, V. Modelling Ultraviolet Irradiance in South Africa. *Radiat. Prot. Dosim.* **2000**, *91*, 181–183. [CrossRef]
10. Modenese, A.; Gobba, F.; Paolucci, V.; John, S.M.; Sartorelli, P.; Wittlich, M. Occupational solar UV exposure in construction workers in Italy: Results of a one-month monitoring with personal dosimeters. In Proceedings of the 2020 IEEE International Conference on Environment and Electrical Engineering and 2020 IEEE Industrial and Commercial Power Systems Europe (EEEIC/I&CPS Europe), Madrid, Spain, 9–12 June 2020; pp. 1–5. [CrossRef]
11. Vitt, R.; Laschewski, G.; Bais, A.F.; Diémoz, H.; Fountoulakis, I.; Siani, A.-M.; Matzarakis, A. UV-Index Climatology for Europe Based on Satellite Data. *Atmosphere* **2020**, *11*, 727. [CrossRef]
12. Utrillas, M.; Marín, M.; Esteve, A.; Salazar, G.; Suárez, H.; Gandía, S.; Martínez-Lozano, J. Relationship between erythemal UV and broadband solar irradiation at high altitude in Northwestern Argentina. *Energy* **2018**, *162*, 136–147. [CrossRef]
13. Bilbao, J.; Román, R.; Yousif, C.; Mateos, D.; de Miguel, A. Total ozone column, water vapour and aerosol effects on erythemal and global solar irradiance in Marsaxlokk, Malta. *Atmos. Environ.* **2014**, *99*, 508–518. [CrossRef]
14. ISO/CIE 17166:2019(E); Erythema Reference Action Spectrum and Standard Erythema Dose. *ISO: Geneva, Switzerland*; CIE: Vienna, Austria, 2019.
15. Leal, S.; Tíba, C.; Piacentini, R. Daily UV radiation modeling with the usage of statistical correlations and artificial neural networks. *Renew. Energy* **2011**, *36*, 3337–3344. [CrossRef]
16. Esteve, A.R.; Marín, M.J.; Tena, F.; Utrillas, M.P.; Martínez-Lozano, J.A. Influence of cloudiness over the values of erythemal radiation in Valencia, Spain. *Int. J. Clim.* **2010**, *30*, 127–136. [CrossRef]
17. Bilbao, J.; Mateos, D.; Yousif, C.; Román, R.; De Miguel, A. Influence of cloudiness on erythemal solar irradiance in Marsaxlokk, Malta: Two case studies. *Sol. Energy* **2016**, *136*, 475–486. [CrossRef]
18. de Miguel, A.; Román, R.; Bilbao, J.; Mateos, D. Evolution of erythemal and total shortwave solar radiation in Valladolid, Spain: Effects of atmospheric factors. *J. Atmos. Sol. -Terr. Phys.* **2011**, *73*, 578–586. [CrossRef]
19. Bilbao, J.; Román, R.; Yousif, C.; Pérez-Burgos, A.; Mateos, D.; de Miguel, A. Global, diffuse, beam and ultraviolet solar irradiance recorded in Malta and atmospheric component influences under cloudless skies. *Sol. Energy* **2015**, *121*, 131–138. [CrossRef]
20. Antón, M.; Serrano, A.; Cancillo, M.; García, J. Influence of the relative optical air mass on ultraviolet erythemal irradiance. *J. Atmos. Sol. -Terr. Phys.* **2009**, *71*, 2027–2031. [CrossRef]
21. McKenzie, R.L.; Matthews, W.A.; Johnston, P.V. The relationship between erythemal UV and ozone, derived from spectral irradiance measurements. *Geophys. Res. Lett.* **1991**, *18*, 2269–2272. [CrossRef]
22. Antón, M.; Cazorla, A.; Mateos, D.; Costa, M.J.; Olmo, F.J.; Alados-Arboledas, L. Sensitivity of UV Erythemal Radiation to Total Ozone Changes under Different Sky Conditions: Results for Granada, Spain. *Photochem. Photobiol.* **2016**, *92*, 215–219. [CrossRef] [PubMed]

23. Sanchez, G.; Serrano, A.; Cancillo, M.L. Modeling the erythemal surface diffuse irradiance fraction for Badajoz, Spain. *Atmos. Meas. Tech.* **2017**, *17*, 12697–12708. [CrossRef]
24. Mateos, D.; Bilbao, J.; de Miguel, A.; Pérez-Burgos, A. Dependence of ultraviolet (erythemal and total) radiation and CMF values on total and low cloud covers in Central Spain. *Atmos. Res.* **2010**, *98*, 21–27. [CrossRef]
25. Bilbao, J.; Román, R.; de Miguel, A.; Mateos, D. Long-term solar erythemal UV irradiance data reconstruction in Spain using a semiempirical method. *J. Geophys. Res. Atmos.* **2011**, *116*, D22211. [CrossRef]
26. Lindfors, A.; Kaurola, J.; Arola, A.; Koskela, T.; Lakkala, K.; Josefsson, W.; Olseth, J.A.; Johnsen, B. A method for reconstruction of past UV radiation based on radiative transfer modeling: Applied to four stations in northern Europe. *J. Geophys. Res. Earth Surf.* **2007**, *112*, D23201. [CrossRef]
27. Buntoung, S.; Janjai, S.; Nunez, M.; Choosri, P.; Pratummasoot, N.; Chiwpreecha, K. Sensitivity of erythemal UV/global irradiance ratios to atmospheric parameters: Application for estimating erythemal radiation at four sites in Thailand. *Atmos. Res.* **2014**, *149*, 24–34. [CrossRef]
28. García-Rodríguez, A.; Granados-López, D.; García-Rodríguez, S.; Díez-Mediavilla, M.; Alonso-Tristán, C. Modelling Photosynthetic Active Radiation (PAR) through meteorological indices under all sky conditions. *Agric. For. Meteorol.* **2021**, *310*, 108627. [CrossRef]
29. Dieste-Velasco, M.I.; García-Rodríguez, S.; García-Rodríguez, A.; Díez-Mediavilla, M.; Alonso-Tristán, C. Modeling Horizontal Ultraviolet Irradiance for All Sky Conditions by Using Artificial Neural Networks and Regression Models. *Appl. Sci.* **2023**, *13*, 1473. [CrossRef]
30. Fatima-Ezzahra, D.; Abdellah, B.; Abdellatif, G. Estimation of ultraviolet solar irradiation of semi-arid area–case of Benguerir. In Proceedings of the 2020 International Conference on Electrical and Information Technologies (ICEIT), Rabat, Morocco, 4–7 March 2020; pp. 1–5. [CrossRef]
31. Alados, I.; Gomera, M.A.; Foyo-Moreno, I.; Alados-Arboledas, L. Neural network for the estimation of UV erythemal irradiance using solar broadband irradiance. *Int. J. Clim.* **2007**, *27*, 1791–1799. [CrossRef]
32. Barbero, F.J.; López, G.; Batlles, F.J. Determination of daily solar ultraviolet radiation using statistical models and artificial neural networks. *Ann. Geophys.* **2006**, *24*, 2105–2114. [CrossRef]
33. Jacovides, C.; Tymvios, F.; Boland, J.; Tsitouri, M. Artificial Neural Network models for estimating daily solar global UV, PAR and broadband radiant fluxes in an eastern Mediterranean site. *Atmos. Res.* **2015**, *152*, 138–145. [CrossRef]
34. Junk, J.; Feister, U.; Helbig, A. Reconstruction of daily solar UV irradiation from 1893 to 2002 in Potsdam, Germany. *Int. J. Biometeorol.* **2007**, *51*, 505–512. [CrossRef]
35. Feister, U.; Junk, J.; Woldt, M.; Bais, A.; Helbig, A.; Janouch, M.; Josefsson, W.; Kazantzidis, A.; Lindfors, A.; Outer, P.N.D.; et al. Long-term solar UV radiation reconstructed by ANN modelling with emphasis on spatial characteristics of input data. *Atmos. Meas. Tech.* **2008**, *8*, 3107–3118. [CrossRef]
36. Malinovic-Milicevic, S.; Vyklyuk, Y.; Radovanovic, M.M.; Petrovic, M.D. Long-term erythemal ultraviolet radiation in Novi Sad (Serbia) reconstructed by neural network modelling. *Int. J. Clim.* **2018**, *38*, 3264–3272. [CrossRef]
37. Alados, I.; Mellado, J.A.; Ramos, F.; Alados-Arboledas, L. Estimating UV Erythemal Irradiance by Means of Neural Networks¶. *Photochem. Photobiol.* **2004**, *80*, 351–358. [CrossRef] [PubMed]
38. Antón, M.; Cancillo, M.L.; Serrano, A.; García, J.A. A Multiple Regression Analysis Between UV Radiation Measurements at Badajoz and Ozone, Reflectivity and Aerosols Estimated by TOMS. *Phys. Scr.* **2005**, *2005*, 21. [CrossRef]
39. Kim, J.; Lee, Y.G.; Koo, J.-H.; Lee, H. Relative Contributions of Clouds and Aerosols to Surface Erythemal UV and Global Horizontal Irradiance in Korea. *Energies* **2020**, *13*, 1504. [CrossRef]
40. Foyo-Moreno, I.; Alados, I.; Alados-Arboledas, L. Adaptation of an empirical model for erythemal ultraviolet irradiance. *Ann. Geophys.* **2007**, *25*, 1499–1508. [CrossRef]
41. ISO 15469:2004(E)/CIE S 011/E:2003; Spatial Distribution of Daylight—CIE Standard General Sky. *ISO: Geneva, Switzerland*; CIE: Vienna, Austria, 2004.
42. Granados-López, D.; Suárez-García, A.; Díez-Mediavilla, M.; Alonso-Tristán, C. Feature selection for CIE standard sky classification. *Sol. Energy* **2021**, *218*, 95–107. [CrossRef]
43. Suárez-García, A.; Díez-Mediavilla, M.; Granados-López, D.; González-Peña, D.; Alonso-Tristán, C. Benchmarking of meteorological indices for sky cloudiness classification. *Sol. Energy* **2020**, *195*, 499–513. [CrossRef]
44. Beyer, H.G.; Martinez, J.P.; Suri, M.T.J.L.; Lorenz, E.; Müller, S.C.; Hoyer-Klick, C.; Ineichen, P. Report on Benchmarking of Radiation Products. Management and Exploitation of Solar Resource Knowledge. In Proceedings of the EUROSUN 2008, 1st International Congress on Heating, Cooling and Buildings, ISES, Lisbon, Portugal, 7–10 October 2008.
45. Gueymard, C.A. Revised composite extraterrestrial spectrum based on recent solar irradiance observations. *Sol. Energy* **2018**, *169*, 434–440. [CrossRef]
46. Erbs, D.; Klein, S.; Duffie, J. Estimation of the diffuse radiation fraction for hourly, daily and monthly-average global radiation. *Sol. Energy* **1982**, *28*, 293–302. [CrossRef]
47. Iqbal, M. *An Introduction to Solar Radiation*; Academic Press: New York, NY, USA, 1983. [CrossRef]
48. Perez, R.; Ineichen, P.; Seals, R.; Michalsky, J.; Stewart, R. Modeling daylight availability and irradiance components from direct and global irradiance. *Sol. Energy* **1990**, *44*, 271–289. [CrossRef]

49. Gueymard, C.A. A reevaluation of the solar constant based on a 42-year total solar irradiance time series and a reconciliation of spaceborne observations. *Sol. Energy* **2018**, *168*, 2–9.
50. Mukaka, M. Statistics corner: A guide to appropriate use of correlation in medical research. *Malawi MesicL J.* **2012**, *24*, 69–71. [CrossRef]
51. Heaton, J. *Artificial Intelligence for Humans, Volume 3: Deep Learning and Neural Networks*; Heaton Research, Inc.: St. Louis, MO, USA, 2015.

materials

MDPI

Article

An Assessment on the Efficiency of Clothing with UV Protection among the Spanish Navy School Students

José Roberto Ribas [1], Sol García Rodríguez [2], Elena Arce Fariña [3] and Andrés Suárez-García [4,*]

[1] Escola Politécnica, Universidade Federal do Rio de Janeiro, Rio de Janeiro 21941-909, Brazil
[2] Research Group Solar and Wind Feasibility Technologies (SWIFT), Electromechanical Engineering Department, University of Burgos, 09006 Burgos, Spain
[3] Department of Industrial Engineering, Ferrol Polytechnic University School, University of A Coruña, 15403 A Coruña, Spain
[4] Defense University Center, Naval Academy, University of Vigo, Plaza de España 2, 36920 Marín, Spain
* Correspondence: andres.suarez@cud.uvigo.es; Tel.: +34-986-804-934

Abstract: Concern about the harmful effects that ultraviolet (UV) rays have on the skin of people who are routinely exposed to solar radiation has driven the industry of skin protection creams, sunglasses and clothing. Spanish Navy personnel are subject to different levels of exposure depending on their rank and function. The objective of this research is to analyze the behavioral variables associated to the effects on the skin caused by UV rays, denoted by the combined effects of perceived susceptibility and perceived severity, on their decision to purchase and wear uniforms with UV protection. A confirmatory analysis using a structural equation modeling (SEM) was performed on a sample of 100 respondents. The model results revealed a strong mediating characteristic of the intention to use, variable associated with the exogenous variables. Attitude towards the use of clothing and social influence, as well as the exogenous variable clothing action planning, on the sun protective clothing use during tactical maneuvers. These relationships were significant with *p*-values close to zero. However, exogenous variables related to perceived susceptibility and perceived severity in exposure to sunlight did not represent a significant influence when mediated by self-efficacy in use. The results revealed the consequence of awareness about the importance of protecting oneself and the influence that usage habits can have on the military with respect to the decision to purchase uniforms with UV protection.

Keywords: Spanish navy; ultraviolet protection; uniforms; perceived efficiency; structural equation model

Citation: Ribas, J.R.; Rodríguez, S.G.; Fariña, E.A.; Suárez-García, A. An Assessment on the Efficiency of Clothing with UV Protection among the Spanish Navy School Students. *Materials* **2022**, *15*, 6227. https://doi.org/10.3390/ma15186227

Academic Editor: Fernando Julian

Received: 16 August 2022
Accepted: 5 September 2022
Published: 8 September 2022

1. Introduction

People whose work involves a lot of exposure to the sun suffer to a greater extent from the consequences of UV radiation. Among these groups of people, the military stands out since, during maneuvers, for example, the military is exposed for all or practically all day and, although it is not always the case, they must train in it, so sooner or later they will have to deal with this problem. Their maneuvers can be performed in places where the solar intensity is high, such as the sun belt region between 35° S and 35° N, where troops may be subjected to high ultraviolet index levels. Moreover, the daily patrols in the area of operations with no more shade, in most cases, than that provided by the garments they wear, the ideal conditions are combined to suffer the consequences of the impact of the UV radiation. Studies for the United States Armed Forces have shown that those who have served in the military have a higher risk of skin cancer than those who have not [1]. Among the results, it should be noted that the members with the highest rate of skin cancer are the pilots of the "US Air Force", both in melanoma and non-melanoma cancer. This is because, as has already been stated in the Introduction section, the higher the altitude, the greater the irradiance on our body. In fact, the level of UV radiation increases by around 15% for every 1000 m of altitude. Another unit clearly affected by this issue is the "10th Mountain

Division" of light infantry, belonging to the US Army. This unit has a high rate of skin cancer due to the amount of time they spend training in the mountains at high altitudes. On the other hand, at the other extreme, the lowest rate is found among military personnel assigned to mechanized units, due to the lower exposure they suffer from being covered most of the time. These results are applicable to the Spanish Armed Forces since, being allies of the United States, they share most of the deployments and areas of operations [2,3].

In most units of the Spanish Navy, the activities carried out there are largely abroad, especially during periods of instruction and training [4,5]. Students undergo a rigorous training program, which exposes them not only to summer heat and sun but also to harsh winter conditions at high altitudes, where the sun is even more intense and UV radiation more concentrated. In addition, marine army corps are subjected to high levels of reflected solar radiation from the sea. Moreover, their activities can be performed in areas of the world close to the Equator, where the impact of UV radiation is much more dominant, such as regions of Africa or the Middle East.

Although the students wear the uniform camouflaged with a cap, hat or helmet as headwear, in the case of the Marines, or the fire-retardant task with a cap in the case of the General Corps and Quartermaster students, there are still areas exposed to radiation, such as the neck and face. The impact of UV radiation is cumulative on our skin [6], so the consequences of overexposure to radiation on our health, whether skin, eye or the immune system, can occur in certain students when over time, evidencing themselves in the performance of their duties as future officers of the Navy.

As for the seafarers, they are not exempt from this problem either. In fact, at sea, the reflection produced by UV rays means that being outdoors, on a rowing boat or on maneuvers, for example, can become more damaging than a patrol in the desert. In fact, the use of sunglasses at sea is more necessary, if possible, than on land. Despite this, similar to the military in land operations, the uniform gear corresponding to sailors also serves to protect themselves from the sun, since headwear should be worn outdoors, such as caps in most countries, cases and long-sleeved fire-retardant material [7].

The incidence of skin cancer is continuously increasing and has reached high proportions worldwide [8–12]. The term "skin cancer" includes a group of malignant neoplasms with very different characteristics (i.e., origin, risk factors and prognosis). There are the following two main groups: cutaneous melanoma and non-melanoma skin cancer (NMSC). NMSC includes squamous cell carcinoma and basal cell carcinoma. NMSC is the most frequently diagnosed group of malignant neoplasms in whites [13].

Clothing provides sun protection by absorbing, scattering and reflecting part of the UV radiation that reaches the surface of the fabric [14]. Fabrics differ in their capacity to reduce UV incidence because they differ in fiber composition and moisture content [15]. According to the Skin Cancer Foundation, the UV protection provided by clothing depends on [16]:

- The porosity, weight and thickness: UV protection is higher the smaller the spaces in the yarns (weave) and the greater the weight and thickness of the fabric [17];
- Color: darker colors offer higher UV protection;
- Tension: UV protection decreases as the fabric stretches;
- Humidity: UV protection decreases when the fabric is wet;
- Washing: washing new garments increases UV protection, especially when they are made of natural fibers (e.g., cotton) [18].

The *Australia/New Zealand Standard for Protective Clothing* (AS/NZS 4399:1996) was the first published standard on methods for determining the ultraviolet protection factor (UPF) of clothing designed for this purpose [14]. This standard divides UPFs into the following three groups: those with ratings from 15 to 24, those with ratings from 25 to 39 and those with ratings between 40 and higher, which offer outstanding protection [19]. In addition to the Australian and New Zealand committees, the International Organization for Standardization (ISO) and other global organizations, such as the Commission on Illumination (CIE), have been working on developing UV-protective fabric standard

papers. A new standard concerning the specifications for test procedures and labeling of sun-protective clothing (EN 13758) has been created by the European Committee for Standardization (CEN) [19]. The amount of ultraviolet light that is transmitted or blocked by textile materials designed to be used for UV protection can also be measured using the American Standard (AATCC TM 183) the GBT18830-2009 national standard of the People's Republic of China, and the UV Standard 801 from the International Testing Association in Europe [20,21]. The UPF results by following these measurement standards do not differ significantly [20].

Ultimately, the problem does not lie in the deficiency of means to be offered by the Armed Forces, but rather in the employment that the military decides to give it. According to a study carried out by the American Academy of Dermatology in 2017 on previously deployed military personnel on a mission, less than 30% of the soldiers interviewed claimed to have used sunscreen regularly, and more than 70% had unprotected skin. The level of awareness must be high, and it must be highlighted among the members of the Armed Forces, since the consequences of the impact of UV radiation on the military are greater than on the rest of the ordinary citizens, and it has been demonstrated. According to another study, this time carried out by the National Cancer Institute of the United States in 2010, it was shown that the index of melanoma diagnosed in patients belonging to the military was higher than the index present in civilian citizens, especially in the age band between 55 and 59 years of age, further demonstrating that the damage caused by overexposure to UV radiation is cumulative, and its consequences do not appear until later stages [1].

Therefore, this problem must be considered in the employment of the military, since the simple fact of being assigned to an area closer to a forest, in the sea, the desert or higher in the mountains implies a factor of considerable risk that cannot be ignored or ignored, since the consequences, if protective measures are not taken, can be lethal.

The literature on the use of SEM to analyze problems with UV radiation in people regularly exposed to the external environment has addressed different objectives. A study was carried out with 148 male external workers with the objective of confirming that these professionals highly exposed to UV radiation could count on an efficient preventive diagnosis, obtained through interventions with UV photographs [22]. The investigation into the beliefs of 334 students at an American university about UV exposure and sunscreen use, as well as the links with skin cancer and protective measures in a cloudy sky [23]. Adoption of the tripartite theory of body image, reasoned action, health belief model and motivational protection theory to test various behavioral models. In this model, the authors confirmed that intention is a mediator of sociocultural influence and tanning behavior [24]. A model to measure the behavior of 273 parents in protecting their children from the carcinogenic effects of sun exposure. The variables used were intention, attitude, subjective norm, action plan, among others [25]. The use of Latent Class Analysis (LCA) to assess classified homogeneous groups of 90 respondents according to constitutional risk, tanning intention, and sun protection behavior (shade, clothing and sunscreen) [26]. The collection of a sample of 261 respondents to propose a model based on knowledge, motivation, health literacy and nutritional literacy to test whether knowledge about health and nutrition was associated with an attitude towards sun exposure [27].

The objective of this research is to analyze the behavioral variables associated with the effects on the skin caused by UV rays, denoted by the combined effects of exogenous variables, on their decision to purchase and wear uniforms with UV protection. The students' perception of the attitude toward uniforms with UV protection should inspire manufacturers to make this option available, showing that the company's efforts will be rewarded with the purchase decision made by students.

2. Materials and Methods

2.1. Structural Equations Model

In its most simplified form, SEM can be understood as the combination of path analysis with factor analysis [28,29] to enable the understanding of complex patterns of interrelationships. In path analysis, the concern is with the causal path of the observed variables [30,31]. In a complete structural equation model, the interest is in the causal path of the constructs (latent variables or factors). Although the acceptance of SEM is growing, the difficulties of its employment should not be underestimated [32]. Variables that are not directly measurable, which are supposedly the factors that cause a set of observed variables (measured or indicators) to vary, are usually called latent variables (or factors). As the latent variable is not measured, it is necessary to give it a metric, which is performed when the value 1 is assigned to one of the paths directed to one of the observed variables that it influences. With this restriction, the remaining paths can be estimated. When each latent variable has only one indicator, the SEM is restricted to path analysis. When each variable has multiple indicators but there are no direct effects connecting them, there is a factor analysis. However, when there are multiple indicators for each latent variable (or factor), as well as paths connecting them, complete structural models are built.

In SEM graphs, the linear regression model implicitly assumes zero measurement error. The error terms of the observed variables are explicitly modeled in SEM. Ignoring such errors can lead to serious distortions, especially when they are significant. Note that these terms should not be confused with residual error terms, also called disturbance errors, which reflect unexplained variance in latent endogenous variables due to unmeasured causes. Structural equation models also include possible direct and indirect effects between their variables [33]. Bearing in mind that a complete structural equation model is the combination of factor analysis and path analysis, it exhibits the following two intrinsically interrelated sections: (i) measurement; (ii) structural. The measurement section of the model corresponds to the factor analysis, and it describes the relationship between latent and observed variables. The measurement model is generally used as an independent (or null) model. In fact, the covariance in the latent variable covariance matrix of the independent model is considered null. The structural section of the model corresponds to the path analysis and represents the direct and indirect effects of the latent variables on each other. In the traditional path analysis, the aforementioned effects occur between observed variables; in SEM, path analysis is fundamentally between latent variables [34].

2.2. Variables Specification and Assessment

This study has focused on a select of students from a military school in Spain that was undergoing outdoor training at the time it was carried out. These respondents answered a questionnaire containing behaviorally observed variables related to the acquisition and use of military clothing with protection against UV rays. To avoid interpretation bias, an explanation was given on the meaning of UV protection from the sun in military clothing and aspects such as price variations, breathability, fit and lightness relative to unprotected clothing. The survey for measuring behavior towards the use of military sun protective clothing (Table 1) was an adaptation of the questionnaire developed by Van Osch et al. [27] to predict the parental use of sunscreen. The survey was distributed to students at the military naval school through Google Forms. Each of the questions was translated into Spanish from the work of Van Osch et al. [27], adapting sunscreen to sun protective clothing and the target audience to military and subordinates. The first version of the questionnaire was found to be difficult to comprehend and therefore a number of improvements were made to it such as better consolidation of the questions and provision of some examples to better explain the questionnaire.

Table 1. Description of the measurement of cognitive concepts and military sun protective clothing use.

Concept	Number of Items	Item Description. Questions
Perceived susceptibility	1	1. If a military member does not protect himself or herself from the sun, the risk of suffering from skin cancer in the future is from very low (1) to very high (5)
Perceived severity	1	2. If a military member would diagnosed skin cancer in the future, I would find this from not serious (1) to very serious (5)
Attitude	5 (α = 0.75)	3. Wearing sun protective clothing during maneuvers is a comfortable way to protect the military from the sun. (1 = not pleasant to 4 = very pleasant) 4. Wearing sun protective clothing for a military member health is: (1 = not important to 4 = very important) 5. Wearing sun protective clothing is annoying during daily life in the military. (1 = very annoying to 4 = not annoying) 6. Wearing sun protective clothing is inconvenient, because I tend to forget it. (1 = very inconvenient to 5 = not inconvenient) 7. Wearing sun protective clothing is unnecessary. (1 = very unnecessary to 4 = not unnecessary)
Social influence	3 (α = 0.73)	8. *Social Modeling*: How often does the military wear sun protective clothing? (1 = hardly ever to 4 = always) 9. *Social Norms*: How important do important military in your environment find it to wear sun protective clothing to protect themselves from the sun? (1 = definitely not important to 4 = definitely important) 10. *Social support*: How important do important military in your environment find it to wear sun protective clothing to protect you from the sun? (1 = definitely not important to 4 = definitely important)
Self-efficacy	1	11. Do you think you will be able to adequately wear sun protective clothing to protect you from the sun? (1 = definitely not to 7 = definitely yes)
Intention	1	12. Do you intend to adequately use sun protective clothing to protect you from the sun? (1 = definitely not to 7 = definitely yes)
Action planning	4 (α = 0.86)	13. Do you plan to buy sunscreen sun protective clothing? 14. Do you plan to bring sun protective clothing with you during military exercises on a sunny day? 15. Do you plan to keep track of time in order to wear sun protective clothing depending on the weather? 16. Do you plan to ask other military to remember you to wear sun protective clothing? (all answers: 1 = definitely not to 7 = definitely yes)
Sun protective clothing use	1	17. How often did you protect yourself from the sun by wearing sun protective clothing when you were outside on a sunny day during past military exercises? (1 = never to 5 = always)

2.3. Model

At this point, an explanation about the latent variables, unobserved exogenous variables and observed variables must be performed. In Figure 1, a high-level flow chart of the methodology is provided. Three latent and five observed variables were applied in this model. Attitude, social influence and action planning were the latent variables. Perceived susceptibility, perceived severity, self-efficacy, intention and sun protection clothing use the observed variables. This workflow model is based on the work of Van Osch et al. [27]. As indicated above, the questionnaire and the model of the relationships between input variables used in the research by Van Osch et al. [27] had to be translated into Spanish and adapted to the objective of the study as follows: to analyze the effectiveness of the use of UV protective clothing in students linked to the military. In other words, Figure 1 shows the hypothesis proposed in the model of dependencies between the variables used in this study.

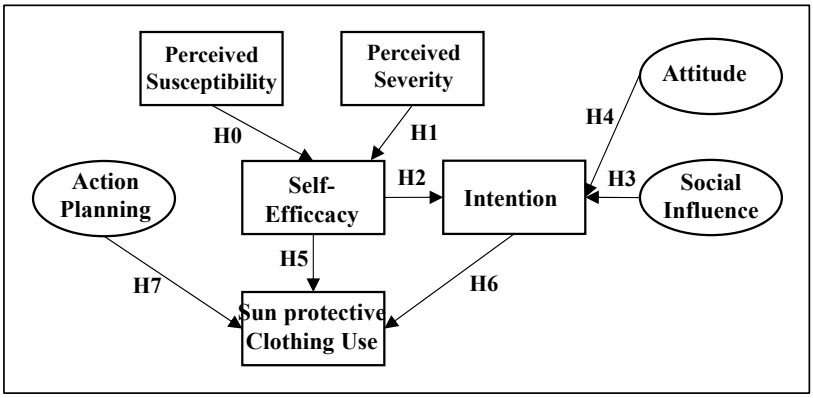

Figure 1. Proposed model for the UV textile usage.

2.4. Participants

The student sample consisted of 127 students from the Naval Military School of Marín (Spain), among whom 80 were from the General Corps, 39 from the Marine Corps and 8 from the Intendancy. Of the participants, 93.70% were male (119 students) and 6.30% were female (8 students). The age of the participants aged from 18 to 36 years (M = 22.52, SD = 2.90).

3. Results

Initially, all measurements underwent assumption tests characteristic of studies involving multivariate analysis [34]. The exogenous observed variables perceived susceptibility (SUS) and perceived severity (SEV), and the latent variables attitude (ATT), action planning (PLN) and social influence (SOC) revealed the absence of multicollinearity. The assumptions of normality and multivariate linearity resulting from the two-by-two combinations of metric variables were met. In order to preserve the model's internal consistency, it is necessary to verify the distinctive robustness between the ATT, PLN and SOC constructs. Adopting the line of reasoning operationalized by Hagger and Chatzisarantis [35], the robustness between the three dimensions was evaluated.

The ATT, PLN and SOC latent variables showed reliability measured by Cronbach's Alpha equal to 0.733, 0.866 and 0.558, respectively, all but one exceeding the minimum value of 0.70 according to Fornell and Larcker [36] and, therefore, meeting the reliability requirements. The chi-square of 307.8 divided by 116 degrees of freedom equal to 2.653 is satisfactory as it surpasses the more conservative significance level of 0.01. After verifying the inexistence of multicollinearity between the ATT, PLN and SOC, the estimate of the hypothetical theoretical relationships was carried out with the support of a structural equation model (SEM) adjusted on the latent variables as can be seen in Figure 2.

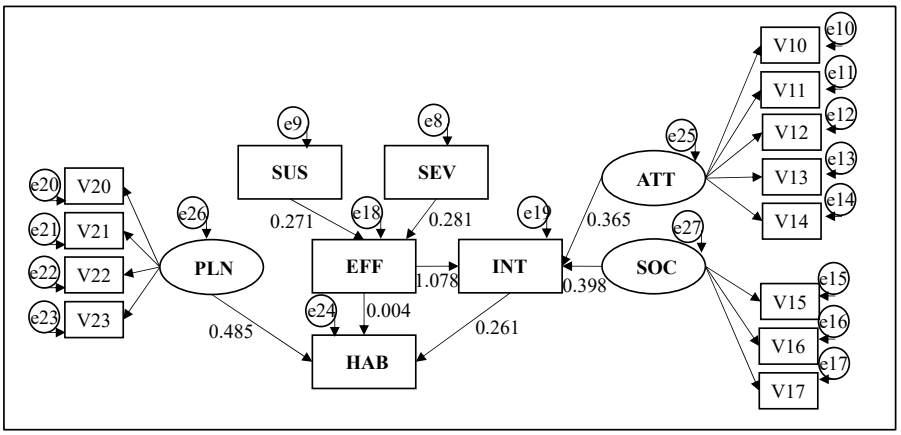

Figure 2. SEM specification for the UV textile usage.

The concern when the theoretical model was initially conceived was about the apparent transposition that ATT could present with PLN and SOC, which, despite the care taken in the semantic conception of the questions, incorporated the risk of interpretation by the respondent. The rationale of the test states that, for instance, if ATT does not turn out to have distinct dimensions of PLN and SOC, causing a forced solution from two factors instead of three, should result in ATT collapsing all or part of the two other constructs' direction. On the other hand, if SOC collapses to the factor where ATT is found or to the factor where PLN is found, we will have the latter two prove their mutual distinction and, therefore, the successful interpretation by the respondent. The obtained results with a two-factor analysis showed that the respondent discriminated between the two constructs since one of the factors incorporated the factorial loads of PLN and SOC, while the other kept the factorial loads of ATT isolated.

Then, the three dimensions underwent an exploratory factor analysis with the aim of validating the hypothesis of the non-occurrence of independence that would harm the isolated explanatory contributions of the covariance among the constructs. A varimax rotation with Kaiser normalization was adopted for the three-factor extraction. The factor loadings resulting from a cut applied to the solution for three factors, whose eigenvalues captured 60.3% of the extracted variance, are shown in Table 2, as well as the corresponding *t*-tests, all significant at the 5% bilateral significance level. Such results denoted the discriminant behavior in the interrelationship between dimensions. It can be seen that factor 1 refers to the observed variables 20 to 23, confirming the latent variable PLN. Likewise, factor 2 refers to the observed variables from 10 to 14, confirming the latent variable ATT. Factor 3 validated two of the three variables observed for the latent variable SOC.

Table 2. Factor loads after varimax rotation with Kaiser normalization.

Variable	Factor 1	Factor 2	Factor 3
V10	0.127	0.749	0.113
V11	0.189	0.650	0.091
V12	0.179	0.726	−0.153
V13	0.013	0.671	−0.012
V14	0.152	0.645	0.187
V15	0.224	−0.007	0.828
V16	0.482	0.140	0.179
V17	0.113	0.121	0.861
V20	0.762	0.244	0.237
V21	0.855	0.090	0.053
V22	0.871	0.046	−0.015
V23	0.783	0.219	0.146

4. Discussion

Regarding the causal relationship that the exogenous variables susceptibility (SUS) and severity (SEV) have over the mediating variable efficiency (EFF), the parameters were estimated as 0.271 with a *p*-value of 0.028 and 0.291 with a *p*-value of 0.084, respectively. This confirms hypotheses H_0 and H_1 at a 10% of significance level, that protecting oneself from the sun prevents the risk of developing skin cancer in the future. Furthermore, in the event of a positive diagnosis of skin cancer, wearing sun-protective clothing would be an effective way of protecting oneself from the sun.

The hypothesis that the mediating variable EFF, together with the latent variables ATT and SOC, may predict Intention (INT) resulted in the following parameters: 1.078, 0.365 and −0.398, respectively. The relationships between EFF→INT and ATT→INT were significant, having their *p*-values close to zero and confirming hypotheses H2 and H4, while SOC-INT was not significant. It means that the positive attitude towards wearing UV-protected clothing for someone to protect from the sun, combined with the perception that wearing clothing with sun protection would be effective, would positively influence the willingness to wear sun protection clothing to protect from the sun in military activities. Additionally,

the social norms that recommend the use of protective clothing do not influence the intention of a military to use this type of clothing.

Finally, in evaluating the influence that the EFF, Action Planning (PLN) and INT variables have on the habit of wearing sun protection clothing (HAB), the parameters were estimated at 0.004, 0.485 and −0.261. The PLN→HAB and INT→HAB relationships were significant with *p*-values close to zero, confirming hypotheses H7 and H6; however, the mediator variable EFF did not show a significant relationship with HAB. This means that when a person plans to wear an outfit with sun protection, one is likely to convert this idealization into a habit of use. On the other hand, the predisposition to wear clothing with sun protection is inversely related to the habit of wearing it, which probably means that the mediator variable INT is treated as a motivation that has yet to materialize, while the endogenous variable HAB was perceived as an action incorporated into a habit of use, no longer requiring reinforcement of motivation. The failure of the EFF variable as a mediator confirms the possibility that the military personnel interviewed do not perceive the existence of a relationship between the belief that clothes with sun protection are effective and their habit of use, probably because the frequent use of an outfit is an already incorporated action that does not require cognitive reinforcement.

5. Conclusions

Modeling with the use of latent variables allowed non-measurable variables, such as beliefs, motivations and attitudes, to compose an explicit structure regarding the use of uniforms with UV protection. The use of measurable scales to reflectively compose latent variables is obviously subject to design and measurement errors; however, mitigated by the statistical rigor in the internal consistency test. The causal relationships involving exogenous variables and latent variables proved to be very useful in explaining the motivational structure and in identifying relevant elements for the adoption of managerial actions that could stimulate interest in uniforms with UV protection.

The results showed that, in general, the responses of the Spanish Marine Corps student sample showed positive manifestations regarding the attitude and decision to buy and use uniforms with UV protection. The results found in the structural equation model partly answer the problem of this research; that is, that the interviewee now has a favorable intention toward the clothing after realizing through the social influence that it provides safety as a positive and uses it in the purchase and use decision. This means that the protective benefit against the harmful effects of the sun's rays is perceived by the interviewee based on their intention to use it and the influence exerted by people in their social life, which are captured in the model by the specified latent variables.

As a practical implication, it is possible to observe that uniforms with protection against UV radiation translate into a feeling of security and, therefore, constitute an attribute that suggests investment on the part of the student, resulting from the utilitarian awareness of clothing and the intrinsic relationship with the feeling of worth. With this, it is noted that the attitude, in addition to encouraging preventive behavior, also contributes to the confirmation of the social influence on the favorable intention towards clothing. The importance of the reputation that UV protection garments have as a focal point for purchase and use intentions by students is highlighted. However, there are no great efforts by suppliers of military uniforms to offer products with this type of protection. Therefore, drawing a parallel with the theory, students' perception of the attitude toward uniforms with UV protection should encourage manufacturers to make this option available, showing that the company's efforts will be rewarded with the purchase decision made by students. This situation demonstrates the need for further studies to investigate and deepen the evaluation of the loyalty process.

As academic contributions, this research provided support for the literature on the connection that occurs between knowledge about the harmful effects of UV radiation, the intention to use UV protective clothing and the consequent purchase intention and decision by Spanish Marine Corps students. Studies on the variables that influence the demand for

uniforms with UV protection are extremely relevant when it is concluded that the effect of UV radiation affects an extremely valuable intangible asset, namely, the health of students.

Author Contributions: Conceptualization, J.R.R. and S.G.R.; methodology, J.R.R.; investigation J.R.R. and S.G.R.; validation E.A.F.; formal analysis S.G.R.; data curation E.A.F. and A.S.-G.; software A.S.-G.; writing—original draft preparation J.R.R. and S.G.R.; writing—review and editing E.A.F.; visualization A.S.-G.; supervision J.R.R.; project administration S.G.R.; funding acquisition S.G.R.; resources A.S.-G. All authors have read and agreed to the published version of the manuscript.

Funding: The authors gratefully acknowledge the financial support provided by the Spanish Ministry of Science & Innovation under the I+D+i state program "Challenges Research Projects" (RTI2018-098900-B-I00) and the Regional Government of Castilla y León (INVESTUN/19/BU/004 and INVESTUN/22/BU/0001).

Institutional Review Board Statement: The study was conducted in accordance with the Declaration of Helsinki, and approved by the Institutional Bioethics Committee of University of Burgos (UBU 44/2021).

Informed Consent Statement: Informed consent was obtained from all subjects involved in the study.

Data Availability Statement: The data that support the findings of this study are available from the corresponding author, upon reasonable request.

Acknowledgments: The authors thank the Defense University Center at the Spanish Naval Academy (CUD-ENM) for all the support provided for this research and the support of UNESCO Chair in Transformative Education: Science, Communication and Society.

Conflicts of Interest: The authors declare no conflict of interest.

References

1. Riemenschneider, K.; Liu, J.; Powers, J.G. Skin cancer in the military: A systematic review of melanoma and nonmelanoma skin cancer incidence, prevention, and screening among active duty and veteran personnel. *J. Am. Acad. Dermatol.* **2018**, *78*, 1185–1192. [CrossRef] [PubMed]
2. Bain, J. Skin Cancer Risk in the Military. 2018. Available online: https://www.skincancer.org/blog/skin-cancer-risk-military/ (accessed on 4 July 2022).
3. Helmandollar, K.J.; Lorei, N.C.; Clement, B.C.; Hoverson, K.R.; Logemann, N.F. Management of Melanoma Patients by Non-Dermatologists in the Military Health System: A Retrospective Observational Study. *Mil. Med.* **2020**, *185*, 506–511. [CrossRef] [PubMed]
4. Gall, R.; Bongiorno, M.; Handfield, K. Skin Cancer in the US Military. *Cutis* **2021**, *107*, 29–33. [CrossRef]
5. Wisco, O.J.; Hajar, T.; Grande, D.J. Commentary: Skin cancer in the military. *J. Am. Acad. Dermatol.* **2018**, *78*, 1193–1194. [CrossRef] [PubMed]
6. Heckman, C.J.; Manne, S.L.; Kloss, J.D.; Bass, S.B.; Collins, B.; Lessin, S.R. Beliefs and intentions for skin protection and UV exposure in young adults. *Am. J. Health Behav.* **2011**, *35*, 699–711. [CrossRef]
7. Wolf, S.T.; Kenney, L.E.; Kenney, W.L. Ultraviolet radiation exposure, risk, and protection in military and outdoor athletes. *Curr. Sports Med. Rep.* **2020**, *19*, 137. [CrossRef]
8. Diepgen, T.L.; Mahler, V. The epidemiology of skin cancer. *Br. J. Dermatol.* **2002**, *146*, 1–6. [CrossRef]
9. De Vries, E.; Van De Poll-Franse, L.V.; Louwman, W.J.; De Gruijl, F.R.; Coebergh, J. Predictions of skin cancer incidence in the Netherlands up to 2015. *Br. J. Dermatol.* **2005**, *152*, 481–488. [CrossRef]
10. Hoey, S.; Devereux, C.; Murray, L.; Catney, D.; Gavin, A.; Kumar, S.; Donnelly, D.; Dolan, O.M. Skin cancer trends in Northern Ireland and consequences for provision of dermatology services. *Br. J. Dermatol.* **2007**, *156*, 1301–1307. [CrossRef]
11. Sáenz, S.; Conejo-Mir, J.; Cayuela, A. Melanoma epidemiology in spain. *Actas Dermo-Sifiliogr.* **2005**, *96*, 411–418. [CrossRef]
12. Staples, M.P.; Elwood, M.; Burton, R.C.; Williams, J.L.; Marks, R.; Giles, G.G. Non-melanoma skin cancer in Australia: The 2002 national survey and trends since 1985. *Med. J. Aust.* **2006**, *184*, 6–10. [CrossRef] [PubMed]
13. De Vries, E.; Coebergh, J.W. Cutaneous malignant melanoma in Europe. *Eur. J. Cancer* **2004**, *40*, 2355–2366. [CrossRef] [PubMed]
14. González, S.; Fernández-Lorente, M.; Gilaberte-Calzada, Y. The latest on skin photoprotection. *Clin Derm.* **2008**, *26*, 614–626. [CrossRef] [PubMed]
15. Wang, S.Q.; Balagula, Y.; Osterwalder, U. Photoprotection: A review of the current and future technologies. *Dermatol. Ther.* **2010**, *23*, 31–47. [CrossRef] [PubMed]
16. Saravanan, D. UV protection textile materials. *AUTEX Res. J.* **2007**, *7*, 53–62.

17. Baji, A.; Agarwal, K.; Oopath, S.V. Emerging developments in the use of electrospun fibers and membranes for protective clothing applications. *Polymers* **2020**, *12*, 492. [CrossRef]
18. Pakdel, E.; Naebe, M.; Kashi, S.; Cai, Z.; Xie, W.; Yuen, A.C.Y.; Montazer, M.; Sun, L.; Wang, X. Functional cotton fabric using hollow glass microspheres: Focus on thermal insulation, flame retardancy, UV-protection and acoustic performance. *Prog. Org. Coat.* **2020**, *141*, 105553. [CrossRef]
19. Gambichler, T.; Laperre, J.; Hoffmann, K. The European standard for sun-protective clothing: EN 13758. *J. Eur. Acad. Dermatol. Venereol.* **2006**, *20*, 125–130. [CrossRef]
20. Ray, A.; Singha, K.; Pandit, P.; Maity, S. Chapter 11—Advanced ultraviolet protective agents for textiles and clothing. In *Advances in Functional and Protective Textiles*; ul-Islam, S., Butola, B.S., Eds.; Woodhead Publishing: Cambridge, UK, 2020; pp. 243–260.
21. Kabir, S.M.; Dhar, A.K.; Koh, J. The influence of a natural UV absorber (*Areca catechu*) on the UV protection and antimicrobial properties of silk and nylon fabrics. *Fibers Polym.* **2021**, *22*, 382–386. [CrossRef]
22. Stock, M.L.; Gerrard, M.; Gibbons, F.X.; Dykstra, J.L.; Mahler, H.I.; Walsh, L.A.; Kulik, J.A. Sun protection intervention for highway workers: Long-term efficacy of UV photography and Skin cancer information on men's protective cognitions and behavior. *Ann. Behavioral. Med.* **2009**, *38*, 225–236. [CrossRef]
23. Julian, A.; Thorburn, S.; Geldhof, J. Health beliefs about UV and skin cancer risk behaviors. *Cancer Control* **2020**, *27*, 1073274819894008. [CrossRef]
24. Hamilton, K.; Kirkpatrick, A.; Rebar, A.; Hagger, M.S. Child sun safety: Application of an integrated behavior change model. *Health Psychol.* **2017**, *36*, 916. [CrossRef] [PubMed]
25. O'Riordan, D.L.; Steffen, A.D.; Lunde, K.B.; Gies, P. A Day at the beach while on tropical vacation: Sun protection practices in a high-risk setting for UV radiation exposure. *Arch. Dermatol.* **2008**, *144*, 1449–1455. [CrossRef] [PubMed]
26. SaeidiFard, N.; Haeri-Mehrizi, A.A.; Akbarzadeh, Z.; Janbozorgi, N.; Montazeri, A.; Yaseri, M.; Shab-Bidar, S. Association of health literacy and nutritional literacy with sun exposure in adults using structural equation modelling. *BMC Public Health* **2022**, *22*, 1162. [CrossRef] [PubMed]
27. Van Osch, L.; Reubsaet, A.; Lechner, L.; Candel, M.; Mercken, L.; De Vries, H. Predicting parental sunscreen use: Disentangling the role of action planning in the intention–behavior relationship. *Psychol. Health* **2008**, *23*, 829–847. [CrossRef] [PubMed]
28. Fan, Y.; Chen, J.; Shirkey, G.; John, R.; Wu, S.R.; Park, H.; Shao, C. Applications of structural equation modeling (SEM) in ecological studies: An updated review. *Ecol. Processes* **2016**, *5*, 1–12. [CrossRef]
29. Mueller, R.O.; Hancock, G.R. Structural equation modeling. In *The Reviewer's Guide to Quantitative Methods in the Social Sciences*; Routledge: London, UK, 2018; pp. 445–456.
30. Mueller, R.O. Structural equation modeling: Back to basics. *Struct. Equ. Model. Multidiscip. J.* **1997**, *4*, 353–369. [CrossRef]
31. Noar, S.M.; Myrick, J.G.; Zeitany, A.; Kelley, D.; Morales-Pico, B.; Thomas, N.E. Testing a social cognitive theory-based model of indoor tanning: Implications for skin cancer prevention messages. *Health Commun.* **2015**, *30*, 164–174. [CrossRef]
32. Raykov, T.; Marcoulides, G.A. A method for comparing completely standardized solutions in multiple groups. *Struct. Equ. Modeling* **2000**, *7*, 292–308. [CrossRef]
33. Abdalla, M.M.; Ribas, J.R.; da Costa Vieira, P.R. The antecedents of word of mouth intentions about a Brazilian tourist destination. *Tour. Manag. Stud.* **2014**, *10*, 104–111.
34. Hair, J.F.; Anderson, R.; Tatham, R.; Black, W. *Multivariate Data Analysis*; Pearson: New York, NY, USA, 2009.
35. Hagger, M.S.; Chatzisarantis, N.L. First-and higher-order models of attitudes, normative influence, and perceived behavioural control in the theory of planned behaviour. *Br. J. Soc. Psychol.* **2005**, *44*, 513–535. [CrossRef]
36. Fornell, C.; Larcker, D.F. Structural equation models with unobservable variables and measurement error: Algebra and statistics. *J. Mark. Res.* **1981**, *18*, 382–388. [CrossRef]